ABSTRACT

Title of Dissertation: MECHANISMS CONTROLLING PHOTOCHEMICAL LOSS OF OZONE IN THE MIDLATITUDE STRATOSPHERE

Laila V. Howar, Doctor of Philosophy, 2026

Dissertation directed by: Professor Ross J. Salawitch, Department of Atmospheric and Oceanic Science, Department of Chemistry and Biochemistry, Earth System Science Interdisciplinary Center

This dissertation evaluates various open-ended issues related to the depletion of stratospheric ozone in the midlatitude Northern Hemisphere (NH) stratosphere and identifies possible sources of uncertainty in global chemistry-climate model predictions of the future recovery of the ozone layer due to the harmful effects of ozone depleting substances. In-situ observations obtained during the Dynamics and Chemistry of the Summer Stratosphere (DCOTSS) mission were analyzed to assess why chlorine activation was not observed, despite the sampling of conditions that several prior studies suggested would lead to rapid heterogeneous chemistry and associated ozone loss in the midlatitude lower stratosphere (LS). Chlorine activation was found to be limited by the availability of inorganic chlorine, adequate partitioning of $ClONO_2$ and HCl to yield appreciable reaction rates, and elevated

levels of NO_x in the lowermost stratosphere from the lofting of boundary layer pollutants. Our chemical trajectory simulations showed that significant chlorine activation could occur for the conditions observed during DCOTSS if stratospheric sulfate surface area density were enhanced either by major volcanic eruptions, or climate intervention efforts that involve enhancement of stratospheric sulfate aerosols. Next, photochemical steady-state modeling of the DCOTSS dataset revealed that calculations employing the latest kinetic recommendations from the NASA Jet Propulsion Laboratory (JPL) compendium systematically overestimate observed NO_2 and $ClONO_2$ by 20-30% and 25-50%, respectively, and provide agreement with observed ClO within ± 5%, in the 18-21 km altitude region. A 500-member Monte Carlo simulation was used to determine that the data could be best fit by a ~23% increase in the formation rate of HNO_3 and a ~12% decrease in the formation rate of $ClONO_2$, relative to the latest JPL recommendation. Both reaction rate adjustments were shown to be more consistent with recommendations provided by the International Union of Pure and Applied Chemistry. The kinetic adjustments that allow for the best agreement between modeled and observed NO_2, $ClONO_2$, and ClO suggest that global models that use current JPL kinetic recommendations may overestimate NO_x-driven ozone loss in the lower stratosphere by ~9%, underestimate halogen-driven loss by ~25%, and underestimate the HO_x-driven loss by ~14%. Finally, trends in Cl_y ($HCl + ClONO_2$) and N_2O observed by the space-borne ACE-FTS instrument in the NH and Southern Hemisphere (SH) midlatitudes from 2004 to 2025 were compared to trends in Cl_y and N_2O simulated by eight global chemistry-climate models (CCMs). These comparisons reveal a slower observed decline of

stratospheric Cl_y than is simulated by the CCMs, particularly for the LS at NH midlatitudes. An estimate of the impact on trends in Cl_y of very short-lived chlorine compounds (VSL-Cl), which are produced by industrial processes and are not yet regulated by the Montreal Protocol and are not considered by the CCMs, led to better agreement between observed and modeled trends in Cl_y, particularly throughout the SH stratosphere and the NH upper stratosphere. For the NH lower stratosphere, the data revealed a decline in N_2O over the past two decades that is indicative of a major change in the stratospheric transport that is not represented in any of the models and is consistent with the observed slower than expected decline in Cl_y. Together, the results of this dissertation highlight the need to continue to improve our understanding of specific chemical and dynamical processes that regulate ozone in the midlatitude stratosphere, such as the formation rates of HNO_3 and $ClONO_2$; the cause of transport changes in the NH lower stratosphere over the past two decades; the role of VSL-Cl species; and, possible harm to the ozone layer by stratospheric sulfate injection.

MECHANISMS CONTROLLING PHOTOCHEMICAL LOSS OF OZONE IN THE MIDLATITUDE STRATOSPHERE

by

Laila Vadney Howar

Dissertation submitted to the Faculty of the Graduate School of the
University of Maryland, College Park, in partial fulfillment
of the requirements for the degree of
Doctor of Philosophy
2026

Advisory Committee:
Professor Ross J. Salawitch, Chair
Professor Timothy P. Canty
Professor Akua A. Asa-Awuku
Dr. Allison M. Ring
Dr. Kenneth E. Pickering

© Copyright by
Laila Vadney Howar
2026

Dedication

To my family and friends, for all their love and support along the way.

Acknowledgements

First and foremost, I would like to express my sincere gratitude to my advisor, Ross Salawitch. Without his support, guidance, and encouragement, I would not be the scientist I am today. The confidence he placed in me throughout this journey, and its many challenges, will always remain with me. I would also like to thank David Wilmouth, who has had great influence on my growth as a scientist and whose contributions were instrumental to the work presented in this dissertation. Next, I would like to thank the entire DCOTSS team, not only for their extraordinary efforts in planning and executing the successful flights and measurements that made much of this dissertation possible, but also for the support, mentorship, and wisdom shared during the many Science Team Meetings over the years. I'd also like to thank the many co-authors who contributed to the papers that form the foundation of this dissertation. Your expertise, feedback, and collaboration greatly improved the quality and impact of this work.

A special thank you goes to the faculty and students of the "AOSC-Chem Group", who provided encouragement, guidance, friendship, and support throughout my time at UMD. I have learned a tremendous amount from all of you, and I am grateful to have been part of such a welcoming and collaborative community. Lastly, I'd like to thank my family and friends, whose support I couldn't have done it all without.

Table of Contents

ABSTRACT 1
Dedication ii
Acknowledgements iii
Table of Contents iv
List of Tables vi
List of Figures vii
List of Abbreviations viii
Chapter 1 : Introduction 1
1.1 Photochemistry of Midlatitude Ozone 4
1.2 Large-scale Dynamical Processes 10
1.3 Threats to Ozone Layer Recovery 11
1.3.1 Greenhouse Gases 11
1.3.2 Halogenated Very-Short-Lived Substances (VSLs) 12
1.3.3 Overshooting Convection 15
1.3.4 Stratospheric Aerosol Enhancements 18
1.4 Slower-than-expected Recovery of Midlatitude Ozone 20
1.5 Outline 22
Chapter 2 : Conditions Necessary for Chlorine Activation in the Midlatitude Summer Lower Stratosphere 25
2.1 Introduction 25
2.2 Data and Methods 29
2.2.1 Measurements 29
2.2.2 Estimate of Cl_y 30
2.2.3 Estimate of NO 34
2.2.4 Photodissociation Frequencies 36
2.2.5 Trajectory Model Description 38
2.2.6 Photochemical Steady State (PSS) Model Description 42
2.3 Results 44
2.3.1 The 10 June 2022 DCOTSS Flight 51
2.3.2 NAMA Summer of 2022 66
2.3.3 Geoengineering and Major Volcanic Eruptions 74
2.4 Conclusions 82
Appendix A 86
Chapter 3 : Quantification of the Effect of Kinetic Uncertainties on Photochemical Loss of Ozone in the Midlatitude Stratosphere 102
3.1 Introduction 102
3.2 Methods 105
3.2.1 Photochemical Steady-State (PSS) Box Model 106
3.2.2 Kinetic Uncertainties and Monte Carlo Simulations 108
3.3 Results and Discussion 112
3.3.1 Measured and Modeled NO_2, $ClONO_2$, and ClO 112
3.3.2 Prior Literature and IUPAC 121
3.3.3 Catalytic Ozone Loss Pathways 126

3.4 Conclusions 128
Appendix B 131
Chapter 4 : Observed and Modeled Trends of Inorganic Chlorine and Nitrous Oxide in the Midlatitude Stratosphere 142
4.1 Introduction 142
4.2 Methods 145
4.2.1 ACE-FTS Retrievals 145
4.2.2 Jungfraujoch Columns 146
4.2.3 EESC, VSL-Cl, Fluorine from HFCs 147
4.2.4 Chemistry-Climate Model Output 150
4.3 Results and Discussion 152
4.3.1 Analysis of ACE-FTS and CCMI-2022 Profiles 152
4.3.2 Analysis of Jungfraujoch Columns 163
4.4 Concluding Remarks 168
Appendix C 173
Chapter 5 : Conclusions and Future Opportunities 178
5.1 Summary and Conclusions 178
5.2 Future Directions 180
5.3 Contributions to Other Papers 187
Bibliography 192

List of Tables

Table 2.1. DCOTSS NASA ER-2 In Situ Measurements Used in This Study 29
Table 3.1. Reactions Assessed and Associated Rate Coefficient Uncertainties. 110
Table 3.2. Average Kinetic Adjustments to 12 key reactions. 119
Table 4.1. List of the CCMI-2022 Models Used in This Study 151

List of Figures

Figure 1.1. Ozone trends in the stratosphere from 2000 to 2020 3
Figure 1.2. Longitudinally averaged cross-section of ozone number density 10
Figure 1.3. Time series of stratospheric chlorine from source gas injection 14
Figure 1.4. The dependence of heterogeneous chlorine activation 17
Figure 1.5. Daily mean mixing ratios of HCl, and ClO 19
Figure 1.6. Time series of total inorganic chlorine 21
Figure 2.1. [H_2O] versus temperature 45
Figure 2.2. Daytime (solar zenith angle <90°) measurements of [O_3] versus [H_2O] 48
Figure 2.3. Time series of the 10 June 2022 research flight 52
Figure 2.4. Flight track for the 10 June 2022 research flight 54
Figure 2.5. Chemical back-trajectory model simulation 58
Figure 2.6. Chemical back-trajectory model simulation 60
Figure 2.7. Mixing ratios of chlorine and nitrogen species modeled forward 62
Figure 2.8. DCOTSS 2022 [NO_x] versus [$ClONO_2$]/[Cl_y] 67
Figure 2.9. Ratio of [NO_2] measured by the CANOE instrument to [NO_2] calculated 68
Figure 2.10. ACE-FTS version 5.2 data obtained over 30–60°N during 2022 70
Figure 2.11. Daytime (solar zenith angle <90°) measurements of [$ClONO_2$] 73
Figure 2.12. ClO mixing ratio at the end of 5-day model simulations 80
Figure 3.1. Average absolute percent change in modeled VMRs 110
Figure 3.2. Measured (black) and modeled (blue) mixing ratios 113
Figure 3.3. Time series for the $\theta \geq 430$ K portion of the 5 June 2022 research flight. 115
Figure 3.4. Modeled versus measured mixing ratios 117
Figure 3.5. Multiplicative scale factors for the members of the MC subset 119
Figure 3.6. Recommended rate coefficients 123
Figure 3.7. 24-hour averaged model output of fraction of total odd-oxygen loss 127
Figure 4.1. Profiles of HCl (a, e), $ClONO_2$ (b, f), HCl+$ClONO_2$ (c, g), and N_2O (d, h) 153
Figure 4.2. Same as Figure 4.1, except for SH midlatitudes 154
Figure 4.3. Trends in HCl+$ClONO_2$ (a, c) and N_2O (b, d) 155
Figure 4.4. Same as for Figure 4.3 159
Figure 4.5. Time series of June-to-November monthly mean total column abundances 164
Figure 4.6. Time series of the ratio of total column 167
Figure 5.1. Laboratory-determined solubility of HCl 182
Figure 5.2. Organic sulfate-mass fractions 183
Figure 5.3. Volume mixing ratios of ClO 184
Figure 5.4. Calculated total inorganic chlorine 189

List of Abbreviations

ACCLIP	Asian Summer Monsoon Chemical and CLimate Impact Project
ACE-FTS	Atmospheric Chemistry Experiment Fourier Transform Spectrometer
ANY	Australian New Years wildfires
AoA	Age of Air
ASM	Asian Summer Monsoon
BDC	Brewer Dobson Circulation
CBr_y	Organic Bromine
CCl_y	Organic Chlorine
CCM	Chemistry-Climate Model
CCMI	Chemistry-Climate Model Initiative
CFCs	Chlorofluorocarbons
Cl_y	Inorganic chlorine
CONUS	Contiguous United States
DCOTSS	Dynamics and Chemistry of the Summer Stratosphere
EESC	Equivalent Effective Stratospheric Chlorine
FRF	Fractional Release Factors
FTIR	Fourier Transform Infrared Spectroscopy
F_y	Fluorine product gases
GHG	Greenhouse Gas
HCFCs	Hydrochlorofluorocarbons
IUPAC	International Union of Pure and Applied Chemistry
JPL-2019	2019 Kinetic recommendations from the NASA Jet Propulsion Laboratory

LS	Lower Stratosphere
MC	Monte Carlo
NAMA	North American Monsoon Anticyclone
NDACC	Network for the Detection of Atmospheric Composition Change
NH	Northern Hemisphere
NO_y	Total nitrogen oxides
ODSs	Ozone-Depleting Substances
PGI	Product Gas Injection
POLARIS	Photochemistry of Ozone Loss in the Arctic Region in Summer
PSS	Photochemical steady state
PyroCb	Pyro-cumulonimbus clouds
QBO	Quasi-biennial oscillation
SAD	Surface Area Density
SGI	Source Gas Injection
SH	Southern Hemisphere
SPARC	Stratosphere-troposphere Processes and their Role in Climate
SSA	Stratospheric Sulfate Aerosols
SZA	Solar Zenith Angle
TROPOMI	TROPOspheric Monitoring Instrument
UTLS	upper troposphere-lower stratosphere
VMR	Volume Mixing Ratio
VSLS	Very Short-Lived Substances
WMO	World Meteorological Organization

Chapter 1 : Introduction

The stratospheric ozone layer shields life on Earth from the Sun's harmful ultraviolet (UV) radiation, which can damage DNA in plants and animals (Barnes et al., 2019; Bernhard et al., 2020). The stratosphere extends from the tropopause (~10−15 km) up to ~50 km and contains around 90% of atmospheric ozone. The ozone layer extends globally and refers to the ~15 to 35 km altitude region, in which the highest concentrations of ozone occur. Stratospheric ozone absorbs UV-B (280−315 nm) radiation from the Sun, which would otherwise reach Earth's surface and make life unsustainable (Brash et al., 1991; Tevini & Teramura, 1989). In the mid-1970s it was discovered that chlorine (Molina & Rowland, 1974) and bromine (Wofsy et al., 1975) (i.e., halogen) containing species participate in a series of chemical reactions that destroy stratospheric ozone. Halogen source gases, most notably, chlorofluorocarbons (CFCs), are human-made long-lived chemicals that were historically used in refrigeration, air conditioning, and as foam blowing agents (e.g., Salawitch et al., 2022). The release of chlorine and bromine atoms from the photolytic decomposition of these anthropogenically sourced ozone-depleting substances (ODSs) caused large reductions in global stratospheric ozone in the late 20th century (Salawitch et al., 2005). Chlorine and bromine containing ozone depleting substances also drive the Antarctic ozone hole, the extensive chemical removal of large amounts of ozone in the Southern Hemisphere polar vortex that occurs each austral spring (McElroy et al., 1986; L. T. Molina & Molina, 1987; Solomon et al., 1986). The Montreal Protocol (1987) established international regulations on the production and consumption of these long-lived halogen source gases. As a result of the Montreal Protocol regulations, the rapid decline in global total column ozone came to a halt in the late 1990s.

Figure 1.1 from the WMO 2022 Scientific Assessment of Ozone Depletion (SAOD) report shows trends in ozone derived from satellite observations and chemistry-climate model simulations (CCMs) from 2000 to 2020 in the Southern Hemisphere (SH) midlatitudes (35°S-60°S), the tropics (20°S-20°N), and the Northern Hemisphere (NH) midlatitudes (35°N-60°N) (WMO, 2022). Observations show clear recovery of stratospheric ozone above 10 hPa (about 30 km altitude) that is well simulated by current CCMs (Figure 1.1; WMO, 2022). However, in the lower stratosphere (below 50 hPa or about 20 km altitude), ozone continued to decline over the 2000 to 2020 time period, particularly at SH and NH midlatitudes, despite the CCM simulated increase. The negative trend for ozone in the tropics is simulated relatively well by CCMs, which has been attributed to an increase in the strength of the Brewer Dobson Circulation (BDC) that injects clean (that is, low ozone) air into the tropical lower stratosphere. The tendency for observed ozone at midlatitudes to lag the modeled recovery extends to the 2022 Chemistry Climate Model Initiative (CCMI-2022), which is the latest set of simulations prepared for the 2026 WMO SAOD report (e.g., Benito-Barca et al., 2025). Currently, there is no clear consensus as to why ozone in the midlatitude lower stratosphere continues to decline, and why models fail to capture these trends in the NH. These model simulations are key for informing policymakers on anthropogenically induced perturbations to stratosphere ozone, as such, there is an urgent need to establish the cause of continued lower stratospheric ozone reductions.

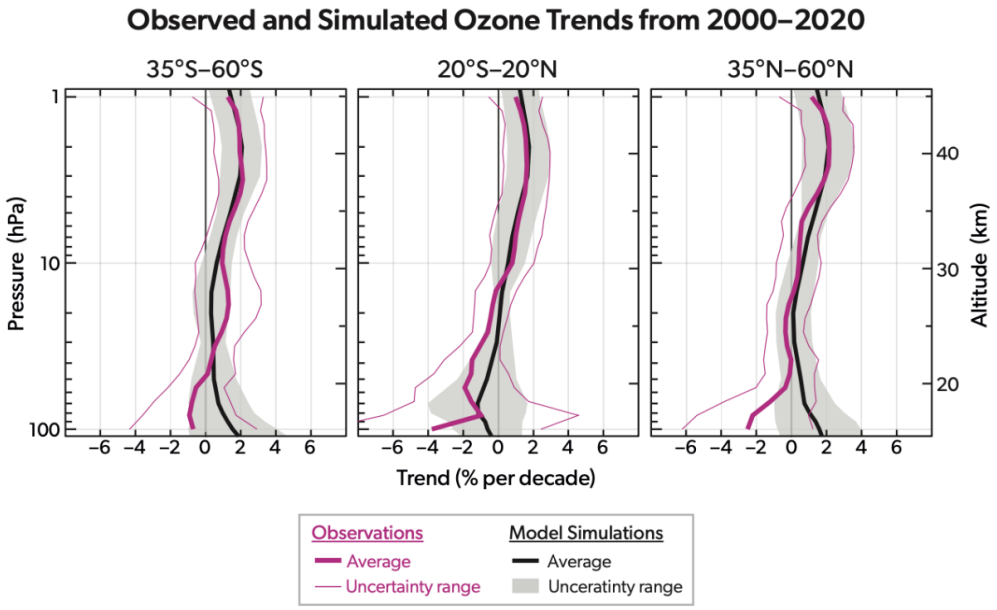


Figure 1.1. Ozone trends in the stratosphere from 2000 to 2020 for the Southern Hemisphere (SH) midlatitudes (35°S-60°S), the tropics (20°S-20°N), and the Northern Hemisphere (NH) midlatitudes (35°N-60°N).Ozone trends derived from chemistry-climate model output are shown in black, where the shading represents the range of uncertainty associated with these model runs. Ozone trends derived from satellite observations are shown in thick magenta lines, where the thin magenta lines represent the range of uncertainty in these observations. Figure ES-5 from the WMO 2022 Scientific Assessment of Ozone Depletion report (WMO, 2022).

There are several emerging and well-established issues that may complicate the recovery of ozone back to pre-1980 levels. Anthropogenic perturbations to climate and stratospheric composition are large sources of uncertainty in ozone layer recovery predictions (WMO, 2022). Recently, the impact of massive wildfires and volcanic eruptions that deposit material into the stratosphere, as well as extreme meteorological conditions, have been implicated as important new factors that have reduced the thickness of the ozone layer (Salawitch et al., 2025 and references therein). While the abundance of halogens in the stratosphere has substantially declined due to the success of the Montreal Protocol, there remain unregulated ODSs that are increasingly contributing to stratospheric halogen levels with rising emissions at the surface (Chipperfield et al., 2020; Hossaini et al., 2015, 2017, 2019). The most important unregulated ODSs are very-short-lived (VSL) chlorine species using in a variety of industrial applications (Laube et al., 2022) as well as minor HCFCs and CFCs emitted to the atmosphere inadvertently

in the chemical feedstock process (Lickley et al., 2024; Vollmer et al., 2021). Increasing greenhouse gas (GHG) concentrations and associated climatic changes will affect stratospheric ozone by altering chemical composition, temperature, tropospheric transport, and circulation patterns (Dhomse et al., 2018; Fleming et al., 2011; Keeble et al., 2021). The interplay of strong dynamic variability, changing large-scale circulation patterns, and evolving atmospheric composition make the midlatitude NH lower stratosphere especially challenging for models to simulate.

This dissertation aims to contribute to the understanding of mechanisms controlling photochemical loss of ozone in the midlatitude NH lower stratosphere and possible sources of uncertainty in global chemistry-climate model predictions of ozone recovery. Chapter 2 of this dissertation evaluates mechanisms that inhibit or enable heterogeneously perturbed ozone loss by anthropogenic halogens in the midlatitude LS. Chapter 3 of this dissertation uses photochemical steady-state model simulations to evaluate the effect of kinetic uncertainties on modeled chlorine and nitrogen partitioning and catalytic ozone loss pathways. Chapter 4 evaluates whether the slower-than-expected recovery of ozone in the midlatitude NH can be attributed to dynamic influences, or inadequate representation of inorganic chlorine by global chemistry-climate models. Finally, Chapter 5 of this dissertation summarizes the work presented in Chapters 2 to 4 and provides recommendations for future studies that build upon these findings.

1.1 Photochemistry of Midlatitude Ozone

The abundance of ozone in the midlatitude lowermost stratosphere is controlled by stratospheric transport, as well as photochemical production and loss (e.g., Garney et al., 2022; Keeble et al., 2021; Oman, et al., 2010a). Chapman (1930) proposed the stratospheric ozone layer can be understood by a simple sequence of reactions (R1−R4) that cycle odd oxygen (O_x =

$O + O_3$). The production of stratospheric ozone occurs through a two-step process involving the photodissociation of O_2 (R1) to form two atomic oxygens, followed by the recombination of O_2 and O to form ozone (R2):

(R1) $O_2 + h\nu \rightarrow O + O$

(R2) $O + O_2 + M \rightarrow O_3 + M$

According to the Chapman (1930) theoretical mechanism, production of ozone is balanced by loss through photodissociation (R3), and reaction with atomic oxygen (R4):

(R3) $O_3 + h\nu \rightarrow O_2 + O$

(R4) $O + O_3 \rightarrow O_2 + O_2$

The cycling of odd-oxygen described by (R1−R4), known as the Chapman Mechanism (Chapman, 1930), was the first photochemical theory to explain the production and loss of stratospheric ozone, and to predict the concentration of ozone that would be present in the stratosphere.

It was later realized that the observed concentration of ozone in the stratosphere is much less than predicted by the Chapman mechanism. Catalytic cycles involving nitrogen oxide radicals ($NO_x = NO + NO_2$), hydrogen oxide radicals ($HO_x = OH + HO_2$), chlorine radicals ($ClO_x = Cl + ClO$), and bromine radicals ($BrO_x = Br + BrO$) (e.g., Bates & Nicolet, 1950; Crutzen, 1970; Molina & Rowland, 1974; Wofsy et al., 1975) also contribute to stratospheric ozone destruction. In the midlatitude stratosphere, catalytic ozone destruction is rate-limited by the following reactions (R5−R11) involving the NO_x, HO_x, ClO_x, and BrO_x families, where each catalytic cycle leads to the loss of two odd oxygens.

(R5) $HO_2 + O_3 \rightarrow OH + 2O_2$

(R6) $NO_2 + O \rightarrow NO + O_2$

(R7) $ClO + O \rightarrow Cl + O_2$

(R8) $ClO + HO_2 \rightarrow HOCl + O_2$

(R9) $ClO + BrO \rightarrow ClOO + Br$
$\rightarrow BrCl + O_2$

(R10) $BrO + HO_2 \rightarrow HOBr + O_2$

(R11) $BrO + O \rightarrow Br + O_2$

The distribution of sunlight, temperature, radical species, and atomic oxygen determine the efficiency of each catalytic cycle. As such, the relative contributions of the catalytic cycles are highly dependent on altitude, latitude, and season. The influence of chemical, thermal, or radiative perturbations on stratospheric ozone depends largely on what catalytic ozone destruction cycle dominates (Wennberg et al., 1994). Understanding the relative role of each catalytic ozone destruction cycle is important for assessing how stratospheric ozone will respond to future anthropogenic perturbations.

Hydrogen oxide radicals (HO_x) are produced by the oxidation of water vapor ($H_2O + O(^1D) \rightarrow OH + OH$) and methane ($CH_4 + O(^1D) \rightarrow OH + CH_3$) in the stratosphere. While water vapor is a natural source of stratospheric HO_x, its abundance has increased due to rising temperature at the cold point tropopause (Yue et al., 2019). Although methane (CH_4) has both natural (e.g., wetlands) and anthropogenic sources (e.g., agriculture, fossil fuels, and decomposing landfill waste), approximately 65% of the current emissions are estimated to be from human activity and the surface concentration of CH_4 is rising at about 0.7%/year (Jackson et al., 2024). HO_x-catalyzed ozone loss (Bates and Nicolet, 1950) dominates below ~25 km through the following reaction sequences (R12 & R5).

(R12) $OH + O_3 \rightarrow HO_2 + O_3$

(R5) $HO_2 + O_3 \rightarrow OH + 2\ O_2$

Net: $O_3 + O_2 \rightarrow 3\ O_2$

An additional HO_x-catalyzed ozone loss cycle rate-limited by $HO_2 + O \rightarrow O_2 + OH$ is important at altitudes above ~45 km (Bates and Nicolet, 1950). This cycle becomes important at higher altitudes, compared to R5, due to the larger abundance of atomic oxygen.

Stratospheric nitrogen oxides (NO_x) are primarily derived from surface emissions of nitrous oxide (N_2O). N_2O has been termed the dominant ozone-depleting substance of the 21st century (Ravishankara et al., 2009), with rising emissions primarily associated with the agricultural industry and fertilizer use (Tian et al., 2024). In the high-altitude stratosphere, N_2O decomposes by photolysis and reaction with $O(^1D)$. The decomposition of N_2O by reaction with $O(^1D)$ is the primary source of stratospheric NO_x (Minschwaner et al., 1993). However, NO_x can also be introduced into the stratosphere by high-flying aircraft emissions (e.g., Crutzen et al., 1972), solar proton events (Solomon & Crutzen, 1981), lightning production (Pickering et al., 2024), and boundary layer pollution lofted up into the stratosphere by overshooting convection (Howar et al., 2025; Poulida et al., 1996). Ozone loss catalyzed by NO_x radicals primarily occurs between 22 to 45 km and results in the loss of two odd oxygens through the following sequence of reactions (R13 & R6) (e.g., Crutzen, 1970, 1971).

(R13) $NO + O_3 \rightarrow NO_2 + O_2$

(R6) $NO_2 + O \rightarrow NO + O_2$

Net: $O_3 + O \rightarrow 2\ O_2$

Stratospheric chlorine and bromine radicals ($ClO_x = Cl + ClO$, $BrO_x = Br + BrO$) are primarily produced from the photodecomposition of long-lived halogen containing compounds, such as chlorofluorocarbons (CFCs), halons, methyl bromide (CH_3Br), hydrochlorofluorocarbons (HCFCs), carbon tetrachloride (CCl_4), and methyl chloroform (CH_3CCl_3) (e.g., Salawitch et al., 2022). These gases comprise the principal ODSs. The long

lifetimes of these source gases in the troposphere allow them to reach the midlatitude lower stratosphere in about three years, and the polar stratosphere in about 5 to 6 years (Engel et al., 2018). Once in the stratosphere, these compounds photodissociate and release reactive Cl and/or Br atoms that participate in catalytic ozone destruction. Loss of HCFCs, CH_3CCl_3, and CH_3Br primarily occur in the troposphere via reaction with OH. Therefore, these species have considerably shorter lifetimes compared to non-hydrogen containing ODSs. Stratospheric halogens also originate from the decomposition of VSL compounds that are not regulated under the Montreal Protocol, discussed further in Section 1.3.2. The amount a VSL species contributes to the total stratospheric halogen budget depends on their lifetime, solubility of resulting product gases, and how quickly emissions are transported into the stratosphere (Liang et al., 2025; Wales et al., 2018). Chlorine-catalyzed ozone loss peaks around ~40 km (Osterman et al., 1997), where volume mixing ratios (VMRs) of ClO maximize. This cycle occurs through the following sequence of reactions (R14 & R7) (Molina & Rowland, 1974; Stolarski & Cicerone, 1974).

(R14) $Cl + O_3 \rightarrow ClO + O_2$

(R7) $ClO + O \rightarrow Cl + O_2$

Net: $O_3 + O \rightarrow 2\ O_2$

In the midlatitude stratosphere, most of inorganic chlorine is bound in reservoir species of HCl and $ClONO_2$, rather than reactive ClO_x (Cl + ClO) (Michelsen et al., 1996; Raymond et al., 2026). The partitioning between reactive and reservoir forms of chlorine is strongly determined by formation of $ClONO_2$ by the three-body reaction of ClO with NO_2 as well as the reaction of Cl with CH_4 that produces HCl. The abundance of reactive forms is greatly enhanced by heterogeneous reactions on the surface of liquid or solid aerosols, which primarily occurs in the cold, wintertime, polar stratosphere (McElroy et al., 1986; Solomon et al., 1986).

The principal heterogeneous reaction that controls photochemical loss of ozone in the midlatitude LS is the hydrolysis of N_2O_5 on sulfate aerosols (R15) (Fahey et al., 1993; McElroy et al., 1992).

(R15) $N_2O_5 + H_2O \rightarrow 2\ HNO_3$

The hydrolysis of N_2O_5 on sulfate aerosols modulates NO_x-catalyzed ozone loss, which enhances photochemical loss of ozone by anthropogenic halogens, under both background conditions for sulfate surface area and times where SSA is enhanced following volcanic eruptions. Heterogeneous reactions involving the chlorine reservoirs (HCl, $ClONO_2$) typically occur under very cold conditions ($T \lesssim 195$ K) in the polar regions and are responsible for extensive spring-time ozone depletion in the polar vortices (McElroy et al., 1986; Solomon et al., 1986).

(R16) $ClONO_2 + HCl \rightarrow HNO_3 + Cl_2$

(R17) $ClONO_2 + H_2O \rightarrow HOCl + HNO_3$

(R18) $HOCl + HCl \rightarrow H_2O + Cl_2$

While these reactions (R16−R18) primarily occur in the polar regions on cold aerosol surfaces, they have been known to occur in midlatitude lower stratosphere during periods of time when stratospheric sulfate aerosols (SSA) are enhanced following major volcanic eruptions (Hofmann & Solomon, 1989; Keim, Fahey, Del Negro, et al., 1996). The rate at which reservoir chlorine is converted into reactive chlorine on the surface of liquid or solid aerosols can be altered under conditions of lower temperature, elevated water vapor, and increased aerosol loading, as discussed in Section 1.3.3 and Section 1.3.4.

1.2 Large-scale Dynamical Processes

In addition to photochemical production and loss mechanisms described above, atmospheric transport and the stratospheric overturning Brewer Dobson Circulation (BDC), are key factors determining the global distribution of ozone (Brewer, 1949; Butchart, 2014; Holton et al., 1995). The BDC describes the large-scale transport of ozone and other trace gases from the tropical tropopause towards the poles. Figure 1.2, from Shaw & Shepherd (2008), shows a longitudinally averaged cross-section of ozone number density as observed by the OSIRIS satellite instrument in March 2004. The arrows in Figure 1.2 illustrate the transport of ozone from the tropics to poles by the BDC, which is particularly active in the winter hemisphere.

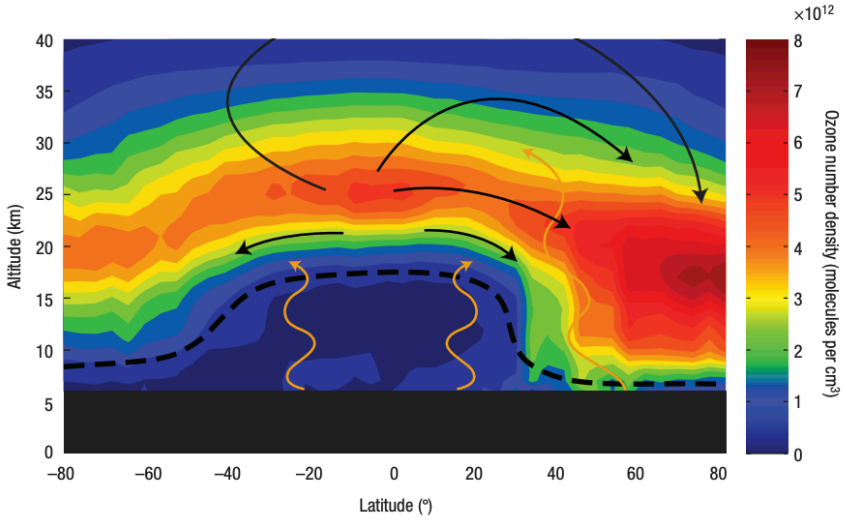


Figure 1.2. Longitudinally averaged cross-section of ozone number density observed by the OSIRIS satellite instrument in March 2004 depicting the Brewer Dobson Circulation. The orange wiggly arrows depict the propagation of tropospheric waves. The dashed line represented to tropopause. The solid black arrows illustrate the mean meridional transport pattern of the Brewer Dobson circulation in the winter hemisphere. Figure 1 from Shaw and Shepard (2008).

The BDC circulation is driven by the breaking and dissipation of planetary-scale waves (Haynes et al., 1991) and is characterized by upwelling in the tropics, poleward transport, and descent in middle to high latitudes. The BDC contains two poleward transport components known as the shallow and deep branches (Baikhadzhaev et al., 2025). The deep branch of the

BDC extends into the upper stratosphere and is particularly strong during winter in each hemisphere (Birner & Bönisch, 2011). The faster shallow branch of the BDC persists year-round in the lower stratosphere of each hemisphere and is driven by the breaking of synoptic-scale waves (Plumb, 2002). Quasi-horizontal mixing induced by the breaking of synoptic and planetary-scale waves also influences the transport and distribution of trace gases in the stratosphere (Marcy et al., 2004; Plumb, 2002; Shepherd, 2007). Given the very long photochemical lifetime of ozone in the lower stratosphere, dynamics have a strong influence on ozone trends in the midlatitude LS. Interannual and long-term changes in the strength of the BDC can significantly impact midlatitude ozone trends (e.g., Fusco & Salby, 1999; Salby & Callaghan, 2004). In addition, synoptic wave forcing events, as well as changes in tropical and polar circulation patterns such as the Quasi-Biennial Oscillation (QBO) and the Arctic Oscillation (AO) (Dall'Amico et al., 2010) also play a role in midlatitude ozone variability.

1.3 Threats to Ozone Layer Recovery

1.3.1 Greenhouse Gases

Rising concentrations of greenhouse gases, such as carbon dioxide (CO_2), methane (CH_4), and nitrous oxide (N_2O) complicate the timing of the recovery of stratospheric ozone back to pre-1980 levels. Stratospheric ozone column is expected to decline in response to rising N_2O concentrations (Ravishankara et al., 2009; Revell et al., 2012) and increase in response to rising concentrations of CH_4 and CO_2 (Fleming et al., 2011; Revell et al., 2012). N_2O provides a source of NO_x in the stratosphere, effectively increasing NO_x catalyzed ozone loss, while also modulating loss with respect to HO_x and halogens (Fleming et al., 2011; Revell et al., 2012). Rising CH_4 concentrations increase in HO_x-catalyzed ozone loss in the upper stratosphere through OH production ($CH_4 + O(^1D) \rightarrow H_2O + OH$) and decrease ClO_x-catalyzed loss through

chlorine deactivation ($Cl + CH_4 \rightarrow HCl + CH_3$) (e.g., Brasseur and Solomon, 2005). Water vapor produced from the oxidation of CH_4 leads to radiative cooling of the middle stratosphere, which slows down rate-limiting ozone destruction reactions, mainly by the suppression of the atomic-O to O_3 ratio (Rosenfield et al., 2002; Vogel et al., 2011). Rising levels of CO_2 cause a net cooling of the stratosphere and are expected to accelerate the BDC, which would lead to a net increase in global stratospheric ozone (Chiodo & Polvani, 2019; Shepherd & McLandress, 2011). The strengthening of the BDC is projected to initiate a super recovery of ozone in the midlatitudes and polar regions, and permanent depletion in the tropics (Dhomse et al., 2018; Oman,et al., 2010b). However, such acceleration and associated super-recovery in middle to high latitudes has yet to be confirmed by observations (Garny et al., 2024). Moreover, climatic changes induced by rising greenhouse gas concentrations are expected to increase wildfire activity and strengthen convective transport into the stratosphere, both of which could have important consequences for stratospheric ozone, as discussed in Sections 1.3.3 and 1.3.4.

1.3.2 Halogenated Very-Short-Lived Substances (VSLs)

Long-lived halogen source gases dissociate in the stratosphere and release reactive halogen species (Cl and/or Br) that participate in catalytic ozone depletion. Since the phase out of these ODSs by the Montreal Protocol in 1987, the total chlorine and bromine content of ODSs in the global troposphere has declined, as shown in Figure ES-1 of (WMO, 2022). However, the response of inorganic chlorine in the stratosphere has not been nearly as fast as the decline of organic precursors (Hossaini et al., 2019; Salawitch et al., 2025; see also Figure 1-12 of WMO (2022)). Rising emissions of unregulated VSL chlorine species (Hossaini et al., 2015, 2019), as well as CCl_4 and minor HCFCs and CFCs emitted to the atmosphere inadvertently in the chemical feedstock process (Lickley et al., 2024; Vollmer et al., 2021) play a role in the slower

than expected decline of stratospheric, inorganic chlorine. Here, VSL species are defined as halogen containing organic compounds with lifetimes for loss in the global troposphere of 0.5 years or less. These gases have historically been thought to be primarily lost in the global troposphere (Ko et al., 2003), which is one reason why VSL chlorine gases are not yet regulated by the Montreal Protocol. However, VSLs can rapidly be transported into the lower stratosphere by strong convective updrafts, where they can contribute to chlorine-catalyzed ozone depletion (Bednarz et al., 2022, 2023; Pan et al., 2024; Wales et al., 2018). The efficiency at which VSL-Cl substances are transported into the stratosphere by deep convection remains an uncertainty in quantifying stratospheric chlorine levels (Filus et al., 2020). While VSL-Cl species are primarily anthropogenically sourced, VSL-Br species are natural in origin (Salawitch, 2005; Wales et al., 2018). With rising stratospheric abundances estimated to be between 2.5 ppt Cl /year (Dubé et al., 2018) to 3.8 ppt Cl/year (Hossaini et al., 2019), VSL-Cl species are becoming an increasingly important source of stratospheric chlorine. The VSL-Cl source of stratospheric chlorine might be particularly important over heavily populated regions where deep convection and anthropogenic emissions coincide (Lauther et al., 2022; Pan et al., 2024; Roozitalab et al., 2024).

The most important VSL-Cl species are dichloromethane (CH_2Cl_2), chloroform ($CHCl_3$), 1,2-dichloroethane ($C_2H_4Cl_2$), and perchloroethylene (C_2Cl_4). These species are primarily emitted by various anthropogenic activities (e.g., Claxton et al., 2020). Figure 1.3 shows a time series of observed (filled circles) and modeled (solid lines) stratospheric chlorine from source gas injection of these four primary VSL-Cl species (WMO, 2022).

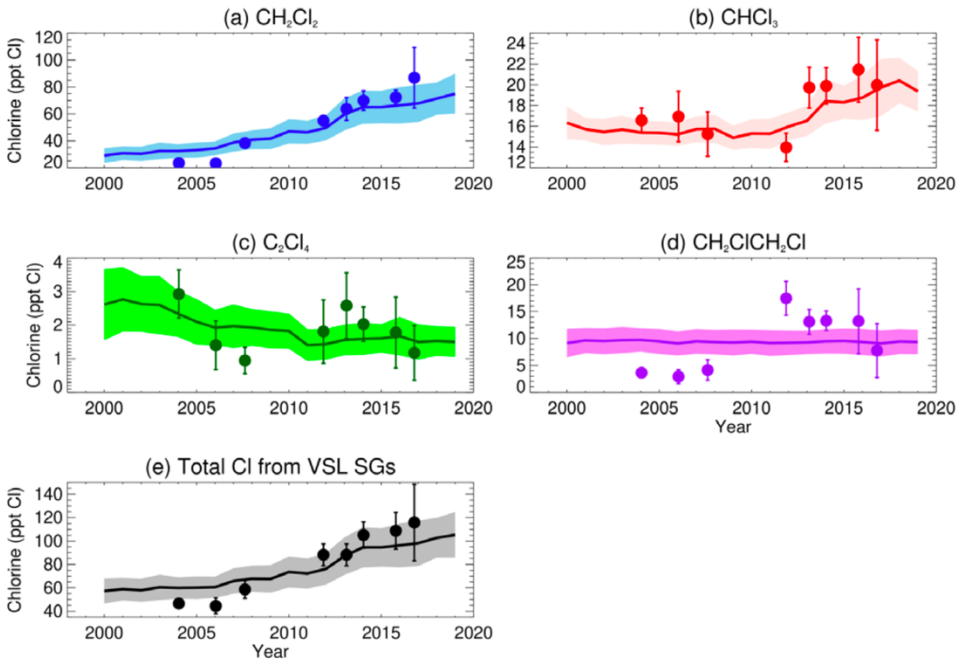


Figure 1.3. Time series of stratospheric chlorine from source gas injection of (a) CH_2Cl_2, (b) $CHCl_3$, (c) C_2Cl_4, (d) CH_2ClCH_2Cl, and (e) total derived from 3-D chemical-transport model simulations (solid lines) and aircraft observations (filled circles). Figure 1-8 from the WMO 2022 Ozone Assessment Report (WMO, 2022).

Total Cl from VSL-Cl source gases has increased from ~60 ppt in the year to 2000 to ~140 ppt by 2021 (Figure 1.3e). The species in which have largest contribution to stratospheric chlorine (dichloromethane and chloroform) are rising steadily over the 2000 to 2021 time period (Figure 1.3a, b). Bednarz et al. (2023) and Dubé et al. (2025b) suggest that future, rising VSL-Cl emissions have a significant impact on total stratospheric chlorine abundances and the expected decline of stratospheric Cl_y back to pre-1980 levels. Current CCMs used to evaluate the recovery of ozone and inform policymaking decisions regarding regulations of ODSs do not include VSL-Cl species (Plummer et al., 2021). As such, VSL-Cl poses a threat to the expected, future recovery of the ozone layer (Bednarz et al., 2023; Chipperfield & Bekki, 2024; Dubé et al., 2025b).

1.3.3 Overshooting Convection

An emerging area of concern is the increasing frequency and intensity of tropopause-penetrating convection, driven by rising global mean temperatures, and the impact on midlatitude stratospheric chemistry and dynamics (e.g., Homeyer & Bowman, 2021). Convective transport of pollutants, trace gases, and water vapor into the lower stratosphere (Poulida et al., 1996) can significantly alter the budgets of stratospheric ozone, NO_x, Cl_y, and HO_x (Fadnavis et al., 2015; Huntrieser et al., 2016a,b; Ott et al., 2009; Pan et al., 2024; Stenchikov et al., 1996). This transport pathway is especially important in regions where deep convection and elevated anthropogenic emissions coincide, such as in the Asian and North American Monsoonal regions (Fischer et al., 2003; Lauther et al., 2022; Li et al., 2005; Pan et al., 2024; Roozitalab et al., 2024). While the impact on the stratosphere of these intense overshooting storms has been studied several decades (Santee et al., 2017), their influence on the chemical, dynamical, and radiative balance of the stratosphere is not fully understood (Clapp et al., 2021).

Injection of H_2O into the stratosphere can augment HO_x-catalyzed ozone loss via production of OH ($H_2O + O(^1D) \rightarrow 2OH$) (Evan et al., 2023) and potentially accelerate ClO_x-catalyzed ozone loss via heterogeneous chlorine activation (Anderson et al., 2012, 2017; Robrecht et al., 2019). Strong convective updrafts also provide an efficient transport pathway for VSL-Cl species to enter the stratosphere, where they can contribute to ClO_x-catalyzed ozone depletion (Ko et al., 2003; Pan et al., 2024). In addition, lightning and upward lofting of boundary layer pollutants associated with intense convective storms can provide an additional source of NO_x in the LS (Dickerson et al., 1994; Pickering et al., 2024), potentially enhancing NO_x-catalyzed depletion of stratospheric ozone.

Models and observations show that summertime convection within the North American Monsoon Anticyclone (NAMA) has a significant influence on the composition of the lower stratosphere over North America (Clapp et al., 2021; Homeyer et al., 2023; Homeyer & Bowman, 2021; Weinstock et al., 2007). During the summer months over the United States deep convective storm systems provide significant amounts of water vapor into the stratosphere (e.g., Homeyer et al., 2023). The North American Monsoon anticyclone (NAMA) acts to partially confine and isolate air masses over CONUS during the summer months. This confinement allows convectively induced water vapor enhancements to persist in the lower stratosphere for periods of a few days to over a week (Weinstock et al., 2007).

Several studies have suggested that tropopause-overshooting convection over CONUS during the summer months can facilitate heterogeneous conversion of chlorine reservoirs (HCl, $ClONO_2$) into reactive ClO, at a level that would rapidly accelerate photochemical loss of ozone in the midlatitude LS (Anderson et al., 2012, 2017; Robrecht et al., 2019). Figure 1.4 shows the dependence of heterogeneous chlorine activation on temperature, water vapor and sulfate loading.

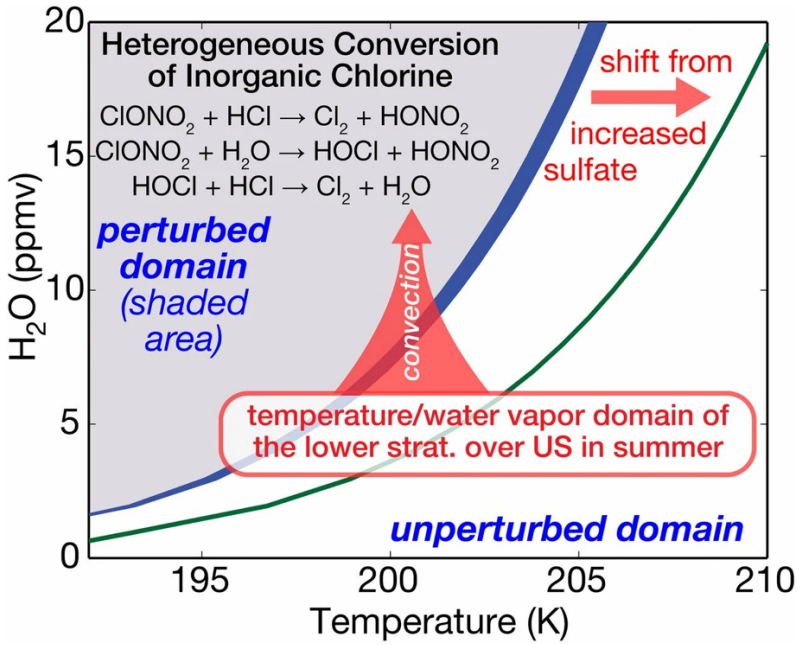


Figure 1.4. The dependence of heterogeneous chlorine activation on temperature, water vapor, and sulfate loading. The green and blue lines represent the threshold at which 10% of chlorine is activated on the order of one day for background aerosol loading (2 $\mu m^2/cm^3$) and enhanced aerosol surface area density (20 $\mu m^2/cm^3$), respectively. Figure taken from Anderson et al. (2012).

The non-linear temperature and water vapor dependence of these reactions allows them to occur at very low temperatures of the polar vortex (≤195 K) (Drdla & Müller, 2012), and in the midlatitudes when levels of water vapor and/or sulfate aerosols are enhanced well above background levels (Anderson et al., 2012). While this process is well understood in polar regions, its relevance to midlatitude ozone depletion is still debated, particularly in the context of increasing convective activity, changes to the stratospheric aerosol layer, cooling of the stratosphere, and increasing anthropogenic emissions of VSL-Cl species. In Chapter 2 of this dissertation, published last year (Howar et al., 2025), we use observations of ClO and many other species obtained during the NASA DCOTSS mission to test the hypothesis that tropopause-overshooting convection over CONUS during summer months facilitates the heterogeneous conversion of chlorine reservoirs (HCl, $ClONO_2$) into reactive ClO.

1.3.4 Stratospheric Aerosol Enhancements

It is well known that stratospheric aerosol enhancements from volcanic eruptions cause rapid ozone depletion by accelerating heterogeneous reactions that enhance reactive chlorine (ClO_x) and sequester reactive NO_x. The eruption of Mount Pinatubo in June 1991 led to record ozone depletion in the Northern Hemisphere due to heterogeneous chemistry that persisted for several years (Hofmann et al., 1994; Keim et al., 1996; Kinnison et al., 1994; Salawitch et al., 2005). However, less well known is the impact that deliberate sulfate injections (Tilmes et al., 2008, 2012) or wildfire plumes may have on stratospheric ozone (Salawitch & McBride, 2022).

Sulfate geoengineering is a potential climate mitigation strategy involving the deliberate injection of sulfate aerosols into the stratosphere to reflect incoming solar radiation and moderate the rise of global mean surface temperature (Bernhard et al., 2020; Crutzen, 2006; National Academies of Sciences, 2021; Tracy et al., 2022; Visioni et al., 2023). This mitigation strategy proposes to inject amounts of sulfate into the stratosphere equivalent or equal to the magnitudes observed in the stratosphere following the eruption of Mount Pinatubo in 1991 (Haywood et al., 2022). The extensive ozone loss that occurred in the NH midlatitude LS stratosphere following this eruption demonstrates the susceptibility of this region to such aerosol enhancements and the threat this mitigation strategy could impose on the health of the ozone layer (Salawitch et al., 2025).

Pyrocumulonimbus (PyroCb) plumes have been observed to cause extensive ozone depletion in the SH midlatitudes. Figure 1.5 shows observations of HCl and ClO from the Microwave Limb Sounder (MLS) and the Atmospheric Chemistry Experiment Fourier Transform Spectrometer (ACE-FTS) collected during the 2020 Australian New Year (ANY) wildfires (red), compared to the climatological averages (black) (Salawitch et al., 2025; Santee,

2022; Solomon et al., 2023). Model calculations assuming standard hydrolysis of N_2O_5 on sulfate aerosols are shown in the green, while calculations that incorporate enhanced solubility of HCl on organic wildfire aerosols are shown in blue.

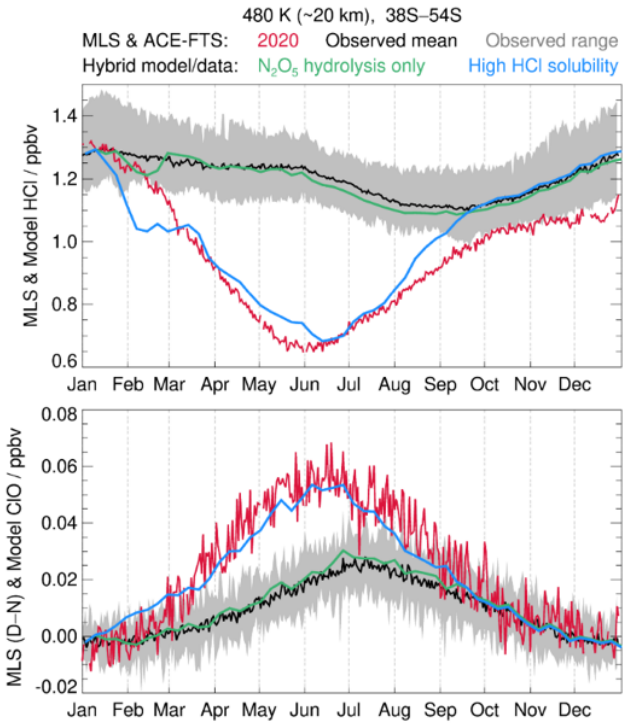


Figure 1.5. Daily mean mixing ratios of HCl, and ClO at the 480 K potential temperature level for 38°S−54°S. The red curves show observations obtained in 2020, while the black curves a show the climatological mean and variability for the 2005−2019 period. Model calculations in which incorporate only N_2O_5 on sulfate aerosols are shown in green, and simulations that incorporate the enhanced solubility of HCl on organic aerosols are shown in blue. Figure 6 from Salawitch et al. (2025), adapted from Santee et al. (2022) and Solomon et al. (2023).

Figure 1.5 shows that substantial suppressions in HCl and large enhancements in ClO observed following the ANY wildfires are likely a result of the enhanced solubility of HCl on organic aerosols and subsequent heterogeneous chlorine activation (Solomon et al., 2023). This event demonstrated that heterogeneous chlorine activation can occur efficiently on organic aerosols produced from extreme wildfires. However, it is unknown how an event of such magnitude would influence stratospheric ozone in the NH. Given that wildfires are expected to increase in frequency and intensity with rising global mean temperatures, understanding the

impact of such perturbations on the stratospheric ozone layer is of crucial importance (Salawitch et al., 2025).

1.4 Slower-than-expected Recovery of Midlatitude Ozone

Chemistry-climate models (CCMs) are used to assess past and future changes in global ozone distributions. The recovery of ozone is primarily dependent on stratospheric halogen abundances and changes in the Brewer Dobson circulation (e.g., Wargan et al., 2018; Weber et al., 2022). CCM simulations and observations are in good agreement that ozone in the upper stratosphere ($\gtrsim$ 32 km) of both hemispheres is recovering in response to declining ODSs regulated under the Montreal Protocol (e.g., Eyring et al., 2010). However, in the NH midlatitude LS, ozone has been on a continuous decline since 1998 (Ball et al., 2018) and current CCMs are unable to reproduce this negative trend (Ball et al., 2020). For the 2000-2020 time period in the NH midlatitudes, chemistry-climate models simulate a ~2% increase per decade in lower stratospheric ozone, whereas merged satellite observations indicate a decline of ~2% per decade over the same period (Figure 1.1) (WMO, 2022). Understanding and resolving this model-observation discrepancy for the midlatitude lower stratosphere (LS) is essential for ensuring the full recovery of the global stratospheric ozone layer.

Several theories have been proposed to explain the lack of recovery of ozone in the NH midlatitude LS. Dynamic influences such as variations in the strength and structure of atmospheric circulation and patterns, have been proposed as contributing factors (Ball et al., 2020; Orbe et al., 2020; Wargan et al., 2018). Circulation changes occurring in response to rising GHGs are not simulated well by most CCM in the NH midlatitudes (Engel et al., 2017; Garny et al., 2024). CCMs simulate much faster transport by the BDC in the NH middle stratosphere ($p <$ 50 hPa) than observational records suggest (Garny et al., 2024). Rising emissions of unregulated

halogenated compounds, such as VSL-Cl and feedstock chemicals, have also been suggested to possibly delay the recovery of NH midaltitude ozone if remained unregulated (Dubé et al., 2025a; Hossaini et al., 2017, 2019, 2024). Dubé et al. (2025a) show that the decline in stratospheric chlorine observed by ACE-FTS from 2004 to 2020 is inconsistent with the tropospheric decline of long-lived ODSs regulated by the Montreal Protocol. For the midlatitude LS, they find that this offset can be explained by rising VSL-Cl species (Dubé et al., 2025a). In addition, 3-D chemical transport model (CTM) simulations supported by aircraft observations indicate that rising VSL-Cl have offset the decline in upper stratospheric HCl by 15% for the 2004 to 2017 time period (Hossaini et al. 2019). It is unclear whether rising VSLS are responsible for the slower-than-expected recovery of ozone in the midlatitude LS.

Few studies of ozone recovery have quantitatively assessed the accuracy of stratospheric halogen simulations in models in the midlatitude lower stratosphere. Figure 1.6 from the (Salawitch, 2022) compares total inorganic chlorine (Cl_y) at 46.5°N from 6 CCM models based on the use of N_2O to select 3 yr old air, to the observed time series of $HCl+ClONO_2$ from the ground-based FTIR instrument deployed at Jungfraujoch, Switzerland (46.54°N, 7.98°E).

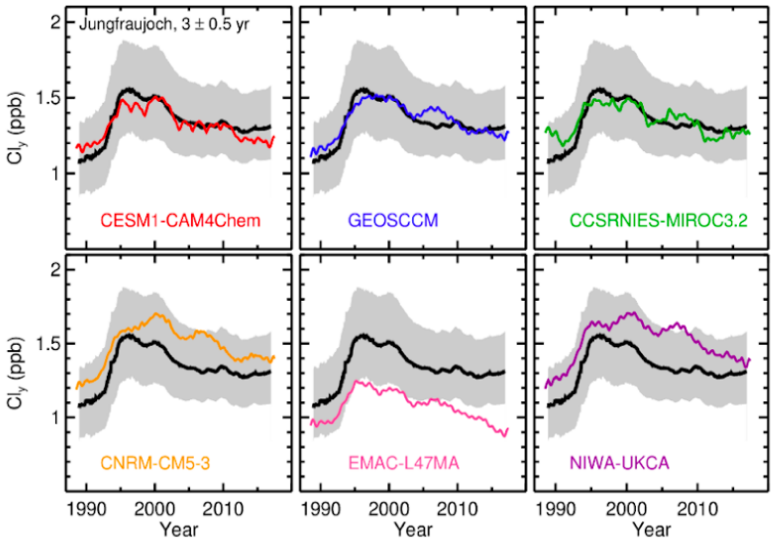


Figure 1.6. Time series of total inorganic chlorine for 3 yr old air from the REF-C2 run of 6 CCMI models at 46.5°N and $HCl+ClONO_2$ observed over Jungfraujoch (black line). The grey shading indicates the range of

$HCl+ClONO_2$ for 3 ± 0.5 yr old air. Here, N_2O was used to identify 3 yr old air. Figure from Salawitch (2022) NASA proposal (Salawitch, 2022).

This figure shows that while some models provide remarkably accurate simulations of stratospheric inorganic Cl measured at a long-running station, others fall either above or below the data (Figure 1.6). An accurate representation of stratospheric chlorine by global models (in the midlatitude lower stratosphere) is essential for providing accurate return dates of Cl_y to pre-1980 levels used in global ozone assessments to guide policy making decisions.

1.5 Outline

The body of work encompassed in this dissertation utilizes aircraft observations, photochemical steady-state modeling, satellite retrievals, and global chemistry-climate model output to evaluate mechanisms controlling photochemical loss of ozone in the midlatitude LS and possible sources of uncertainty in global chemistry-climate model predictions of ozone recovery.

Chapter 2 of this dissertation evaluates conditions necessary for heterogeneous chlorine activation in the NH midlatitude LS. This work utilizes measurements obtained in the midlatitude NH LS during the Dynamics and Chemistry of the Summer Stratosphere (DCOTSS) mission to investigate a theory set forth by Anderson et al. (2012) that convective injection of water vapor into the stratosphere could dramatically accelerate chlorine activation and ozone loss in the NH midlatitude LS. During the DCOTSS mission, substantial stratospheric water vapor enhancements were observed within plumes that had overshot the tropopause. However, this work reveals chlorine activation large enough to affect photochemical loss of ozone was not observed during either summer deployment, despite the sampling of conditions in which prior studies suggested rapid heterogenous chemistry would occur (Anderson et al., 2012, 2017; Robrecht et al., 2019). For the cold, wet airmasses observed during DCOTSS, our modeling and

observational analysis shows that chlorine activation was primarily limited by availability of inorganic chlorine (Cl_y) and chlorine nitrate ($ClONO_2$), and insufficient time to reduce the large amount of NO_x present in these air masses. This work shows that the injection of sulfate into the stratosphere, at levels sufficient to mitigate global warming, would lead to chlorine activation at a level that could result in catalytic loss of stratospheric ozone for the conditions observed during DCOTSS. This work has been published as Howar et al. (2025).

In Chapter 3, photochemical steady-state box model simulations are compared to in-situ observations of NO_2, $ClONO_2$, and ClO obtained during the DCOTSS mission. Photochemical steady-state modeling analysis of the DCOTSS dataset reveals that calculations employing current kinetic recommendations from the Jet Propulsion Laboratory (JPL) kinetic compendium (Burkholder et al., 2019) systematically overestimate observed NO_2 and $ClONO_2$ in the 18 to 21 km altitude region. Monte Carlo simulations presented in Chapter 3 reveal that a faster rate for nitric acid formation (+23%) and a slower rate for chlorine nitrate formation (-12%), substantially improve the agreement between observations and model output. The kinetic adjustments in which were found to provide the best model observation agreement, imply that the current JPL-2019 kinetic recommendations may overestimate NO_x-catalyzed ozone loss and underestimate loss with respect to halogens and hydrogen oxides. This work highlights areas in which future atmospheric work and/or laboratory studies may be needed and identifies a possible important source of uncertainty in global-chemistry climate model predictions of ozone layer recovery.

In Chapter 4 we compare trends in Cl_y ($HCl+ClONO_2$) and N_2O observed by ACE-FTS and simulated by CCMI-2022 models for the 2004−2025 time period. We also examine the evolution of total column chlorine ($HCl+ClONO_2$) and total column fluorine ($HF+2xCOF_2$)

observed by ground-based Fourier-Transform Infrared Spectrometer (FTIR) stationed over Jungfraujoch, Switzerland (46.54°N, 7.98°E) from 1990 to 2025. The motivation of this investigation is to evaluate whether the slower-than-expected recovery of ozone in the NH LS can be attributed to changes in stratospheric halogen abundances, or rather, changes in global circulations patterns. ACE-FTS data show that chlorine in the NH midlatitude lower stratosphere is not declining as quickly as expected, based on projections assuming compliance with the Montreal Protocol. Trends in N_2O observed by ACE-FTS indicate structural changes in the BDC have occurred over the 2004-2025 time period. Current CCMs are unable to reproduce the observed trends in N_2O and $HCl+ClONO_2$ in the NH lower stratosphere. We show that these model-observation discrepancies likely source from model deficiencies in dynamics, as well as an incomplete representation of inorganic chlorine sources, such as very-short-lived chlorine species.

Chapter 2 : Conditions Necessary for Chlorine Activation in the Midlatitude Summer Lower Stratosphere

2.1 Introduction

The abundance of ozone in the midlatitude lowermost stratosphere (LS) is controlled by stratospheric transport as well as photochemical loss (e.g., Garny et al., 2022; Keeble et al., 2021; Oman et al., 2010b). It has long been recognized that the reaction of gas phase N_2O_5 on sulfuric acid droplets is an important process for increasing photochemical loss of ozone in the midlatitude LS by anthropogenic halogens, under both background conditions for sulfate surface area in the LS (Fahey et al., 1993; Hofmann & Solomon, 1989; McElroy et al., 1992; Solomon, 1999) and periods of time when sulfate surface area is enhanced following major volcanic eruptions (Fahey et al., 1993; Kinnison et al., 1994; Salawitch et al., 2005; Solomon et al., 1996; Wilmouth et al., 2023). Building on this framework, Anderson et al. (2012) proposed that localized, enhanced mixing ratios of stratospheric water vapor (H_2O) driven by convective injection into the LS during summer over the central United States (US) could enhance the photochemical loss of ozone due to heterogeneous chemical reactions involving HCl and $ClONO_2$ for temperatures in the range of 200–205 K. The rate of these reactions exhibit a strong non-linear dependence as a function of temperature and water vapor such that they can occur rapidly at the very low temperatures of the polar vortex ($\lesssim$195 K) (Drdla & Müller, 2012), as well as in the midlatitude LS when the H_2O mixing ratio is elevated well above background (Anderson et al., 2012).

The theory of enhanced photochemical loss of ozone due to chlorine activation (i.e., elevated mixing ratios of ClO, hereafter [ClO]), driven by heterogeneous reactions involving

HCl and $ClONO_2$ has received considerable attention in the past decade. Anderson et al. (2017) analyzed Next-Generation Weather Radar (NEXRAD) network data and showed that convective overshoots associated with the North American Monsoon Anticyclone (NAMA) would lead to enhanced [H_2O] in regions of the LS that are both cold enough and have sufficient amounts of total inorganic chlorine (Cl_y) to increase the risk of ozone loss over the Great Plains region of the US. Robrecht et al. (2019) evaluated the [H_2O] threshold necessary for chlorine activation to occur in the LS over North America, and concluded that [ClO] could exceed 100 parts per trillion by volume (pptv) if [H_2O] was as high as 15 parts per million by volume (ppmv) (which is about a factor of three larger than background levels of [H_2O] in the midlatitude LS), with loss of O_3 occurring if low temperatures and elevated [H_2O] persist for 24–36 hr. The [ClO] ≅ 100 pptv value calculated by Robrecht et al. (2019) was found for a model run with [Cl_y] = 156 pptv. As an important point of reference, the model run highlighted by Anderson et al. (2012) assumed [Cl_y] = 1,000 pptv, but at a higher altitude. [Cl_y] increases with both altitude and latitude. As discussed in Section 2.3 of this work, the Anderson et al. (2012) and Robrecht et al. (2019) studies had notable differences in the assumed abundance of [NO_x] ([NO] + [NO_2]) and [$ClONO_2$]/[Cl_y].

Elevated [ClO] in the midlatitude, lower stratosphere has been observed. Keim et al. (1996) reported in situ observations of [ClO] that reached nearly 100 pptv in the LS over North America together with near-zero [NO_x], which was ascribed to chlorine activation and suppression of NO_x by heterogeneous reactions involving N_2O_5, HCl, and $ClONO_2$. The enhanced [ClO] layer of Keim et al. (1996) extended over a 0.5 km range of altitude and was associated with [H_2O] ~16 ppmv, temperatures as low as ~206 K, and sulfate surface area density (SAD) enhanced by the eruption of Mount Pinatubo. Smaller enhancements of [ClO]

were observed in regions of the lower stratosphere, at background levels of [H_2O], due to enhancements of SAD following this eruption. These volcanically induced enhancements of [ClO] led to reductions in total column ozone (TCO) at midlatitudes of both hemispheres due to photochemical loss caused by reactions involving ClO and BrO, which are particularly important upon consideration of the supply of stratospheric bromine from short-lived biogenic compounds (Salawitch et al., 2005).

Analyses of satellite measurements over North America have shown that some, but not all, of the conditions needed for chlorine activation commonly occur. Schwartz et al. (2013) examined measurements of [H_2O], [HCl], and [ClO] from the Microwave Limb Sounder (MLS) on the NASA Aura satellite together with temperature from the Goddard Earth Observing System version 5 (GEOS-5) data assimilation system. They concluded that air parcels are commonly cold and wet enough for chlorine activation to occur. However, [HCl] was observed by MLS to be between about 200 and 400 pptv for background conditions that would be conducive to chlorine activation if "wet enough", over the pressure range 82.5–100 hPa, with an estimated 2 sigma uncertainty <200 pptv (Livesey et al., 2011). This amount of [HCl] falls below the 850 pptv of [HCl] assumed by Anderson et al. (2012), yet is above the value of [HCl] highlighted by Robrecht et al. (2019) of 149.5 pptv. The Robrecht et al. (2019) value for [HCl] of 149.5 pptv is based on in situ observations of [CH_4] obtained in the northern hemisphere (NH) midlatitude LS during the SEAC^{4}RS campaign in 2013, combined with a Cl_y versus CH_4 relation based on measurements of halogens from the Atmospheric Chemistry Experiment Fourier Transform Spectrometer (ACE-FTS) instrument. Schwartz et al. (2013) deemed MLS measurements of [ClO] at 100 hPa too uncertain to "preclude definitive confirmation of the chlorine activation posited in Anderson et al. (2012)".

Schoeberl et al. (2020) examined a decade's worth of data from MLS and the Ozone Monitoring Instrument on Aura, along with meteorological fields for the LS over North America. They concluded that the most significant effect of the NAMA on TCO was caused by meteorological uplift of the tropopause that under certain circumstances could drive up to a 20 DU reduction in TCO, which could be accompanied by a small amount of chemically induced loss of TCO (between ~1 and 8.4 DU of loss, depending on available Cl_y). This 1 to 8.4 DU chemical loss of TCO is considerably smaller than the 7% column reduction for altitudes below 18 km (where convective plumes are most commonly observed) that was estimated using a box model by Anderson and Clapp (2018). Schoeberl et al. (2020) also stated that "it is possible that heterogeneous chemistry is taking place [in the LS over the US] within a layer too shallow to be detected by MLS".

We investigate the potential for chlorine activation in the midlatitude LS using measurements of temperature, pressure, [ClO], [$ClONO_2$], [NO_2], [H_2O], [O_3], organic halogens, aerosol surface area density (SAD), and related quantities acquired over North America during the summers of 2021 and 2022 by instruments aboard the NASA ER-2 aircraft during the Dynamics and Chemistry of the Summer Stratosphere (DCOTSS) mission (Bowman et al., 2026). Several of the DCOTSS flights conducted during both summers were specifically designed to assess chemical conditions within air masses that had convectively overshot the local tropopause (Homeyer et al., 2023). We evaluate conditions necessary for chlorine activation based on data analysis, backward and forward chemical trajectory modeling, as well as a comparison of data collected by instruments aboard the ER-2 with observations from the ACE-FTS on the SCISAT satellite (Boone et al., 2023). In our trajectory model simulations, ozone is held constant because of its long photochemical lifetime in the midlatitude LS. Our focus is

primarily on data collected during summer 2022, because the sampling of cold, wet conditions needed for chlorine activation tends to be more frequent during this summer compared to 2021. In Section 2.2, we provide a description of the measurements and modeling framework. Results are discussed in Section 2.3, followed by concluding remarks in Section 2.4.

2.2 Data and Methods

2.2.1 Measurements

We use measurements obtained during the NASA DCOTSS field campaign conducted during the summers of 2021 and 2022 out of Salina, Kansas (Bowman et al., 2026; Homeyer et al., 2023). During this mission, convective outflow within the region of the NAMA was extensively sampled using a suite of instruments aboard the NASA ER-2. Aircraft observations obtained during DCOTSS (NASA/LARC/SD/ASDC, 2022a) used in this study, along with measurement uncertainties, are detailed in Table 2.1. A few quantities important to our analyses were not measured during DCOTSS and are estimated along the ER-2 flight tracks in various manners. In particular, the mixing ratio of total inorganic chlorine [Cl_y] is inferred from the decomposition of organic chlorine species, as described in Section 2.2.2. [HCl] is estimated from the difference between [Cl_y] and the sum of [ClO] and [$ClONO_2$], both of which are measured by the HAL instrument.

Table 2.1. DCOTSS NASA ER-2 In Situ Measurements Used in This Study

Instrument	Species	Data Precision ± Accuracy	References
Harvard Halogens (HAL)	ClO	2 pptv ± 17%	Stimpfle et al., 2004; Wilmouth et al. (2026)
	$ClONO_2$	5 pptv ± 20%	
Harvard Herriott Hygrometer (HHH) as part of	H_2O	< 0.10 ppmv ± 5–10%	Weinstock et al., 1994; Hintsa et al., 1999; Sargent et al., 2013

Harvard Water Vapor (HWV)			
Advanced Whole air Sampler (AWAS)	Organic Cl gases (CFCs, HCFCs, Halons, VSLS), Ethane	± ~2–20%	Smith et al., 2024; Pan et al., 2024
UAS Chromatograph for Atmospheric Trace Species (UCATS)	O_3	2 ppbv + 2%	Hintsa et al., 2021
	N_2O	1.5 ppbv ± 0.5%	
	SF_6	0.05 pptv ± 0.5%	
	CFC-11	~1% ± 0.5%	
Harvard University Picarro Cavity Ringdown Spectrometer (HUPCRS)	CO	3.2 ppbv ± 1.25 ppbv	Pittman et al., 2025
	CH_4	0.2 ppbv ± 3.6 ppbv	
Compact Airborne Nitrogen diOxide Experiment (CANOE)	NO_2	50 pptv ± 10%	St. Clair et al., 2019
DCOTSS Portable Optical Particle Spectrometer (DPOPS)	Aerosol Surface Area Density (SAD)	± 20%	Li et al., 2023
Meteorological Measurement System (MMS)	Temperature (T)	0.05 K ± 0.3 K	Scott et al., 1990
	Pressure (p)	0.003 hPa ± 0.3 hPa	
	Potential Temperature (θ)	± 0.5–1.5 K	

2.2.2 Estimate of Cl_y

A key part of our analysis involves estimating the mixing ratio of total inorganic chlorine, [Cl_y], along each ER-2 flight track. For this estimate, we use a suite of organic chlorine gas measurements (see Text 2A.1 in Appendix A) obtained by the Advanced Whole Air Sampler

(AWAS) (Pan et al., 2024; Smith et al., 2024) and [CFC-11] measured by the UAS Chromatograph for Atmospheric Trace Species (UCATS) (Hintsa et al., 2021) instrument on the ER-2 during the DCOTSS campaign. The UCATS measurements are reported as dry-air mole fraction, which we treat as being equivalent to part per volume mixing ratio (VMR). Our estimate of [Cl_y] is based on the method described in Woodbridge et al. (1995), where inorganic chlorine is calculated as the difference between total organic chlorine measured at the tropopause [$Cl_{TOT\text{-}TROP}$] and organic chlorine measured in the stratosphere [CCl_y]; that is, [Cl_y] = [$Cl_{TOT\text{-}TROP}$] − [CCl_y]. This difference is calculated as a function of [CFC-11] and represents the photochemical conversion of chlorine from organic to inorganic form as parcels progress further into the stratosphere and are exposed to high-energy photons and oxidants such as OH and $O(^1D)$. A quadratic fit is used to approximate the [Cl_y] versus [CFC-11] relation to account for the slight curvature in the data, following the approach of Woodbridge et al. (1995).

[CCl_y] is derived from the atomic-weighted total chlorine content of all organic chlorine species measured by the AWAS instrument. During DCOTSS, ~32 AWAS samples were acquired for each flight, leading to a time spacing of approximately 10 min between samples (Pan et al., 2024; Smith et al., 2024). We compute [CCl_y] with and without the consideration of Very Short-Lived (VSL) chlorine species as a function of [CFC-11] as measured by AWAS (Figure 2A.1 in Appendix A). Here, as is common in the literature, VSL chlorine species refers to gases with photochemical lifetimes for removal less than 0.5 years (Ko et al., 2003), which are not regulated by the Montreal Protocol (Laube et al., 2022). The formulation of CCl_y that considers only long-lived source gases, [CCl_y^{LL}], includes the 12 principal chlorinated ozone-depleting substances (ODSs) that are highlighted in Table 7A-1 of the 2022 Scientific Assessment of Ozone Depletion report (Daniel et al., 2022) (see Text 2A.1 in Appendix A). The

formulation of CCl_y that includes both long-lived and VSL chlorine species, [CCl_y^{LL+VSL}], includes the 12 principal chlorinated ODSs as well as [CH_2Cl_2], [$CHCl_3$], [C_2Cl_4], [CH_2ClCH_2Cl], [$CHBrCl_2$], [$CHBr_2Cl$], and [CH_2BrCl], all measured by AWAS. We do not include $C_3H_6Cl_2$ in the suite of VSL-Cl compounds, even though this species was reported to be present at mixing ratios as high as 70 pptv in the outflow of the East Asian summer monsoon (Pan et al., 2024), because measurements of this compound were not available during DCOTSS. The high levels of $C_3H_6Cl_2$ measured during ACCLIP are influenced by source regions in East Asia, and this compound is lost rapidly (lifetime of about 20 days) due to reaction with OH (Perry et al., 1977). Therefore, measurements obtained during ACCLIP are likely not representative of concentrations present within convectively influenced air masses in the NAMA (Lauther et al., 2022; Roozitalab et al., 2024).

[$Cl_{TOT\text{-}TROP}$] is the total amount of organic chlorine (CCl_y) at the time of stratospheric entry. We determine [$Cl_{TOT\text{-}TROP}$] at the time of DCOTSS by evaluating the quadratic relationship between [CCl_y] and [CFC-11] at [CFC-11] specified at the tropopause, [CFC-11_{TROP}] (see Figure 2A.1 in Appendix A). Two estimates of [CFC-11_{TROP}] are used in our computation of [$Cl_{TOT\text{-}TROP}$]: one assumes that [CFC-11_{TROP}] is equal to the globally averaged tropospheric value of [CFC-11] given in Table 7A-1 of Daniel et al. (2022), interpolated to the appropriate summer (i.e., either summer of 2021 or 2022). The other estimate of [CFC-11_{TROP}] uses the average value of [CFC-11] measured at the dynamic tropopause (potential vorticity = 2×10^{-6} m^2 s^{-1} K kg^{-1}) during DCOTSS by the UCATS instrument (see Text 2A.1 of Appendix A for additional details). Here, the corresponding globally and locally derived values of [$Cl_{TOT\text{-}TROP}$] represent the uncertainty in the tropospheric origin of sampled air and define the upper and lower limits of our LL and LL + VSL estimates.

Due to the success of the Montreal Protocol, [$Cl_{TOT\text{-}TROP}$] has been steadily declining over time (Daniel et al., 2022; WMO, 2022). Therefore, to accurately assess [$Cl_{TOT\text{-}TROP}$], we must consider how the amount of chlorine entering the stratosphere has changed over time (Woodbridge et al., 1995). We use measurements of [SF_6] from the UCATS instrument (Hintsa et al., 2021) along each flight track, together with NOAA Global Monitoring Laboratory (GML) ground-based, monthly surface mean measurements of [SF_6] (Dutton et al., 2023), to estimate the time of stratospheric entry (Engel et al., 2002; Ray et al., 2024). We determine the time of stratospheric entry as the date for which [SF_6] observed in the stratosphere during DCOTSS matches the GML ground-based measurement of [SF_6]. We then use the time series of ODS mixing ratios given in Table 7A-1 of Daniel et al. (2022) to determine how much higher chlorine levels were at the time of stratospheric entry, which is reflected by the slight slope in the lines for [$Cl_{TOT\text{-}TROP}$] shown in Figure 2A.1 in Appendix A. This [$Cl_{TOT\text{-}TROP}$] age of air correction is time-based and not a function of [CFC-11_{TROP}]; therefore, no adjustment is applied to [CFC-11_{TROP}]. The upper and lower limits of our [$Cl_{TOT\text{-}TROP}$] estimate mentioned previously, are further distinguished by which aggregate of GML [SF_6] surface measurements—either Global average or NH average—are used to estimate the time of stratospheric entry (see Text 2A.1 in Appendix A for additional details).

Using the upper and lower limits of our time-corrected [$Cl_{TOT\text{-}TROP}^{LL}$] and [$Cl_{TOT\text{-}TROP}^{LL+VSL}$] estimates, we compute four versions of [Cl_y] to provide a robust estimate of uncertainty (see Figure 2A.1 in Appendix A). The variation among the four [Cl_y] estimates ([$Cl_y{}^{LL}{}_{Lower\text{-}Limit}$], [$Cl_y{}^{LL}{}_{Upper\text{-}Limit}$], [$Cl_y{}^{LL+VSL}{}_{Lower\text{-}Limit}$], [$Cl_y{}^{LL+VSL}{}_{Upper\text{-}Limit}$]) represents the uncertainty in the contribution of VSL chlorine (VSL-Cl) and the origin of the air sampled. We define our "best estimate" of [Cl_y] as the average between [$Cl_y{}^{LL}{}_{Lower\text{-}Limit}$] and [$Cl_y{}^{LL+VSL}{}_{Upper\text{-}$

$_{Limit}$]. We compute [Cl_y] for each UCATS measurement of [CFC-11] along every ER-2 flight track. UCATS measurements of [CFC-11] are available at a much higher time resolution (approximately every 75 s) than AWAS measurements of [CFC-11] (about every 10 min). Scatter plots of AWAS [CFC-11] versus UCATS [CFC-11] (averaged to AWAS sampling intervals) fall along the one-to-one line with quite high correlations (see Figure 2A.2 in Appendix A); therefore, measurements of [CFC-11] provided by the two instruments are used interchangeably without any correction for instrumental difference. At times when UCATS [CFC-11] is not measured, we use a linear relationship with [CH_4], which is measured more frequently, to estimate [CFC-11] (see Figure 2A.3 in Appendix A).

2.2.3 Estimate of NO

The abundance of [NO_x] along each flight track of the ER-2 is another key part of our analysis. Observations of [NO_2] are reported every second by the CANOE instrument (similar to St. Clair et al., 2019), and measurements of [O_3] are made every 2 s by the UCATS instrument (Hintsa et al., 2021) (see Table 2.1 for accuracy and precision). We compute [NO] along each flight track for which valid data for [NO_2], [ClO], and [O_3] exist, using the following instantaneous photochemical steady state (PSS) relation

$$[\mathrm{NO}] = \frac{\mathrm{J_{NO2}}[\mathrm{NO_2}]}{\mathrm{k_{NO+O3}}[\mathrm{O_3}] + \mathrm{k_{ClO+NO}}[\mathrm{ClO}]} \quad (2.1)$$

where values of the rate constants and k_{ClO+NO} are from the most recent JPL Kinetic Data Evaluation (version 19-5) (Burkholder et al., 2019) and (the photodissociation frequency of NO_2) is found using the NO_2 cross-section from the same source, as described in Section 2.2.4. A more sophisticated treatment of the [NO]/[NO_2] ratio would consider reactions of NO with HO_2 and RO_2, in addition to the reactions of NO with O_3 and ClO (e.g., Equation 2 of Shah et al., 2023).

This treatment would be needed in the troposphere. For the stratospheric flight tracks of interest in our study, we estimate that neglecting these additional reactants results in less than a 10% difference in [NO] compared to values of [NO] found using the more sophisticated expression, which is well within the overall uncertainty of [NO_x]. This 10% difference estimate is based upon our analysis of PSS simulations of DCOTSS observations conducted using a full stratospheric chemical mechanism (Section 2.2.6), as shown in Figure 2A.4 in Appendix A.

The steady-state relationship in Equation 2.1 has previously been validated for the lower stratosphere using in situ measurements of [NO], [NO_2], [O_3], and [ClO] during the POLARIS campaign (Del Negro et al., 1999). This study utilized a chemiluminescence instrument for measurements of [NO] and [NO_2] and a resonance fluorescence instrument for [ClO]. Our use of estimated [NO] introduces significant additional uncertainty in the resulting estimate of [NO_x], particularly in the UT/LS where low [O_3] and low temperature drives the [NO]/[NO_2] ratio to high values, resulting in the computed value of [NO_x] being dominated by estimated [NO]. These uncertainties are reflected in the figures and analysis presented in Section 2.3.

The reaction between NO and O_3 has been found to exhibit non-Arrhenius behavior at the low temperature range of 200–225 K (Birks et al., 1976; Borders & Birks, 1982; Michael et al., 1981). This behavior is particularly significant in the cold environments of our study, where the steep temperature dependence of this rate constant must be accurately known for proper estimates of NO_x in the midlatitude LS (Cohen et al., 2000). For these reasons, we adopt the non-Arrhenius expression for the NO + O_3 rate constant from the JPL 19-5 chemical kinetics compendium (Burkholder et al., 2019). As shown in Figure 2A.5 in Appendix A, the JPL 19-5 non-Arrhenius expression aligns quite closely with both the Arrhenius and non-Arrhenius recommendations for the NO + O_3 rate constant given by IUPAC over the temperature range

relevant to this study. Conversely, the rate constant found using the Arrhenius expression of JPL 19-5 results in a rate constant that is about 8% lower than the average of the other three values (i.e., both values from IUPAC and the JPL19-5 non-Arrhenius recommendation). All four estimates of this rate constant lie well within the uncertainty range given by JPL 19-5 (Figure 2A.5 in Appendix A).

2.2.4 Photodissociation Frequencies

The photodissociation frequencies (*J* values) used in this study (Table 2A.1 in Appendix A) were found using a radiative transfer model that accounts for Rayleigh scattering (Prather, 1981; Salawitch et al., 1994). This model is constrained by profiles of temperature, pressure, and [O_3] on a 2 km altitude grid, from the ground to 80 km altitude, as well as surface albedo and surface pressure. Level 2 data products retrieved from the TROPOspheric Monitoring Instrument (TropOMI) onboard the Copernicus Sentinel-5 Precursor (S5P) satellite (Veefkind et al., 2012) provide daily maps of surface albedo using geometry-dependent Lambertian Equivalent Reflectivity retrievals under clear-sky conditions for 1 nm-wide wavelength bins between 328 and 2314 nm (Tilstra et al., 2024). We bilinearly interpolate the TropOMI data as a function of latitude and longitude, to estimate surface albedo at each point along the ER-2 flight track. Profiles of temperature as a function of altitude are based on measurements provided by the Stratospheric Aerosol and Gas Experiment III onboard the International Space Station (SAGEIII-ISS) for both summer 2021 and 2022. The SAGEIII-ISS temperature profiles (Wang et al., 2020), available in swath files (NASA/LARC/SD/ASDC, 2024) that start at the surface and extend to 80 km, are averaged onto 4° latitude bins, from 12°N to 60°N.

Profiles of [O_3] needed for the computation of J-values are constrained in a multi-step process that utilizes data from ozonesondes as well as the MLS instrument onboard the NASA Aura satellite (Livesey et al., 2022). The MLS instrument provides monthly, zonal mean retrievals of [O_3] from approximately ~10–100 km at 4° latitude intervals. Version 5.1 of MLS [O_3] was used (Schwartz et al., 2021), because this version was the latest retrieval available at the time *J* values were calculated. A series of DCOTSS ozonesonde (NASA/LARC/SD/ASDC, 2022b) launches provide observations of [O_3] from the surface up to about 30–35 km (Hall et al., 2016; Sterling et al., 2018). These ozonesondes were launched from Corpus Christi, Texas (27.8°N), Salina, Kansas (38.8°N), Boulder, Colorado (40.0°N), and Grand Forks, North Dakota (47.8°N) during the summers of 2021 and 2022, designed to coordinate with ER-2 flights based out of Salina, KS. Monthly profiles of [O_3] are constructed for each launch site as a function of the mean latitude of collected measurements. These sonde profiles of [O_3] are linearly interpolated as a function of latitude onto a 4° latitude grid, ranging from 28°N to 48°N, to provide measurements of [O_3] at altitudes not reported by MLS (≤10–12 km) (see Text 2A.2 and Figure 2A.6).

To create a smooth and continuous ozone profile grid that spans from 0 to 80 km in altitude and 12°N to 60°N in latitude, we combine the interpolated ozonesonde profiles with the MLS retrievals and linearly interpolate across both dimensions onto a 4° latitude and 2 km altitude spaced grid. This two-dimensional interpolation scheme, which utilizes Delaunay triangulation (Musin, 1997), estimates ozone mixing ratios based on geometric relationships between neighboring data points, ensuring consistency across both latitude and altitude. Values that fall outside the convex hull of the interpolation scheme are manually extrapolated as a function of latitude. However, these extrapolated values constitute less than 1% of our ozone

profile grid and are found primarily at altitudes below 2 km and latitudes approximately ≤20°N and ≥50°N. The interpolated ozone profiles for June of 2022 are depicted in Figure 2A.6 of Appendix A.

We determine the profile of [O_3] at each point along the ER-2 flight track as a function of latitude and sampling month, using the interpolated ozone profile grid as described below. Each profile is linearly weighted according to its proximity to the nearest latitude bin. Observations of TCO from TropOMI provide an account of global ozone distribution at a higher spatial (5.5 × 3.5 km) and temporal (daily) resolution than is represented in our sonde-MLS profile data set. To align our data with TropOMI observations, we bilinearly interpolate TropOMI Level 2 version 2.1 TCO retrievals (Copernicus Sentinel-5P, 2018) along the ER-2 flight tracks and adjust each sonde-MLS ozone profile by a constant multiplicative factor to match TCO reported by TropOMI. These profiles are only scaled by a small factor of 0.98 ± 0.05 (see Figure 2A.7 in Appendix A). This scaling step accounts for spatial and temporal variations in ozone that may not be fully captured in our sonde-MLS data set and ensures that our profiles are accurately adjusted to reflect near real-time ozone distributions.

2.2.5 Trajectory Model Description

We use a 4th-order Runge-Kutta method to simulate the behavior of chlorine and nitrogen species over time, along prescribed trajectories. This is a new model developed to quantify the impacts of the chemical environment (i.e., initial [$ClONO_2$], [NO_x], and aerosol SAD) on chlorine activation for the cold, wet air masses observed during DCOTSS. We simulate mixing ratios of HCl, $ClONO_2$, ClO, HOCl, ClOOCl, Cl, Cl_2, NO, NO_2, HNO_3, N_2O_5, and NO_3 forward and backward in time, from the point of ER-2 intercept. Mixing ratios are calculated on a time-step of 10 s because of the stiffness of the chemical system. This time-step

of 10 seconds corresponds to the fastest chemical transition, in our system of equations, which is the photolysis of NO_3. In this model, we use a simplified chemical scheme that consists of 40 gas phase reactions, 4 heterogeneous reactions ($ClONO_2$ + HCl, $ClONO_2$ + H_2O, HOCl + HCl, and N_2O_5 + H_2O), and 9 photolysis reactions involving O_3, $ClONO_2$, HOCl, NO_2, Cl_2, ClOOCl, HNO_3, N_2O_5, and NO_3. A list of these reactions can be found in Table 2A.1 in Appendix A. Gas phase reaction rate constants, heterogeneous reaction probabilities, and photolysis frequencies are calculated using data from the JPL Kinetic Evaluation version 19-5 (Burkholder et al., 2019). A plot of reaction probability as a function of temperature from our model code for the four heterogeneous reactions on sulfate aerosols considered in the model (see Text 2A.2), shown in Figure 2A.8 of Appendix A, compares extremely well with Figure 5-1 of Burkholder et al. (2019).

The quantities [CO], [CH_4], [O_3], [H_2O], and aerosol SAD are kept constant with time at the values observed at the time of ER-2 intercept. Our analysis of the lifetime of ozone with respect to photochemical loss for the conditions encountered during DCOTSS supports the use of constant values for [O_3] within the trajectory model (see Text 2A.4 and Figure 2A.9). The concentrations of HO_2 and atomic oxygen (O) are calculated at each time step using the steady-state relations:

$$[O] = \frac{J_{O3}[O_3]}{k_{O+O2+M}[O_2][M]} \quad (2.2)$$

$$[HO_2] = \frac{[OH](k_{OH+O3}[O_3] + k_{OH+CO}[CO] + k_{OH+ClO}[ClO])}{k_{HO2+O3}[O_3] + k_{HO2+NO}[NO] + k_{HO2+ClO}[ClO]} \quad (2.3)$$

We estimate [OH] as a function of solar zenith angle (SZA) using a modification to the parameterization described by Hanisco et al. (2001). Their parameterization, based on in situ measurements of [OH] in the lower stratosphere during two prior ER-2 campaigns, was designed

to be used for air densities [M] less than 2.5×10^{18} molecules/cm^3. The cold, wet air masses that are the subject of our investigation were typically sampled at lower altitudes (and hence higher [M]) than the original Hanisco et al. parameterization. Consequently, we have analyzed output of [OH] from our PSS model simulations (Section 2.2.6) of five DCOTSS 2022 flights and determined that the best fit to [OH] is found by multiplying the Hanisco et al. parameterization by 0.76. The smaller calculated values of [OH] at higher [M] for the cold, wet air masses sampled during DCOTSS, compared to the prior observations of [OH], is consistent with the altitude-dependent attenuation of ultraviolet radiation that results in the production of $O(^1D)$ from the photolysis of O_3. Further details on the PSS-based parameterization of [OH] are given in Figure 2A.10 of Appendix A.

Unless otherwise noted, the trajectory simulations are initialized with measured values of [O_3], [H_2O], [CH_4], [CO], [ClO], [$ClONO_2$], aerosol SAD, temperature, and pressure. We also initialize with [NO_x] inferred from measured [NO_2] (Section 2.2.3), and [HCl] found from the difference between [Cl_y] (Section 2.2.1) and [$ClONO_2$] + [ClO]. We initialize [HOCl], [ClOOCl], [Cl], [Cl_2], [NO], [N_2O_5], and [NO_3], which were not measured, assuming local, instantaneous steady state at the beginning of each simulation. Mixing ratios of HNO_3 are initialized by applying a linear fit, developed between ACE-FTS [HNO_3] and [N_2O] during the summer of 2022 over the US (Boone et al., 2023), to mixing ratios of N_2O measured by the UCATS instrument during DCOTSS.

We obtain photodissociation frequencies as a function of time in these simulations by parameterizing *J* values, calculated along the ER-2 flight track using full spherical geometry as described in Section 2.2.4, as a function of SZA and pressure. First, we bin the *J* values obtained for DCOTSS 2021 and 2022 (described in Section 2.2.4) according to pressure levels (i.e., 50 to

100, 100 to 200, 200 to 300 hPa, etc.). At each pressure level, for each photolytic species, we establish a quadratic relationship between the *J* value and SZA. Along each trajectory, we calculate *J* values as a function of SZA, using these quadratic relations, for the two pressure levels adjacent to the pressure of the trajectory. We then take the linearly weighted interpolation of these two *J* values, according to their proximity to the actual pressure level. Here, SZA is calculated along the trajectories as a function of time, latitude, and longitude, and the vertical interpolation is done as a function of the logarithm of pressure.

Our model simulations do not account for mixing with neighboring air masses or the dissipation of water vapor, which is a reasonable assumption within the mean time frame (∼5 days) that parcels typically remain within the NAMA (Chang et al., 2023). The anticyclonic circulation in the UT/LS associated with the North American Monsoon confines air masses, reducing the impact of mixing and dissipation processes compared to conditions outside the NAMA. This confinement helps maintain elevated water vapor levels and cold temperature anomalies in the lower stratosphere, supporting the assumption that [H_2O] and temperature remain relatively stable over a 5-day period, despite the possibility of some mixing and dissipation (Chang et al., 2023).

In Section 2.3.2, we describe both back-trajectory and forward-in-time chemical model simulations from the time of ER-2 intercept. The chemical backward-trajectory model simulations utilize isentropic back-trajectories (NASA/LARC/SD/ASDC, 2022c) described in Chang et al. (2023). These isentropic trajectories provide a history of particle positions (latitude, longitude, and altitude) prior to the time of the ER-2 intercept, along with temperature and pressure from the European Center for Medium-range Weather Forecasts Reanalysis v5 (ERA5) (Hersbach et al., 2020) interpolated to the particle positions. These trajectories are calculated

every second along the ER-2 flight path and extend backward in time at hourly synoptic intervals. Gridded NEXRAD WSR-88D Radar (GridRad) (Homeyer & Bowman, 2022; NASA/LARC/SD/ASDC, 2022d) products are used in conjunction with isentropic back trajectories to provide a matching of ER-2 observations to tropopause-overshooting convection that may have influenced individual measurements. This overshoot matching provides insight into the amount of time each parcel has spent in the stratosphere prior to ER-2 intercept. Our back-trajectory model simulations are initialized at this estimated time and location of stratospheric injection and run forward to the time of ER-2 intercept, using temperature and pressure provided along the isentropic back-trajectories. In contrast, our forward-in-time simulations begin at the ER-2 intercept and are run forward with temperature and pressure held constant. We note that the trajectories use winds from the ERA5 global reanalysis, which do not account for transport by convection; as such, we do not consider these trajectories to provide a precise account of the convective motion prior to stratospheric injection. For illustrative purposes, our forward-in-time model simulations assume constant latitude, longitude, temperature, and pressure based on the observed values, letting SZA vary with time of day. These simulations are further detailed in Section 2.3.2.

2.2.6 Photochemical Steady State (PSS) Model Description

We have simulated data acquired during summer 2022 for 5 DCOTSS flights using a well-established PSS model that relies on a full stratospheric chemical mechanism (Salawitch et al., 1994; Wales et al., 2018). The PSS model calculations are conducted to evaluate the accuracy of the chemical mechanism used within the trajectory model, to evaluate [OH] along the flights tracks of interest, and to investigate the cause of elevated [NO_x] (inferred from measured [NO_2]) near the tropopause. All gas phase reaction rate constants, heterogeneous

reaction probabilities, and photolysis frequencies are from Burkholder et al. (2019). We also use their non-Arrhenius expression for the NO + O_3 rate constant. The PSS simulations are initialized using measured values of [O_3], [H_2O], [CH_4], [CO], [C_2H_6], aerosol SAD, temperature, and pressure (Table 2.1). Values of total inorganic chlorine are from the "best estimate" (average of [$Cl_y^{LL}{}_{\text{Lower-Limit}}$] and [$Cl_y^{LL+VSL}{}_{\text{Upper-Limit}}$]) described in Section 2.2.2. Values of total inorganic bromine ([Br_y]) are found using the approach described by Wales et al. (2018), allowing for the influence of the VSL source and adjusting for the decline in the long-lived brominated organic source gases between 2014 and 2022. The PSS simulations are constrained using values of [NO_y] found from the relation between ACE-FTS measurements of the sum of [HNO_3] + [NO] + [NO_2] + 2 × [N_2O_5] + [HO_2NO_2] + [$ClONO_2$] versus [N_2O] over CONUS during the summer of 2022, as shown in Figure 2A.11 of Appendix A. Finally, the PSS simulations assume steady state for all computed species over the diel cycle, allowing for varying SZA over the course of the 24-hr day (Salawitch et al., 1994).

PSS simulations were conducted for the 2 June, 5 June, 8 June, 10 June, and 8 July DCOTSS flights of summer 2022 (Bowman et al., 2026). Figure 2A.10 (Appendix A) shows [OH] as a function of SZA from the PSS simulations of these five flights. As described in Section 2.2.5, the PSS output is used to adjust the [OH] parameterization of Hanisco et al. (2001) for use within the trajectory model. Figure 2A.9 (Appendix A) shows a time series of the PSS simulation for the 10 June 2022 flight, which is the primary focus of this study. As detailed in Text 2A.4, this figure shows the long photochemical lifetime of O_3 (with respect to chemical loss) for the calculated, steady state abundance of radicals (including [BrO]), the excellent PSS simulation of measured [ClO] throughout the flight, as well as close agreement between

[NO]/[NO_2] found using the simplified chemical mechanism of the trajectory model and the full chemical mechanism of the PSS model.

*2.3 **Results***

Temperature, water vapor, and other key observations from the DCOTSS campaign are analyzed to determine how frequently conditions conducive to heterogeneous chlorine chemistry on sulfate aerosols occurred in the midlatitude lower stratosphere during the summer months of 2021 and 2022. One metric to assess conditions suitable for heterogeneous chemistry is the chlorine activation temperature threshold, T_{ACL}, the temperature below which substantial chlorine activation occurs in the polar regions. Drdla and Müller (2012) define T_{ACL} as the temperature below which 10% of chlorine is activated within approximately one day (i.e., chlorine reactivity of 0.1 day^{-1}) in the polar regions. Their T_{ACL} parameterization is based on model results that established a relationship between chlorine reactivity and temperature across a broad range of stratospheric conditions ([H_2O]: 2–20 ppmv, θ: 375–700 K, SAD: 1–100 $\mu m^2/cm^3$). In Figure 2.1, we evaluate evidence for chlorine activation during the two DCOTSS summer deployments with respect to this polar chlorine activation threshold. This figure shows DCOTSS 2021 (Figure 2.1a) and DCOTSS 2022 (Figure 2.1b) measurements of temperature and [H_2O], colored by measured [ClO], in relation to T_{ACL} at 80 hPa and 120 hPa. These pressure levels (i.e., 80 and 120 hPa) encompass the range of pressures that cold and wet conditions were observed in the stratosphere during DCOTSS.

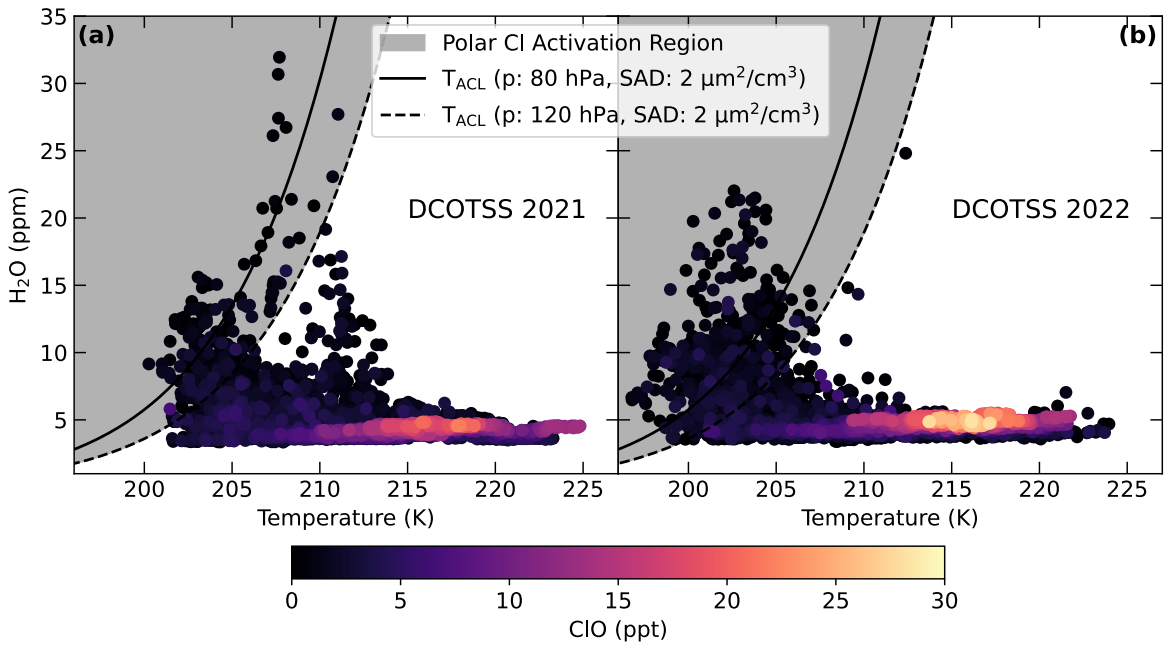


Figure 2.1. [H_2O] versus temperature colored by measured [ClO] for DCOTSS 2021 (a) and DCOTSS 2022 (b). The data are layered in ascending order to show the highest ClO mixing ratios on top. Black curved lines indicate the temperature threshold (T_{ACL}) for chlorine activation in the polar regions at an aerosol surface area density (SAD) of 2 $\mu m^2/cm^3$ and pressure (p) level of 120 hPa (dashed line) and 80 hPa (solid line). T_{ACL} is calculated using the Drdla and Müller (2012) parameterization and indicates where 10% of Cl is activated within 1 day. Data are filtered by 375 K < θ < 700 K, the recommended potential temperature range for use of the Drdla and Müller (2012) T_{ACL} parameterization. During DCOTSS, the maximum value of θ was 521 K.

Conditions that would lead to substantial chlorine activation in the polar regions, depicted in the gray-shaded regions of Figure 2.1, are frequently observed in the stratosphere during both DCOTSS summer deployments. Here and throughout, the location of the ER-2 in the stratosphere is determined based on the lapse rate tropopause found using ERA5 temperatures (Hersbach et al., 2020). In 2021, 1.2% and 5.1% of data crossed the T_{ACL} thresholds at 80 and 120 hPa, respectively (Figure 2.1a), compared to 5.9% and 10.9% in 2022 (Figure 2.1b). Temperatures within these chlorine activation regions are, on average, 1.8 K (80 hPa T_{ACL}) and 2.1 K (120 hPa T_{ACL}) lower in 2022 than in 2021. Furthermore, 0.14% (2021) and 2.6% (2022) of these parcels were observed at the temperature (T < 202 K) and water vapor ([H_2O] > 11 ppmv) levels associated with the Robrecht et al. (2019) projections of significant chlorine activation in the midlatitude LS. Consequently, our study primarily focuses on data collected in

2022. Measurements of [ClO] within these chlorine activation regions for both summer deployments are very low (Figures 2.1a and 2.1b), averaging less than 1 part per trillion (ppt) each year; therefore, observations during both summers show no evidence of chlorine activation for the conditions commonly associated with large amounts of chlorine activation in the polar regions. The highest mixing ratios of ClO (~30 pptv) are observed outside the presumed region of chlorine activation, at concentrations consistent with gas-phase partitioning at higher altitudes (about 18–20 km) (Salawitch et al., 1994). The absence of significant enhancements of [ClO] within convectively influenced stratospheric air masses observed during both DCOTSS summer deployments suggests that chlorine activation, at levels sufficient to cause chemical loss of ozone in the midlatitude LS, did not occur in 2021–2022 under the T and [H_2O] conditions similar to those reported by previous studies (Anderson et al., 2012, 2017; Robrecht et al., 2019). We note that SAD was about 2–4 times larger in 2021 compared to 2022, between potential temperatures of 380–500 K, due to the influence of the eruption of La Soufrière in 2021 (Li et al., 2023).

Although the T and [H_2O] conditions within overshooting plumes may facilitate the conditions necessary for chlorine activation by heterogeneous reaction, this process also requires an adequate supply of inorganic chlorine (Cl_y). For significant levels of Cl_y to be present within these lower stratospheric convectively influenced air masses, either convective injection of inorganic chlorine species from the decomposition of VSL chlorine compounds in the troposphere (i.e., product gas injection or PGI), or the mixing of convectively detrained air with the background stratosphere would need to take place. Inorganic chlorine products from PGI are highly soluble and are likely removed by washout processes before reaching the stratosphere (Ko et al., 1997), resulting in only a minor contribution to stratospheric [Cl_y] in the midlatitude lower stratosphere. Therefore, in our study, we focus on how convective detrainment and subsequent

mixing with chemically aged stratospheric air contributes to [Cl_y] within the cold and wet air masses sampled in the LS during DCOTSS.

We use plots of measured [O_3] and [H_2O], which are distinctly different for the background stratosphere and troposphere, to quantitatively evaluate mixing between tropospheric and stratospheric air masses (Pan et al., 2014). Figure 2.2 shows measurements of [O_3] and [H_2O] obtained during DCOTSS 2022, colored by the departure of temperature from the frost point ($T - T_{ICE}$) (Figures 2.2a and 2.2d) (List, 1951), estimated [Cl_y] (Figures 2.2b and 2.2e), and measured [ClO] (Figures 2.2c and 2.2f). The shaded regions occupied by the gray points in Figure 2.2 depict stratospheric and tropospheric background conditions, which are defined by the median mixing ratios of water vapor (4.6 ppmv) and ozone (114.8 ppbv) observed above and below the ERA5 lapse rate tropopause, respectively. The mixing ratios of H_2O and O_3 that fall within the background regions of the stratosphere and troposphere form a distinct “L” shape on all the panels of Figure 2.2. Deviations from this compact relationship signify mixing between stratospheric and tropospheric air masses, with larger deviations from the background data indicating a more pronounced degree of mixing (Pan et al., 2014).

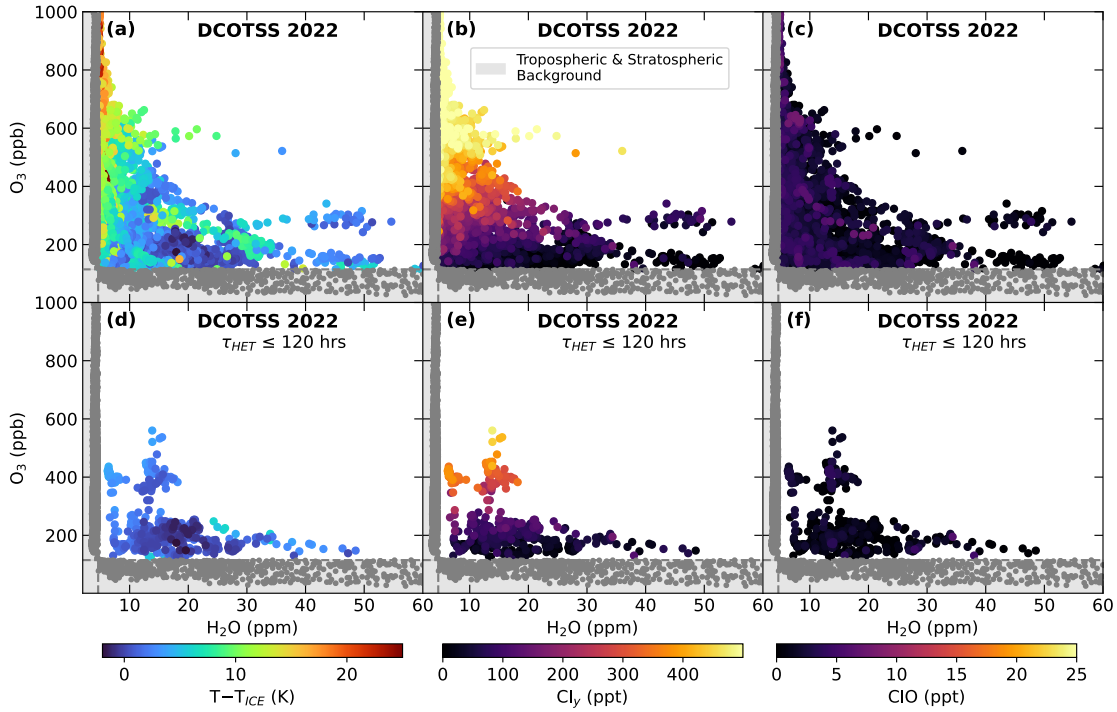


Figure 2.2. Daytime (solar zenith angle <90°) measurements of [O_3] versus [H_2O] for DCOTSS 2022. Background stratospheric and tropospheric observations are colored in gray within shaded regions. Air parcels outside of the specified background regions are colored by $T - T_{ICE}$ in panels (a) and (d), estimated [Cl_y] in panels (b) and (e), and measured [ClO] in panels (c) and (f). Scatter points in the left column are layered in descending order, and data in the middle and right columns are layered in ascending order. Panels (d) through (f) show only the background regions and parcels in which the heterogeneous time constants (τ_{HET}) ≤ 120 hr. At times where [ClO] and [$ClONO_2$] (for the computation of τ_{HET}) are not measured, these quantities are linearly interpolated as a function of time.

We have used the departure of temperature from the frost point ($T - T_{ICE}$) rather than T_{ACL} to reference conditions suitable for chlorine activation in Figure 2.2. The Drdla and Müller (2012) T_{ACL} parameterization utilized in Figure 2.1 relies on model results initialized with 1 ppbv of [$ClONO_2$] and 2 ppbv of [HCl], which are representative of typical polar stratospheric conditions. Since this chlorine partitioning differs considerably between polar and midlatitude regions, using this T_{ACL} parameterization for the midlatitude lower stratosphere can result in an overestimation of the temperature at which significant chlorine activation occurs. Therefore, in our study, we make use of $T - T_{ICE}$ along with heterogeneous reaction probabilities and time constants to identify air masses with conditions favorable for chlorine activation. Although ice is not the primary reactive surface for heterogeneous chemistry in the midlatitude LS, T_{ICE} serves

as a humidity-dependent temperature reference that closely aligns with high reaction probabilities on sulfuric acid aerosol surfaces (Figure 2A.12 in Appendix A).

Relatively high levels of [Cl_y]—though not necessarily frequent–were observed within convectively influenced air masses during DCOTSS 2022. As shown in Figure 2.2b, air masses with water vapor mixing ratios above the ~11 ppmv activation threshold suggested by Robrecht et al. (2019) were observed alongside mixing ratios of Cl_y greater than 100 pptv. However, the majority (~64%) of parcels with [Cl_y] > 100 pptv and [H_2O] > 11 ppmv were observed at temperatures too high for chlorine activation (Robrecht et al., 2019), exceeding T_{ICE} or 200 K by at least 5 K. Elevated levels of [Cl_y] and [H_2O] at these temperatures, as well as the observed aerosol SAD, would not lead to chlorine activation (Robrecht et al., 2019). Therefore, in the bottom row of Figure 2.2, we focus exclusively on moist air parcels with temperatures low enough for chlorine activation to occur.

The bottom row in Figure 2.2 is filtered to only show parcels that have temperatures low enough and water vapor mixing ratios high enough for chlorine activation to occur within the 5-day mean residence time of parcels within the NAMA (Chang et al., 2023). The filter retains only data in which one of the heterogeneous time constants (τ_{HET}) ($ClONO_2$ + HCl, $ClONO_2$ + H_2O, and HOCl + HCl) is less than this 120 hr (5 day) time threshold (see Text 2A.3 in Appendix A). The NAMA, such as other upper-tropospheric anticyclonic circulations, is characterized by high water vapor mixing ratios and cold temperature anomalies in the lower stratosphere (Chang et al., 2021, 2023). Consequently, once air masses exit the NAMA and move further into the midlatitude stratosphere, they are less likely to remain at temperatures low enough for chlorine activation (Chang et al., 2023). In this paper, we will frequently refer to "heterogeneously suitable" air masses as being those with heterogeneous time constants for

chlorine activation that are below 5 days (i.e., $\tau_{HET} \leq 120$ hr). When filtering the data using this time constant constraint, we are able to identify observations in which low temperature and high water vapor are observed simultaneously. Temperatures within these heterogeneously suitable parcels are, on average, within 3 K of the frost point (Figure 2.2d). These cold and wet air masses are primarily observed within ~1 km altitude of the local tropopause.

The majority of these heterogeneously suitable air masses have mixing ratios of inorganic chlorine (Cl_y) that are too low to induce an enhancement of [ClO] at a level that would lead to significant ozone depletion (Figures 2.2e and 2.2f). About 86% of the air masses that reside within the mixing region of Figure 2.2e (i.e., outside the identified tropospheric and stratospheric background regions) have Cl_y mixing ratios below 100 pptv. Similarly, during DCOTSS 2021, almost all parcels that met our time constant constraint ($\tau_{HET} \leq 120$ hr) were observed with low [Cl_y] < 100 pptv (see Text 2A.5 and Figure 2A.13 in Appendix A). Consequently, for most observations during the DCOTSS mission, the absence of chlorine activation can be attributed to the scarcity of inorganic chlorine present within these convectively influenced air masses due to their relatively young chemical age.

However, there is a cluster of data points with elevated mixing ratios of Cl_y (>300 pptv) that meet our heterogeneous time constant constraint of $\tau_{HET} \leq 120$ hr (warm colored points, Figure 2.2e). These air parcels exhibit water vapor and ozone mixing ratios greater than 12 ppmv and 350 ppbv, respectively. Yet, there is no evidence of activation for these parcels, as shown by the low mixing ratios of [ClO] (Figure 2.2f). The remainder of this investigation will explain why, during DCOTSS 2022, [ClO] was typically low (<5 pptv) for these air masses, despite the presence of conditions cold enough and wet enough and occasionally with sufficient Cl_y to meet the conditions usually associated with model projections of chlorine activation in the midlatitude

LS (Anderson et al., 2012, 2017; Robrecht et al., 2019). These Cl_y-rich air parcels were sampled primarily during the 10 June 2022 DCOTSS research flight, discussed below in Section 2.3.1.

2.3.1 The 10 June 2022 DCOTSS Flight

In this section, we provide a detailed analysis of the 10 June 2022 research flight to investigate the absence of elevated [ClO] within air masses that appear to have suitable conditions for chlorine activation. During this research flight, instruments on the NASA ER-2 sampled fresh convective outflow material over eastern Texas, which had recently detrained into the background stratosphere. Figure 2.3 provides a time series of in situ measurements of $[H_2O]$, T, [ClO], and $[ClONO_2]$, and calculated quantities T_{ICE}, $[NO_x]$, γ, τ_{HET}, $[Cl_y]$, and [HCl] for the time period during which the detrained air parcel was sampled. The gray-shaded region depicts the flight segment for which the heterogeneous time constant (τ_{HET}) for chlorine activation falls below 120 hr. In the gray-shaded region of this flight, cold (200.9 ± 1.5 K) and moist (11.5 ± 3.8 ppmv) air parcels with elevated levels of $[Cl_y]$ (301.3 ± 30.8 pptv) were sampled at SZA below 30° at 114 ± 5 hPa (here, numerical quantities indicate the mean and 1σ standard deviation of data within the gray shaded region of Figure 2.3).

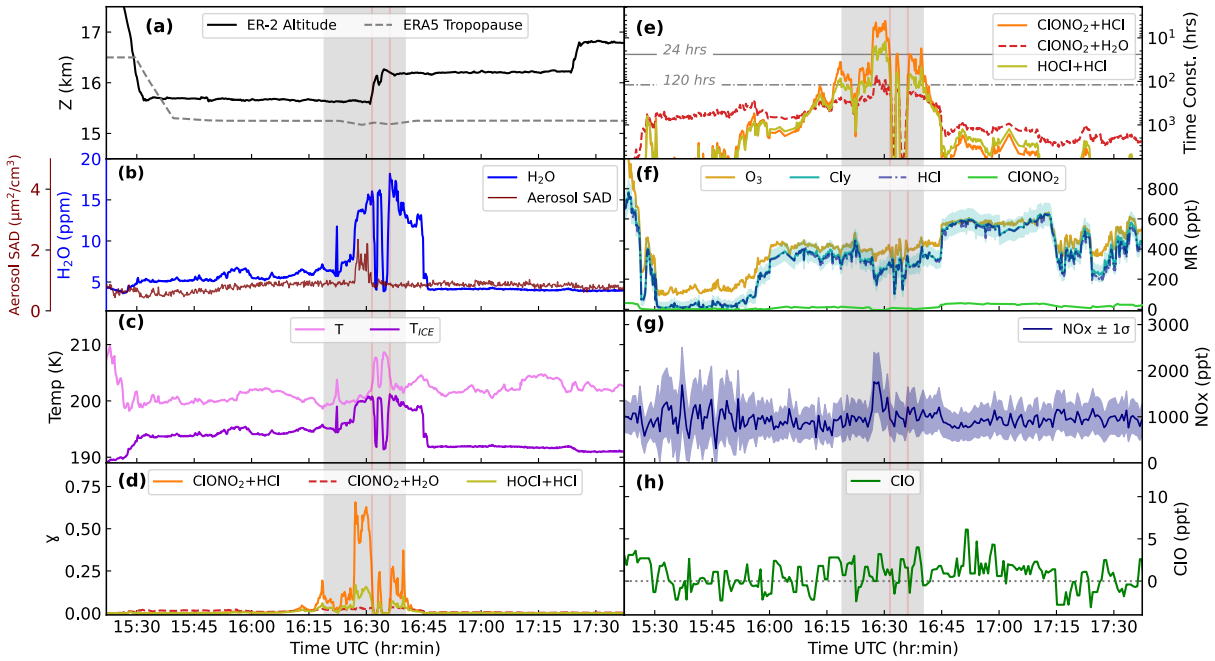


Figure 2.3. Time series of the 10 June 2022 research flight from 15:15 UTC to 17:45 UTC. Panel (a) shows the ER-2 altitude (solid black) and ERA5 tropopause height (dotted gray). Panel (b) shows measured [H_2O] in blue and aerosol SAD in maroon on the secondary y-axis. Panel (c) shows the measured temperature (solid pink) and calculated frost point (T_{ICE}) (solid purple). Panels (d) and (e) show the reaction probabilities (γ) and time constants (τ_{HET}) of $ClONO_2$ + HCl (solid orange), $ClONO_2$ + H_2O (dashed red), and HOCl + HCl (solid gold), respectively. Panel (f) shows measured [O_3] (gold), [$ClONO_2$] (lime), estimated [Cl_y] (turquoise) with shading indicating the upper and lower limits, and [HCl] in the dash-dotted dark blue; a simple estimate from [Cl_y] − ([$ClONO_2$] + [ClO]). Panel (g) shows calculated [NO_x] ([NO] + [NO_2]) in navy, along with 1σ uncertainties denoted by the shading. Panel (h) shows measured [ClO] in green. The shaded region denotes the first and last instances in which one of the heterogeneous time constants falls below 120 hr (16:18 UTC to 16:10 UTC). The red vertical lines indicate the times (16:31 UTC and 16:36 UTC) at which there is the largest potential for chlorine activation with respect to water vapor, temperature, and Cl_y.

The low temperatures, high water vapor mixing ratios, and elevated [Cl_y] observed in the stratosphere within the gray-shaded segment of Figure 2.3 suggest the potential for chlorine activation. Corresponding peaks in the heterogeneous reaction probabilities (Figure 2.3d) and minima in the time constants (Figure 2.3e) illustrate that *T* and [H_2O] conditions favorable for chlorine activation were observed at a time when sufficient [Cl_y] (>300 pptv) was available to activate. However, small mixing ratios of ClO (1.4 ± 1.7 pptv) within these cold, wet, Cl_y-rich air parcels are evident (Figure 2.3h). Additionally, observed mixing ratios of $ClONO_2$ are too low within the shaded region (5.1 ± 4.5 pptv) (Figure 2.3f) to provide either a sufficient reaction partner for HCl, or for chlorine activation by the hydrolysis of $ClONO_2$.

For significant chlorine activation to occur, Robrecht et al. (2019) show that cold and wet conditions must be sustained for a minimum of 24–36 hr for [H_2O] ≈ 11 ppmv and ∼5 hr for [H_2O] approaching 20 ppmv, depending on temperature. Given that this plume is estimated to have entered the stratosphere only ∼12–18 hr prior to sampling, we explore whether this air mass had been exposed to cold and wet conditions long enough to facilitate a significant enhancement of [ClO], or whether the low levels of [$ClONO_2$] and high levels of [NO_x] present were the primary inhibitors to chlorine activation. Although the entire period within the gray-shaded region (16:18 to 16:40 UTC) could be important for chlorine activation, our back-trajectory analyses presented below is focused on two parcels observed at 16:31 UTC and 16:36 UTC on 10 June 2022 (airplane markers, Figure 2.4), which are characterized by high [Cl_y], high [H_2O], and low temperature. These isentropic back-trajectories, described in Chang et al. (2023), trace the parcels back to their stratospheric injection times and locations, identified by overshooting GridRad echo top heights (Homeyer & Bowman, 2022) (Figure 2.4). Figure 2.4 also shows values of $T - T_{ICE}$ along the back-trajectories, calculated under the assumption that [H_2O] remained constant at the value measured during the ER-2 intercept. These results indicate that temperatures remained low and suitable for chlorine activation along the back trajectory of each parcel.

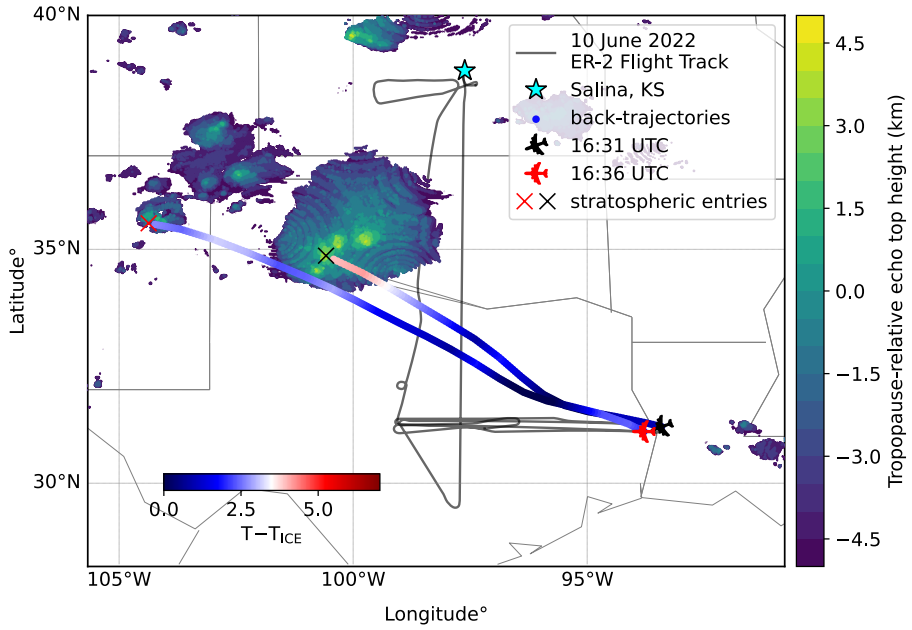


Figure 2.4. Flight track for the 10 June 2022 research flight (solid gray) overlaying GridRad echo top heights relative to the tropopause from two timestamps (04:00 UTC 10 June 2022, 22:20 UTC 9 June 2022). Two ER-2 intercepts, at 16:31 UTC and 16:36 UTC, are highlighted in black and red airplane markers, respectively. The back-trajectories, colored by $T - T_{ICE}$, represent the mean of an ensemble of trajectories for each parcel. These back-trajectories are traced back to their respective source overshoot locations, indicated by the x markers. The starting location of this research flight, Salina, KS, is indicated by a light blue star.

The ER-2 intercept at 16:31 UTC, depicted in Figure 2.4, is one of two key intercepts analyzed in this study to examine the evolution of conditions favorable for chlorine activation following recent convective injection into the stratosphere. This air parcel was estimated to have entered the stratosphere approximately 12.5 hr before the ER-2 intercept, originating from convective activity at 04:00 UTC on 10 June 2022. This convection reached echo top heights of around 17 km, exceeding the ERA5 lapse rate tropopause by 2.8 km. At the time of the ER-2 intercept (16:31 UTC), this parcel was observed 0.6 km above the tropopause with elevated [H_2O] of 16 ppmv and temperature of 202.8 K, alongside relatively high [Cl_y] (296 pptv) and [O_3] (379 ppbv). This intercept is particularly relevant to our study because of the notably low temperatures that were sustained along the parcel's back-trajectory, reaching as low as 199.5 K approximately 4 hr before the ER-2 intercept.

The second ER-2 intercept highlighted in Figure 2.4, observed at 16:36 UTC, offers an opportunity to examine a parcel that has been in the stratosphere for a longer period of time. This parcel originated from overshooting convection that occurred 18.1 hr before the ER-2 intercept, at 22:20 UTC on 9 June 2022. The convective overshoot echo top heights [at the source] reached 17 km, 1.9 km above the ERA5 lapse-rate tropopause. At the time of ER-2 intercept, the parcel was observed to be about 1 km above the local ERA5 tropopause, with a water vapor mixing ratio of 18.2 ppmv and temperature of 204 K. This measurement of [H_2O] was the largest observed in the stratosphere during the 10 June 2022 flight. Furthermore, this parcel was observed with large mixing ratios of Cl_y (345.6 pptv) and O_3 (382.7 ppbv), 1–2 standard deviations (σ) above the median values ([Cl_y]: 132.2 ± 130.8 pptv; [O_3]: 260.4 ± 98.9 ppbv) observed in air masses with conditions favorable for heterogeneous chemistry ($\tau_{HET} \leq 120$ hr) in 2022. Overall, Figure 2.4 illustrates that these parcels have remained sufficiently cold for a sustained period prior to the ER-2 intercept, with temperatures on average remaining within a degree or two of the frost point along both trajectories.

To explore the factors limiting chlorine activation within these Cl_y-rich, heterogeneously suitable parcels, we perform back-trajectory chemical model simulations for the two intercepts highlighted in Figure 2.4. A description of the model framework can be found in Section 2.2.5. In these simulations, we assess whether an enhancement of [ClO] would have been observed at the time of the ER-2 intercept for the initial conditions used by Anderson et al. (2012) and Robrecht et al. (2019) or if the lack of chlorine activation can be attributed to insufficient processing time. It is important to note that these prior studies examined lower pressure levels of 90–100 hPa, where mixing ratios differ compared to this analysis, which is focused on pressure levels between 100 and 120 hPa (which is where most cold and wet conditions were observed

during DCOTSS 2022). As such, our model runs are intended to provide insight into the potential for chlorine activation for observed conditions, except for higher $[ClONO_2]/[Cl_y]$ and lower $[NO_x]$ than observed, rather than a direct comparison to the previously published modeling results.

Utilizing $[NO_x]$ initializations from Robrecht et al. (2019) and Anderson et al. (2012) allows us to evaluate the likelihood of chlorine activation under the possibility that $[NO_x]$ may be lower than our steady-state calculations, as would occur if our estimate of [NO] is biased high due to inadequacies in our understanding of the kinetic terms that link NO and NO_2 in the midlatitude LS (Cohen et al., 2000; Jaeglé et al., 1994; Sen et al., 1998; Silvern et al., 2018). Additionally, we examine whether enhancement of [ClO] could have been observed at the time of ER-2 intercept had aerosol SAD been elevated to magnitudes commonly associated with geoengineering scenarios or major volcanic eruptions (Tilmes et al., 2022).

Figure 2.5 shows the chemical back-trajectory model results for the ER-2 intercept at 16:31 UTC on 10 June 2022. The simulations are initialized at the estimated time of stratospheric injection and run to the time of ER-2 intercept ("time 0"). Temperature and pressure vary along the back-trajectory, however $[H_2O]$ is kept constant at 16 ppmv, the mixing ratio observed at the time of intercept. All model runs in Figure 2.5 are initialized with near zero [ClO] of 0.1 pptv. In Figure 2.5, we present four model simulations that illustrate the chemical evolution of [ClO] (Figure 2.5c) and $[NO_x]$ (Figure 2.5d) that are distinguished by initializations of $[ClONO_2]/[Cl_y]$, $[NO_x]$, and aerosol SAD. The first model simulation (solid brown lines) is initialized with $[ClONO_2]/[Cl_y]$ and $[NO_x]$ at the time of ER-2 intercept ($[ClONO_2]/[Cl_y] = 0.02$ and $[NO_x] = 960$ pptv). Since $[ClONO_2]/[Cl_y]$ and $[NO_x]$ at the time of stratospheric injection were unknown, we initialized with the values associated with the time of ER-2 intercept. Although these quantities

likely differed at the time of stratospheric injection, our results show that the model calculations are largely insensitive to the chosen initializations over the 18-hour time period. The second model simulation (solid blue lines) is initialized with values of $[ClONO_2]/[Cl_y]$ and $[NO_x]$ from Robrecht et al. (2019) (0.04 and 289 pptv, respectively). The third simulation (solid red lines) is initialized using values of $[ClONO_2]/[Cl_y]$ and $[NO_x]$ from Anderson et al. (2012) (0.15 and 700 pptv, respectively). The last simulation (dotted black lines) is initialized with the values of $[ClONO_2]/[Cl_y]$ and $[NO_x]$ observed at the time of ER-2 intercept and an aerosol SAD of 10 $\mu m^2/cm^3$, which represents either a major volcanic or stratospheric sulfate aerosol injection enhancement. The other model runs were initialized with the average aerosol SAD of 1.13 $\mu m^2/cm^3$ that was observed within the gray-highlighted flight segment in Figure 2.3. Because the precise aerosol SAD at the time of stratospheric injection is unknown, we use the average SAD observed in the sampled convective outflow in the gray-shaded region of Figure 2.3 (spanning 10–18 hr post injection) as a proxy for initializing the back-trajectory model. Although short-lived enhancements in SAD may occur during stratospheric injection, aerosol SAD is held constant for these simulations as the short duration of these enhancements limits any substantial effect on chlorine activation (see Text 2A.6 and Figure 2A.14 in Appendix A).

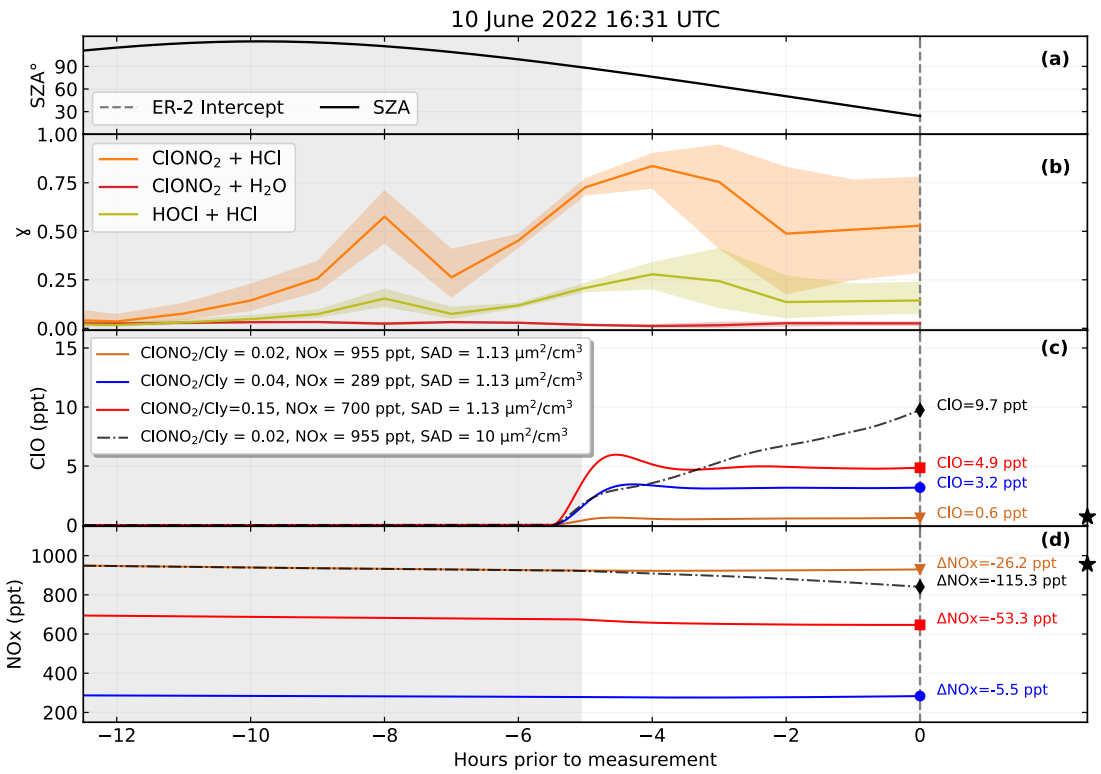


Figure 2.5. Chemical back-trajectory model simulation from the time of stratospheric injection to the time of ER-2 intercept on 16:31 UTC 10 June 2022 ("time 0"). Panel (a) shows Solar Zenith Angle (SZA); shaded regions indicate SZA > 90°. Panel (b) shows the mean and range of heterogeneous reaction probabilities (solid lines and shaded regions, respectively). Panels (c) and (d) show simulated mixing ratios of ClO and NO_x, respectively. The various lines in panels (c) and (d) represent model results for varying initial conditions of $[NO_x]$, $[ClONO_2]/[Cl_y]$, and aerosol SAD. Results initialized with values of $[ClONO_2]/[Cl_y]$, $[NO_x]$, and SAD encountered during this intercept are represented by the solid brown lines (triangle symbol at intercept). Results using Robrecht et al. (2019) initializations are represented by the solid blue lines (circle). Results using Anderson et al. (2012) initializations are represented by the solid red lines (square). Dotted black lines (diamond) represent results initialized the same as the brown, except with a higher aerosol SAD of 10 $\mu m^2/cm^3$; all other results are initialized with an aerosol SAD = 1.13 $\mu m^2/cm^3$. All model runs are initialized with the twilight $[NO]/[NO_2]$ ratio of 0.94, which is based on steady state conditions at the start of the trajectory. Measured [ClO] and calculated $[NO_x]$ at the time of ER-2 intercept are indicated by black stars on panels (c) and (d), respectively. Values of [CO], $[CH_4]$, $[O_3]$, $[H_2O]$, and aerosol SAD are kept constant with time.

Figure 2.5 illustrates how sustained elevated reaction probabilities and varying initial conditions influence [ClO] and $[NO_x]$ at the time of ER-2 intercept. Figure 2.5b shows that reaction probabilities (γ) remain elevated for a significant portion of the back-trajectory, with reaching up to 0.9 approximately 4 hr before the ER-2 intercept. The first model simulation for [ClO] in Figure 2.5c (brown solid line) shows only a minimal increase at "time 0," when initializing with the values of $[ClONO_2]/[Cl_y]$ and $[NO_x]$ observed at the time of the ER-2 intercept. This limited increase in [ClO] is due to a combination of high $[NO_x]$, low

[$ClONO_2$]/[Cl_y], and insufficient processing time. When initializing with the Robrecht et al. (2019) values of [$ClONO_2$]/[Cl_y] and [NO_x], the simulation shows slightly higher [ClO], 3.2 pptv, at the time of ER-2 intercept (blue solid line, Figure 2.5c) primarily due to the lower initial [NO_x]. A larger increase in [ClO] is produced at the time of ER-2 intercept upon use of the Anderson et al. (2012) values for the initialization of [$ClONO_2$]/[Cl_y] and [NO_x]. However, the resulting value of [ClO] for this initialization is only 4.9 pptv because modeled values of [NO_x] are still elevated. The largest value of [ClO], equal to 9.7 pptv, occurs when initializing with an aerosol SAD of 10 $\mu m^2/cm^3$. Additional simulations with elevated aerosol SAD are discussed in Section 2.3.3.

Figure 2.6 presents the results of the back-trajectory simulation for the ER-2 intercept at 16:36 UTC on 10 June 2022. These simulations are initialized the same as described in Figure 2.5, except for the first and last model runs (solid and dotted lines, respectively) which are instead initialized with the values of [$ClONO_2$]/[Cl_y] and [NO_x] associated with this intercept ([$ClONO_2$]/[Cl_y] = 0.01 and [NO_x] = 1,209 pptv). This air mass spent approximately ~18 hr in the stratosphere prior to the ER-2 intercept, 5.5 hr longer than the intercept detailed in Figure 2.5. Furthermore, the air parcel simulated in Figure 2.6 had higher abundances of [Cl_y] (345.6 pptv), [O_3] (382.7 ppbv), and [H_2O] (18.2 ppmv) than the air parcel simulated in Figure 2.5.

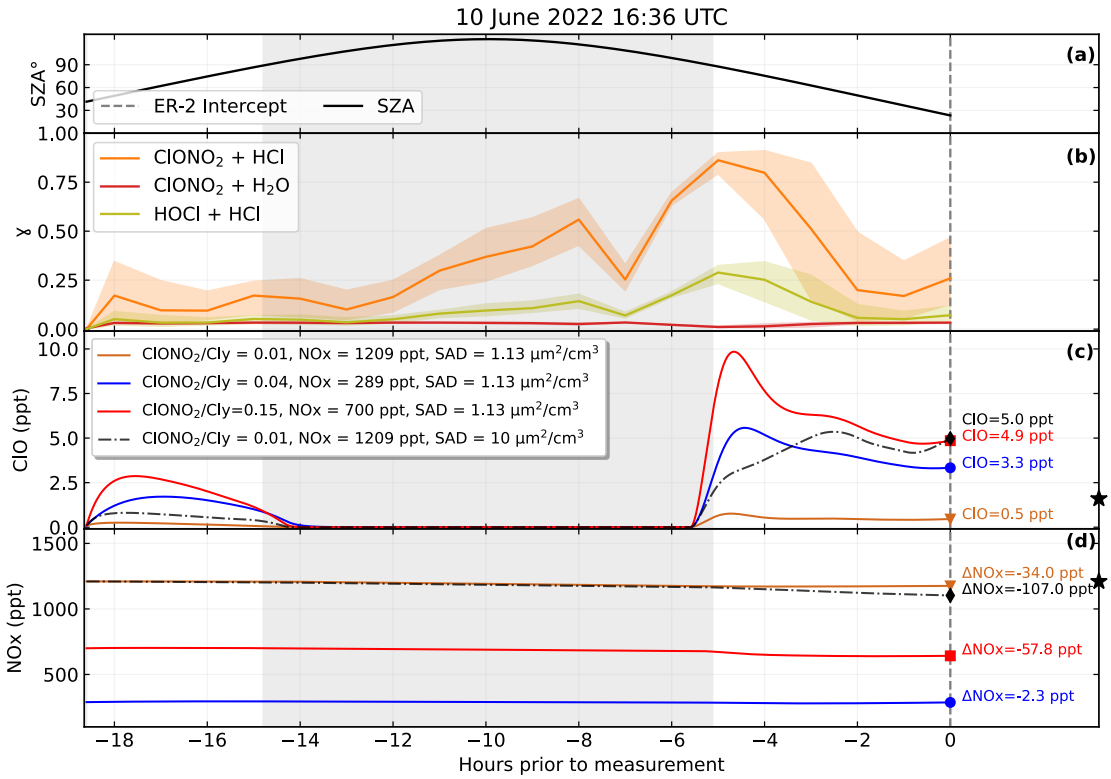


Figure 2.6. Chemical back-trajectory model simulation from the time of stratospheric injection to the time of ER-2 intercept on 16:36 UTC 10 June 2022 ("time 0"). Panel (a) shows Solar Zenith Angle (SZA); shaded regions indicate SZA > 90°. Panel (b) shows the mean and range of heterogeneous reaction probabilities (solid lines and shaded regions, respectively). Panels (c) and (d) show simulated mixing ratios of ClO and NO_x, respectively. The various lines in panels (c) and (d) represent model results for varying initial conditions of $[NO_x]$, $[ClONO_2]/[Cl_y]$, and aerosol SAD. Results initialized with values of $[ClONO_2]/[Cl_y]$, $[NO_x]$, and SAD encountered during this intercept are represented by the solid brown lines (triangle symbol at intercept). Results using Robrecht et al. (2019) initializations are represented by the solid blue lines (circle). Results using Anderson et al. (2012) initializations are represented by the solid red lines (square). Dotted black lines (diamond) represent results initialized the same as the brown, except with a higher aerosol SAD of 10 $\mu m^2/cm^3$; all other results are initialized with an aerosol SAD = 1.13 $\mu m^2/cm^3$. All model runs are initialized with the daytime $[NO]/[NO_2]$ ratio of 4.06, which is based on steady state conditions at the start of the trajectory. Measured [ClO] and calculated $[NO_x]$ at the time of ER-2 intercept are indicated by black stars on panels (c) and (d), respectively. Values of [CO], $[CH_4]$, $[O_3]$, $[H_2O]$, and aerosol SAD are kept constant with time.

For the 16:36 UTC intercept, our model simulations show similar enhancements of [ClO] at the time of ER-2 intercept (solid brown lines, Figure 2.6c) to those illustrated in Figure 2.5, despite longer exposure to cold and wet conditions. Similar to the parcel simulated in Figure 2.5, this parcel exhibited low $[ClONO_2]/[Cl_y]$ and high $[NO_x]$, both of which contribute to the small values of [ClO] at the time of ER-2 intercept. The enhancement of [ClO] at intercept time is limited by the slow removal of $[NO_x]$, as shown in Figure 2.6d, particularly in simulations

initialized with lower [$ClONO_2$]/[Cl_y] ratios (e.g., 0.01 and 0.04) and the average aerosol surface area density (SAD) of 1.13 $\mu m^2/cm^3$. Although the simulation with higher aerosol SAD of 10 $\mu m^2/cm^3$ results in slightly elevated [ClO] (~5 ppt), the small reduction in [NO_x], in relation to the initial value of 1,209 pptv, indicates that the exposure to cold and wet conditions was still insufficient to drive significant chlorine activation, consistent with findings in Figure 2.5.

Together, Figures 2.5 and 2.6 demonstrate that the Cl_y-rich air parcels observed during DCOTSS 2022 were not exposed to low temperatures and high water vapor conditions long enough prior to ER-2 sampling to allow for significant chlorine activation to be observed. Even if the simulated air parcels had higher initial [$ClONO_2$]/[Cl_y] and lower initial [NO_x], as used by Anderson et al. (2012) and Robrecht et al. (2019), or a higher aerosol SAD, there was still insufficient time to remove [NO_x] and elevate [ClO] by the time of ER-2 intercept. Robrecht et al. (2019) and Anderson et al. (2012) show much larger enhancements of [ClO] ($\gtrsim$100 pptv), compared to our model runs, because their simulations were initialized at slightly lower temperatures and extended much further in time, to 80 and 120 hr respectively, compared to our 12.5 and 18.1 hr simulations. As shown below, higher abundances of [ClO] do occur for longer processing times, particularly for simulations using the Anderson et al. (2012) initialization.

We next examine forward model simulations to quantify the level of chlorine activation that would have been observed if the 16:36 UTC air parcel had remained intact and been sampled after continued exposure to cold and wet conditions further out in time. We have chosen to show forward model simulations for the 16:36 UTC air parcel rather than the 16:31 UTC parcel (Figure 2.5) because the higher levels of [Cl_y], [H_2O], and [O_3] observed for this intercept provide conditions more favorable for chlorine activation. However, our model simulations for the 16:31 UTC yield similar results (not shown). These simulations are further used to quantify

the sensitivity of chlorine activation over an extended period to initial values of [$ClONO_2$]/[Cl_y], [NO_x], and aerosol SAD. Figure 2.7 shows five of these forward model simulations, initialized at the time of the ER-2 intercept at 16:36 UTC on 10 June 2022, each distinguished by different initial values of [$ClONO_2$]/[Cl_y], [NO_x], and aerosol SAD. We extend these simulations 120 hr forward to represent the approximate time frame that parcels may have remained intact and exposed to the cold conditions of the NAMA (Chang et al., 2023). Temperature and pressure are kept constant at T = 200 K and P = 100 hPa, the values corresponding to the peak in heterogeneous reaction probabilities along the parcel's back-trajectory (Figure 2.6b). Additionally, [H_2O] is held constant at 18.2 ppmv, the value observed at the time of the ER-2 intercept. These simulations are designed to represent the full extent of chlorine activation that could occur, without loss of [O_3], if T and [H_2O] had been conserved at these measured levels for 5 days.

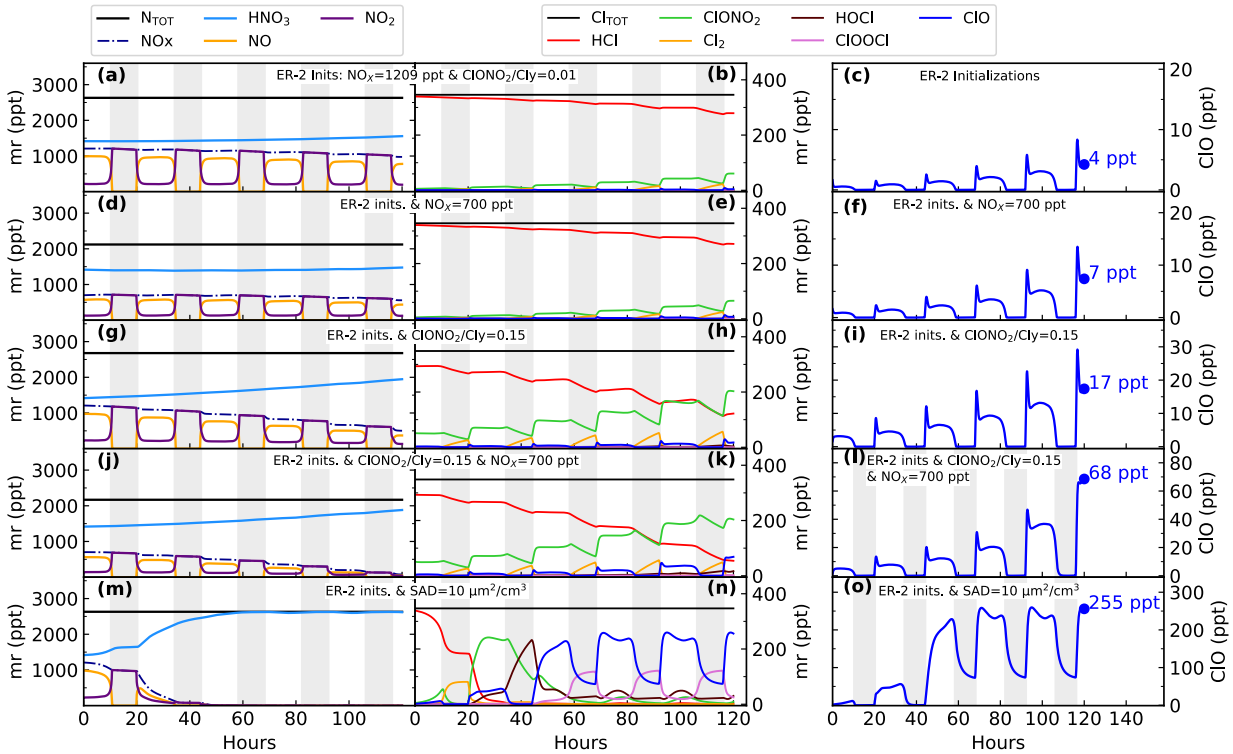


Figure 2.7. Mixing ratios of chlorine and nitrogen species modeled forward 120 hr from the time of 10 June 2022 ER-2 intercept at 16:36 UTC. The left panel shows the evolution of [NO] (gold), [NO_2] (purple), [NO_x]

([NO] + [NO_2]; navy, dash-dotted line), [HNO_3] (light blue), and [N_{TOT}] (black). The middle column shows the evolution of [HCl] (red), [$ClONO_2$] (lime), [HOCl] (brown), [Cl_2] (gold), [ClOOCl] (pink), and [ClO] (blue). ClO is highlighted again in the right column, with changing y-axis limits. The various rows represent different pairings of initial conditions. Panels (a)–(c) are initialized with the values obtained at the 16:36 UTC ER-2 intercept, referred to as the "ER-2 initializations" or "ER-2 inits." Panels (d)–(f) initialized with ER-2 inits and [NO_x] = 700 pptv. Panels (g)–(i) are initialized with ER-2 inits and [$ClONO_2$]/[Cl_y] = 0.15. Panels (j)–(l) are initialized with [NO_x] = 700 pptv and [$ClONO_2$]/[Cl_y] = 0.15. Panels m–o are initialized with the ER-2 inits and an aerosol SAD = 10 $\mu m^2/cm^3$. All model runs are initialized with the daytime [NO]/[NO_2] ratio of 4.6, which is based on steady state conditions at the start of this trajectory. The gray shaded regions correspond to time where solar zenith angle >90°. As in the previous simulations, mixing ratios of CO, CH_4, O_3, H_2O, as well as aerosol SAD and T are kept constant with time at the values observed at the time of ER-2 intercept.

The first model run is based on the conditions observed at the 16:36 UTC ER-2 intercept (Figures 2.7a , 2.7b, and 2.7c). This simulation is initialized with [Cl_y] = 345 pptv, [$ClONO_2$]/[Cl_y] = 0.01, [ClO] = 1.6 pptv, [HNO_3] = 1.42 ppbv, [NO_x] = 1,209 pptv, and aerosol SAD = 0.87 $\mu m^2/cm^3$, as observed at the time of ER-2 intercept. All other species (HOCl, Cl, Cl_2, NO_3, N_2O_5) are initialized in steady state. In contrast to our back-trajectory simulations presented in Figures 2.5 and 2.6, which were initialized with the average aerosol SAD encountered within the gray-shaded region of Figure 2.3 of 1.13 $\mu m^2/cm^3$ (to account for possible variations in aerosol SAD following stratospheric injection), our forward model simulations are initialized with aerosol SAD of 0.87 $\mu m^2/cm^3$, the observed value at the ER-2 intercept of the 16:36 UTC air parcel. In the three subsequent model runs, we use the same set of initial conditions detailed above, except with adjusted initial values for [NO_x] and [$ClONO_2$]/[Cl_y]. The fifth model run initializes with an aerosol SAD of 10 $\mu m^2/cm^3$ to represent possible volcanic or stratospheric sulfate aerosol injection enhancements, which will be discussed in Section 2.3.3.

The model results in Figures 2.7a–2.7c allow us to examine whether chlorine activation would have been observed for the 16:36 UTC intercepted air parcel had it been exposed to cold and wet conditions for an extended period. Here, the chlorine reservoirs (HCl and $ClONO_2$) remain relatively stable throughout the 5-day period (Figure 2.7b), and changes in [HNO_3] and

[NO_x] with time are relatively consistent with gas phase partitioning (Figure 2.7a). The slight increase in [$ClONO_2$] computed after 120 hr (Figure 2.7b) is due to heterogeneous chemistry that produces ClO and is followed by the ClO + NO_2 reaction. However, [ClO] remains low (Figure 2.7c) because of the excess [NO_x] that remains in the system (Figure 2.7a), consistent with our findings from Figure 2.6. Although chlorine activation at the time of ER-2 intercept may have been limited by insufficient processing time (Figure 2.6), extending the exposure to 5 days results in an enhancement of [ClO] to about 4 pptv (Figure 2.7c). This enhancement of [ClO] is too small to appreciably affect ozone due to the presence of high levels of [NO_x] that remain in the air parcel (Figure 2.7a). These cold and wet conditions would need to persist for upwards of 20 days for [ClO] to exceed [NO_x] in this simulation (not shown). However, mixing between this moist parcel and the background stratosphere would likely lead to dilution, preventing significant chlorine activation before this timescale is reached.

We next assess whether chlorine activation would have been observed further out in time had [NO_x] been lower than what is calculated using the steady-state expression (Figures 2.7d–2.7f). This simulation is initialized with [NO_x] at 700 pptv, as used in Anderson et al. (2012), instead of 1,209 pptv observed at the time of ER-2 intercept (Figure 2.7a). The Anderson et al. (2012) value of 700 ppt resides just below the propagated 1σ uncertainty of [NO_x] for this intercept. The 509 pptv reduction in [NO_x] allows for an increase of [ClO] at 120 hr, from 4 to 7 pptv (Figure 2.7f). However, chlorine activation remains limited by the insufficient availability of a reaction partner for HCl, which slows the rate of the key heterogeneous reaction (HCl + $ClONO_2$) and consequently limits the sequestration of [NO_x].

Model simulations in Figures 2.7g–2.7i are initialized with a [$ClONO_2$]/[Cl_y] ratio of 0.15, as used in Anderson et al. (2012) for a higher altitude, instead of 0.01 observed at the time

of ER-2 intercept. The 0.14 increase in $[ClONO_2]/[Cl_y]$ allows for ClO mixing ratios at 120 hr to increase from 4 to 17 pptv. The more pronounced changes of $[ClONO_2]$ and [HCl] in this simulation, compared to the previous two, reveal the sensitivity of heterogeneous reaction rates to the partitioning of the two primary chlorine reservoirs. The large increase in $[ClONO_2]$ seen in Figure 2.7h is a result of heterogeneous processing; however, enhancement of [ClO] remains suppressed by the high levels of $[NO_x]$ that persist.

The fourth model simulation is designed to investigate the combined impact of low initial $[NO_x]$ and high initial $[ClONO_2]/[Cl_y]$ on chlorine activation for this air parcel. This model simulation (Figures 2.7j–2.7l) is initialized with both the Anderson et al. (2012) values for $[ClONO_2]/[Cl_y]$ (0.15) and $[NO_x]$ (700 pptv). Here, [ClO] reaches 68 pptv after 120 hr (20% activation)—a 12-fold increase from our first model simulation (Figure 2.7c). Therefore, if this air parcel had contained less $[NO_x]$ and an initial $[ClONO_2]$ abundance that was at least 15% of $[Cl_y]$, much larger enhancements of [ClO] could have been observed further out in time. In contrast, Robrecht et al. (2019) initialized with much less $[Cl_y]$ (156 pptv) and lower $[ClONO_2]/[Cl_y]$ (0.04) than Anderson et al. (2012), and they still found [ClO] enhanced upwards of ∼100 pptv after about 80 hr.

The Robrecht et al. (2019) study initialized with much lower $[NO_x]$ (289 pptv) than was calculated for this intercept (1,209 pptv), which significantly reduced the time frame required to activate chlorine in their simulation initialized with $[H_2O]$ = 15 ppmv and temperatures in the range of 197–202 K. Figure 2A.15 in Appendix A is analogous to Figure 2.7, except the values of initial $[ClONO_2]/[Cl_y]$ and $[NO_x]$ are taken from Robrecht et al. (2019). Figure 2.7 and Figure 2A.15 in Appendix A show that a combination of higher $[ClONO_2]/[Cl_y]$ and lower $[NO_x]$ than observed for this ER-2 intercept are both needed to result in chlorine activation over the 5-day

period of the simulation. In the next section, we will assess whether values of $[ClONO_2]/[Cl_y]$ and $[NO_x]$ favorable for chlorine activation occurred simultaneously within any of the cold and wet air parcels sampled during DCOTSS 2022.

2.3.2 NAMA Summer of 2022

In the prior section, we established the importance of initial values of $[ClONO_2]/[Cl_y]$ and $[NO_x]$, in addition to $[H_2O]$, $[Cl_y]$, and T, for activation of chlorine in the LS. Here, we analyze all DCOTSS 2022 data to assess whether $[ClONO_2]/[Cl_y]$ ratios were high enough and $[NO_x]$ mixing ratios low enough to enable chlorine activation in the midlatitude LS. Figure 2.8 shows $[ClONO_2]/[Cl_y]$ and $[NO_x]$ observed for DCOTSS 2022, along with the assumptions made for $[ClONO_2]/[Cl_y]$ and $[NO_x]$ in the Anderson et al. (2012) and Robrecht et al. (2019) studies. Here, we filter the data to only show parcels with $[Cl_y] > 100$ pptv to select air parcels with enough inorganic chlorine present to provide potentially important levels of $[ClONO_2]/[Cl_y]$. Figure 2.8b further limits the data to air parcels for which the minimum heterogeneous time constant (τ_{HET}) for chlorine activation is less than 120 hr.

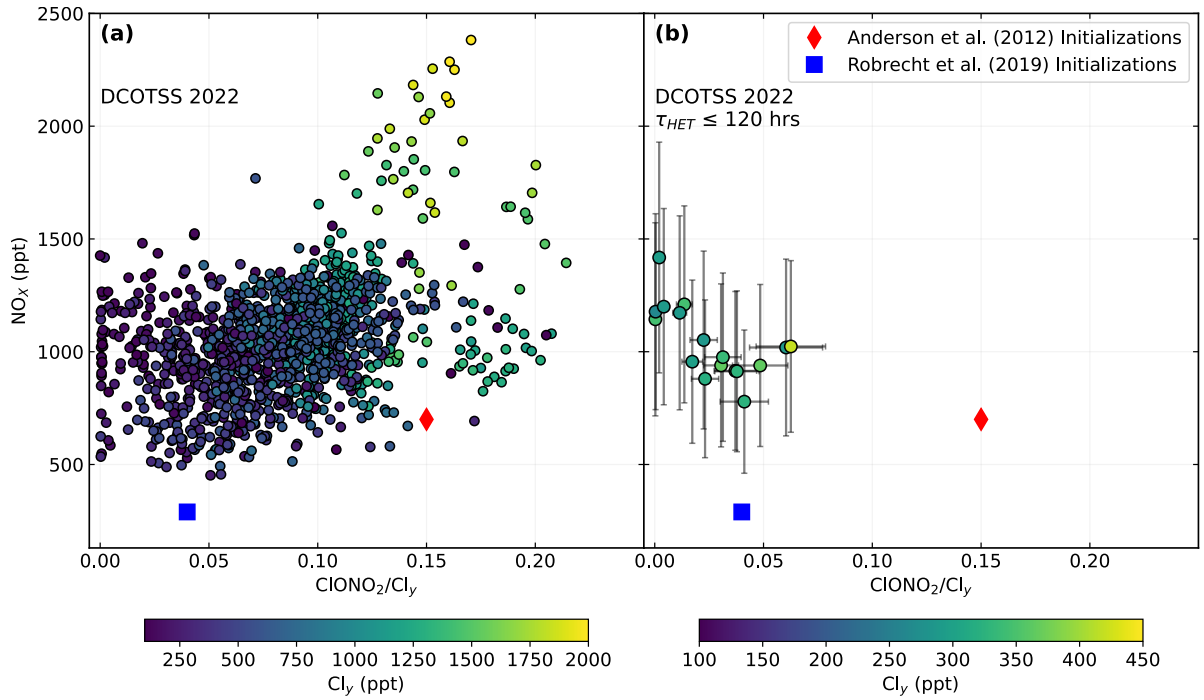


Figure 2.8. DCOTSS 2022 [NO_x] versus [$ClONO_2$]/[Cl_y] colored by estimated [Cl_y]. All data in panels (a) and (b) are filtered for [Cl_y] > 100 pptv. Panel (a) shows all DCOTSS 2022 observations. Panel (b) shows only parcels where τ_{HET} < 120 hr, along with ±1σ uncertainties. Initializations from Anderson et al. (2012) and Robrecht et al. (2019) are shown in red and blue markers, respectively.

Figure 2.8a shows that most data acquired during DCOTSS 2022 cluster around higher mixing ratios of NO_x compared to the initial conditions used in the prior studies of Anderson et al. (2012) and Robrecht et al. (2019). The [$ClONO_2$]/[Cl_y] observed during DCOTSS spans a large range, including the initial conditions used in these prior studies. When the data are filtered to show only air parcels with heterogeneously suitable conditions ($\tau_{HET} \leq 120$ hr), only 1% of the data points remain (Figure 2.8b). Although there is some overlap between ER-2 observations of [$ClONO_2$]/[Cl_y] and [NO_x] with the Anderson et al. (2012) and Robrecht et al. (2019) initializations for the large-scale sampling (Figure 2.8a), this overlap disappears when the data are filtered by the heterogeneous time constant constraint (Figure 2.8b). Although the Anderson et al. (2012) initialization of [NO_x] at 700 pptv falls within a reasonable range of our propagated 1σ uncertainties, the Robrecht et al. (2019) initialization of [NO_x] at 289 pptv lies well outside our uncertainty range. All air parcels observed with heterogeneously suitable conditions

($\tau_{HET} \leq 120$ hr) with [Cl_y] > 100 pptv during DCOTSS 2022 had [$ClONO_2$]/[Cl_y] ratios too low to allow for heterogeneous processing to occur at a rate that would convert NO_x to HNO_3 within the median time frame that parcels reside within the NAMA (~5 days). Even if NO_x mixing ratios were 40% lower than calculated using the steady-state expression, as suggested as possible in the LS by Jaeglé et al. (1994), they would still be too high to permit substantial chlorine activation under these conditions due to the lack of $ClONO_2$ (i.e., chemically aged air). These limiting factors add to the already established conditions of sufficient [Cl_y] and [O_3] abundances (Schwartz et al., 2013; von Hobe et al., 2011) as well as the requirements involving temperature and [H_2O] (Anderson et al., 2012, 2017; Robrecht et al., 2019).

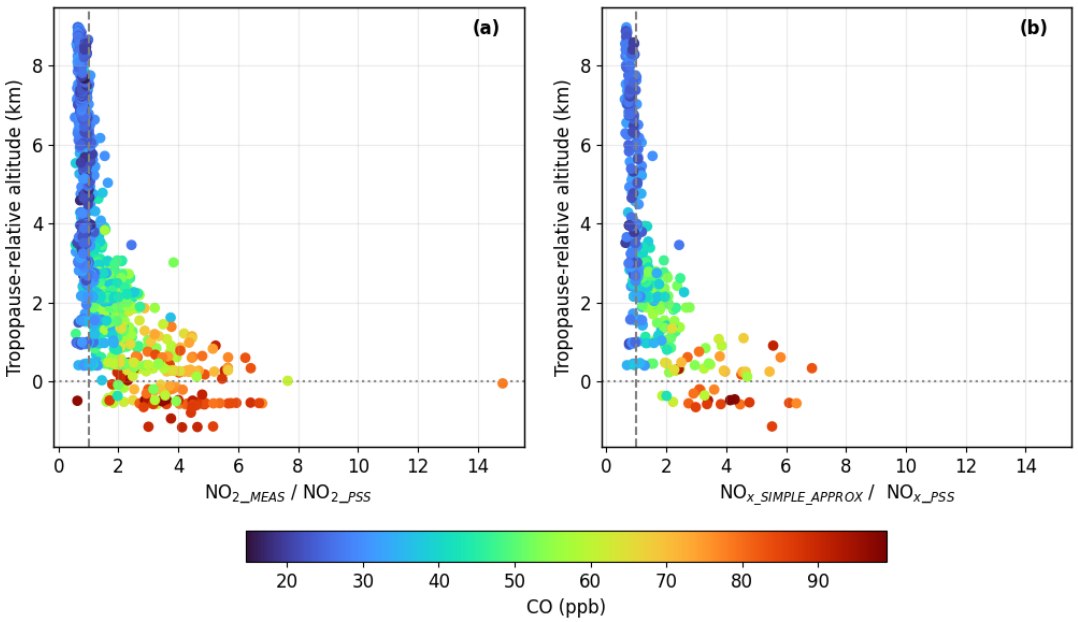


Figure 2.9. Ratio of [NO_2] measured by the CANOE instrument to [NO_2] calculated from our photochemical steady state (PSS) model simulations (panel a), and ratio of [NO_x] calculated from our simple expression (see Equation 2.1) to [NO_x] from our PSS model simulations (panel b), shown as a function of altitude relative to the ERA5 tropopause. Data are colored by measured [CO]. The dashed vertical line indicates a 1:1 ratio. The dotted horizontal line marks the ERA5 lapse rate tropopause.

Figure 2.9 shows the ratios of measured [NO_2], and [NO_x] inferred from measured [NO_2] using Equation 2.1 ("$NO_{x_SIMPLE_APPROX}$"), to the values of [NO_2] and [NO_x] found using the PSS simulation of five DCOTSS 2022 flights (Section 2.2.6). This ratio is shown as a function of

altitude relative to the ERA5 lapse rate tropopause, and the color bar indicates associated values of [CO] measured by the Harvard University Picarro Cavity Ringdown Spectrometer instrument (Table 2.1). A value of unity for this ratio indicates that [NO_x] inferred from measured [NO_2] is consistent with the amount of [NO_x] that is supplied from the decomposition of N_2O, since the [NO_y] versus [N_2O] relation used to constrain the photochemical model is representative of the large-scale, midlatitude stratosphere (see Figure 2A.11 in Appendix A). Figure 2.9 shows that inferred [NO_x] is significantly larger than steady state [NO_x] near the tropopause, in a manner that is strongly correlated with [CO]. This observation suggests that vertical transport of combustion-driven pollution (Fischer et al., 2000) is influencing the abundance of [NO_x] in cold, wet air masses observed during DCOTSS 2022. Lightning may also play a role in the elevated levels of [NO_x] observed in these air masses (Huntrieser et al., 2016a,b; Pérez-Invernón et al., 2023; Pickering et al., 2024), especially below the tropopause, where the correlation between [CO] and measured-to-modeled [NO_2] ratios is less apparent. For the gray shaded region of Figure 2.3, the mean value of inferred [NO_x] is ∼1,200 pptv, the PSS value of [NO_x] is ∼900 pptv, and the value of [NO_x] used by Robrecht et al. (2019) is 289 pptv. The Robrecht et al. value is about equal to the 2σ lower limit of 260 pptv for inferred [NO_x] during DCOTSS 2022.

We next use ACE-FTS data (Boone et al., 2023) to evaluate whether the low values of [$ClONO_2$]/[Cl_y] during DCOTSS 2022 are typical of the midlatitude LS. Figure 2.10 shows ACE-FTS measurements of profiles of [$ClONO_2$] (Figure 2.10a), [HCl] (Figure 2.10b), and the [$ClONO_2$]/([$ClONO_2$] + [HCl]) fraction (Figure 2.10c) over 30–60°N in 2022. To account for the instrument's increased sampling at high latitudes (see Text 2A.7 and Figure 2A.16 in Appendix A), the ACE-FTS data were first grouped into 5° latitude bins and averaged. These 5° latitude

averages were subsequently averaged together to produce annual, December, January, February (DJF), and JJA (June, July, August) averages within the 30–60°N region. The shaded region indicates the altitude range (~13.1–17.4 km) over which air parcels with heterogeneous time constants of less than 120 hr were observed during DCOTSS 2022. For simplicity, we will refer to the [$ClONO_2$]/[$ClONO_2$ + HCl] ratio depicted in Figure 2.10c as [$ClONO_2$]/[Cl_y].

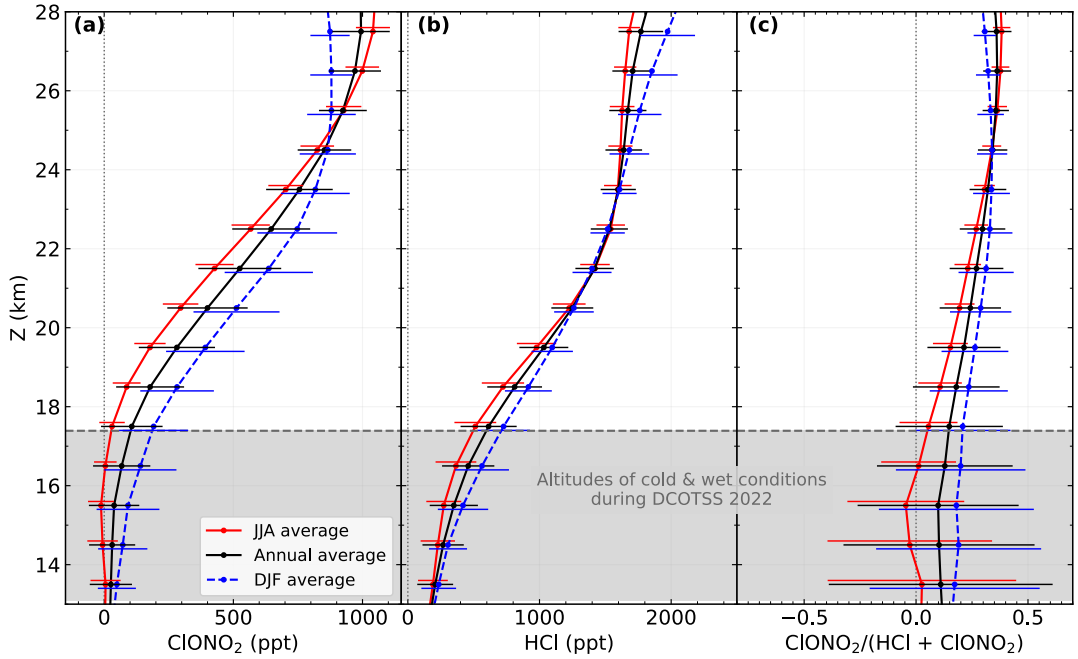


Figure 2.10. ACE-FTS version 5.2 data obtained over 30–60°N during 2022, showing annual (black), December, January, February (dashed blue), and JJA (red) averages. Panel (a) shows ACE-FTS [$ClONO_2$], panel (b) shows [HCl], and panel (c) shows [$ClONO_2$]/([HCl] + [$ClONO_2$]). Error bars indicate the standard deviation among the averaged profiles. The shaded regions indicate the range of altitudes where $\tau_{HET} \leq 120$ hr during DCOTSS 2022.

Figure 2.10 reveals significant seasonal variation in [$ClONO_2$] and [$ClONO_2$]/[Cl_y] and in the midlatitude lowermost stratosphere. Within the shaded region, the annual averages of [$ClONO_2$]/[Cl_y] (black line, Figure 2.10c) reach up to 0.15, consistent with the initialization used by Anderson et al. (2012) as well as the 2004 annual average profiles shown by Nassar et al. (2006). The winter (DJF) and annual ACE-FTS averages show higher magnitudes of [$ClONO_2$] and [$ClONO_2$]/[Cl_y] compared to the summer averages due to the increased descent of the Brewer-Dobson Circulation during winter that transports Cl_y-rich air from higher altitudes

into the LS. The ACE-FTS data suggest that the presence of sufficient [$ClONO_2$], between ~13 and 17 km, to provide a reaction partner for HCl is notably absent during summer months. However, below ~18 km, the ACE-FTS retrievals of [$ClONO_2$] are subject to increased noise, often resulting in negative values when VMRs approach zero (Mahieu et al., 2005; Wolff et al., 2008). Although these negative values lack physical meaning, the mean value of [$ClONO_2$] shown in Figure 2.10a indicates that the actual VMR is at or below the detection limit. In summary, the ACE-FTS data suggest that for the altitude regions in which conditions conducive to chlorine activation were commonly observed during DCOTSS, most Cl_y was likely present as HCl (Figure 2.10c). We omit ACE-FTS [HOCl] from Figure 2.10 as the majority of measurements within this region are indistinguishable from zero by the ACE-FTS instrument. Furthermore, we find that chlorine activation via HOCl + HCl is slow compared to $ClONO_2$ + HCl for the conditions observed during DCOTSS (see Figure 2A.9h in Appendix A). The tendency for the vast majority of inorganic chlorine to be present as HCl is consistent with our findings from DCOTSS data, as well as earlier in situ measurements of [$ClONO_2$] and [HCl] at pressures >100 hPa for the high northern latitude, lower stratosphere (Voss et al., 2001).

Here, we offer a brief comment about how conditions could change in the future. If the convective influence of enhanced [H_2O] and low temperature were to extend to 18 km and higher altitudes, which is higher than observed during DCOTSS (gray-shaded region in Figure 2.10), the concentration of $ClONO_2$ observed by ACE-FTS at these altitudes would favor chlorine activation. At 18–20 km altitude, a larger fraction of organic VSL chlorine and bromine compounds have decomposed compared to lower altitudes (Wamsley et al., 1998; Woodbridge et al., 1995). Bromine monoxide that forms following the decomposition of natural, biogenic VSL bromine compounds provides an important reaction partner for ClO (Salawitch

et al., 2005). The VSL source of chlorine will likely become more important in the future, because the majority of these gases are anthropogenic and the stratospheric injection of these species is rising, because these gases are not regulated by the Montreal Protocol (Chipperfield et al., 2020; Hossaini et al., 2015, 2017, 2019). Should the cooling of the stratosphere associated with global warming (Garny et al., 2022; Steiner et al., 2020) lead to a higher altitude for the cold, wet conditions that follow convective injection, the ozone loss due to chlorine activation described by prior modeling studies (Anderson & Clapp, 2018; Anderson et al., 2012, 2017; Robrecht et al., 2019) could occur.

Douglass et al. (1995) and Grooß et al. (1997, 2011) offer theoretical insight that explains why the majority of inorganic chlorine (Cl_y) would exist as HCl within the convectively influenced air masses sampled during DCOTSS (Figure 2.8). Their studies examined the [Cl]/[ClO] ratio and the mechanism by which chlorine activation and ozone depletion cycles terminate in polar regions. They showed that when O_3 mixing ratios drop below 500–1,000 ppbv, partitioning shifts toward high values of the [Cl]/[ClO] ratio, resulting in active chlorine species such as ClO, ClOOCl, and Cl being rapidly converted back to HCl. We extend this theory to better understand the onset of chlorine activation in the midlatitude regions. The equation governing the [Cl]/[ClO] ratio provided in Douglass et al. (1995),

$$\frac{[\mathrm{Cl}]}{[\mathrm{ClO}]} = \frac{\mathrm{J_{NO2}} \mathrm{k_{ClO+NO}} [\mathrm{NO_2}]}{\mathrm{k_{NO+O3}} \mathrm{k_{Cl+O3}} [\mathrm{O_3}]^2 + \mathrm{k_{Cl+O3}} \mathrm{k_{ClO+NO}} [\mathrm{O_3}][\mathrm{ClO}]} \quad (2.4)$$

is used to evaluate this theory against DCOTSS 2022 observations in Figure 2.11.

Figure 2.11 shows measured [$ClONO_2$] versus the calculated [Cl]/[ClO] ratio, colored by [O_3], for data collected during DCOTSS 2022. Here, the [Cl]/[ClO] ratio is found using Equation 2.4 of Douglass et al. (1995). The cyan markers on Figure 2.11 indicate air parcels with

heterogeneous time constants ≤120 hr. The [Cl]/[ClO] ratio is computed from ER-2 measurements of [O_3], [NO_2], [ClO], J values for NO_2 (described in Section 2.2.3), and the JPL kinetics (Burkholder et al., 2019) recommendation for the five reactions used in the expression. Most importantly, all the cyan markers are associated with low mixing ratios of O_3, below 500 ppbv.

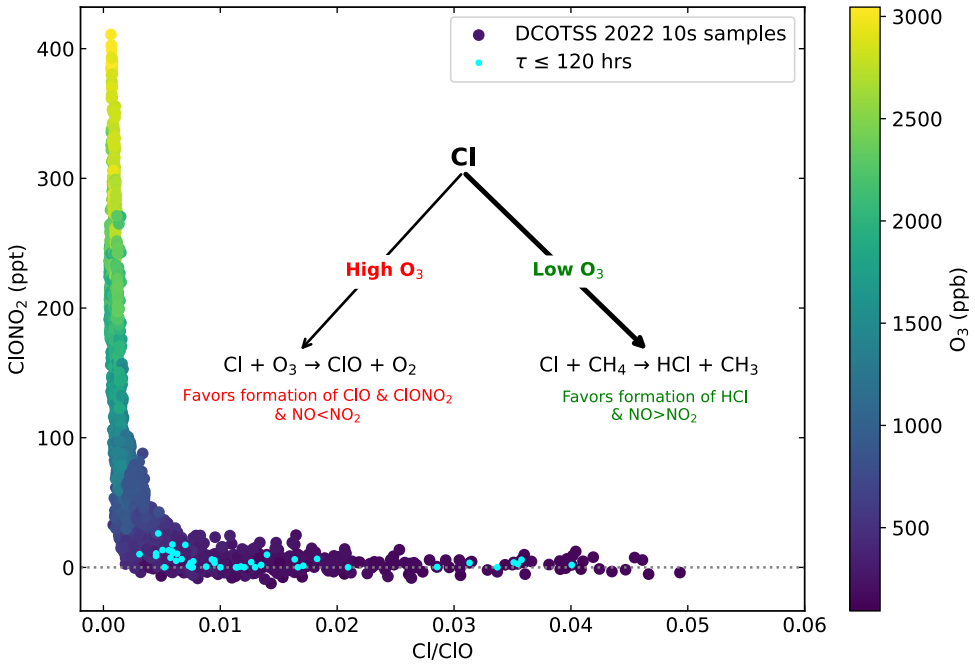


Figure 2.11. Daytime (solar zenith angle <90°) measurements of [$ClONO_2$] versus calculated [Cl]/[ClO], colored by measured [O_3]. Cyan markers indicate parcels with $\tau_{HET} \leq 120$ hr.

Figure 2.11 illustrates that under conditions of low ozone ([O_3] < 500 ppbv), typical of the cold, wet air masses observed during DCOTSS (Figures 2.2d–2.2f), rapid gas phase chemical partitioning shifts reactive chlorine (Cl + ClO) toward atomic Cl. Under these low [O_3] conditions, loss of Cl from the reaction with O_3 (that produces ClO) slows down. The abundance of Cl rises, and the reaction of Cl with CH_4 (that produces HCl) speeds up, leading to the conversion of nearly all available inorganic chlorine to HCl. Additionally, the [NO]/[NO_2] ratio increases because the NO + O_3 → NO_2 + O_2 reaction is slowed under low ozone mixing ratios,

meaning less NO_2 is reformed after its photodissociation. This increases the tendency for ClO to react with NO to form Cl, rather than reacting with NO_2 to form $ClONO_2$. These chemical changes that take place under low [O_3] cause the [$ClONO_2$]/[Cl_y] ratio to become very small. Therefore, this chemical repartitioning (Douglass et al., 1995; Grooß et al., 1997, 2011) explains why [$ClONO_2$]/[Cl_y] ratios were observed to be uniformly low at the lowest stratospheric altitudes sampled in DCOTSS, and nearly all Cl_y that was present presumably exists as HCl (which was not measured). The relatively low mixing ratios of O_3 (<500 ppbv) within the cold and wet air masses sampled during DCOTSS can be attributed to their young age and proximity to the tropopause. A large and sustained perturbation to heterogeneous chemistry, whether through enhanced [H_2O] or increased aerosol SAD, would need to occur for heterogeneous reaction rates to outpace chlorine deactivation under background ozone conditions in the midlatitude lowermost stratosphere.

2.3.3 Geoengineering and Major Volcanic Eruptions

In the midlatitude stratosphere, sulfate aerosols provide surfaces for heterogeneous reactions that activate chlorine and suppress NO_x to take place (Fahey et al., 1993; Hofmann & Solomon, 1989; McElroy et al., 1992; Solomon, 1999; Solomon et al., 1996). Enhancements in stratospheric aerosols accelerate these heterogeneous reactions by increasing the surface area of particles in which these reactions take place (Drdla & Müller, 2012; Robrecht et al., 2019; Solomon, 1999; Solomon et al., 1996). As observed following major volcanic eruptions, enhancements in stratospheric sulfate aerosols (SSA) can lead to significant ozone depletion perturbed by heterogeneous chemistry (Fahey et al., 1993; Hofmann & Solomon, 1989; Johnston & McKenzie, 1989; Kinnison et al., 1994; Salawitch et al., 2005; Solomon et al., 1996).

The largest perturbation to [ClO]/[Cl_y] observed in the midlatitude LS due to heterogeneous chemistry occurred following the eruption of Mount Pinatubo in June 1991 (Keim et al., 1996). This eruption resulted in record ozone depletion at NH midlatitudes, which persisted for several years following the eruption (Hofmann et al., 1994; Kinnison et al., 1994; Salawitch et al., 2005). The magnitude of ozone loss following this event provides direct evidence of the significant role that enhanced SSA can have on heterogeneous chlorine activation in midlatitudes. Following the eruption of Mount Pinatubo, the 2011 Nabro eruption in Eritrea resulted in the largest injection of SO_2 into the UTLS (e.g., Fairlie et al., 2014) and has been linked to a ~4%–5% reduction in lower stratospheric ozone (Haskins, 2014). The January 2022 Hunga eruption led to significant increases in [ClO] and decreases in [HCl] and [O_3] in the tropics and the midlatitude Southern Hemisphere stratosphere (Santee et al., 2023; Wilmouth et al., 2023; Zhang et al., 2024), due to the injection of a modest amount of SO_2 and an enormous amount of water vapor into the stratosphere (Millan et al., 2022; Vömel et al., 2022). All observations during DCOTSS were obtained at times and places that were unaffected by the Hunga eruption.

Furthermore, Thornton et al. (2007) reported substantial chlorine activation (50%) in the midlatitude LS over CONUS during the WB-57F Aerosol Mission (WAM) in April 1998 within a region of high aerosol SAD (5–20 $\mu m^2/cm^3$) and elevated water vapor (20–25 ppm), perturbed from gravity-wave induced tropospheric mixing. Their findings provide additional evidence that chlorine activation is highly sensitive to the combination of high aerosol surface area density and elevated [H_2O]. Therefore, it is essential to evaluate the effect that SSA enhancements could have on convectively influenced air masses in today's midlatitude stratosphere, especially with the future possibility of sulfate geoengineering.

Sulfate geoengineering is a climate mitigation strategy proposed to moderate global mean temperatures through the injection of additional sulfate into the stratosphere (Bernhard et al., 2023; Crutzen, 2006; National Academies of Sciences, 2021; Tracy et al., 2022; Visioni et al., 2023). An annual injection rate of SO_2 (gaseous precursor of SSA) of about 8–16 million tonnes is needed to reduce global mean surface temperature by about 1°C by the end of the century, which is comparable to the stratospheric injection of SO_2 following the eruption of Mount Pinatubo (Haywood et al., 2022). An injection at these proposed magnitudes could accelerate heterogeneous reactions that activate chlorine and suppress NO_x, thereby increasing the risk of chlorine-catalyzed ozone destruction (Haywood et al., 2022; Tilmes et al., 2008, 2012). The simulated enhancement in the SAD of SSA from stratospheric aerosol injection (SAI) is governed by chemical processes, aerosol microphysics, stratospheric transport, and interactions with radiation, all of which depend on the specific injection strategy and how these processes are represented in models (Haywood et al., 2022; Heckendorn et al., 2009; Tilmes et al., 2022). Tilmes et al. (2022) show that SAI could increase background aerosol SAD in the northern midlatitudes from 5 to 20 $\mu m^2/cm^3$ in the first two decades of implementation, to over 40 $\mu m^2/cm^3$—levels comparable to those observed after the Mount Pinatubo eruption (Thomason et al., 1997)—over the next century, depending on the injection strategy and interactive chemistry model used. The response of midlatitude lower stratosphere ozone to SAI is further complicated by how stratospheric dynamics and chemistry, including chlorine activation and NO_x sequestration, will evolve over time (WMO, 2022).

In contrast, Robrecht et al. (2021) investigate the impact of SAI in the midlatitude lowermost stratosphere using a series of model runs termed Geoengineering Large Ensemble Simulations (GLENS). They found that less than 1% of ozone is depleted via heterogeneous

chlorine activation, upon application of SAI within the Whole Atmosphere Community Climate Model (WACCM). However, convectively enhanced water vapor in the LS is likely underestimated in these GLENS simulations, because convection implemented in WACCM does not consider overshooting convection (Robrecht et al., 2021). Furthermore, Robrecht et al. (2021) find that there is a positive temperature bias of 2–4 K in the GLENS simulations compared to observations obtained within tropopause-overshooting convection during the SEAC^{4}RS campaign. Therefore, the potential for heterogeneous chlorine activation may be underestimated by large-scale models that lack representation of the cold and wet conditions present in the midlatitude LS during the summer months. The magnitude of ozone loss (~8% to 10%) (Salawitch et al., 2005; Solomon et al., 1998) observed following the eruption of Mount Pinatubo in 1991 exemplifies that enhancements in aerosol SAD can accelerate heterogeneous chemistry at a level that would lead to significant ozone loss when paired with the cold and wet conditions of the midlatitude LS. Due to the continued decline of anthropogenic halogen levels, the response of stratospheric ozone to future volcanic eruptions may differ from that observed following the 1991 Mount Pinatubo eruption. However, this impact remains uncertain, owing to rising emissions of VSLS, increasing GHG concentrations, and the possibility of stratospheric injection of volcanic hydrogen halides by certain types of eruptions (Klobas et al., 2017; Østerstrøm et al., 2023).

Here we show that under elevated stratospheric water vapor conditions (>11 ppmv), as observed during DCOTSS, future enhancements in the SAD of SSA from sulfate geoengineering could significantly accelerate chlorine activation in the midlatitude stratosphere (Anderson et al., 2017). We use forward model simulations, described in Section 2.2.5, to assess how increasing aerosol SAD can affect chlorine activation in the context of DCOTSS 2022

observations. The simulations presented in Figures 2.7m–2.7o (Section 2.3.1) show the impact of elevated aerosol SAD on chlorine activation for our high [Cl_y] case sampled during the 10 June 2022 research flight. This model simulation is initialized with meteorological values and gaseous mixing ratios associated with the 16:36 UTC ER-2 intercept and an aerosol SAD of 10 $\mu m^2/cm^3$. This model simulation (Figures 2.7m–2.7o) shows that an enhancement in SAD to 10 $\mu m^2/cm^3$, a magnitude associated with the geoengineering of climate by sulfate injection (Tilmes et al., 2022), would significantly accelerate heterogeneous chemistry for this Cl_y-rich parcel. Mixing ratios of NO_x are rapidly reduced and converted into HNO_3 within the first three diurnal periods (Figure 2.7m), releasing ClO from the $ClONO_2$ reservoir. Mixing ratios of ClO above 100 pptv are observed approximately 60 hr into the model run. Enhancements of [ClO] reach 255 pptv after 5 days, a stark contrast to the 4 pptv found when initializing the model with the observed aerosol SAD of 0.87 $\mu m^2/cm^3$ (Figure 2.7c). Elevated aerosol SAD allows these heterogeneous reactions to compete effectively with the chlorine deactivation processes. The rapid buildup of $ClONO_2$ in cold, wet air parcels under elevated SAD conditions could enable chlorine activation to occur even for initial [$ClONO_2$]/[Cl_y] levels that are close to 0 (Figures 2.7n and 2.7o). The considerable reduction in time required to lower [NO_x] and elevate [ClO] under elevated aerosol SAD would increase the likelihood of chlorine activation in the midlatitude LS, as processes such as dissipation of water vapor would play a much smaller role in limiting the potential for chlorine activation. This model simulation suggests that substantial enhancement of [ClO] would be observed within 60–120 hr for one of the high [Cl_y] air parcels sampled during DCOTSS if SAD was increased to a level projected under future sulfate geoengineering scenarios.

Figure 2.12 is designed to evaluate the potential for chlorine activation under enhanced aerosol SAD for conditions more commonly observed during DCOTSS 2022, with low [Cl_y] abundances (in contrast to the special high-[Cl_y] case presented in Figures 2.7m–2.7o). The figure shows [ClO] computed at the end of a 5-day forward trajectory simulation as a function of aerosol SAD (abscissa) and [H_2O] (lines). All simulations are initialized with the median values of [Cl_y] (132 pptv), [$ClONO_2$]/[Cl_y] (0.028), [O_3] (260.4 ppbv), [NO_x] (938 pptv), and [ClO] (0.7 pptv) observed within air masses for which $\tau_{HET} \leq 120$ hr. These model runs are conducted for three stratospheric values of [H_2O]: the background value of 4.63 ppmv, the median value of 13.71 ppmv found within the $\tau_{HET} \leq 120$-hr air masses, and the 95th percentile value of 17.38 ppmv for these same air masses. The solid and dashed green arrows indicate the ranges of SAD that could result from SAI over the first two decades of implementation and by the end of the century (Tilmes et al., 2022). We keep [O_3] constant for the simulations shown in Figure 2.12, even though the high values of [ClO] (approaching 100 ppt) at the end of some of the simulations would result in a modest (i.e., 5%) reduction of [O_3] at the end of the 5-day simulation as shown by Figure 2 of Robrecht et al. (2019), because our paper is focused on chlorine activation rather than ozone loss.

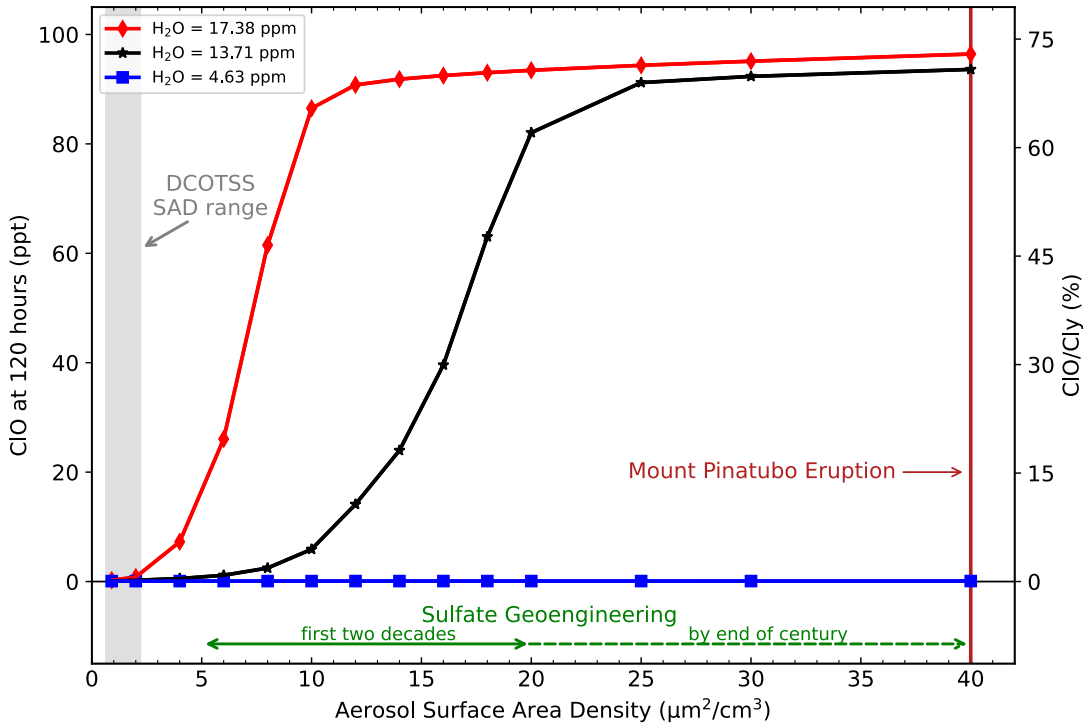


Figure 2.12. ClO mixing ratio at the end of 5-day model simulations as a function of aerosol surface area density, initialized with the median values of air masses with τ_{HET} < 120 hr during DCOTSS 2022, with varying water vapor mixing ratios. All model runs are initialized with the daytime [NO]/[NO_2] ratio of 5.6, appropriate for steady state conditions at the start of the trajectory. The blue line shows results initialized with background stratospheric [H_2O] at 4.63 ppmv. Results initialized with the median (13.71 ppmv) and 95th percentile of water vapor (17.38 ppmv) within the $\tau_{HET} \leq 120$ hr air masses are shown in the black and red lines, respectively. Values of [CO], [CH_4], [O_3], [H_2O], and T are kept constant with time in each model run. The shaded region indicates the range of aerosol surface area densities encountered within τ_{HET} < 120 hr air masses. Peak aerosol surface area density enhancement following the Mount Pinatubo eruption (Thomason et al., 1997) is represented by the dark red vertical line. The range of aerosol SAD simulated to occur with sulfate geoengineering within the first two decades of implementation and the possible range over the next century (Tilmes et al., 2022) are represented by the solid and dashed green arrows, respectively.

When initializing with the background [H_2O] of 4.63 ppmv, there is no simulated increase in chlorine activation with increasing SAD (Figure 2.12, blue line). However, as reported by Thornton et al. (2007), elevated [H_2O] in conjunction with high aerosol SAD may be necessary for activation rates to compete with deactivation. Upon initializing with [H_2O] = 13.7 ppmv, the model shows a much larger increase in [ClO] with aerosol SAD. Here, the largest enhancements of [ClO] are simulated at aerosol surface area densities of 25 $\mu m^2/cm^3$, which are often associated with major volcanic eruptions but also fall within the range of SAD that could result from sulfate geoengineering within the next century (Tilmes et al., 2022). When

initializing the model with [H_2O] = 17.4 ppmv, values of [ClO] are significantly elevated, approaching ~100 pptv within the range of aerosol SAD that could occur during the first two decades of SAI implementation (Tilmes et al., 2022). Although these simulations are run under the median conditions, significantly higher [ClO] could be observed with a higher starting [Cl_y] (>300 pptv), as illustrated in Figures 2.7m–2.7o. Enhancements of [ClO] are minimal for all three simulations whenever aerosol SAD is below ≲3 $\mu m^2/cm^3$, which is above the typical range of 0.65–2.2 $\mu m^2/cm^3$ observed for heterogeneously suitable air parcels observed during DCOTSS 2022 (gray shaded region, Figure 2.12). The risk of chlorine activation grows substantially for convectively influenced air masses under the higher values of SAD that could occur upon future climate mitigation efforts that utilize stratospheric sulfate aerosol injection.

Aerosol SAD was approximately 2–4 times higher in 2021 than in 2022 (Figure 2A.17 in Appendix A) due to the influence of the La Soufrière eruption (Li et al., 2023). This enhancement of aerosol SAD was associated with a decline in TCO at high latitudes of both hemispheres; however, these reductions were small and fall within range of the natural variability of TCO (Li et al., 2023). During DCOTSS 2021, aerosol SAD was occasionally observed at magnitudes (≳3 $\mu m^2/cm^3$) in which chlorine activation could occur if accompanied by the low temperature and elevated water vapor observed in 2022 (Figure 2.12). However, in 2021, these SAD enhancements were rarely observed alongside conditions favorable for heterogeneous chemistry. Aerosol surface area density is included in our calculation of heterogeneous time constants, and as shown in Figures 2A.13d–f in Appendix A, very few 2021 observations satisfy the combined criteria of low temperature, elevated water vapor, and high aerosol SAD. The lack of chlorine activation in these cases can be attributed to insufficient [Cl_y], which averaged 49.8 ± 37.5 pptv for the air parcels with heterogeneous time constants below

120 hr. Furthermore, our analysis of the [O_3] versus [N_2O] relation during both summer DCOTSS deployments shows no evidence for aerosol mediated loss of ozone due to the La Soufrière eruption (Figure 2A.18 in Appendix A).

Pyro-cumulonimbus clouds (pyroCb) produced by severe wildfires can inject fire material and aerosol particles into the lower stratosphere (Fromm et al., 2000, 2022). The stratospheric aerosols associated with pyroCb injection following the Australian wildfires of late 2019 and early 2020 consisted of organic material (Bernath et al., 2022). Large enhancements of [ClO] and [$ClONO_2$], together with a considerable suppression of [HCl], were observed over broad regions of the Southern Hemisphere midlatitude stratosphere following this aerosol enhancement (Santee et al., 2022; Strahan et al., 2022). These changes in the partitioning of stratospheric, inorganic chlorine have been attributed to the dissolution of HCl within the organic, pyroCb aerosols and subsequent heterogeneous reactions (Salawitch & McBride, 2022; Solomon et al., 2022). The impact on [ClO] of a large pyroCb event under the cold, wet conditions observed during DCOTSS is the subject of active investigation.

2.4 Conclusions

Our study shows that significant enhancements of stratospheric ClO within the convective outflow of the North American Monsoon Anticyclone (NAMA) at levels sufficient to rapidly deplete ozone were not observed during DCOTSS for either summer 2021 or 2022. This enhancement of ClO was absent within air masses exhibiting the temperatures and water vapor conditions previously deemed conducive to chlorine activation within the midlatitude, lowermost stratosphere (Anderson & Clapp, 2018; Anderson et al., 2012, 2017; Robrecht et al., 2019), although the altitudes of these observations are lower than considered in previous studies. During DCOTSS, ~71% of air parcels with temperature and humidity conditions suitable for chlorine

activation resided near the tropopause, where inorganic chlorine (Cl_y) and ozone mixing ratios are usually too low to facilitate an enhancement of ClO capable of causing significant ozone depletion.

For significant levels of Cl_y to be present within these lower stratospheric convectively influenced air masses, one of two conditions must occur. Either mixing with chemically aged air parcels would need to take place, or the direct injection of inorganic chlorine from the decomposition of VSL organic chlorine species must occur. Most (78%) of the well-mixed air masses that contained both elevated levels of Cl_y and H_2O sampled during DCOTSS exhibited temperatures too high ($T - T_{ICE} > 5$, $T \gtrsim 205$ K) for chlorine activation to occur rapidly. Nonetheless, there were a few exceptions during DCOTSS 2022. On occasion, we observed Cl_y-rich air parcels ($Cl_y > 300$ pptv) alongside elevated H_2O mixing ratios (>11 ppmv) and temperatures low enough for chlorine activation, as determined by our heterogeneous time constant constraint ($\tau_{HET} < 120$ hr). Chemical back-trajectory model simulations show these Cl_y-rich air parcels had insufficient exposure time to meteorological and humidity conditions conducive to chlorine activation before the time of ER-2 intercept.

Our forward model simulations show that if these Cl_y-rich air parcels had been exposed to conditions conducive to chlorine activation for another 5 days, the lack of a sufficient reaction partner for HCl (i.e., low $ClONO_2/Cl_y$) and secondarily, the high mixing ratios of NO_x, would have resulted in values of ClO much lower than those associated with modeled projections of significant ozone loss in the midlatitude, lowermost stratosphere ($ClO \geq 100$ pptv) (Anderson et al., 2012; Robrecht et al., 2019). The model simulations of Anderson et al. (2012) and Robrecht et al. (2019) were conducted for higher altitudes (lower pressures) than the present analyses, which are specifically guided by conditions observed during DCOTSS. During these

summers, the air parcels that exhibited meteorological conditions suitable for rapid heterogeneous chemistry as well as high [Cl_y] tended to have nearly all the inorganic chlorine present in the form of HCl. The absence of chlorine nitrate and the presence of elevated NO_x for these air masses was a limiting factor for chlorine activation. Our model simulations show that for ClO to become elevated, NO_x must first be sequestered into the reservoir HNO_3 (via heterogeneous $ClONO_2$ reactions and N_2O_5 hydrolysis). During DCOTSS, [NO_x] was too high to allow large enhancements of [ClO] to occur within the average time frame that convectively injected air parcels remain intact within the NAMA (~5 days) (Chang et al., 2023). The elevated levels of NO_x within these freshly injected air parcels were likely due to the influences of tropospheric pollution and perhaps the formation of NO_x by lightning (e.g., Fischer et al., 2000; Pérez-Invernón et al., 2023; Pickering et al., 2024).

We also show, based on forward chemical trajectory modeling of the DCOTSS data, that elevated aerosol surface area densities (SAD) will reduce the time required for chlorine activation by accelerating heterogeneous chemistry. For levels of sulfate aerosol SAD observed during prior major volcanic eruptions and considered as "possible" for climate mitigation via stratospheric sulfate injection, we show that enhancements of ClO to mixing ratios large enough to cause significant ozone depletion could occur for the meteorological and chemical conditions observed during DCOTSS. Full evaluation of the impact of enhanced SAD on the abundance of TCO is needed, using three-dimensional model simulations of the midlatitude lower stratosphere that have been critically evaluated using the comprehensive DCOTSS measurements of temperature, pressure, [ClO], [$ClONO_2$], [H_2O], [NO_2], [O_3], and tracers used to infer [Cl_y] collected during the summers of 2021 and 2022.

Finally, we note that this study is only for summers 2021 and 2022, and the absence of chlorine activation may not extend to other years. The significant differences in temperature and aerosol SAD observed between 2021 and 2022 highlight the interannual variability that is possible. Temperature in the LS during summer 2022, the focus of this study, was ~2 K lower in the potential chlorine activation regions than observed during 2021. Part of the colder conditions during 2022 could be due to sampling earlier in summer, compared to 2021. In the future, the stratosphere is expected to cool due to increasing concentrations of CO_2, CH_4, and H_2O (Garny et al., 2022; Steiner et al., 2020), making it more likely that the necessary threshold conditions for chlorine activation could be met. Stratospheric inorganic chlorine is expected to continue to slowly decline due to the effectiveness of the Montreal Protocol (Daniel et al., 2022); however, this decline will occur against a backdrop of rising chlorine due to anthropogenic VSL chlorine species that are not yet regulated (Chipperfield et al., 2020; Hossaini et al., 2015, 2017, 2019). As such, continued monitoring of chlorine and water vapor in the lower stratosphere over populated midlatitude regions is necessary (Salawitch et al., 2025).

Appendix A

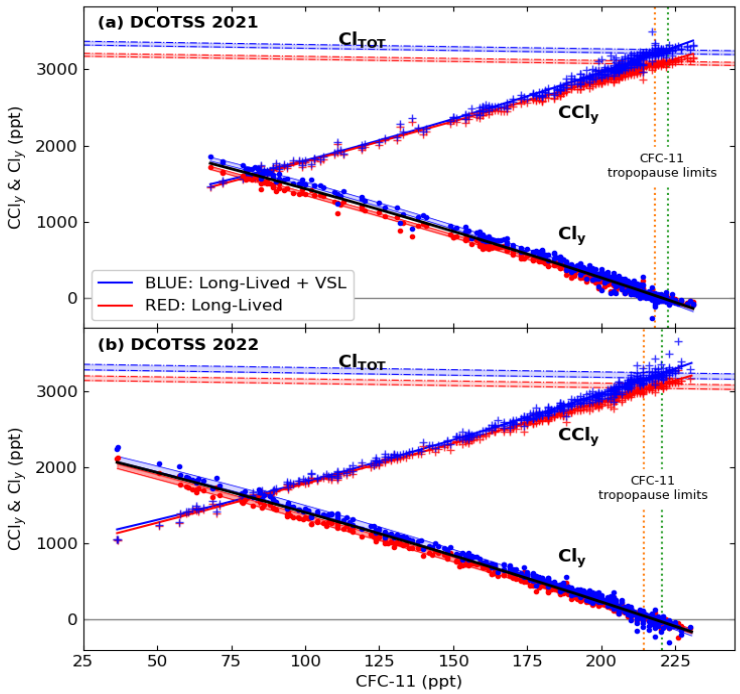


Figure 2A.1. AWAS CFC-11 versus [CCl_y] (red & blue plus signs) and [Cl_y] (red & blue circles) for DCOTSS 2021 (a) and DCOTSS 2022 (b). All quantities associated with only long-lived organic Cl species are shown in red, and quantities associated with both long-lived + very short-lived (VLS) species are shown in blue. The quadratic relations between [CCl_y] and [Cl_y] with CFC-11 are indicated by solid red and blue lines. Where the shading between the two [Cly] quadratic fits represents the range between the upper and lower limit formulations. Lower and upper tropopause limits of [CFC-11], ($CFC\text{-}11_{TROP}$) are represented in the vertical orange and green dotted lines, respectively. The lower and upper limits of [$Cl_{TOT\text{-}TROP}$] are depicted in the red and blue dash-dotted lines. The lower and upper limits of $[Cl_{TOT\text{-}TROP}]^{LL}$ (red dash-dotted lines) are 3067 ppt and 3105 ppt for 2021, and 3042 ppt and 3099 ppt for 2022, respectively. The lower and upper limits of $[Cl_{TOT\text{-}TROP}]^{LL+VSL}$ (blue dash-dotted lines) are 3210 ppt and 3258 ppt for 2021, and 3177 ppt and 3244 ppt for 2022, respectively. The two quadratic relations between [CFC-11] and [CCl_y] are described by the following equations: $CCl_y^{LL}(CFC\text{-}11) = 0.003401\times[CFC\text{-}11]^2 + 9.758\times[CFC\text{-}11] + 776.9$, $CCl_y^{LL+VSL}[CFC\text{-}11] = 0.01123\times[CFC\text{-}11]^2 + 8.269\times[CFC\text{-}11] + 870.2$. The quadratic relations between [CFC-11] and our four formulations for [Cl_y] are described by the equations: $Cl_y^{LL}{}_{Lower\text{-}Limit}(CFC\text{-}11) = -0.004148\times[CFC\text{-}11]^2 - 10.08\times[CFC\text{-}11] + 2366$, $Cl_y^{LL}{}_{Upper\text{-}Limit}(CFC\text{-}11) = -0.004171\times[CFC\text{-}11]^2 - 10.08\times[CFC\text{-}11] + 2427$, $Cl_y^{LL+VSL}{}_{Lower\text{-}Limit}(CFC\text{-}11) = -0.01201\times[CFC\text{-}11]^2 - 8.602\times[CFC\text{-}11] + 2413$, $Cl_y^{LL+VSL}{}_{Upper\text{-}Limit}(CFC\text{-}11) = -0.01204\times[CFC\text{-}11]^2 - 8.603\times[CFC\text{-}11] + 2485$. Here [CFC-11] values should all be dry air mole fractions in ppt.

Text 2A.1. Cl_y Estimation

The components involved in our estimate of inorganic chlorine, [Cl_y] (section 2.2.2) are depicted in Figure 2A.1 for DCOTSS 2021 and 2022. Our calculation of organic chlorine ([CCl_y]) includes the 12 organic chlorine species: CFC-11, CFC-12, CFC-113, CFC-114, CFC-115, CCl_4, HCFC-22, HCFC-141b, HCFC-142b, Halon-1211, CH_3Cl, & CH_3CCl_3 and the 6 very short-

lived (VSL) organic chlorine species: CH_2Cl_2, $CHCl_3$, Cl_2Cl_4, CH_2ClCH_2Cl, $CHBrCl_2$, & CH_2BrCl, all measured by the AWAS instrument on board the NASA ER-2 during DCOTSS. The quadratic relation between AWAS [CFC-11] and [CCl_y] depicted in Figure 2A.1 is used to determine the value of total organic chlorine at stratospheric entry, [$Cl_{TOT\text{-}TROP}$] as a function of [CFC-11_{TROP}]. The upper and lower limits for both our long-lived and long-lived + VSL formulations of [$Cl_{TOT\text{-}TROP}$], discussed in the section 2.2.2, are distinguished by what value of [CFC-11] is specified at the tropopause (dotted vertical lines in Figure 2A.1) and what scale of NOAA GML SF_6 measurements are used to determine age of air.

The lower limit is defined by the average value of [CFC-11] at the dynamic tropopause, which is 218 ppt for DCOTSS 2021 and 214.5 pptv for DCOTSS 2022. Here we use the dynamic tropopause (potential vorticity = 2×10^{-6} m^2 s^{-1} K kg^{-1}) rather than the WMO lapse rate tropopause, because the vertical gradient of CFC-11 measured during DCOTSS is observed to be nearly constant below the dynamic tropopause, whereas the vertical gradient of CFC-11 exhibits a decline across the lapse rate tropopause. The upper limits, found in Table 7A-1 of the 2022 WMO Ozone Assessment Report (Daniels et al., 2022), are 222.45 pptv for 2021 and 220.6 pptv for 2022. As described in the section 2.2.2, we use NOAA GML SF_6 measurements to estimate mean stratospheric age of air. Northern hemisphere averaged SF_6 measurements are used for the lower limit formulation, and for the upper limit we use globally averaged SF_6 measurements. The quadratic relations between AWAS [CFC-11] and [Cl_y] seen in Figure 2A.1 are utilized to estimate [Cl_y] along the flight track at a higher time resolution, with [CFC-11] measured by the UCATS instrument (see Figure 2A.2).

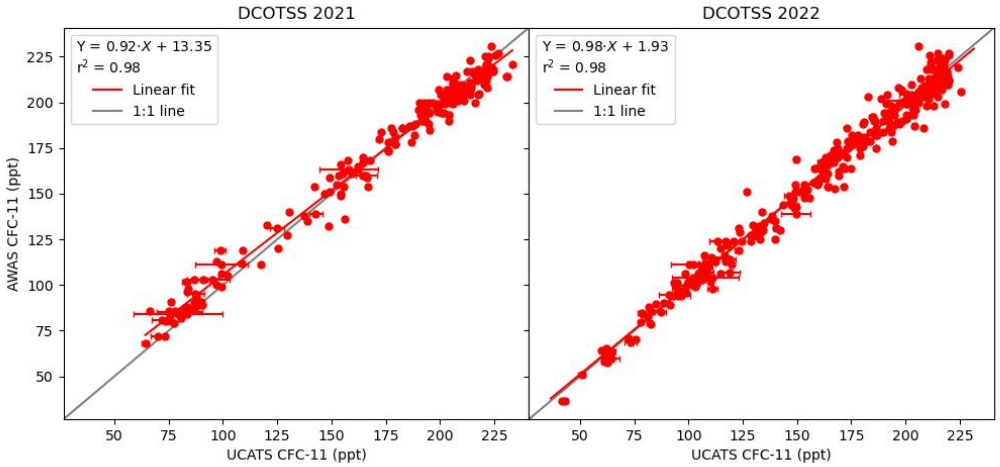


Figure 2A.2. CFC-11 measured by the Advanced Whole Air Sampler (AWAS) instrument versus CFC-11 measured by the UAS Chromatograph for Atmospheric Trace Species (UCATS) instrument for DCOTSS 2021 (left panel) and DCOTSS 2022 (right panel). UCATS data are averages within AWAS sampling intervals, where error bars indicate the standard deviation of UCATS CFC-11 within each AWAS sampling interval. Red solid lines indicate linear fits to the data; grey lines indicate one to one line.

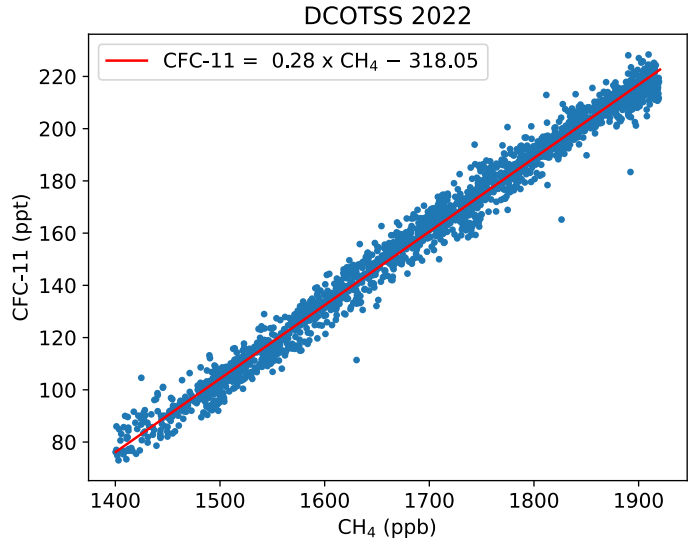


Figure 2A.3. UCATS [CFC-11] versus HUPCRS [CH_4] for DCOTSS 2022. The red line indicates the linear fit used to estimate [CFC-11] along the flight track, for times when [CFC-11] was not reported. The linear fit is only applied for CH_4 mixing ratios between 1400 to 1900 ppb.

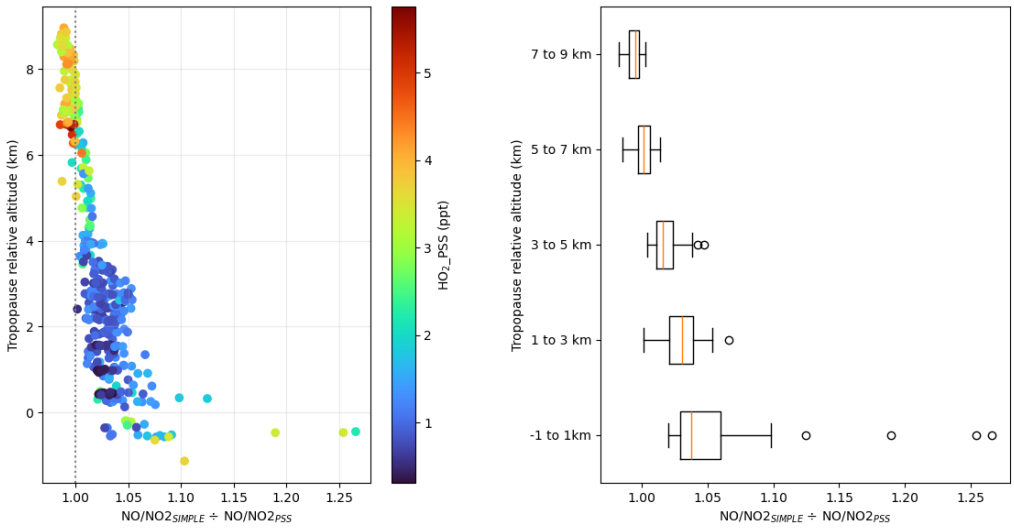


Figure 2A.4. Ratio of [NO]/[NO_2] calculated using the simplified expression ($NO/NO2_{SIMPLE}$; Eq. 2.1) to that derived from the full photochemical steady state simulation ($NO/NO2_{PSS}$). In the left panel this ratio is plotted against altitude relative to the ERA5 lapse-rate tropopause, colored by HO_2 mixing ratio derived from the PSS model, for the five flights that have been simulated using the steady state model (section 2.2.6). The right panel shows a box-and-whisker plot of the $NO/NO2_{SIMPLE}$ to $NO/NO2_{PSS}$ ratio, binned in 2-km intervals relative to the tropopause. Boxes show the interquartile range, the orange line denotes the median, and whiskers represent the 5th and 95th percentiles. In the manuscript, we report the 95th percentile deviation, calculated within ±1 km of the tropopause, as the basis for our approximately 10% bias in [NO]/[NO_2] due to the exclusion of RO_2 species in the chemical mechanism (Table 2A.1) of the trajectory model.

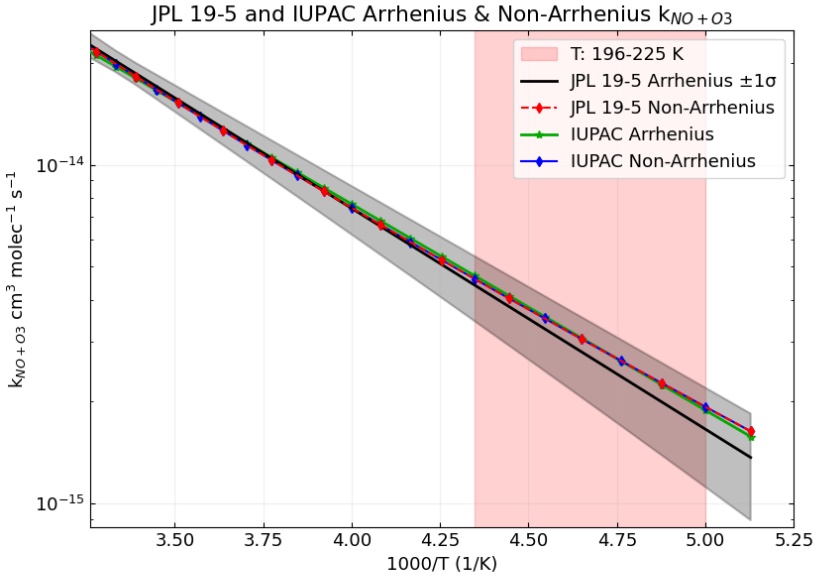
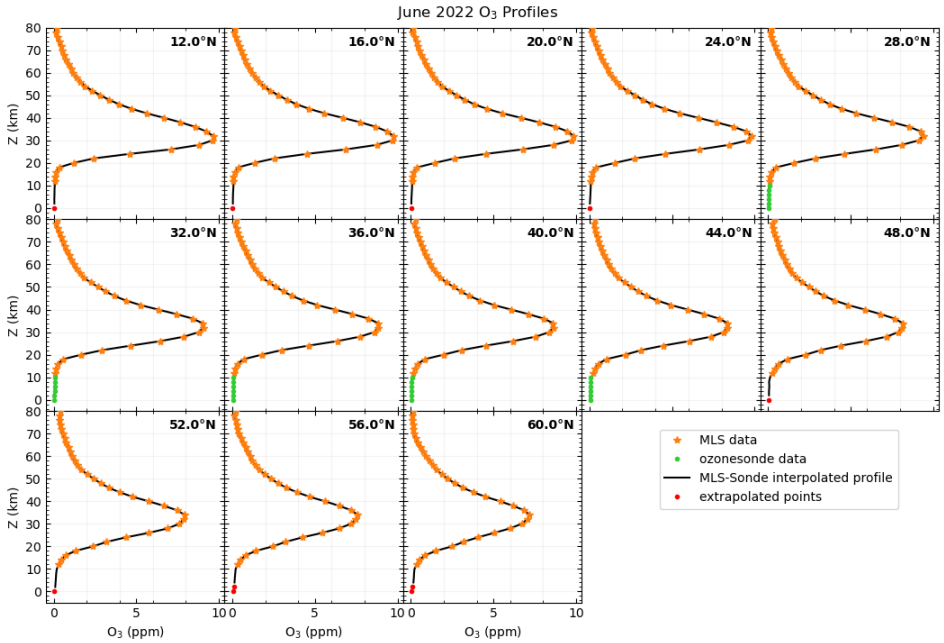


Figure 2A.5. Temperature dependence of the NO+O_3 reaction rate constant. The y-axis is a log scale, and the x-axis is the inverse of temperature (1000/T). The black solid line shows the JPL 19-5 Arrhenius expression with its associated ± 1 sigma uncertainties in the grey-shaded region. The JPL 19-5 non-Arrhenius expression is shown in the dashed red line with diamond markers. The IUPAC Arrhenius expression is shown in the solid green line with star markers. The IUPAC non-Arrhenius expression is shown in the solid blue line with diamond markers. The shaded red region indicated the temperature range of focus in our study ~196-225 K.

<u>Text 2A.2.</u> Ozone profiles used to constrain radiative transfer model.

Profiles of [O_3] needed for the computation of J-values described in section 2.2.4 are formulated as illustrated in Figure 2A.6. We combine MLS data from ~10-100km with DCOTSS ozonesonde data (0-10km) and linearly interpolate onto a 12-60°N latitude and 0-80 km grid. This grid has a 4° latitude spacing and 2 km altitude spacing. Values outside the convex hull of the interpolation scheme are manually interpolated as a function of latitude at each altitude (red markers in Figure 2A.3). These profiles are scaled by a multiplicative factor to match total column ozone retrieved by the TROPOMI instrument (Figure 2A.7).



<u>Figure 2A.6.</u> Vertical profiles of [O_3] from 0 to 80 km every 4° latitude. MLS data in the orange markers, interpolated DCOTSS ozonesonde data shown in the green markers, and the interpolated profile of combined sonde-MLS data is shown in black. Extrapolated data are shown in the red markers.

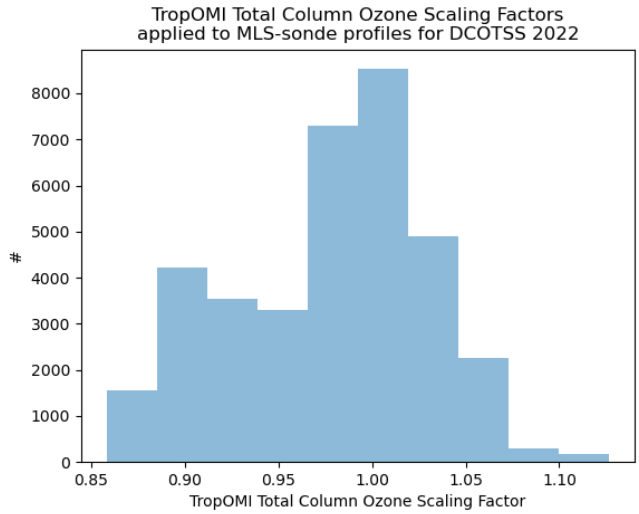


Figure 2A.7. TropOMI Total Column Ozone multiplicative factors used to scale MLS-sonde profiles for DCOTSS 2022.

Text 2A.3. Heterogeneous Reaction Probabilities

The reaction probabilities (i.e. reaction uptake coefficients, γ) on sulfate water aerosols are calculated using data from the JPL Kinetic Evaluation version 19-5 (Burkholder et al., 2019). The calculated reaction probabilities of $ClONO_2$ + HCl, $ClONO_2$ + H_2O, HOCl + HCl, and N_2O_5 + H_2O compare extremely well with Figure 5-1 of Burkholder et al. (2019). In Section 2.3., we frequently use the departure of temperature from the frost point ($T-T_{ICE}$) to reference air masses with conditions suitable for heterogeneous chlorine chemistry. In Figure 2A.8 we show that heterogeneous reaction probabilities align well with the frost point temperature departure. We use these reaction probabilities to calculate the time constants of these reactions. These time constants depend on reaction probability (γ), aerosol surface area density (SAD), and the mean molecular velocity of the gas phase reactant (v) for each reaction, calculated as:

$$\tau = \frac{1}{0.25 \times \gamma \times SAD \times v}$$

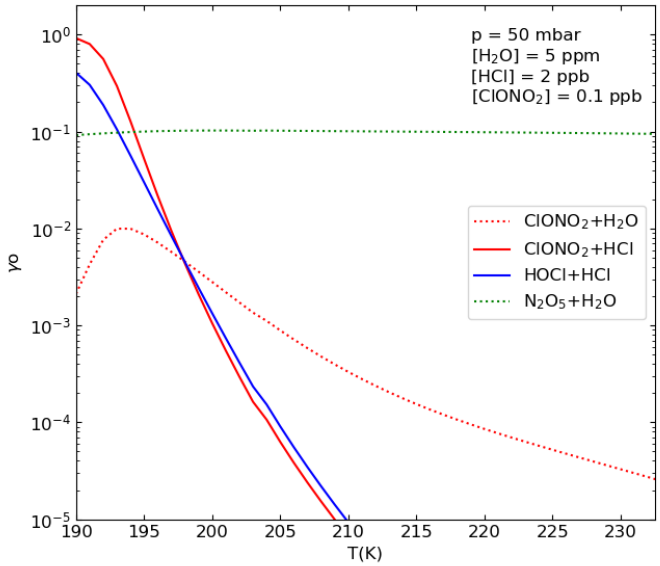


Figure 2A.8. Reaction probabilities (reactive uptake coefficients) of $ClONO_2$ + H_2O (red dotted), $ClONO_2$ + HCl (solid red), HOCl + HCl (solid blue), and N_2O_5 + H_2O (dotted green) on sulfate aerosols calculated based on the recommendations of the JPL 19-5 kinetic evaluation. Probabilities are calculated as a function of temperature at 50 mb pressure, 5 ppm of [H_2O], 2 ppb of [HCl], and 0.1 ppb of [$ClONO_2$].

Text 2A.4. Trajectory Model Assumptions

Figure 2A.9c and 2A.9d show that the long photochemical lifetime of O_3 (with respect to chemical loss) for the calculated, steady state abundance of radicals is between two and 10 months for the conditions encountered during the 10 June 2022 research flight, supporting our use of constant values for [O_3] within the trajectory model.

We have chosen not to include bromine reactions in our trajectory model because the air masses investigated in this study are characterized by very low [ClO] and [BrO] (Figure 2A.9b, 2A.9f), making ozone loss via ClO + BrO negligible under these conditions. As illustrated in Figure 2A.9c, the lifetime of ozone with respect to loss from the ClO + BrO reaction exceeds 100 years under these conditions, indicating that this catalytic cycle contributes negligibly to ozone loss in the midlatitude lower stratosphere air masses sampled during DCOTSS. Furthermore, Figure 2A.9h shows that the inclusion of HOBr + HCl heterogeneous reaction would have a minimal

impact on chlorine activation compared to the $ClONO_2$ + HCl reaction, for conditions sampled during DCOTSS.

We do not represent RO_2 radicals in the chemical scheme of our trajectory model. Figure 2A.9l compares PSS model output (which includes CH_3OO and its relevant reactions with NO and ClO) to our simplified expression for NO/NO_2 that omits RO_2. The excellent agreement between both estimates of NO/NO_2 demonstrates that the inclusion of RO_2 radicals would have a very small influence on [NO_x] for the conditions of focus in this study. Furthermore, RO_2 + NO and RO_2 + ClO reactions contribute negligibly to the partitioning of NO_x and ClO in our modeled environment, compared to the major reactions NO + O_3, ClO + NO_2, and ClO + NO that are included in the trajectory model (Figures 2A.9j and 2A.9k).

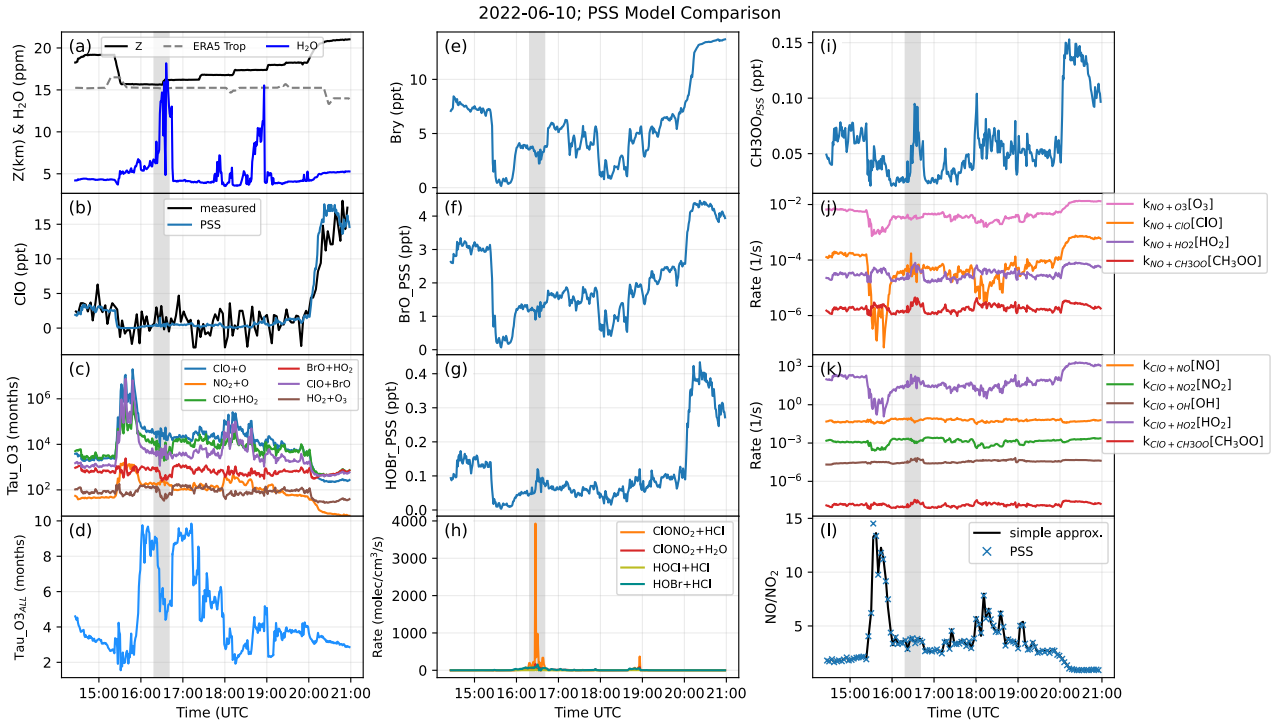


Figure 2A.9. Time series for the 10 June 2022 research flight showing in situ measurements and photochemical steady state (PSS) model output. Panel (a) shows ER-2 altitude (black), ERA5 tropopause (dashed grey), and measured [H_2O] (blue). Panel (b) shows measured [ClO] (black) and [ClO] simulated by the PSS model (blue). Panel (c) shows the lifetime of ozone (in months) with respect to loss from ClO+O (blue), NO_2+O (orange), ClO+HO_2 (green), BrO+HO_2 (red), ClO+BrO (purple), and HO_2+O_3 (brown). Panel (d) shows the lifetime of ozone (in months) for all processes included in the photochemical steady-state model. Panel (e) shows [Br_y] estimated along the ER-2 flight track. Panel (f) shows PSS model output for [BrO]. Panel (g) shows PSS model output for

[HOBr]. Panel (h) shows heterogeneous reaction rates for $ClONO_2$+HCl (orange), $ClONO_2$+H_2O (red), HOCl+HCl (gold), and HOBr+HCl (dark turquoise). Panel (i) shows PSS model output for [CH_3OO]. Panel (j) shows instantaneous reaction rates along the flight track for NO+O_3 (pink), NO+ClO (orange), NO+HO_2 (purple), and NO+CH_3OO (red). Panel (k) shows instantaneous reaction rates for ClO+NO (orange), ClO+NO_2 (green), ClO + OH (brown), ClO + HO_2 (purple), and ClO+CH_3OO (red). Panel (l) shows NO/NO_2 from our simple expression (equation 2.1) in black, and NO/NO_2 from the PSS model in blue. Shaded regions in all panels highlight periods where heterogeneous time constants for chlorine activation (τ_{HET}) fall below 120 hours, as shown in Figure 2.3.

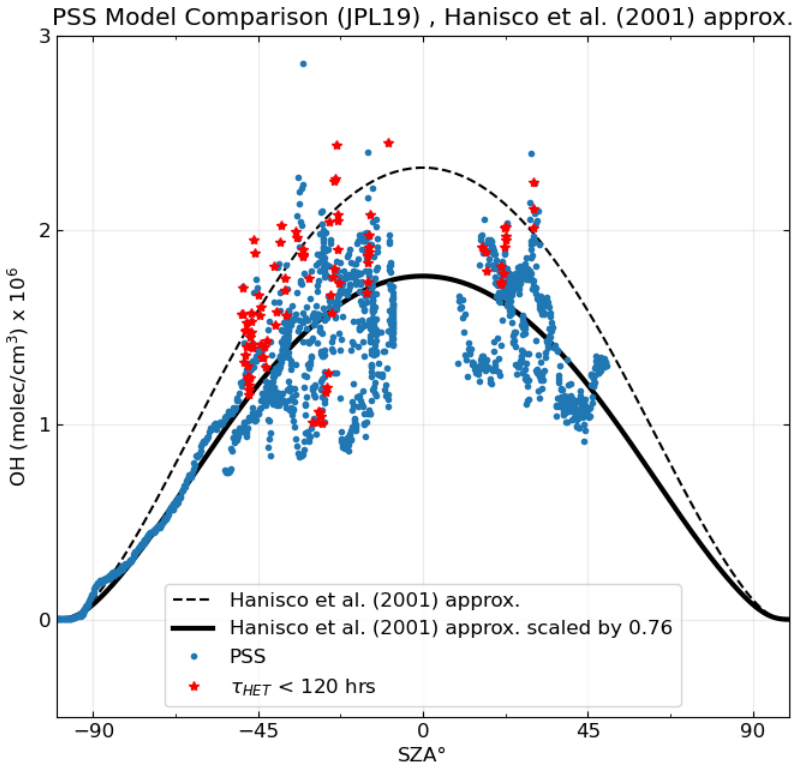


Figure 2A.10. Estimated concentrations of OH as a function of solar zenith angle (SZA). Blue circles show output from the photochemical steady-state (PSS) model for five DCOTSS 2022 flights. Negative values of SZA are for times prior to local, solar noon. Red stars indicate air parcels with conditions favorable for heterogeneous chemistry ($\tau_{HET} \leq 120$ hours). Higher concentrations of OH simulated by the PSS for the heterogeneously suitable air parcels demonstrate that the variability in OH is primarily driven by H_2O. The dashed black line shows the SZA-based OH approximation from Hanisco et al. (2001), while the solid black line shows our modified version of that parameterization, scaled by a factor of 0.76. The Hanisco et al. (2001) parameterization was designed to be used only for air densities less than 2.5×10^{18} molecules/cm^3. We scale the Hanisco et al. (2001) approximation to account for the higher mean air density of the DCOTSS observations, which is $3.0 \pm 1.25 \times 10^{18}$ molecules/cm^3. The scaling factor 0.76 is chosen because it minimizes the difference between the PSS model output and the Hanisco et al. (2001) approximation.

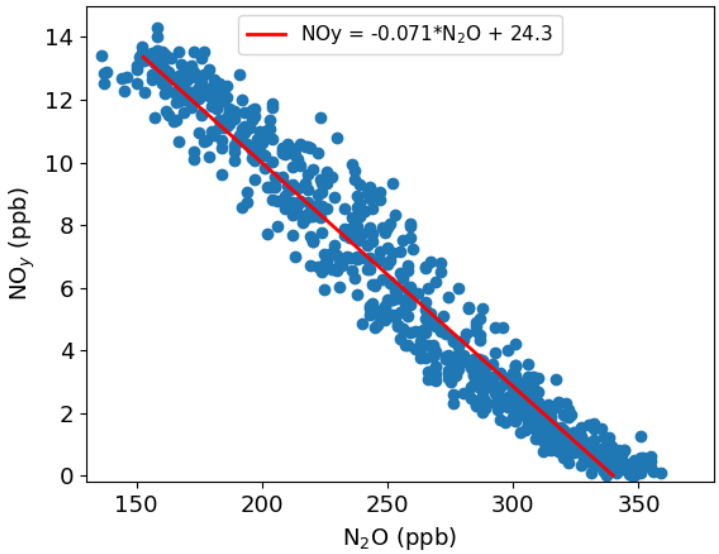


Figure 2A.11. ACE-FTS retrievals of [NO_y] ([NO] + [NO_2] + 2x[N_2O_5] + [HNO_3] + [HO_2NO_2] + [$ClONO_2$]) versus [N_2O] over CONUS during the summer of 2022, over altitudes of 12 to 20 km (Boone et al., 2023). The red line represents the linear fit to the data used to estimate [NO_y] ([NO] + [NO_2] + [NO_3] + 2x[N_2O_5] + [HNO_3] + [HNO_2] + [HO_2NO_2] + [$ClONO_2$] + [$ClNO_2$] + [ClONO] + [HOONO] + [$BrNO_2$] + [$BrNO_3$]) along the DCOTSS flight track as input for our PSS model calculations.

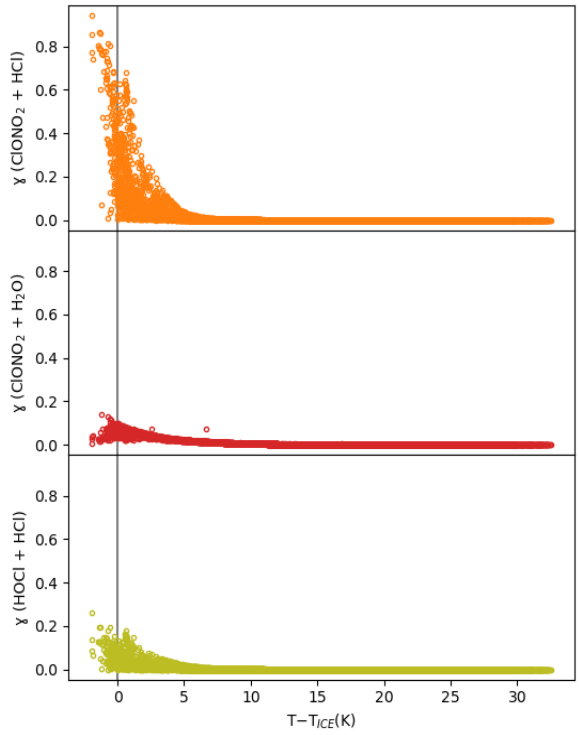


Figure 2A.12. Reaction probabilities of $ClONO_2$ + HCl (top panel), $ClONO_2$ + H_2O (middle panel), and HOCl + HCl (bottom panel) on sulfate aerosols for DCOTSS 2022 versus $T-T_{ICE}$.

Text 2A.5. DCOTSS 2021 H_2O versus O_3

DCOTSS 2022 is the primary focus of this study because of the greater number of instances in which conditions suitable for chlorine activation were sampled within Cl_y-rich air parcels. For completeness, Figure 2A.13 shows the DCOTSS 2021 version of Figure 2.2. The number of observations found within the mixed layer with conditions suitable for chlorine activation and sufficient Cl_y is much lower in summer 2021 compared to summer 2022.

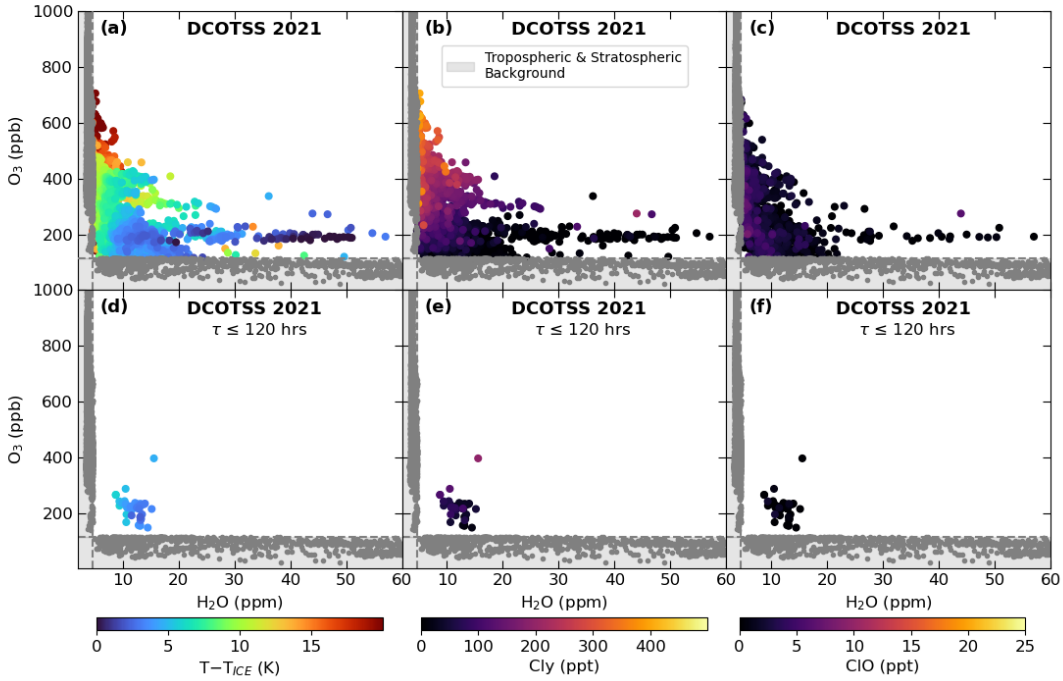


Figure 2A.13. Daytime measurements (SZA < 90°) of O_3 vs. H_2O for DCOTSS 2021 10s measurements. Background stratospheric and tropospheric air parcels from all flights colored in grey, mixed air parcels colored by $T-T_{ICE}$ in panels (a) & (d), estimated Cly in panels (b) & (e), and measured ClO in panels (c) & (f). Data in the left column are layered in descending order, and data in the middle and right columns are layered in ascending order. Panels (d) through (f) only show mixed parcels in which the heterogeneous time constants (τ_{HET}) < 120 hrs.

Text 2A.6.

Figure 2A.14 summarizes aerosol SAD as a function of convective age (Homeyer, 2024) for air parcels sampled within the potential temperature range where heterogeneous suitable air parcels were sampled during DCOTSS 2022 ($\theta = 367 \pm 23.4$ K). This figure illustrates that elevated SAD is observed primarily within active convection (< 6 hours), but declines rapidly thereafter. Median aerosol SAD values for "recent" (6 hours to 1.5 days) and "aged" (1.5 to 5 days)

convection are comparable to background levels, suggesting that aerosol dilution occurs within hours of stratospheric injection. Therefore, while short-lived spikes in aerosol SAD may occur during injection, their short duration likely limits any substantial effect on chlorine activation.

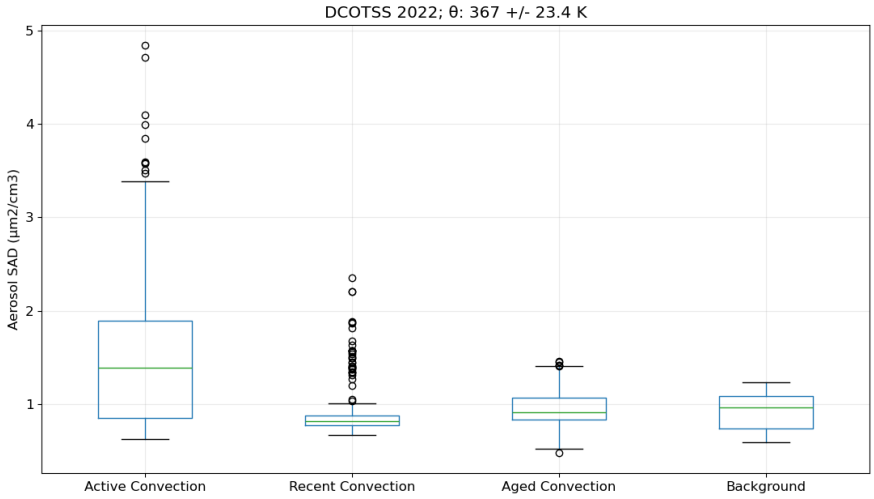


Figure 2A.14. Boxplots of aerosol surface area density (SAD) measured during DCOTSS 2022 within two standard deviations of the median potential temperature at which air parcels suitable for heterogeneous chemistry were observed (θ = 367 ± 23.4 K). Aerosol SAD is grouped by convective age, provided by Homeyer (2024). Active convection is for air parcels < 6 hours old, recent convection is for parcels 6 hours to 1.5 days old, and aged convection is for 1.5 to 5 days old air parcels. "Background" refers to parcels above the ERA5 tropopause, without convective enhancement of water vapor (i.e., $H_2O \leq 4.63$ ppm).

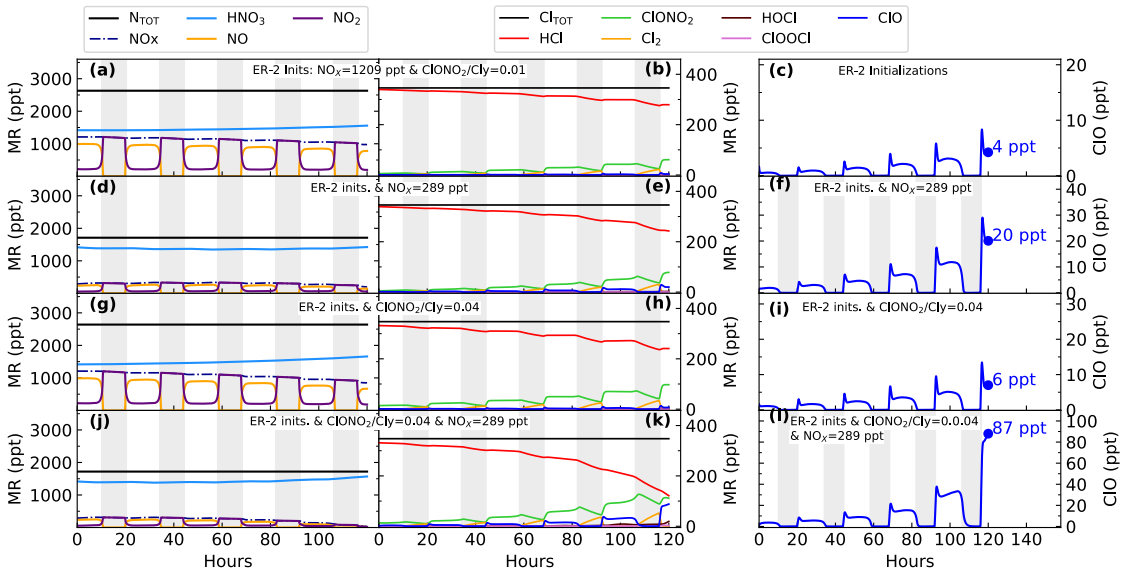


Figure 2A.15. Mixing ratios of chlorine and nitrogen species modeled forward 120 hours from the time of 10 June 2022 ER-2 intercept at 16:36 UTC. The left panel shows the evolution of [NO] (gold), [NO_2] (purple), [NO_x] ([NO] + [NO_2]; navy, dash-dotted line), [HNO_3] (light blue), and [N_{TOT}] (black). The middle column shows the evolution of [HCl] (red), [$ClONO_2$] (lime), [HOCl] (brown), [Cl_2] (gold), [ClOOCl] (pink), and [ClO] (blue). ClO is

highlighted again in the right column, with changing y-axis limits. The various rows represent different pairings of initial conditions. Panels a-c initialized with the values obtained at the 16:36 UTC ER-2 intercept, referred to as the "ER-2 initializations" or "ER-2 inits". Panels d-f are initialized with ER-2 inits and $[NO_x] = 289$ pptv. Panels g-i are initialized with ER-2 inits and $[ClONO_2]/[Cl_y] = 0.04$. Panels j-l are initialized with $[NO_x] = 289$ pptv and $[ClONO_2]/[Cl_y] = 0.04$. The grey shaded regions correspond to time where SZA > 90°. Mixing ratios of CO, CH_4, O_3, H_2O, as well as aerosol SAD and T are kept constant with time at the values observed at the time of ER-2 intercept.

Text 2A.7. ACE-FTS Latitudinal Sampling Distribution.

ACE-FTS data collected over midlatitudes during the summer of 2022 exhibits a sampling bias toward higher latitudes, which should be accounted for when averaging these profiles. Figure 2A.16 shows the latitudinal sampling distribution of the profile averages presented in Figure 2.10. To correct for this high latitude sampling bias, we take the average of 5° latitude binned averages from 30-60°N for the ACE-FTS data shown in Figure 2.10.

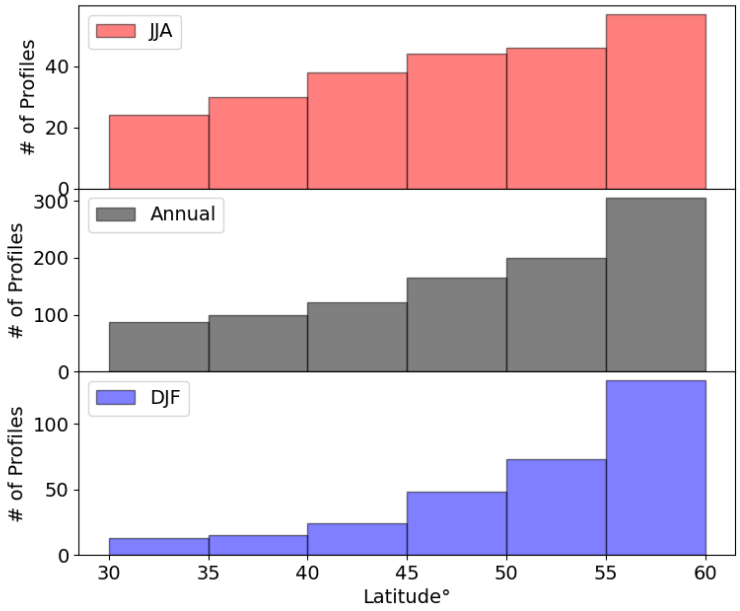


Figure 2A.16. Latitudinal distribution of 2022 ACE-FTS data 30-60°N showing the number of profiles in each 5° latitude bin for the summer (JJA) average (a) annual average (b), and the winter (DJF) average in (c)

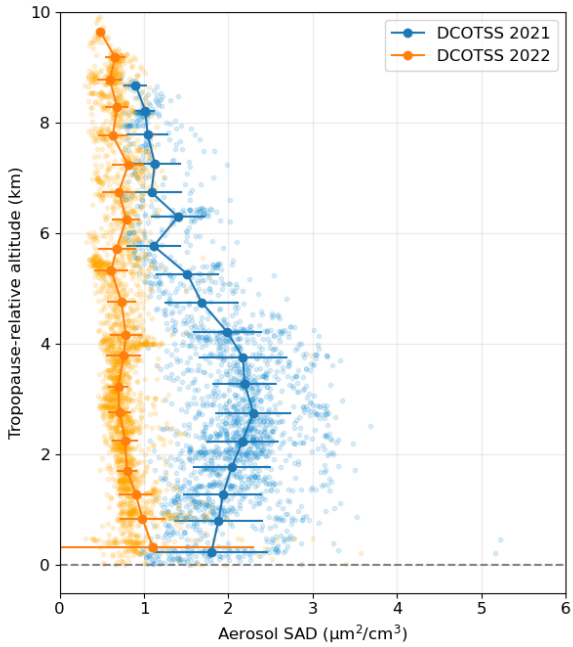


Figure 2A.17. Aerosol surface area density (SAD) as a function of altitude relative to the ERA5 lapse-rate tropopause for DCOTSS 2021 (blue) and DCOTSS 2022 (orange). Translucent markers represent individual measurements above the ERA5 tropopause. Filled markers show mean SAD values in 0.5 km altitude bins, with error bars indicating the standard deviation within each bin.

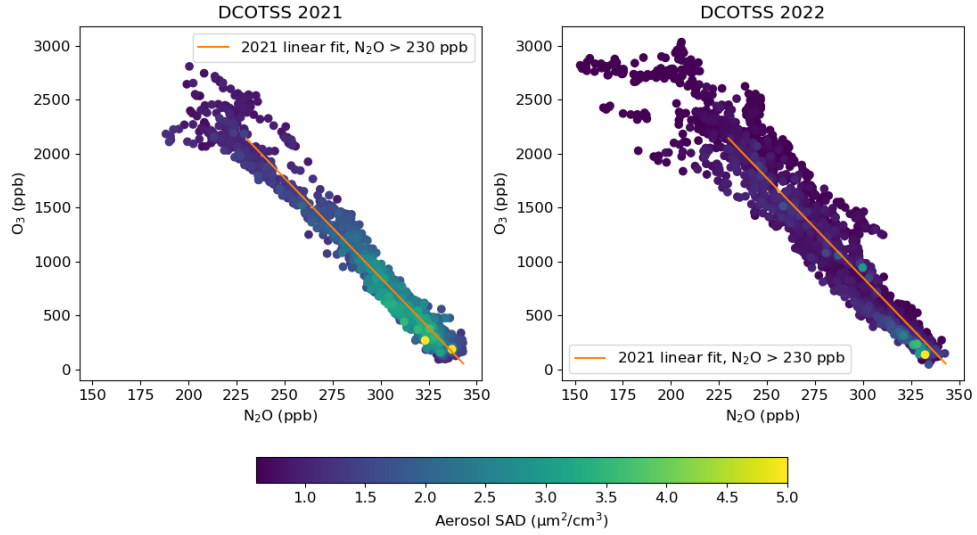


Figure 2A.18. [O_3] versus [N_2O] colored by aerosol SAD for DCOTSS 2021 (left panel) and DCOTSS 2022 (right panel). The orange lines on both panels represent the linear fit to the 2021 data where [N_2O] > 230 ppb.

Table 2A.1. Reactions incorporated in 4th order Runge-Kutta Model

Reaction Type	**Reactions**

Heterogeneous	(1)	$ClONO_2 + HCl$	→	$HNO_3 + Cl_2$
	(2)	$ClONO_2 + H_2O$	→	$HNO_3 + HOCl$
	(3)	$HOCl + HCl$	→	$Cl_2 + H_2O$
	(4)	$N_2O_5 + H_2O$	→	$2\ HNO_3$
Photodissociation	(1)	$O_3 + hv$	→	$O_2 + O$
			→	$O_2 + O(^1D)$
	(2)	$ClONO_2 + h\nu$	→	$Cl + NO_3$
			→	$ClO + NO_2$
	(3)	$Cl_2 + h\nu$	→	$Cl + Cl$
	(4)	$HOCl + h\nu$	→	$OH + Cl$
	(5)	$ClOOCl + h\nu$	→	$ClO + ClO$
	(6)	$HNO_3 + h\nu$	→	$OH + NO_2$
	(7)	$N_2O_5 + hv$	→	$NO_3 + NO_2$
	(8)	$NO_2 + hv$	→	$NO + O$
	(9)	$NO_3 + hv$	→	$NO_2 + O$
			→	$NO + O_2$
Gas phase	(1)	$O + O_2 + M$	→	$O_3 + M$
	(2)	$ClO + NO_2 + M$	→	$ClONO_2 + M$
	(3)	$ClO + NO$	→	$Cl + NO_2$
	(4)	$ClO + ClO + M$	→	$ClOOCl + M$
	(5)	$ClO + ClO$	→	$Cl_2 + O_2$
	(6)	$ClO + ClO$	→	$Cl_2 + O_2$
	(7)	$ClO + OH$	→	$Cl + HO_2$
			→	$HCl + O_2$
	(8)	$ClO + HO_2$	→	$HOCl + O_2$
	(9)	$ClO + O$	→	$Cl + O_2$
	(10)	$HCl + OH$	→	$H_2O + Cl$
	(11)	$HCl + O$	→	$OH + Cl$
	(12)	$ClONO_2 + OH$	→	$HOCl + NO_3$
	(13)	$ClONO_2 + O$	→	$ClO + NO_3$
	(14)	$ClONO_2 + Cl$	→	$Cl_2 + NO_3$
	(15)	$HOCl + OH$	→	$H_2O + ClO$
	(16)	$HOCl + O$	→	$OH + ClO$
	(17)	$Cl + CH_4$	→	$HCl + CH_3$
	(18)	$Cl + O_3$	→	$ClO + O_2$
	(19)	$Cl + NO_3$	→	$ClO + NO_2$
	(20)	$Cl + HO_2$	→	$HCl + O_2$
			→	$ClO + OH$
	(21)	$Cl_2 + OH$	→	$HOCl + Cl$
	(22)	$ClOOCl + OH$	→	$HOCl + ClOO$
	(23)	$ClOOCl + M$	→	$ClO + ClO + M$
	(24)	$NO + O_3$	→	$NO_2 + O_2$
	(25)	$NO + O + M$	→	$NO_2 + M$
	(26)	$NO_2 + O_3$	→	$NO_3 + O_2$

(27)	$NO_2 + O + M$	→	$NO_3 + M$
(28)	$NO_2 + O$	→	$NO + O_2$
(29)	$NO_2 + OH + M$	→	$HNO_3 + M$
(30)	$HO_2 + NO$	→	$NO_2 + OH$
(31)	$HNO_3 + OH$	→	$H_2O + NO_3$
(32)	$HNO_3 + O$	→	$OH + NO_3$
(33)	$NO_3 + NO_3$	→	$2NO_2 + O_2$
(34)	$NO_3 + O$	→	$O_2 + NO_2$
(35)	$NO_3 + NO_2 + M$	→	$N_2O_5 + M$
(36)	$NO_3 + NO$	→	$2NO_2$
(37)	$N_2O_5 + M$	→	$NO_3 + NO_2 + M$
(38)	$OH + O_3$	→	$HO_2 + O_2$
(39)	$OH + CO + M$	→	$HO_2 + CO_2$
		→	$H + CO_2$
(40)	$HO_2 + O_3$	→	$OH + 2O_2$

Note: We assume the first product of reaction 40, HOCO, reacts with O_2 to form HO_2 and CO_2, as described in note K3 of Burkholder et al. (2019).

Chapter 3 : Quantification of the Effect of Kinetic Uncertainties on Photochemical Loss of Ozone in the Midlatitude Stratosphere

3.1 Introduction

Photochemical loss of ozone in the midlatitude stratosphere is controlled by catalytic cycles involving odd-oxygen ($O_x = O + O_3$), nitrogen oxides (NO_x=NO+NO_2), hydrogen oxides (HO_x=OH+HO_2), chlorine radicals (ClO_x=Cl+ClO), and bromine radicals (BrO_x=Br+BrO) (e.g., Bates & Nicolet, 1950; Crutzen, 1970; Molina & Rowland, 1974; Wofsy et al., 1975). The response of stratospheric ozone to natural or anthropogenic perturbations depends on the relative contribution of these catalytic cycles, and the processes that couple odd hydrogen, nitrogen and halogen radical species (Wennberg et al., 1994). Of critical importance, ozone in the Northern Hemisphere (NH) midlatitude lower stratosphere (LS) ($\lesssim$ 21 km) is not recovering as quickly as predicted by current chemistry-climate models (Ball et al., 2018, 2020; Benito-Barca et al., 2025; Dietmüller et al., 2021; WMO, 2022). Our ability to simulate photochemical loss of ozone and recovery relies heavily on laboratory-determined reaction rates and absorption cross-sections provided by compendiums such as the NASA Jet Propulsion Laboratory (JPL) chemical kinetics evaluation (Burkholder et al, 2019) and by the International Union of Pure and Applied Chemistry (IUPAC) evaluated kinetic data for atmospheric chemistry (Atkinson et al., 2004, 2007). Refinements in relevant laboratory determined kinetics along with continued monitoring of stratospheric radical abundances are key for advancing our quantification of the photochemical loss of stratospheric ozone, and informing policy decisions related to ozone depleting substances (ODSs). Comparisons between photochemical calculations and atmospheric

observations can be used to elucidate possible sources of uncertainty and to specify where future laboratory measurements may be needed.

The extent to which anthropogenic perturbations influence photochemical loss of ozone in the midlatitude LS is dependent on the relative contributions of the catalytic cycles involving halogens, NO_x and HO_x radicals to the total ozone loss rate. NO_x radicals not only directly catalyze ozone loss, but also modulate ozone loss by HO_x, ClO_x, and BrO_x radicals (e.g., Wennberg et al., 1994). The influence that nitrogen oxides have on the relative contribution of these catalytic cycles is directly proportional to the partitioning between NO_x and total reactive nitrogen (NO_y) (Gao et al., 1999). Several studies have reported significant discrepancies between modeled and observed NO_x to NO_y ratios, with observed concentrations exceeding modeled values for the middle to high latitude stratosphere for altitudes below ~40 km (Berthet et al., 2006; Gao et al., 1999; Jucks et al., 1999; Osterman et al., 1999; Portmann et al., 1999; Sen et al., 1998). Furthermore, the adjustments to rate coefficients for reactions controlling NO_x to NO_y partitioning, such as $NO_2+OH+M \rightarrow HNO_3+M$ and $HNO_3+OH \rightarrow H_2O+NO_3$, that are needed to resolve these discrepancies, have been found to have a considerable impact on the modeled photochemical ozone loss rate (Dubey et al., 1998; Gao et al., 1999; Portmann et al., 1999).

In addition, several studies have reported model-observation discrepancies in the partitioning of inorganic chlorine (Cl_y) species for the middle to high latitude stratosphere (Bonne et al., 2000; Michelsen et al., 1996; Stimpfle et al., 1999; Voss et al., 2001; Webster et al., 1994). The first simultaneous in-situ observations of ClO, $ClONO_2$, and HCl obtained during Photochemistry of Ozone Loss in the Arctic Region in Summer (POLARIS) campaign during April to September of 1997 reveal that photochemical models, assuming JPL-1997 or JPL-2000

kinetic recommendations, overestimate observed $ClONO_2$/HCl by 55-60% (Voss et al., 2001). Similarly, Michelsen et al. (1996) found that models assuming JPL-1994 kinetics overestimate $ClONO_2$/HCl observed by the shuttle-borne Atmospheric Trace Molecule Spectroscopy (ATMOS) instruments by up to a factor of 3 in the 20 to 50 km altitude range. In contrast, Sen et al. (1999) report balloon-based measurements of HCl and $ClONO_2$ that are relatively consistent with the modeled Cl_y partitioning, with differences less than 10% below 35 km. The source of these model-observation discrepancies had, in part, been prescribed to deficiencies in prior kinetic recommendations for reactions linking ClO and HCl (Dubey et al., 1998; Michelsen et al., 1996), which has since been revised in more recent kinetics recommendations. The model-observation discrepancies involving the partitioning of chlorine and nitrogen species reported here, as well as numerous revisions to kinetic recommendations, have prompted our re-evaluation of catalytic ozone loss pathways in the midlatitude stratosphere.

In situ measurements obtained during the DCOTSS field campaign by instruments on board the NASA ER-2 aircraft (Bowman et al., 2026) provide an opportunity to examine the photochemistry controlling NO_x and ClO_x radicals in the midlatitude NH stratosphere. We compare photochemical steady state box model simulations to observations of NO_2, $ClONO_2$, and ClO obtained during DCOTSS to evaluate how well recommendations from the latest JPL kinetics evaluation (Burkholder et al., 2019; hereafter JPL-2019) simulate fractional loss of odd-oxygen with respect to halogens, NO_x, and HO_x radicals. Following the methods of earlier work (Kawa et al., 2009; Stolarski et al., 1978; Stolarski & Douglass, 1986) we perform a set of Monte Carlo (MC) simulations in which the rate coefficients of 12 key reactions are perturbed within their $\pm 2\sigma$ uncertainty limits and stochastically combined. We use these MC simulations to quantify the set of kinetic perturbations that allow for consistency between measured and

modeled mixing ratios of NO_2, $ClONO_2$, and ClO, and what implications these kinetic adjustments have on catalytic ozone loss pathways. Such comparisons allow us to identify the chemical reactions that contribute the largest potential sources of uncertainty in modeled NO_2, $ClONO_2$, and ClO, which could possibly serve as a guide for future laboratory work.

3.2 Methods

We focus on nine flights conducted during DCOTSS in the summer of 2022 in which daytime (Solar Zenith Angle, SZA < 75°) measurements of [NO_2], [$ClONO_2$], and [ClO] are reported by instruments onboard the NASA ER-2. Here and throughout, square brackets are used to denote the volume mixing ratio (VMR) of measured species. The nine flights cover the latitude range of 29°N to 56°N, and altitudes up to ~ 21 km (Table 3B.1 of Appendix B). Observations obtained during the DCOTSS mission used in this study are outlined in Table 3B.2 of Appendix B (Howar et al., 2025) and briefly described below. The Harvard Halogens instrument (HAL) uses chemical titration-resonance fluorescence to make measurements of ClO and thermal dissociation-chemical titration-resonance fluorescence to obtain measurements of $ClONO_2$ (Wilmouth et al., 2026). Values of [ClO] and [$ClONO_2$] are reported every 35 seconds, with estimated accuracies of 17% and 20% and precisions of 2 ppt and 5 ppt, respectively. The Compact Airborne Nitrogen dioxide Experiment (CANOE) instrument uses non-resonant laser induced fluorescence (LIF) to obtain measurements of [NO_2] (St. Clair et al., 2019), which are reported every one second with an estimated accuracy of 10% and an offset uncertainty of 50 ppt (St. Clair et al., 2019). In addition to [NO_2], [$ClONO_2$], and [ClO], our analysis utilizes observations of [O_3], [CO], [CH_4], [H_2O], [SF_6], [C_2H_6], [N_2O], mixing ratios of organic chlorine species, aerosol surface area density (SAD), temperature, potential temperature, and pressure

obtained during the DCOTSS flights. The accuracy and precision, as well as the instrument used to obtain each measurement, are summarized in Table 3B.2 of Appendix B.

3.2.1 Photochemical Steady-State (PSS) Box Model

Photochemical steady state (PSS) box model (Wales et al., 2018; Salawitch et al., 1994a, 1994b) calculations were performed along the individual flight tracks of the nine DCOTSS 2022 flights at a one-minute time resolution. For the temperature, pressure, and latitude at which each air parcel was sampled, we assume a balance between production and loss for each gas over the 24 hour long diel cycle. Reaction rates and absorption cross sections for the 233 reactions incorporated in our photochemical box-model are adopted from JPL-2019. Photodissociation frequencies (J-values) are calculated using a radiative transfer model (Prather, 1981; Salawitch et al., 1994a) constrained by total column ozone and ultraviolet albedo specified from observations obtained by the TROPOspheric Monitoring Instrument (TROPOMI) onboard the Copernicus Sentinel-5 Precursor (S5P) satellite (Veefkind et al. 2012). Profiles of [O_3], derived from ozonesonde (Hall et al., 2016; Sterling et al., 2018) and MLS observations (Livesey et al., 2022), were scaled to match total column abundances measured by TROPOMI at each point along the flight track. Temperature profiles are specified by observations obtained by the Stratospheric Aerosol and Gas Experiment III onboard the International Space Station (SAGEIII-ISS) (Wang et al., 2020). Photodissociation frequencies and rate constants are calculated at the location of each DCOTSS measurement (for the selected flights) for a full diel cycle (at the latitude and pressure of the observation) in 15-minute intervals. Howar et al. (2025) provides further detailed information regarding the computation of photodissociation frequencies.

A variety of measurements are used as model inputs (that is, constraints) for the PSS simulations. Model inputs consist of measurements of [H_2O], [CH_4], [CO], [C_2H_6], and aerosol

surface area density. Values of [Cl_y] and [Br_y] were inferred from UCATS and AWAS organics (Table 3B.2) and [NO_y] was specified from observations obtained by the Canadian Atmospheric Chemistry Experiment Fourier Transform Spectrometer (ACE-FTS) instrument (Boone et al., 2023). For times when [CO] and [C_2H_6] were not reported, we approximate their respective mixing ratios using various piecewise, linear fits with O_3. We estimate [NO_y] along the ER-2 flight tracks from a linear relationship between [NO_y] ($NO + NO_2 + 2xN_2O_5 + HNO_3 + HNO_4 + ClONO_2$) and [$N_2O$] observed by ACE-FTS over CONUS from 12 to 22 km during the summer of 2022 (Boone et al., 2023) (Figure 3B.1). The 1σ uncertainty in [NO_y] is defined by the 33rd and 67th percentiles (67% confidence limits) of [NO_y] within 10 ppb binned intervals of [N_2O].

Following the work of Woodbridge et al. (1995), [Cl_y] is calculated as the difference between total organic chlorine at the tropopause and organic chlorine measured in the stratosphere (Figure 3B.2). Organic chlorine [CCl_y] is calculated as the chlorine-atomicity-weighted sum of the VMR of 12 long-lived source gases (CFC-11, CFC-12, CFC-113, CFC-114, CFC-115, CCl_4, HCFC-22, HCFC-141b, HCFC-142b, Halon-1211, CH_3Cl, & CH_3CCl_3) and 6 very short-lived species (CH_2Cl_2, $CHCl_3$, Cl_2Cl_4, CH_2ClCH_2Cl, $CHBrCl_2$, & CH_2BrCl) measured using air samples collected by the AWAS instrument. Further information regarding our estimate of [Cl_y] can also be found in Howar et al. (2025). Inorganic bromine mixing ratios ([Br_y]) are estimated in a similar manner, from the decomposition of long-lived (CH_3Br, Halon-1211, Halon-1301, Halon-2402) and very short-lived (VSL) organic bromine species (CH_2Br_2, $CHBr_3$, $CHBrCl_2$, $CHBr_2Cl$, CH_2BrCl) measured by AWAS. A quadratic relation between the sum of the bromine-atomicity-weighted VMR of these 10 species, versus the VMR of CFC-11, is used to define source gas injection of bromine (Figure 3B.3 in Appendix B). We also include a fixed contribution of 2.8 ppt to our estimate of [Br_y], which represents product gas injection by VSL

species, based on Table 1-6 of the WMO 2022 Ozone Assessment Report (WMO, 2022). The 1σ uncertainties in our estimates of [Cl_y] and [Br_y] are defined by the 33rd and 67th percentiles (67% confidence limits) of these quantities, within 5 ppt binned intervals of [CFC-11]. Further details regarding our uncertainty estimates for [Cl_y] and [Br_y] are given in Text 3B.1 of Appendix B.

3.2.2 Kinetic Uncertainties and Monte Carlo Simulations

We now describe the Monte Carlo (MC) simulations central to this study. We first identify 24 reactions which contribute at least 5% to the production or loss of ClO, $ClONO_2$, HCl, NO_x, HNO_3, NO_3, and N_2O_5 (Table 3B.3 of Appendix B). These species are the primary reactive and reservoir forms of chlorine and nitrogen in the lower stratosphere. The rate coefficients of these 24 reactions are perturbed to their ± 1σ temperature dependent uncertainty limits in model sensitivity simulations conducted at a 5-minute time resolution along the stratospheric portion of the nine flights. For completeness, we also conducted sensitivity simulations for 23 other reactions (Table 3B.3) that had been suggested by prior literature as being potentially important contributors to the uncertainty in the photochemical loss of ozone in the lower stratosphere. The temperature dependent uncertainty limits of bimolecular and termolecular reaction rates are calculated in accordance with the JPL-2019 recommendation, as follows:

$$f(T) = f(298\ K) \exp\left|g\left(\frac{1}{T} - \frac{1}{298}\right)\right| \quad (3.1)$$

Here, $f(298\ K)$ is the JPL uncertainty estimate at 298 K and g describes how the uncertainty increases away from 298 K. Uncertainty factors for photodissociation reactions are taken directly from Table 4-2 of JPL-2011 (Sander et al., 2011) and represent the combined uncertainty in the respective cross sections and quantum yields. The upper and (lower) 1σ limits are found by

multiplying (dividing) the rate coefficient by the value of $f(T)$ for the specific reaction. Similarly, the upper and lower 2σ limits are found by multiplying and dividing the rate coefficients by $f(T)^2$, respectively.

For the MC simulations, we selected only those reactions for which a 1σ increase or decrease in the rate coefficient at DCOTSS-relevant temperatures causes at least a 10% shift in either modeled [NO_2], [$ClONO_2$], or [ClO], compared to model results found using the JPL-2019 recommendation for all reactions. Figure 3.1 shows the average absolute percent change in modeled [NO_2], [$ClONO_2$], and [ClO] that occurs when increasing and decreasing the rate coefficients of these 12 reactions by their 1σ temperature-dependent uncertainty limits (red and blue bars, respectively). We find that only 10 out of the 47 evaluated reactions result in at least a 10% change in modeled [NO_2], [$ClONO_2$], or [ClO], when the rate coefficient is perturbed to the ±1σ uncertainty limit. We additionally include the reactions HO_2+NO_2+M and $Cl+CH_4$ for a total of 12 in the MC simulations, because the impact of changing the rate coefficient for these two reactions either lies very close or exceeds the 10% threshold when the 5th and 95th percentiles of the modeled impacts are considered. Table 3.1 provides the parameters (f_{298} and g) used to calculate the uncertainty for each reaction, alongside the JPL evaluation for the most recently evaluated kinetics. Our use of a 10% threshold is designed to identify the reactions that have the largest inherent uncertainties that can be tested using the DCOTSS measurements of [NO_2], [$ClONO_2$], and [ClO].

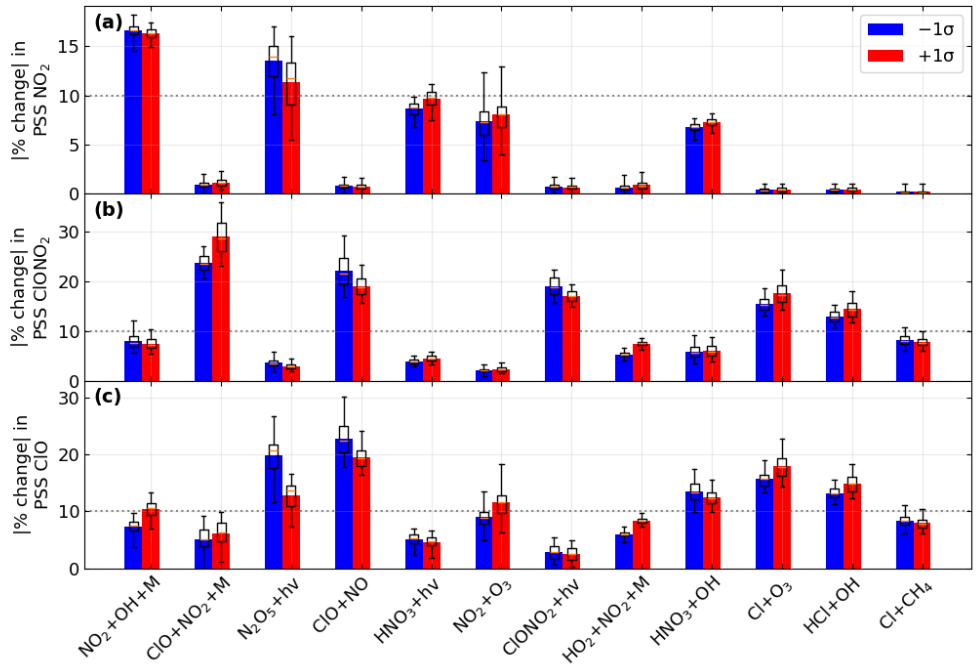


Figure 3.1. Average absolute percent change in modeled VMRs of NO_2 (a), $ClONO_2$ (b), and ClO (c) from the JPL-2019 recommendation with respect to 1σ increases (red bars) and decreases (blue bars) in the rate coefficient of the 12 reactions named on the horizontal axis. The length, whiskers, and horizontal lines of the corresponding boxplots illustrate the 25th and 75th percentiles, the 5th and 95th percentiles, and the median of the absolute percent changes, respectively. These ± 1σ kinetic shifts are assessed at a 5-minute time resolution along the ER-2 flight track for each of the nine DCOTSS flights that are the focus of this study.

Table 3.1. Reactions Assessed and Associated Rate Coefficient Uncertainties. Twelve reactions of focus in this study and associated 1σ uncertainties at 215 K

Reaction	f(298 K)	g	f(215 K)	Last Updated Recommendation	Last Evaluated
$NO_2+OH+M \rightarrow HNO_3 + M$	1.30	100	1.48	JPL-2006	JPL-2015
$ClO+NO_2+M \rightarrow ClONO_2+M$	1.30	50	1.39	JPL-2006	JPL-2010
$N_2O_5 + h\nu \rightarrow NO_2 + NO_3$	2.00	n.a.	2.00	JPL-2006	JPL-2015
$ClO + NO \rightarrow NO_2 + Cl$	1.15	100	1.31	JPL-1982	JPL-2010
$HNO_3 + h\nu \rightarrow OH + NO_2$	1.30	n.a.	1.30	JPL-2006	JPL-2015
$NO_2 + O_3 \rightarrow NO_3 + O_2$	1.15	150	1.40	JPL-1990	JPL-2019
$ClONO_2 + h\nu \rightarrow ClO + NO_2$	1.30	n.a.	1.30	JPL-2006	JPL-2015
$HO_2+NO_2+M \rightarrow HO_2NO_2+M$	1.06	400	1.79	JPL-2015	JPL-2015
$HNO_3 + OH \rightarrow H_2O + NO_3$	1.12	50	1.20	JPL-2019	JPL-2019
$Cl + O_3 \rightarrow ClO + O_3$	1.15	50	1.23	JPL-2006	JPL-2006
$HCl + OH \rightarrow H_2O + Cl$	1.10	50	1.17	JPL-2009	JPL-2009
$Cl + CH_4 \rightarrow HCl + CH_3$	1.05	50	1.12	JPL-2015	JPL-2015

For the MC simulations the rate coefficients of the 12 reactions given in Table 3.1 are randomly varied within a lognormal distribution that peaks at the JPL-2019 recommendation,

with boundaries at the respective ±2σ uncertainty limit for each reaction. Scale factors (that is, the ratio of the randomly varied ratio coefficient to the JPL-2019 value of the rate coefficient) are shown in Figure 3B.4 of Appendix B. Given the skewed nature of a lognormal distribution, the average value of these multiplicative scale factors does not equal unity. Therefore, upon evaluation of the results in Section 3.3, we normalize the multiplicative scale factors by their respective input distribution means, as described by Fish and Burton (1997). For the 500 MC simulations, the rate coefficients for the 12 reactions shown in Table 3.1 are varied using these multiplicate scale factors in random combinations that are statistically uncorrelated. For simplicity, we calculate the ± 2σ reaction uncertainty limits that define the boundary of the multiplicative scale factors for a fixed temperature of 215 K, which corresponds to the average sampled temperature within the 18 to 21 km region during DCOTSS. For each PSS model run, the measured temperature is used.

The MC simulations are run for a select number of points along the nine flight tracks of focus in this study, for which simultaneous daytime (SZA > 75°) measurements of [NO_2], [$ClONO_2$], and [ClO] are reported. We restrict our analyses to potential temperatures (θ) ≥ 430 K, the potential temperature level corresponding to the upper extent of convective influence observed during DCOTSS 2022 (Sayres et al., 2024). These simulations are run at a varying time resolution of ~370 seconds along each flight track, depending upon the simultaneous availability of measured [NO_2], [$ClONO_2$], and [ClO]. Mixing ratios of $ClONO_2$ are provided at a 35 second time resolution in intervals separated by approximately 210 to 350 seconds, depending on when the dissociation heater cycle reaches its maximum temperature (~500 K) (Wilmouth et al., 2026). The time resolution of the MC simulations corresponds to the middle of the $ClONO_2$ sampling interval in which all three species (that is, NO_2, $ClONO_2$, and ClO) are simultaneously reported.

3.3 Results and Discussion

3.3.1 Measured and Modeled NO_2, $ClONO_2$, and ClO

Figure 3.2 shows measured and modeled mixing ratios of NO_2, $ClONO_2$ and ClO for the nine research flights conducted during DCOTSS in summer of 2022 that are central to our analysis, for modeled mixing ratios computed using JPL-2019 kinetic recommendations for all 233 reactions. Below ~18 km and ~430 K, the modeled mixing ratios are in relatively good agreement with observations. In a prior study, we linked model underestimates of observed [NO_2] at lower altitudes to the lofting of boundary layer pollutants into the stratosphere by deep convection (Howar et al., 2025). At higher potential temperatures ($\theta \geq 430$ K), model values found using JPL-2019 kinetics systematically overestimate observed [NO_2] (Figure 3.2a) and [$ClONO_2$] (Figure 3.2b) by 20-30% and 25-50%, respectively. These overestimates fall outside the 10% ± 50 ppt and 20% ± 5 ppt uncertainty in measured [NO_2] and [$ClONO_2$] (Table 3B.2 of Appendix B), respectively, particularly at the highest sampled potential temperatures. The model provides very good (within 5%) agreement with measured [ClO] (Figure 3.2c), except for the two highest potential temperature bins of 515 and 520 K, for which the model underestimates observed [ClO] by ~22%.

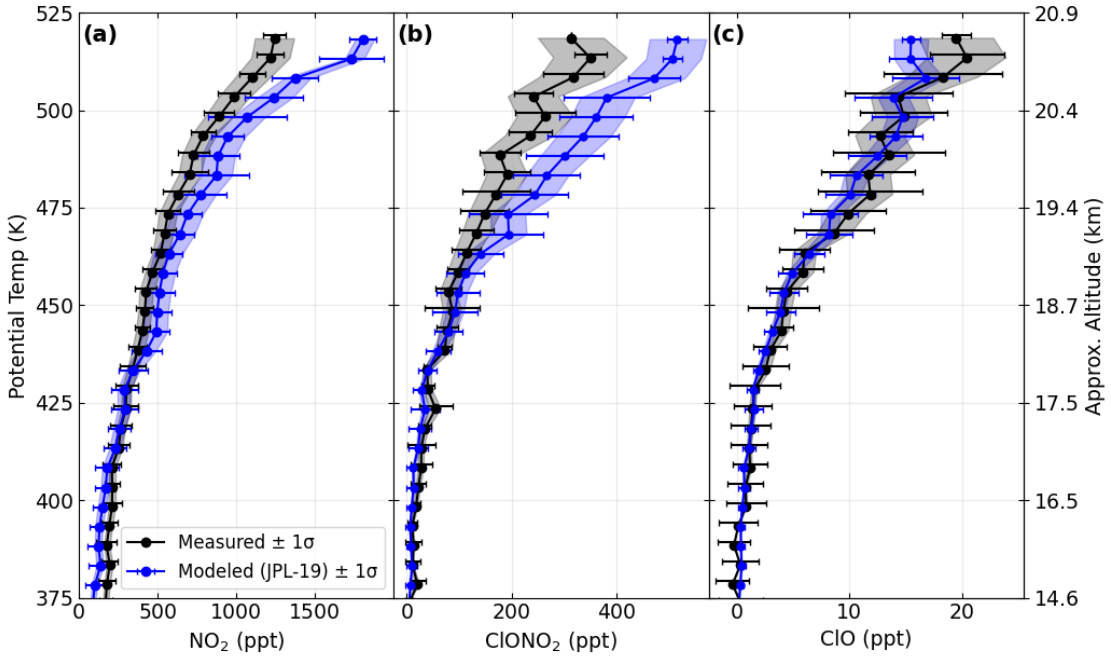


Figure 3.2. Measured (black) and modeled (blue) mixing ratios of NO_2 (a), $ClONO_2$ (b) and ClO (c) as a function of potential temperature (left axis) and approximate altitude (right axis) for nine research flights of DCOTSS 2022. Model runs are conducted at a 1-minute time resolution using JPL-2019 kinetic recommendations. Data are binned into 5 K potential temperature (θ) intervals, where the error bars show the standard deviation of the quantities within each θ bin. Error bars for the model calculations are staggered slightly in the vertical, to provide visibility. The black shading corresponds to the ± 1σ measurement uncertainties in [NO_2], [$ClONO_2$], and [ClO] provided in Table 3B.2. The blue shading corresponds to the ± 1σ uncertainty of inputs [Cl_y] and [NO_y] propagated onto modeled [NO_2], [$ClONO_2$], and [ClO]. Altitude on the right axis corresponds to the average altitude within each 15 K potential temperature bin; we term this quantity approximate altitude because altitude versus θ varies from flight to flight.

The variations in modeled [NO_2], [$ClONO_2$], and [ClO] are subject to uncertainties in rate coefficients as well as model inputs. The most important inputs to the model that affect the comparison to these measured radicals are the prescribed values of [NO_y] and [Cl_y]. To account for the influence of uncertainties in input [NO_y] and [Cl_y] (described in Section 3.2), we propagate the ± 1σ uncertainty in [NO_y] onto modeled [NO_2], and the 1σ uncertainty in [Cl_y] onto modeled [ClO]. For [$ClONO_2$], a root-sum-of squares propagation of ± 1σ uncertainties for both [NO_y] and [Cl_y] is used. These model input uncertainties are shown using blue shading in Figure 3.2. The error bars in Figure 3.2 show the standard deviation of [NO_2], [$ClONO_2$] and [ClO] within each 5 K potential temperature bin.

While the modeled and observed mixing ratios have overlapping 1σ uncertainties for some potential temperature levels, the model consistently overestimates observed [NO_2] and [$ClONO_2$] at high potential temperatures (that is, above $\theta \geq 475$ K) by an amount that exceeds the model input uncertainty associated with input [NO_y] and [Cl_y] and the measurement uncertainty, which motivates the rest of this study. Next, we explore whether adjustments to the rate coefficients of the 12 key reactions listed in Table 3.1, within their respective ± 2σ uncertainties, can account for the model-observation discrepancies for [NO_2] and [$ClONO_2$], while at the same time preserving the overall good agreement for [ClO].

Figure 3.3 shows a time series of model inputs for altitude, latitude, [O_3], and [CO] (panels a and b), as well as time series of modeled and measured [NO_2], [$ClONO_2$] and [ClO] (panels c to h) for the 5 June 2022 research flight. This flight was selected based on the broad latitude (41 to 56°N) and altitude range that was sampled. As in Figure 3.2, modeled mixing ratios found using JPL-2019 kinetic recommendations for all rate coefficients largely overestimate observed mixing ratios of NO_2 and $ClONO_2$ at high altitudes (solid blue lines, Figure 3.3c, d). At potential temperatures above 430 K, modeled [NO_2] and [$ClONO_2$] exceed the measured mixing ratios by 34% and 50%, respectively, and modeled [ClO] falls within 15% of the measured VMR. Figures similar to Figure 3.3 for the other eight research flights are shown in Figures 3B.5 to 3B.12 of the Appendix B. Although the tendency for the model to overestimate [$ClONO_2$] and [NO_2] at high altitudes is seen across all nine flights when using JPL-2019 kinetics, some flights exhibit better agreement than others.

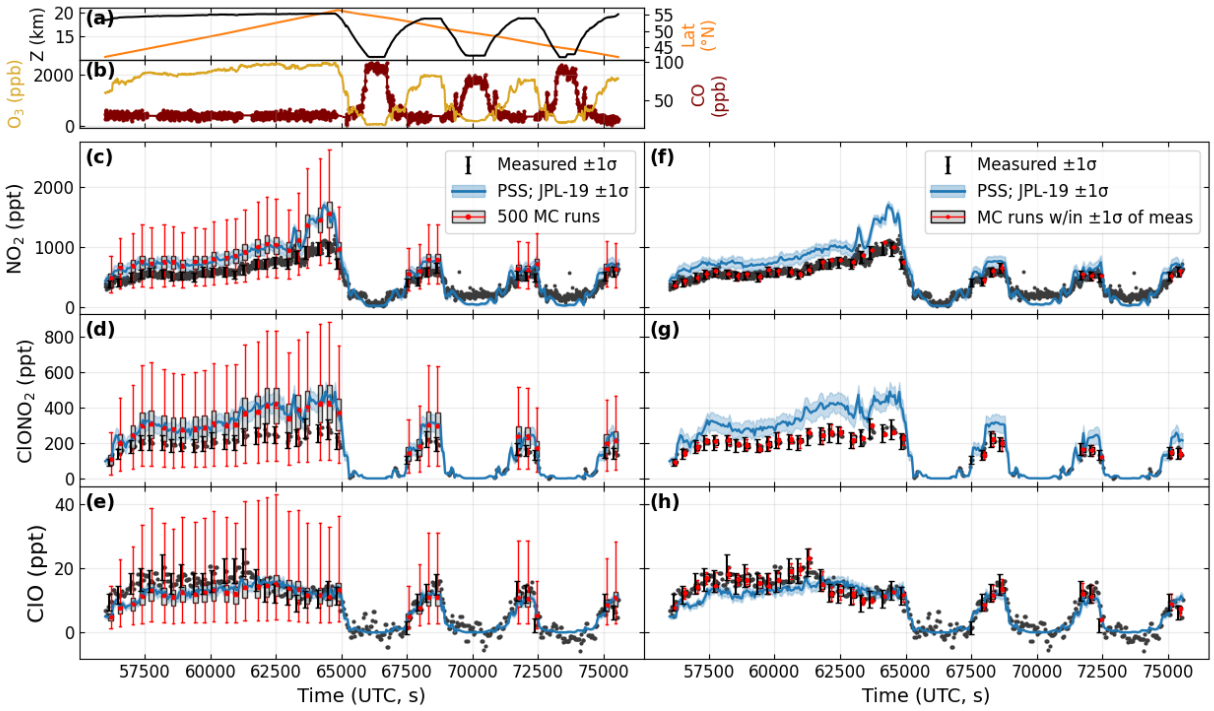


Figure 3.3. Time series for the $\theta \geq 430$ K portion of the 5 June 2022 research flight. Panel (a) shows altitude (black line; left axis) and latitude (orange line; right axis) of the ER-2 flight track. Panel (b) shows ozone mixing ratio (gold, left axis) and CO mixing ratio (maroon circles, right-axis). The maroon line in panel (b) represents mixing ratios of CO estimated from an O_3-CO relation, for times at which [CO] was not reported. Measured mixing ratios of NO_2, $ClONO_2$, and ClO are represented by the black markers in panels (c & f), panels (d & g), and panels (e & h), respectively. The black error-bars represent the ± 1σ measurement uncertainties (Table 3B.2) and are shown only at times for which the MC simulations are run. These error-bars are shifted slightly in the horizontal direction, to enhance visibility. One minute PSS model output, using JPL-2019 kinetics, are represented in panels (c) through (h) by solid blue lines and shading, where the shading represents the uncertainty in input [Cl_y] and [NO_y] propagated onto modeled [NO_2], [$ClONO_2$], and [ClO]. The boxplots in panels (c) through (h) show the mean (red circles), minimum and maximum (red whiskers), and 25th and 75th interquartile range (grey box) of the 500 member MC simulation (panels c-h), and the subset of these MC runs for which computed values of [NO_2], [$ClONO_2$], and [ClO] all fall within the ± 1σ measurement uncertainties of each of these three species (panels f-h). The first and last segments of the flight track are excluded from all PSS model runs, as measurements of [CO] are not available during the ascent and descent of the aircraft.

The distribution of modeled [NO_2], [$ClONO_2$], and [ClO] from the 500 member MC simulation is shown in the boxplots on Figure 3.3c-e. The red whiskers in Figure 3.3c-e show the minimum and maximum [NO_2], [$ClONO_2$], and [ClO] from the ensemble; the red circle markers represent the average of these quantities. The MC simulation is applied only for data collected at $\theta \geq 430$ K. Values of high [CO] and low [O_3] (Figure 3.3b) observed at lower potential temperatures are indicative of the potential influence of boundary layer pollution due to deep

convection (Howar et al., 2025). As illustrated in Figure 3.3c-e, modeled [NO_2], [$ClONO_2$], and [ClO] are highly sensitive to perturbations in the rate coefficients of the 12 reactions listed in Table 3.1. The measured mixing ratios of NO_2, $ClONO_2$, and ClO are encompassed by the lower and upper limits of the 500 member ensemble at each point along the flight track (red whiskers, Figure 3.3c-e) suggesting that, although the source of these model-observation discrepancies is unclear, adjustments in the 12 reaction rate coefficients alone could reconcile these model-observation discrepancies.

To evaluate which combination of kinetic shifts provides better consistency between the measured and modeled mixing ratios compared to the simulation using JPL-2019 kinetics, we evaluate the subset of these 500 MC runs that show good agreement with measured [NO_2], [$ClONO_2$], and [ClO]. Figure 3.3f-h show model output for members of the full ensemble for which modeled [NO_2], [$ClONO_2$], and [ClO] simultaneously fall within the ± 1σ measurement uncertainty of each species. The boxplots in Figure 3.3f-h show the distribution of modeled [NO_2], [$ClONO_2$], and [ClO] within this MC subset. As for Figure 3.3c-e, the range and average of model output for this subset are denoted by red whiskers and circle markers, respectively. The greatly reduced whisker sizes in Figure 3.3f-h compared to Figure 3.3c-e demonstrates that the selected subset of kinetic perturbations can simultaneously reproduce measured [NO_2], [$ClONO_2$], and [ClO] for the 5 June 2022 research flight. Ensemble members within this so-called “subset” are selected on a point-by-point basis from the full MC simulation, which is conducted at ~370 second intervals along the flight track. In other words, some of the box and whisker symbols in Figure 3.3f-h might represent many members of the full ensemble, whereas other symbols might represent only a few ensemble members.

Figure 3.4 shows the result of applying the methodology of the selection of ensemble members that exhibit agreement to within the ± 1σ measurement uncertainty for NO_2, $ClONO_2$, and ClO across all nine flights. The black error bars in Figure 3.4 show the 1σ uncertainty in the three measured quantities, as provided in Table 3B.2. Measured versus modeled mixing ratios of NO_2 (Fig. 3.4a), $ClONO_2$ (Fig. 3.4b), and ClO (Fig. 3.4c) are shown for model runs that assume JPL-2019 kinetics (black markers), and the subset of ensemble members that exhibit agreement with the observations at the 1σ level (red markers). The red error bars and markers in Figure 3.4 show the range and average of the MC subset and the grey boxplots show the 25th and 75th percentiles of the distributions.

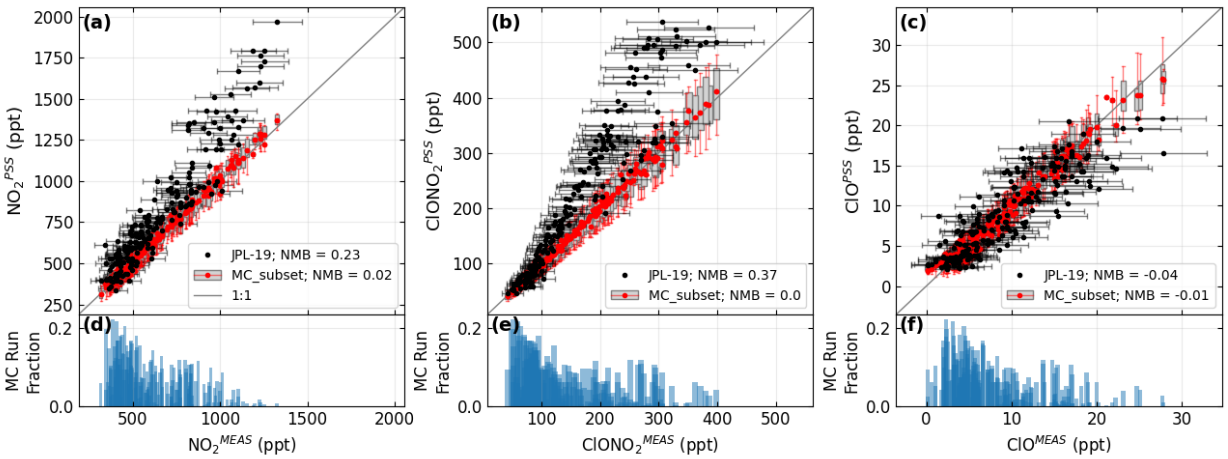


Figure 3.4. Modeled versus measured mixing ratios of NO_2 (a), $ClONO_2$ (b), and ClO (c) for the $\theta \geq 430$ K portions of all nine DCOTSS research flights of focus in this study. Black markers indicate the measured quantities versus model output assuming JPL-2019 kinetics, where the horizontal error bars show the ± 1σ uncertainty in the measured mixing ratios. The boxplots illustrate the distribution of the MC runs that fall within ± 1σ measurement uncertainties ("MC subset"), where the height of the boxplot represents the 25th and 75th percentiles, the whiskers represent the minimum and maximum, and the red stars represent the average of the MC subset. The MC subset only considers runs that simultaneously fall within the ± 1σ uncertainty of measured [NO_2] (10% ± 50 ppt), [$ClONO_2$] (20% ± 5 ppt) and [ClO] (17% ± 2 ppt). The bar plots in panels (d-f) illustrate the fraction of the 500 MC runs that fall within uncertainty of measured [NO_2], [ClO], and [$ClONO_2$] simultaneously ("MC Run Fraction"). The bar plots are semi-transparent to illustrate regions that have overlapping entries. The text boxes in panels (a), (b), and (c) provide the absolute normalized mean bias (NMB) between the measured and modeled quantities.

Constraining our MC runs by the measurement uncertainty of one species alone, rather than all three simultaneously, does not lead to considerable improvement in model-observation

agreement for the unconstrained species, indicating the somewhat independent nature of these model-observation discrepancies and the absence of a single common bias. Figure 3.4d-f shows the fraction of the full 500-member MC ensemble selected for the MC subset, as a function of the observed mixing ratios of the three key species. The fraction of MC runs that satisfy our three-species measurement uncertainty constraint varies across the measurement distribution, with higher fractions more prevalent at low [NO_2], [$ClONO_2$], and [ClO] (Figs. 3.4e-f).

Figure 3.5 summarizes the kinetic modifications to the 12 key reactions, for the MC subset that exhibits 1σ agreement between modeled and measured mixing ratios of NO_2, $ClONO_2$, and ClO, for the $\theta \geq 430$ K portions of all nine flights. Table 3.2 provides the mean and standard deviation of the multiplicative scale factors shown in Figure 3.5. The reactions in Figure 3.5 and Table 3.2 are shown in order of the absolute value of the mean multiplicative scale factor, relative to the JPL-2019 recommendation.

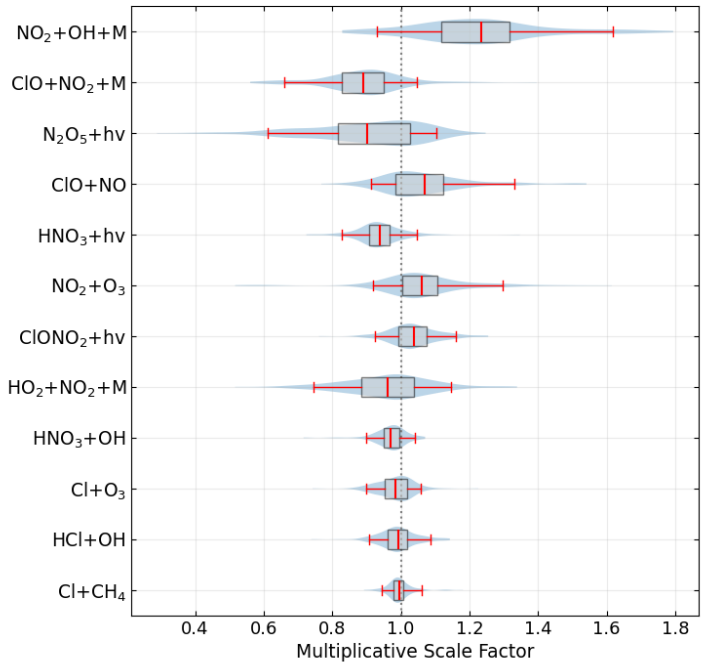


Figure 3.5. Multiplicative scale factors for the members of the MC subset that simulates [NO_2], [$ClONO_2$], and [ClO] to within ± 1σ of the measured value, for the 12 reactions considered throughout, for the θ ≥ 430 K portions of the nine summer 2022 DCOTSS research flights. Scale factors are computed relative to the JPL-2019 recommendation, such that a value of 1.0 indicates no kinetic adjustment. The width of each boxplot shows the 25th and 75th percentiles of the multiplicative scale factors of the MC subset; the red lines show the mean. The red whiskers show the 5th and 95th percentiles. The light blue shading shows a kernel density plot (also known as a violin plot) of the probability distribution of the full range of multiplicative scale factors. Here, multiplicative scale factors are first computed for the average of all members of a subset that matches observed [NO_2], [$ClONO_2$], and [ClO] at a specific time; these averaged scale factors are then used to find the distribution shown in this figure. Scale factors are first averaged for each measurement point, before distributions are computed, to provide a more uniform weighting across the full measurement range of [NO_2], [$ClONO_2$], and [ClO] due to the tendency of a larger fraction of ensemble members showing good agreement with all three species for smaller mixing ratios.

Table 3.2. Average Kinetic Adjustments to 12 key reactions. Average and standard deviation of multiplicative scale factors that provide 1σ agreement with measured and modeled [NO_2], [$ClONO_2$], and [ClO], along with the percent change in modeled [NO_2], [$ClONO_2$], and [ClO] for the individual reaction shifts.

Reaction	Average multiplicative scale factor ± 1σ	Percent change relative to JPL-2019 for individual shifts			
		% change [NO_2]	% change [$ClONO_2$]	% change [ClO]	Σ |% change|
$NO_2 + OH + M \rightarrow HNO_3 + M$	1.23 ± 0.19	−8.97%	−4.15%	+5.25%	18.37%
$ClO + NO_2 + M \rightarrow ClONO_2 + M$	0.88 ± 0.12	+0.37%	−9.21%	+1.88%	11.46%
$N_2O_5 + hv \rightarrow NO_2 + NO_3$	0.90 ± 0.17	−1.85%	+0.50%	+2.38%	4.73%
$ClO + NO \rightarrow Cl + NO_2$	1.07 ± 0.13	+0.16%	−5.11%	−5.22%	10.49%
$HNO_3 + h\nu \rightarrow NO_2 + OH$	0.94 ± 0.07	−2.12%	−0.97%	+1.15%	4.24%
$NO_2 + O_3 \rightarrow NO_3 + O_2$	1.06 ± 0.14	−1.31%	+0.39%	+1.74%	3.44%
$ClONO_2 + h\nu \rightarrow ClO + NO_2$	1.04 ± 0.07	+0.08%	−2.58%	+0.37%	3.03%

$HO_2 + NO_2 + M \rightarrow HO_2NO_2 + M$	0.96 ± 0.13	−0.06%	+0.44%	+0.52%	1.02%
$HNO_3 + OH \rightarrow H_2O + NO_3$	0.97 ± 0.05	−1.21%	+1.05%	+2.30%	4.56%
$Cl + O_3 \rightarrow ClO + O_2$	0.98 ± 0.05	+0.03%	−1.67%	−1.68%	3.38%
$HCl + OH \rightarrow H_2O + Cl$	0.99 ± 0.06	+0.01%	−0.78%	−0.78%	1.57%
$Cl + CH_4 \rightarrow HCl + CH_3$	1.0 ± 0.04	Not assessed	Not assessed	Not assessed	Not assessed

Of the 12 reactions, the largest kinetic shifts are found for $k_{NO2+OH+M}$ (+23%), $k_{ClO+NO2+M}$ (−12%), $j_{N2O5+hv}$ (+10%), k_{ClO+NO} (+7%), $j_{HNO3+hv}$ (−6%), and k_{NO2+O3} (+6%). The 25th percentile of the increase in the rate of $k_{NO2+OH+M}$ exceeds unity, and the 75th percentile of the decrease in the rate of $k_{ClO+NO2+M}$ is less than unity, which supports the notion that the DCOTSS data are better simulated by an increase in the formation rate of HNO_3 ($k_{NO2+OH+M}$) and a decrease in the formation rate of $ClONO_2$ ($k_{ClO+NO2+M}$) relative to the JPL-2019 recommendation. Figure 3.5 shows that some of the other reaction rate increases or decreases (i.e., j_{HNO3}, k_{NO2+O3}, j_{ClONO2}, $k_{HNO3+OH}$) relative to JPL-2019 are also significant at either the 25th or 75th percentile of the range of the distribution from the MC ensemble. Conversely, upon examination of the standard deviation about the mean of the MC ensemble (Table 3.2), only the multiplicative scale factors for $k_{NO2+OH+M}$ and $k_{ClO+NO2+M}$ are significant at the 1σ level. These alternate statements are based upon the fact that the distribution of the multiplicative scale factors is not Gaussian. Figure 3.5 and Table 3.2 both show that the JPL-2019 evaluation falls furthest from the output of our MC simulation for the three body formation rates of HNO_3 and $ClONO_2$.

The shifts to the rate coefficients needed to obtain good agreement with measured [NO_2], [$ClONO_2$], and [ClO] are not truly independent, due to the design of the MC simulations. For instance, a large shift in the NO_2+OH+M rate coefficient could result in the associated ensemble member passing the 1σ selection due to an improvement in simulated [NO_2], despite a change one of the other 11 reactions rate coefficients leading to slightly worse agreement with measured

[ClO] or [$ClONO_2$]. This aspect of the MC subset is reflected by the considerable width of the kernel density plots shown in Figure 3.5.

To address the interdependence of the reaction coefficient shifts inherent in the MC simulation, we individually perturb the rate coefficient of each reaction listed in Table 3.2 by their respective mean multiplicative scale factors found from the MC subset. The $\theta \geq 430$ K portion of all nine flights is then simulated using these individual perturbations, and the resulting impact on modeled [NO_2], [$ClONO_2$], and [ClO] is shown in Table 3.2. We find that a 23% increase in the JPL-2019 recommendation for $k_{NO2+OH+M}$ results in about a 9% drop in [NO_2], a 4% decline in [$ClONO_2$], and a 5% increase in [ClO]; all three of these computed changes help resolve the model-observation discrepancy of the JPL-2019 simulation shown in Figures 3.2 and 3.3. A 12% decrease in the JPL-2019 recommendation for $k_{ClO+NO2+M}$ has the largest effect (9% reduction) in computed [$ClONO_2$], with a modest [ClO] increase (about 2%) and a very small (0.4%) increase in [NO_2]. The reactions in Table 3.2 are listed in accordance with the order shown in Figure 3.5.

The last column of Table 3.2 shows the sum of the absolute value of perturbations to the computed VMRs of NO_2, $ClONO_2$, and ClO for these individual reaction changes. The largest perturbations are caused by the changes to the three body formation rates of HNO_3 and $ClONO_2$. The generally descending absolute values of these summed perturbations, as the rows of Table 3.2 progress from top to bottom, supports the validity of the ranking of these 12 reactions found by the full MC simulation (Figure 3.5).

3.3.2 Prior Literature and IUPAC

The salient finding from the MC simulations is that DCOTSS observations of [NO_2], [$ClONO_2$], and [ClO] are best simulated by a ~23% increase in the formation rate of HNO_3

($k_{NO2+OH+M}$) and a ~12% decrease in the formation rate of $ClONO_2$ ($k_{ClO+NO2+M}$) relative to the JPL-2019 recommendation. Model values found using JPL-2019 kinetics systematically overestimate observed [NO_2] and [$ClONO_2$] by 20-30% and 25-50%, respectively, over the 430 to 520 K potential temperature range. The JPL-2019 model provides good agreement (differences generally less than 5%) with measured [ClO], except above 515 K, for which the model underestimates observed [ClO] by nearly 22%.

Kinetic recommendations for the reactions that govern NO_x to NO_y partitioning have received considerable prior attention, given persistent model-observation discrepancies in [NO_x]/[NO_y] reported over the past three decades. Comparison of our results to the prior literature is complicated by numerous changes in the JPL recommended rate coefficient, based on either new laboratory studies or at times re-interpretation of older studies. Figure 3.6a shows the rate coefficient for NO_2+OH+M as a function of potential temperature calculated using the JPL-1997 (Demore et al., 1997), JPL-2000 (Sander et al., 2000), JPL-2019 (Burkholder et al., 2019), and IUPAC (Atkinson et al., 2004, 2007) recommendations, for meteorological conditions during DCOTSS. This figure also shows the 23% increase in the JPL-2019 recommended value of this rate coefficient found from the MC simulation.

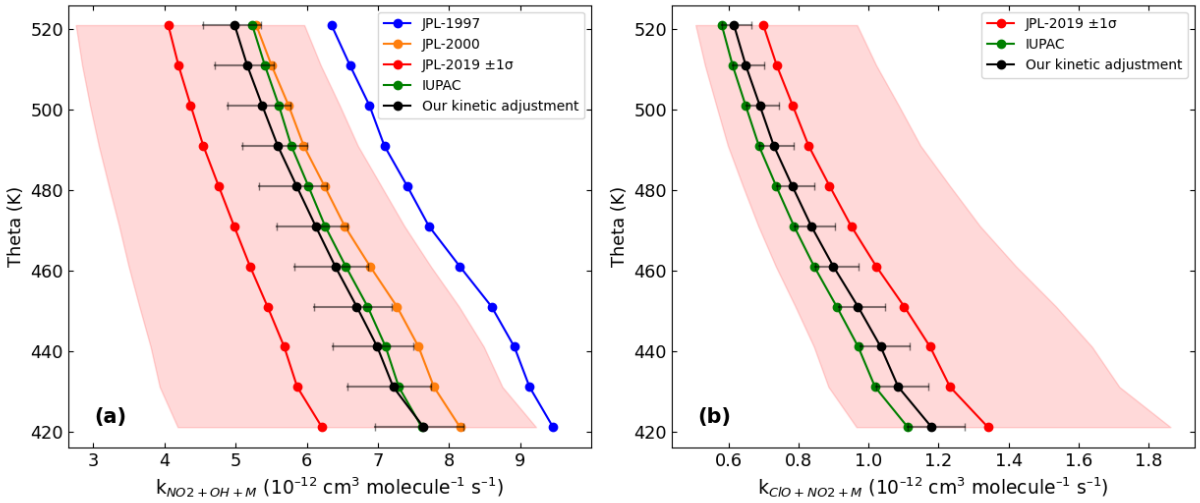


Figure 3.6. Recommended rate coefficients for the NO_2+OH+M (a) and ClO+NO_2+M reactions (b) binned into 10 K potential temperature intervals for the temperature and pressure range sampled during the nine flights of focus of DCOTSS 2022. The red and green lines are calculated using the JPL-2019 and IUPAC recommendations, respectively. The light red shading shows the 1σ uncertainty in the JPL-2019 rate coefficients. The JPL-1997 and JPL-2000 kinetic recommendations are shown in the blue and orange in panel b, respectively. The black line represents the average ± 1σ kinetic adjustment to the JPL-2019 recommendations that allows for 1σ agreement between modeled and measured [NO_2], [$ClONO_2$], and [ClO] during DCOTSS over the 430 to ~520 K potential temperature range sampled during the nine flights. The black error bars show the JPL-2019 recommendation scaled by the 25th and 75th percentiles of the MC subset multiplicative scale factors for $k_{NO2+OH+M}$ (a) and $k_{ClO+NO2+M}$ (b) shown in Figure 3.5.

Our kinetic adjustment to $k_{NO2+OH+M}$ is in excellent agreement with the IUPAC (last revised in 2017) and is also relatively consistent with the JPL-2000 recommendation (Figure 3.6a). The light red shading shows the 1σ uncertainty in the JPL-2019 recommendation for $k_{NO2+OH+M}$, evaluated as a function of the mean temperature and pressure profiles during the nine research flights. For simplicity, the uncertainty in this rate coefficient from earlier JPL recommendations as well as IUPAC are not shown. Clearly, the IUPAC recommendation as well as the value for $k_{NO2+OH+M}$ that best fits the data from the MC simulation are both well within the JPL-2019 uncertainty range.

Prior studies that used the JPL-1997 kinetic recommendation found modeled [NO_x]/[NO_y] to be 10-40% lower than ER-2 and balloon-borne observations obtained in middle to high latitudes of the Northern Hemisphere stratosphere (Gao et al., 1999; Jucks et al., 1999;

Osterman et al., 1999; Sen et al., 1998). Osterman et al. (1999) and Jucks et al. (1999) suggested a 35% decrease in the JPL-1997 value for $k_{NO2+OH+M}$ would largely resolve $[NO_x]/[NO_y]$ model-observation discrepancies. Kondo et al. (2000), Portmann et al. (1999), and Prasad (2003) found that the JPL-2000 update kinetics for $k_{NO2+OH+M}$ yielded much better agreement between modeled and observed $[NO_2]/[HNO_3]$ and $[NO_x]/[NO_y]$. Figure 3.6a shows that our average kinetic adjustment of +23% to $k_{NO2+OH+M}$ is relatively consistent with the JPL-2000 recommendation in which the prior studies found relatively good model-observation agreement for $[NO_x]/[NO_y]$.

The JPL-2006 evaluation suggested considerable changes to $k_{NO2+OH+M}$, to allow for a secondary product channel that leads to the formation of pernitrous acid (HOONO). The recommendation for $k_{NO2+OH+M}$ has remained unchanged since the JPL-2006 evaluation and is therefore denoted JPL-2019 in Figure 3.6a. The JPL-2019 recommendation is on average 35% slower than the JPL-1997 recommendation and 24% slower than the JPL-2000 recommendation for the temperature and pressure range in this study. The large differences between the JPL-1997, JPL-2000, and JPL-2019 kinetic recommendations for $k_{NO2+OH+M}$ largely explain why model-observation discrepancies in $[NO_2]$ reported here differ substantially from prior studies (Gao et al., 1999; Jucks et al., 1999; Osterman et al., 1999; Sen et al., 1998). The IUPAC recommendation for this reaction also considers the formation of HOONO. The recommendations have slightly different branching ratios for HOONO (~12% for JPL-2019 and ~9% for IUPAC, for the temperatures and pressures of this study). The JPL-2019 and IUPAC recommendations provide quite different values for the low-pressure limit of this reaction; furthermore, the JPL recommendation uses a value of 0.6 for the broadening factor at the center of the fall-off curve (F_c), whereas IUPAC uses a value of 0.41. The laboratory study of Amedro

et al. (2019) found that for conditions typical of 20 km (T = 215 K, M ~ 2×10^{18} molecule cm^{-3}), the JPL-2019 recommendation for $k_{NO2+OH+M}$ underestimates their measured value by 20%, while the IUPAC recommendation overestimates the measured value by 5%. Finally, Amedro et al. (2020) suggests the rate coefficient increases when more water vapor is present, which is a factor not considered in either the JPL or IUPAC compendiums.

It is important to note that our chemical mechanism does not consider secondary product channels of HO_2+NO that yield HNO_3 or HOONO, identified by theoretical work (Zhang & Donahue, 2006). The formation of HNO_3 and/or HOONO from the three-body reaction of HO_2+NO+M is highly uncertain. Neither JPL nor IUPAC provide firm recommendations for this three-body reaction channel, but IUPAC places an upper limit on the branching ratio for HNO_3 formation of 0.05%. Assuming a branching ratio of 0.05%, we estimate this pathway would increase HNO_3 formation by less than 0.5% for the conditions sampled above 430 K potential temperature during DCOTSS 2022. In addition, Butkovskaya et al. (2005, 2007) and Mertens et al. (2022) present laboratory results that show this reaction proceeds almost entirely towards formation of OH and NO_2 under atmospheric conditions, with less than 1% proceeding the termolecular route.

As noted in the Section 3.1, prior analyses of measured and modeled ClO, $ClONO_2$, and HCl tended to focus on prior kinetic recommendations for reactions linking ClO and HCl rather than the formation rate of $ClONO_2$ (Bonne et al., 2000; Dubey et al., 1998; Michelsen et al., 1996; Sen et al., 1999; Stimpfle et al., 1999; Voss et al., 2001; Webster et al., 1994). Consequently, it is difficult to relate our MC simulation finding of a ~12% decrease in the $ClONO_2$ formation rate to the prior literature. Wilmouth et al. (2026) compared measured [$ClONO_2$] and steady-state [$ClONO_2$] from measured [ClO], [NO_2], and J_{ClONO2} and $k_{ClO+NO2+M}$

for 29 DCOTSS research flights conducted in summers 2021 and 2022. They concluded good agreement within uncertainty between steady-state and measured [$ClONO_2$], with a slope of 1.21 for a linear fit to these two terms. Their analysis suggests a small high bias in the JPL-2019 recommendation for $k_{ClO+NO2+M}$, consistent with our finding that DCOTSS data are best simulated with a 12% reduction in $k_{ClO+NO2+M}$ relative to JPL-2019.

We now compare our DCOTSS-based finding to the most recent JPL and IUPAC recommendations for $k_{ClO+NO2+M}$. Figure 3.6b shows $k_{ClO+NO2+M}$ as a function of potential temperature from JPL-2019 and IUPAC, for meteorological conditions during DCOTSS, as well as the 12% decrease in the JPL-2019 recommended value found from the MC simulation. The JPL recommended value for $k_{ClO+NO2+M}$ has remained unchanged since 1994, and the IUPAC recommended rate coefficient has remained unchanged since 2005. The IUPAC recommendation is approximately ~17% slower than the JPL-2019 recommendation. The JPL-2019 formulation specifies a temperature dependence for the high-pressure limit, whereas IUPAC gives a temperature independent value for the high-pressure limit. Also, JPL-2019 recommendation uses $F_c = 0.6$, whereas IUPAC uses $F_c = 0.4$. The kinetic adjustment to the formation rate of $ClONO_2$ found by the MC simulation of DCOTSS data lies between these two recommendations, exhibiting somewhat better agreement with the IUPAC value. Both the IUPAC recommendation as well as the value for $k_{ClO+NO2+M}$ that best fits the data from the MC simulation are both well within the JPL-2019 uncertainty range (Figure 3.6b).

3.3.3 Catalytic Ozone Loss Pathways

Figure 3.7 shows the fractional loss of odd-oxygen ($O_x = O + O_3$) with respect to halogens (Figure 3.7a), NO_x (Figure 3.7b), and HO_x (Figure 3.7c) found assuming JPL-2019 kinetic recommendations (black symbols), and the kinetic adjustments that provide 1σ agreement

(that is the MC subset discussed in Section 3.3.1) with observed [NO_2], [$ClONO_2$], and [ClO] (colored symbols). Relative to the JPL-2019 recommendation, the MC subset yields a ~9% decrease (±1σ range of 0 to 17.5% decrease) in the relative contribution of NO_x-catalyzed to the total odd-oxygen loss, a 25% increase (±1σ range of 2.3 to 48% increase) in the contribution of halogens to odd-oxygen loss, and a 14% increase (±1σ range of 0.72% decrease to 27% increase) in the contribution of HO_x to odd-oxygen loss (Figure 3.7d).

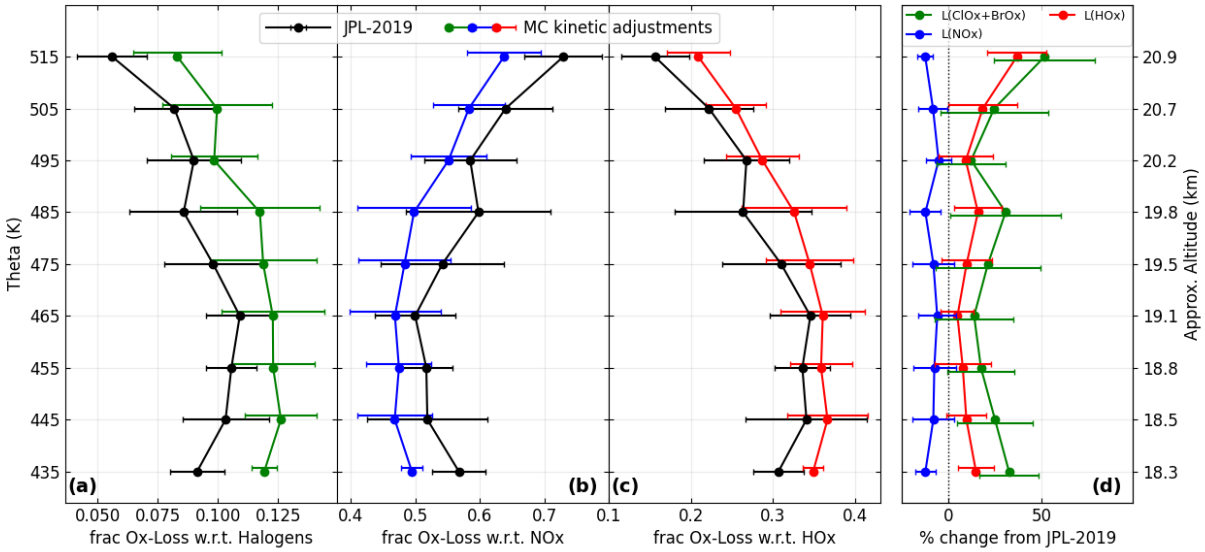


Figure 3.7. 24-hour averaged model output of fraction of total odd-oxygen loss (O_x = O + O_3) with respect to halogen loss reactions (a) (2×ClO+O, 2×BrO+O, 2×ClO+BrO, 2×ClO+HO_2, 2×BrO+HO_2), (b) NO_x loss reactions (2×NO_2+O), and (c) HO_x loss reactions (2×HO_2+O_3, O+OH, 2×O+HO_2, O_3+H, H+HO_2, OH+HO_2, 2×HO_2+HO_2), shown as a function of potential temperature. Model outputs are binned into 10 K potential temperature intervals. Results assuming JPL-2019 kinetics are shown in black, where markers and error bars denote the mean and standard deviation within each θ bin. In panels (a-c) the green, blue, and red markers and error bars show the mean and standard deviation of the MC ensemble averages that provide 1σ agreement between measured and modeled [NO_2], [$ClONO_2$], and [ClO] within each potential temperature bin. Panel (d) shows the percent change in fractional loss of O_x with respect to halogens (green), NO_x (blue) and HO_x (red) relative to JPL-2019 recommendation, imposed by our kinetic adjustments. Overlapping error bars on the various panels are staggered slightly upwards or downwards to provide visibility.

The reduced [NO_x]/[NO_y] ratio imposed by the kinetic adjustments of the MC subset is largely responsible for the shifts in the relative contribution of these catalytic ozone loss cycles. Because of the strong interdependence of these catalytic cycles, the reduction in NO_x-catalyzed ozone loss effectively increases the relative contribution of halogens and HO_x at all altitudes. Of

the adjustments made to the 12 reaction rate coefficients, the increase in the rate of NO_2+OH+M is responsible for the largest shift in the fractional contributions of NO_x, halogens, and HO_x to odd-oxygen loss (see Table 3B.4 of Appendix B). Prior studies (Gao et al., 1999; Portmann et al., 1999) have also illustrated the importance of nitrogen partitioning and the rate coefficient for the NO_2+OH+M reaction when providing ozone loss estimates.

Although the NO_x-catalytic cycle remains the dominant loss pathway for O_x under the conditions sampled here, the reduction imposed by our kinetic adjustments implies ozone in this region may be more sensitive to perturbations in the stratospheric abundances of halogens and hydrogen oxides than assumed by models using JPL-2019 kinetics. This sensitivity could become especially important for regions like the Asian Summer Monsoon, where convective injection of very-short-lived chlorine (VSL-Cl) species into the stratosphere frequently occurs (e.g., Liang et al., 2025). Anthropogenic VSL-Cl species are rising in emissions and are not currently regulated under the Montreal Protocol (WMO, 2022). Reducing uncertainties in the relative contribution of halogenated ozone loss is key for informing policy-making decisions regarding regulation of VSL-Cl species. Given that ozone in the midlatitude NH lower stratosphere is not recovering as predicted by current chemistry-climate models (Ball et al., 2018, 2020; Benito-Barca et al., 2025; Dietmüller et al., 2021; WMO, 2022), constraining uncertainties in key reaction rate coefficients is important for obtaining accurate photochemical ozone loss estimates.

3.4 Conclusions

We compare photochemical steady-state box model calculations to in-situ measurements of NO_2, $ClONO_2$, and ClO obtained in the daytime NH midlatitude stratosphere (~18 to 21 km) over a latitude range of 29 to 56°N over North America during the DCOTSS mission of summer

2022. For the conditions sampled during DCOTSS 2022, photochemical steady state model calculations that use JPL-2019 kinetic recommendations systematically overestimate observed mixing ratios of NO_2 and $ClONO_2$ by 20 to 30% and 25 to 50%, respectively. Measured ClO is simulated well, with modeled values generally within 5% of observation, except for the highest altitudes (close to 21 km), where the model tends to underestimate ClO by about 22%. We use a Monte Carlo simulation of kinetic uncertainties to show that systematic adjustments to a small number of chemical reactions, which govern nitrogen and chlorine partitioning, can provide 1σ agreement between the modeled and observed mixing ratios of NO_2, $ClONO_2$, and ClO. The largest kinetic shifts relative to JPL-2019 are found for $k_{NO2+OH+M}$ (+23%), $k_{ClO+NO2+M}$ (−12%), $J_{N2O5+hv}$ (−10%), k_{ClO+NO} (+7%), $J_{HNO3+hv}$ (−6%), and k_{NO2+O3} (+6%). The 25th percentile of the increase in the rate of $k_{NO2+OH+M}$ exceeds unity, and the 75th percentile of the decrease in the rate of $k_{ClO+NO2+M}$ is less than unity, which supports the notion that DCOTSS measurements are better simulated by an increase in the formation rate of HNO_3 ($k_{NO2+OH+M}$) and a decrease in the formation rate of $ClONO_2$ ($k_{ClO+NO2+M}$) relative to the JPL-2019 recommendation. The modifications to $k_{NO2+OH+M}$ and $k_{ClO+NO2+M}$ found here result in closer agreement to the latest IUPAC recommendation for these two rate coefficients, and are also well within the JPL-2019 1σ uncertainty for both reactions.

The kinetic adjustments that provide consistency with measured NO_2, $ClONO_2$, and ClO during DCOTSS imply that the use of JPL-2019 kinetics may overestimate NO_x-catalyzed odd-oxygen loss, and underestimate loss by halogens and hydrogen oxide radicals. These findings highlight the sensitivity of modeled ozone loss in the midlatitude stratosphere to uncertainties in a few key rate coefficients that govern the NO_x to NO_y ratio, and the abundances of ClO and $ClONO_2$ in the lower stratosphere. We suggest the community would particularly benefit from

future laboratory work on the reactions that govern the formation of HNO_3 and $ClONO_2$, at temperatures and pressures relevant for the midlatitude, lower stratosphere. Further work is needed, such as comparison with data collected during other aircraft campaigns, to evaluate whether the kinetic sensitivities identified here are robust.

Appendix B

Table 3B.1. Nine flights of focus in Chapter 3.

Flight Date	Latitude Range Sampled	Max Altitude Sampled
20220513	33.6°N–38.19°N	20.89 km
20220526	35.85°N–38.78°N	20.56 km
20220602	35.87°N–39.18°N	20.90 km
20220605	38.75°N–56.36°N	20.26 km
20220608	34.26–43.76°N	21.04 km
20220610	29.48°N–38.78°N	21.05 km
20220621	35.75°N–48.71°N	20.70 km
20220624	38.76°N–44.66°N	20.92 km
20220629	31.5°N–47.73°N	21.02 km

Table 3B.2. DCOTSS NASA ER-2 in-situ measurements used in this study.

Instrument	Species	Data Precision ± Accuracy	References
Harvard Halogens (HAL)	ClO	2 pptv ± 17%	Stimpfle et al., 2004; Wilmouth et al. (2026)
	$ClONO_2$	5 pptv ± 20%	
Harvard Herriott Hygrometer (HHH) as part of Harvard Water Vapor (HWV)	H_2O	< 0.10 ppmv ± 5–10%	Weinstock et al., 1994; Hintsa et al., 1999; Sargent et al., 2013
Advanced Whole air Sampler (AWAS)	Organic Cl gases (CFCs, HCFCs, Halons, VSLS), Ethane	± ~2–20%	Smith et al., 2024; Pan et al., 2024
UAS Chromatograph for Atmospheric Trace Species (UCATS)	O_3	2 ppbv + 2%	Hintsa et al., 2021
	N_2O	1.5 ppbv ± 0.5%	
	SF_6	0.05 pptv ± 0.5%	
	CFC-11	~1% ± 0.5%	
Harvard University Picarro Cavity Ringdown Spectrometer (HUPCRS)	CO	3.2 ppbv ± 1.25 ppbv	Pittman et al., 2025
	CH_4	0.2 ppbv ± 3.6 ppbv	
Compact Airborne Nitrogen diOxide Experiment (CANOE)	NO_2	50 pptv ± 10%	St. Clair et al., 2019

DCOTSS Portable Optical Particle Spectrometer (DPOPS)	Aerosol Surface Area Density (SAD)	± 20%	Li et al., 2023
Meteorological Measurement System (MMS)	Temperature (T)	0.05 K ± 0.3 K	Scott et al., 1990
	Pressure (p)	0.003 hPa ± 0.3 hPa	
	Potential Temperature (θ)	± 0.5–1.5 K	

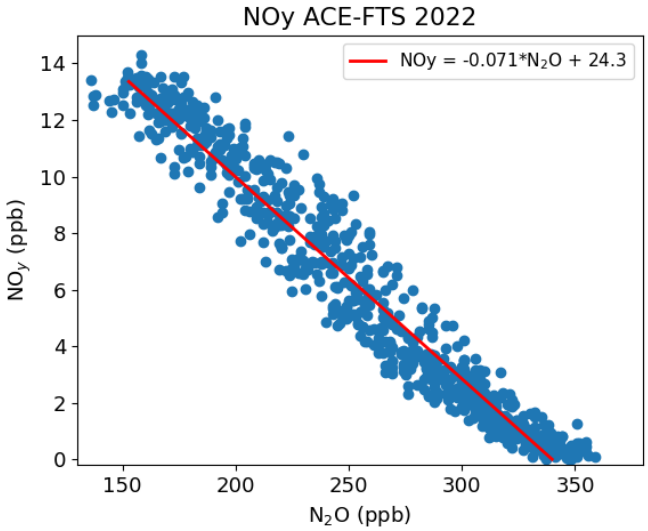


Figure 3B.1. ACE-FTS retrievals of [NO_y] ([NO] + [NO_2] + 2×[N_2O_5] + [HNO_3] + [HO_2NO_2] + [$ClONO_2$]) versus [N_2O] over CONUS during the summer of 2022 from 12 to 22 km. The red line represents the linear fit to the data used to estimate [NO_y] along the DCOTSS flight track. 1σ uncertainties are estimated by the 67% confidence limits of [NO_y] for 5 ppb [N_2O] binned intervals.

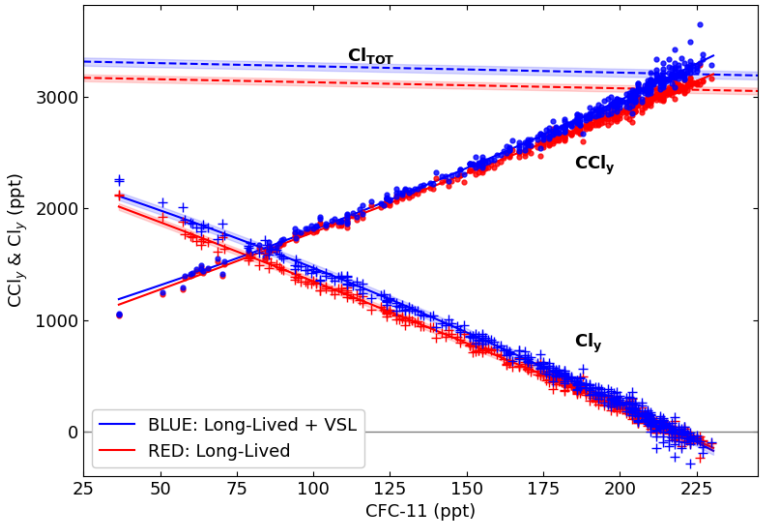


Figure 3B.2. AWAS [CCl_y] (red & blue circle markers) and [Cl_y] (red & blue plus sign markers) versus [CFC-11] for DCOTSS 2022. All quantities associated with only long-lived organic chlorine species are shown in red, and quantities associated with both long-lived + very short-lived (VSL) species are shown in blue. The quadratic relations between both [CCl_y] and [Cl_y] with [CFC-11] are indicated by solid red and blue lines, and the shading between the two [Cl_y] quadratic fits represents the range between the upper and lower limit formulations. The two quadratic relations between [CFC-11] and [CCl_y] are described by the following equations: CCl_y^{LL}(CFC-11) = $0.003401\times[\text{CFC-11}]^2 + 9.758\times[\text{CFC-11}] + 776.9$ and CCl_y^{LL+VSL}(CFC-11) = $0.01123\times[\text{CFC-11}]^2 + 8.269\times[\text{CFC-11}] + 870.2$. The quadratic relations between [CFC-11] and our four formulations for [Cl_y] are described by the equations: $Cl_y^{LL}{}_{\text{Lower-Limit}}$ (CFC-11) = $-0.004148\times[\text{CFC-11}]^2 - 10.08\times[\text{CFC-11}] + 2366$, $Cl_y^{LLUpper\text{-}Limit}$ (CFC-11) = $-0.004171\times[\text{CFC-11}]^2 - 10.08\times[\text{CFC-11}] + 2427$, $Cl_y^{LL+VSL}{}_{\text{Lower-Limit}}$ (CFC-11) = $-0.01201\times[\text{CFC-11}]^2 - 8.602\times[\text{CFC-11}] + 2413$, $Cl_y^{LL+VSL}{}_{\text{Upper-Limit}}$ (CFC-11) = $-0.01204\times[\text{CFC-11}]^2 - 8.603\times[\text{CFC-11}] + 2485$. Here [CFC-11] values are all be dry air mole fractions in ppt.

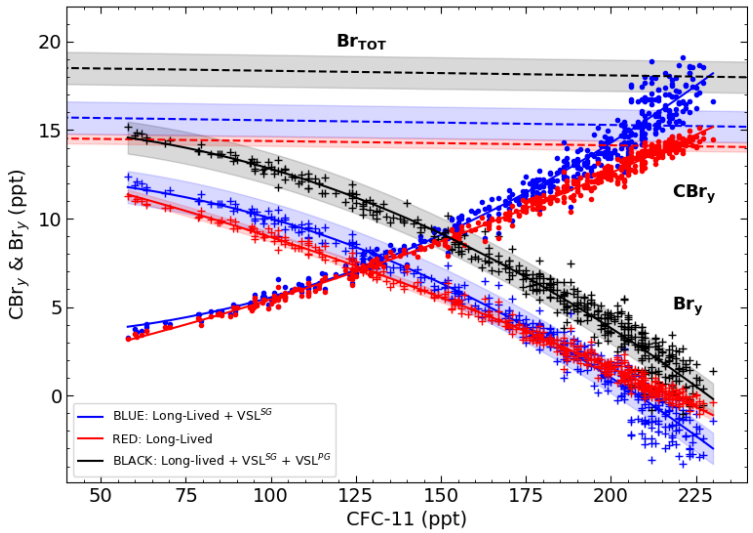


Figure 3B.3. AWAS [CBr_y] (red & blue plus signs) and [Br_y] (red, blue, and black plus sign markers) versus [CFC-11] for DCOTSS 2022. All quantities associated with only long-lived organic bromine species are shown in red, and quantities associated with both long-lived + very short-lived (VSL) species are shown in blue. The black markers represent possible contributions to Br_y from VSL product gas injection (PGI), at a fixed amount of 2.8 ppt (Tabel 1-6; WMO, 2022). The three formulations of Br_{TOT} are depicted in the red, blue, and black dash-dotted lines, respectively. The shading represents the uncertainty associated with the upper and lower limit formulations of Br_{TOT} described in Text 3B.1. The quadratic relations between both [CBr_y] and [Br_y] with [CFC-11] are indicated by solid red, blue, and black lines. The two quadratic relations between [CFC-11] and [CBr_y] are described by the following equations: CBr_y^{LL}(CFC-11) = $1.17\text{e-}4\times[\text{CFC-11}]^2 + 0.036\times[\text{CFC-11}] + 0.623$, $CBr_y^{LL+VSL\text{-}SG}$[CFC-11] = $3.36\text{e-}4\times[\text{CFC-11}]^2 - 0.014\times[\text{CFC-11}] + 3.54$. The quadratic relations between [CFC-11] and our two formulations for [Br_y] are described by the equations: Br_y^{LL} (CFC-11) = $-1.17\text{e-}4\times[\text{CFC-11}]^2 - 0.038\times[\text{CFC-11}] + 13.98$, $Br_y^{LL+VSL\text{-}SG}$(CFC-11) = $-3.36\text{e-}4\times[\text{CFC-11}]^2 + 0.011\times[\text{CFC-11}] + 12.26$. Here [CFC-11] values are all be dry air mole fractions in ppt.

Text 3B.1. Uncertainty Estimates of [Cl_y] and [Br_y]

We account for the uncertainty in total amount of organic chlorine and bromine at the tropopause, $Cl^{TOT\text{-}TROP}$ and $Br^{TOT\text{-}TROP}$, by defining upper and lower bounds on our Cl_y and Br_y estimates. The upper bound is defined by the value of $Cl^{TOT\text{-}TROP}$ and $Br^{TOT\text{-}TROP}$ associated with

the globally averaged value of tropospheric CFC-11 in Table 7A-1 of Daniel et al. (2022) of 220.6 ppt. The lower bound is defined by the average value of [CFC-11] measured at the dynamic tropopause observed during DCOTSS of 214.6 ppt. The spread between our four formulations of Cl_y (± one standard deviation) provide us with an approximate 25% 1σ uncertainty in Cl_y. Although only source gas species were measured during DCOTSS, we include a fixed contribution of 2.8 ppt to represent Br_y derived from product gases, following the estimate provided in Table 1-6 of the WMO 2022 Ozone Assessment Report. This value reflects the typical stratospheric contribution of VSL chlorine from PGI based on observations and model simulations. While we do not include an additional estimate for Cl from product gases that may arise from decomposition in the troposphere, the difference between the upper limit formulations of Cl_y of ~23 ppt is comparable to the estimated product gas contribution of 25 pptv provided in Table 1-6 of WMO, 2022. Further details are provided in Howar et al. (2025). For our PSS model simulations, we use the $Bry^{LL+VSL(PGI+SGI)}$ and the Cly^{LL+VSL} formulations.

Table 3B.3. Reactions that contribute at least 5% to the total production or loss of ClO, $ClONO_2$, HCl, NO_x, HNO_3, NO_3,and N_2O_5. These reactions were evaluated at their ± 1σ temperature dependent uncertainty limits in our model sensitivity simulations. Reactions are listed in no particular order.

1. $NO_2 + NO_3 + M \rightarrow N_2O_5 + M$
2. $N_2O_5 + h\nu \rightarrow NO_2 + NO_3$
3. $N_2O_5 + H_2O$ (het) $\rightarrow 2HNO_3$
4. $NO_2 + OH + M \rightarrow HNO_3 + M$
5. $BrONO_2 + H_2O$ (het)–> $HOBr + HNO_3$
6. $HNO_3 + h\nu \rightarrow OH + NO_2$
7. $HNO_3 + OH \rightarrow H_2O + NO_3$
8. $NO_2 + O_3 \rightarrow NO_3 + O_2$
9. $NO + OH + M \rightarrow HNO2 + M$
10. $BrONO_2 + h\nu \rightarrow Br + NO_3$
11. $ClONO_2 + h\nu \rightarrow Cl + NO_3$
12. $NO_3 + NO \rightarrow 2NO_2$
13. $NO_3 + h\nu \rightarrow NO + O_2$
14. $NO_3 + h\nu \rightarrow NO_2 + O$
15. $HO_2 + NO_2 + M \rightarrow HO_2NO_2 + M$
16. $ClO + NO_2 + M \rightarrow ClONO_2 + M$

17. $BrO + NO_2 + M \rightarrow BrONO_2 + M$
18. $ClONO + h\nu \rightarrow Cl + NO_2$
19. $ClONO_2 + h\nu \rightarrow ClO + NO_2$
20. $Cl + CH_4 \rightarrow HCl + CH_3$
21. $C_2H_6 + Cl \rightarrow HCl + C_2H_5$
22. $HCl + OH \rightarrow Cl + H_2O$
23. $Cl + O_3 \rightarrow ClO + O_2$
24. $ClO + NO \rightarrow Cl + NO_2$

Additional reactions perturbed to their ± 1σ uncertainty in our PSS sensitivity simulations:

1. $NO_2 + OH + M \rightarrow HOONO + M$
2. $NO_2 + O + M \rightarrow NO_3 + M$
3. $HNO_4 + h\nu \rightarrow OH + NO_3$
4. $HNO_4 + h\nu \rightarrow HO_2 + NO_2$
5. $HNO_4 + OH \rightarrow H_2O + NO_2 + O_2$
6. $ClO + HO_2 \rightarrow HOCl + O_2$
7. $ClO + OH \rightarrow Cl + HO_2$
8. $ClO + OH \rightarrow HCl + O_2$
9. $ClONO_2 + O \rightarrow ClO + NO_3$
10. $ClONO_2 + OH \rightarrow HOCl + NO_3$
11. $ClONO_2 + Cl \rightarrow Cl_2 + NO_3$
12. $ClONO_2 + HCl\ (het) \rightarrow Cl_2 + HNO_3$
13. $ClONO_2 + H_2O\ (het) \rightarrow HOCl + HNO_3$
14. $HCl + HOCl\ (het) \rightarrow Cl_2 + H_2O$
15. $BrONO_2 + h\nu \rightarrow BrO + NO_2$
16. $OH + O_3 \rightarrow HO_2 + O_2$
17. $HO_2 + O_3 \rightarrow OH + 2O_2$
18. $OH + CO \rightarrow HO_2 + CO_2$
19. $HOCl + h\nu \rightarrow OH + Cl$
20. $HO_2 + BrO \rightarrow HOBr + O_2$
21. $HOBr + h\nu \rightarrow OH + Br$
22. $HO_2 + NO \rightarrow NO_2 + OH$
23. $BrO + NO \rightarrow Br + NO_2$

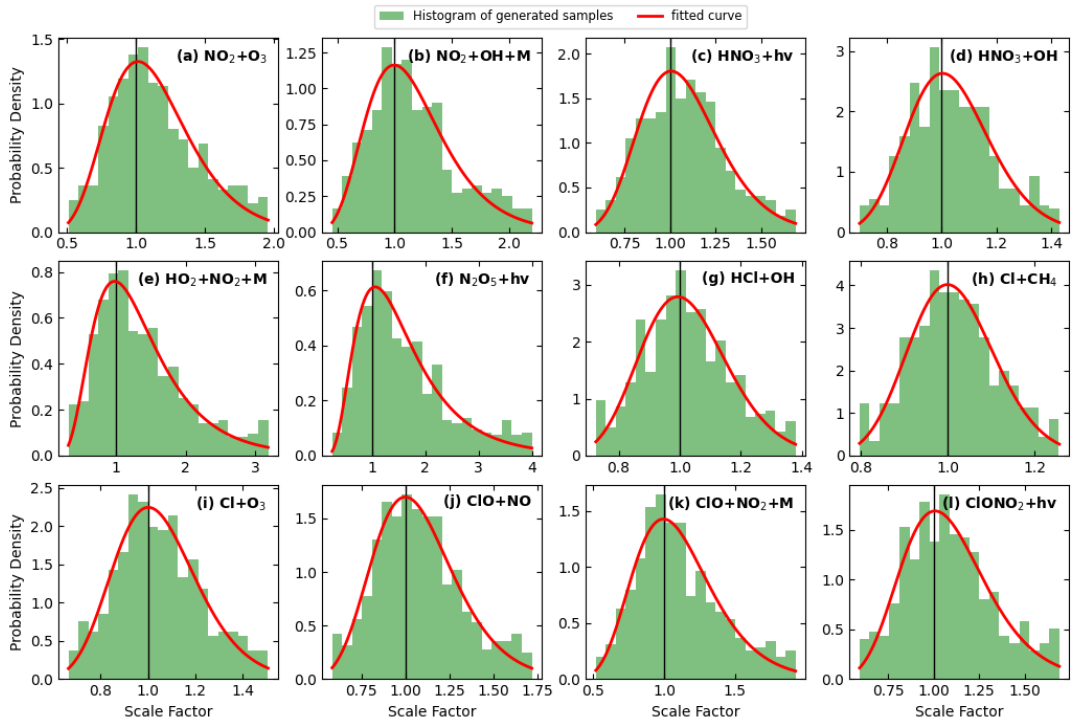


Figure 3B.4. Probability distribution of 500 multiplicative scale factors used to adjust the rate coefficient of the 12 key reactions in our Monte Carlo Simulations. The randomly generated histograms are shown in green, and the smoothed lognormal curve is shown in red.

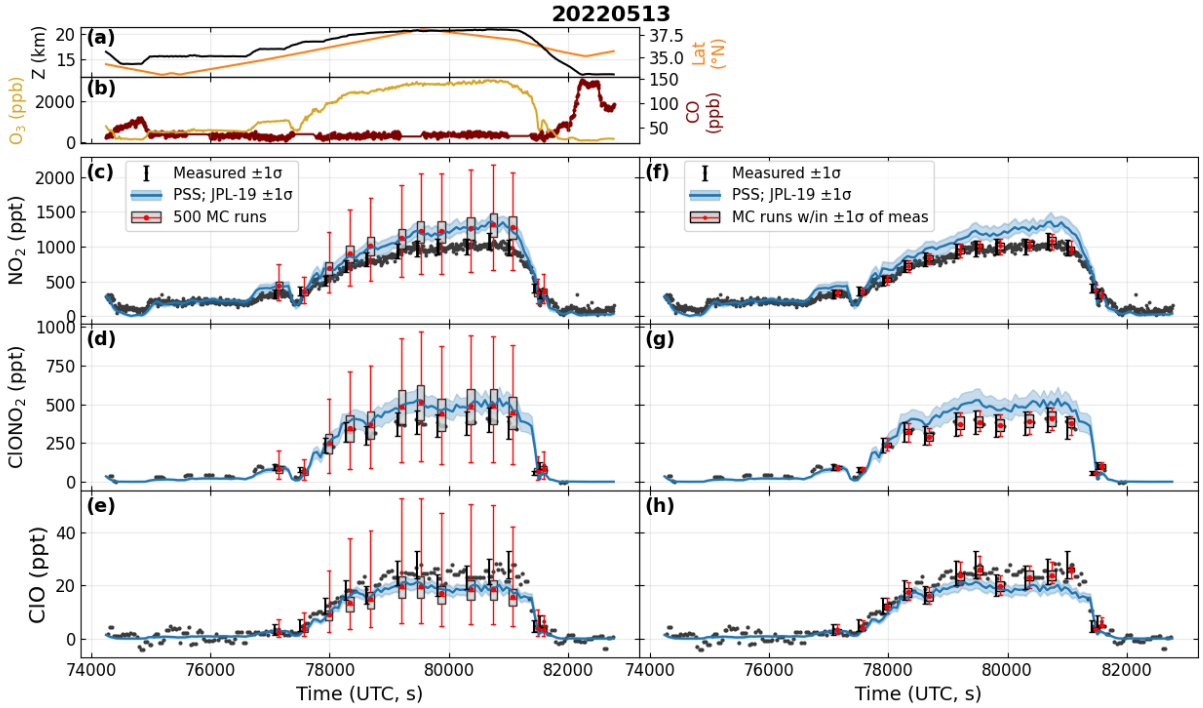


Figure 3B.5. Time series for research flight conducted on 13 May 2022. Panel (a) shows altitude (black line; left axis) and latitude (orange line; right axis) of the ER-2 flight track. Panel (b) shows ozone mixing ratios (gold, left axis) and CO mixing ratios (maroon, right-axis). The maroon line in panel (b) represents mixing ratios of CO estimated from an O_3-CO relation for times at which [CO] was not reported. Measured mixing ratios of NO_2,

$ClONO_2$, and ClO are represented by the black markers in panels (c & f), panels (d & g), and panels (e & h), respectively. The black error-bars represent the 1σ measurement uncertainties (Table 1) and are shown only at times for which the MC simulations are run. These error-bars are staggered slightly to the left for illustrative purposes. One minute PSS model output, using JPL-19 kinetics, are represented in panels (c-h) by solid blue lines and shading, where the shading represents the 1σ uncertainty in input [Cl_y] and [NO_y] propagated onto modeled [NO_2], [$ClONO_2$], and [ClO]. The boxplots in panels (c-e) show the mean (red circles), minimum and maximum (red whiskers), and 25th and 75th interquartile range (grey box) of 500 MC simulations, and the subset of MC runs that fall within the 1σ measurement uncertainties of [NO_2], [$ClONO_2$], and [ClO] simultaneously (panels f-h).

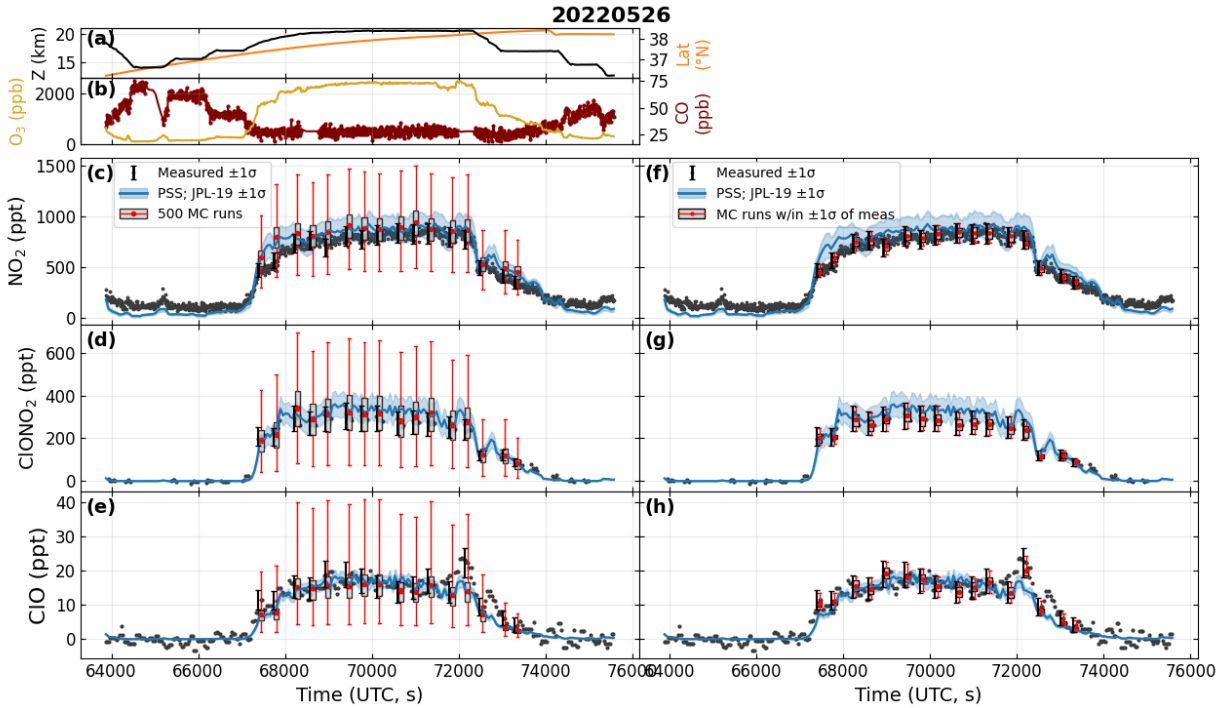


Figure 3B.6. Same as for Figure 3B.5 but for research flight conducted on 26 May 2022.

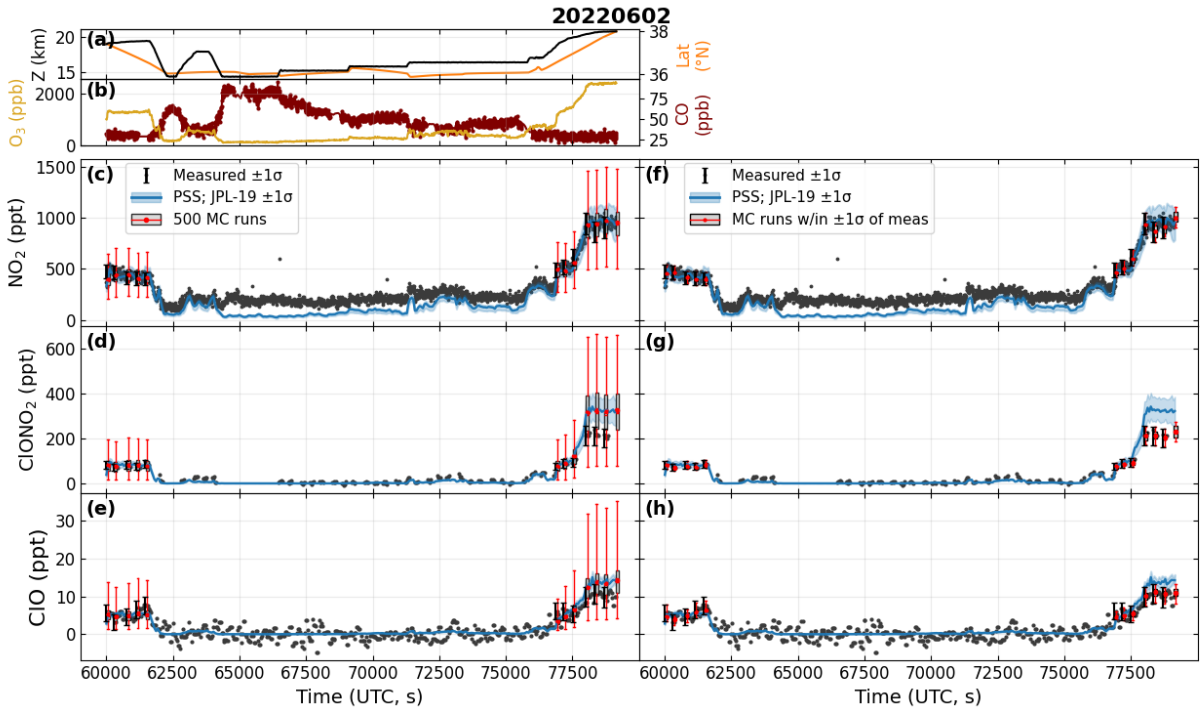


Figure 3B.7. Same as for Figure 3B.5 but for research flight conducted on 02 June 2022.

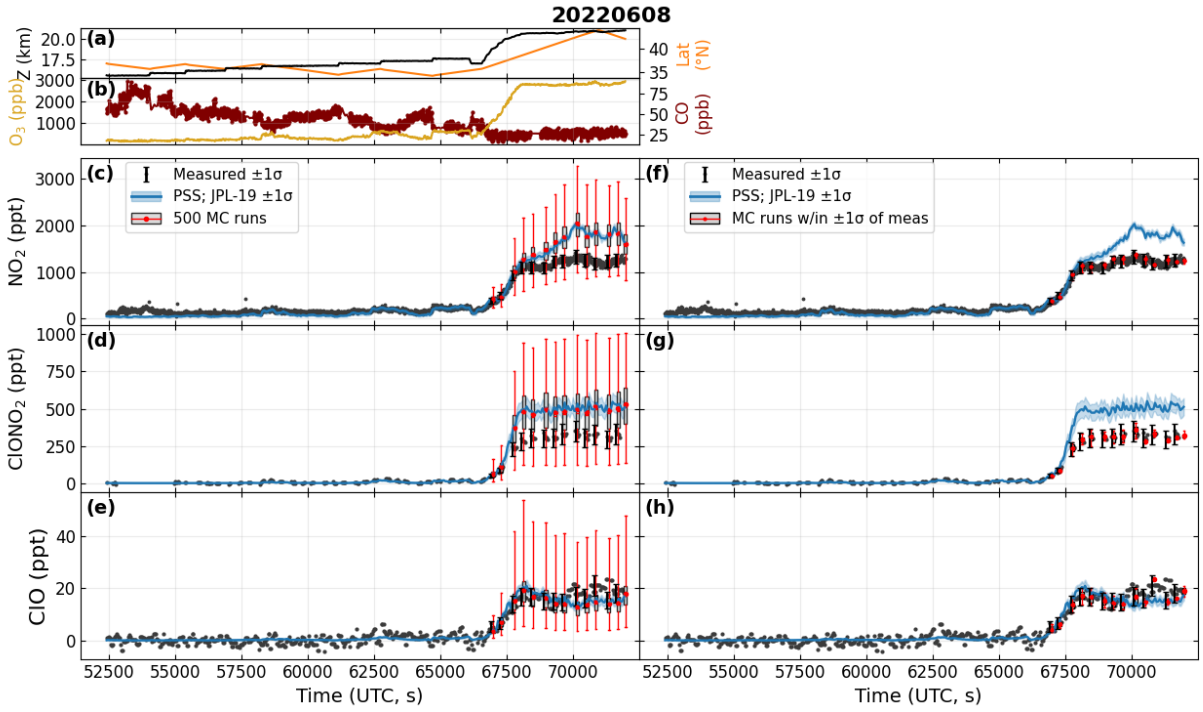


Figure 3B.8. Same as for Figure 3B.5 but for research flight conducted on 08 June 2022.

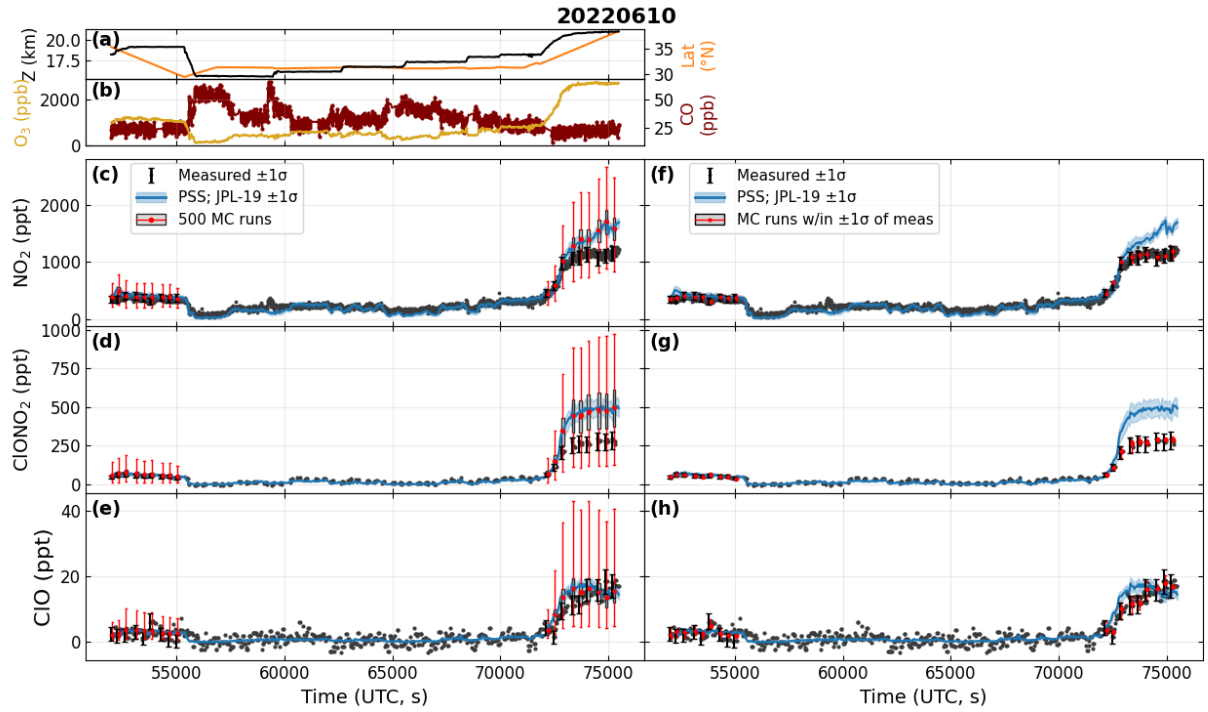


Figure 3B.9. Same as for Figure 3B.5 but for research flight conducted on 10 June 2022.

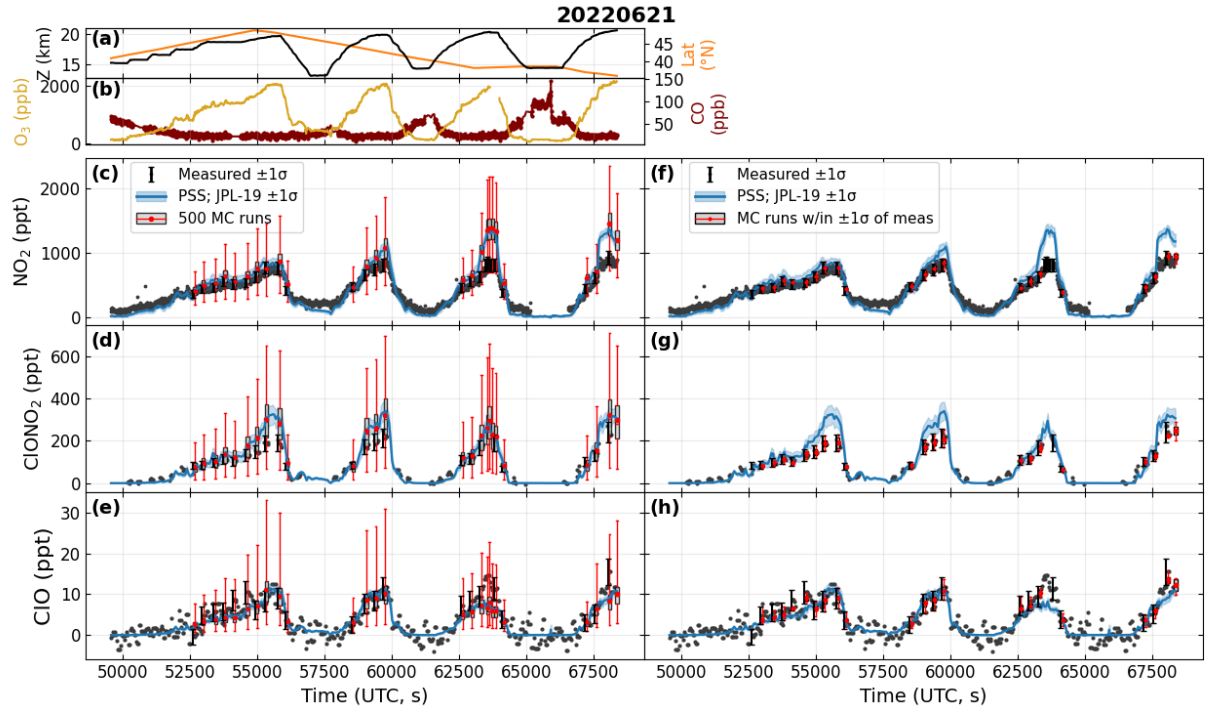


Figure 3B.10. Same as for Figure 3B.5 but for research flight conducted on 21 June 2022.

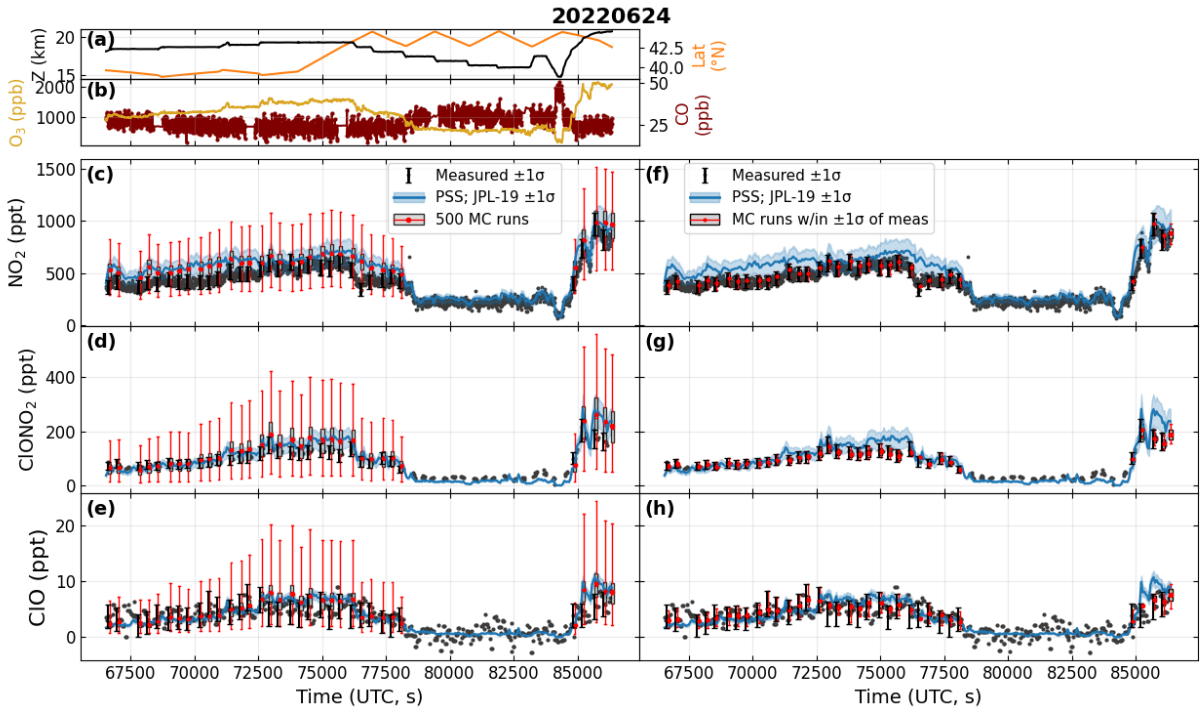


Figure 3B.11. Same as for Figure 3B.5 but for research flight conducted on 24 June 2022.

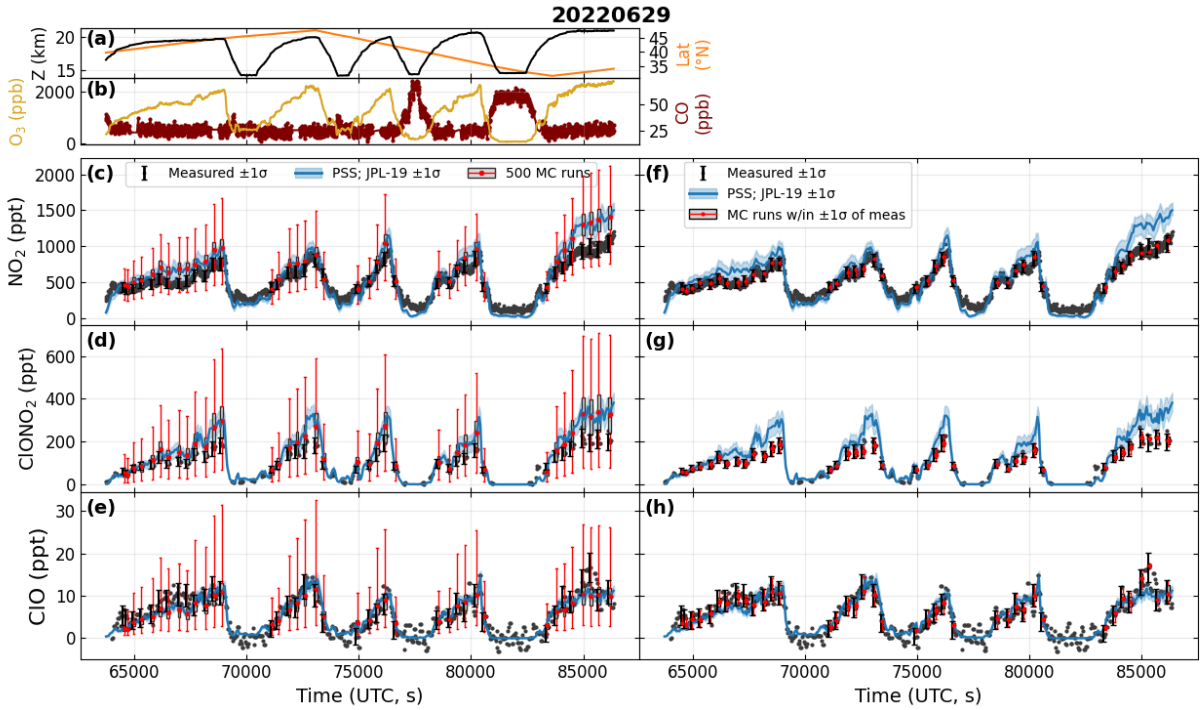


Figure 3B.12. Same as for Figure 3B.5 but for research flight conducted on 29 June 2022.

Table 3B.4. Percent change in 24-hour averaged fractional loss of Odd-Oxygen ($O_x = O + O_3$) with respect to halogens (ClO_x & BrO_x), NO_x, and HO_x that occurs when perturbing the rate coefficient of the 12 reactions by the multiplicative scale factors listed in column 2.

Reaction		Percent Change relative to JPL-2019

	Multiplicative scale factor ± 1σ	Fraction of O_x loss w.r.t ClO_x+BrO_x	Fraction of O_x loss w.r.t NO_x	Fraction of O_x loss w.r.t HO_x
NO_2+OH+M → HNO_3+M	1.23 ± 0.19	+12.27%	-5.72%	+6.39%
ClO+NO_2+M →$ClONO_2$+M	0.89 ± 0.12	+0.63%	+0.19%	-0.42%
ClO + NO → Cl + NO_2	1.07 ± 0.13	-2.73%	+0.37%	+0.12%
N_2O_5+hv →NO_2+NO_3	0.90 ± 0.17	+3.07%	-1.68%	+2.28%
NO_2 + O_3 → NO_3 + O_2	1.06 ± 0.14	+2.41%	-1.33%	+1.79%
HNO_3 + OH → H_2O + NO_3	0.97 ± 0.05	+2.46%	-1.49%	+2.13%
HNO_3 + hv → NO_2 + OH	0.94 ± 0.07	+2.68%	-1.27%	+1.46%
$ClONO_2$ + hv → ClO + NO_2	1.04 ± 0.07	+0.10%	+0.04%	-0.12%
HO_2 + NO_2 +M → HO_2NO_2	0.96 ± 0.13	+0.35%	-0.26%	+0.48%
Cl + O_3 → ClO + O_2	0.98 ± 0.05	-0.87%	+0.12%	+0.03%
HCl + OH → H_2O + Cl	0.99 ± 0.06	-0.42%	+0.06%	-0.03%
Cl + CH_4 → HCl + CH_3	1.0 ± 0.04	Not assessed	Not assessed	Not assessed

Chapter 4 : Observed and Modeled Trends of Inorganic Chlorine and Nitrous Oxide in the Midlatitude Stratosphere

4.1 Introduction

Stratospheric ozone plays a crucial role in protecting densely populated regions from harmful UV exposure (Lee-Taylor et al., 2026; Madronich & Gruijl, 1994). Therefore, it is essential to understand the processes controlling the thickness of the ozone layer, especially the past depletion of ozone due to human release of ozone-depleting substances (ODSs) and the recovery of the ozone layer due to the ban on the production of ODSs brought about by the Montreal Protocol (WMO, 2022). The Montreal Protocol and subsequent amendments have banned the global production of long-lived ODSs, including chlorofluorocarbons (CFCs), halons, methyl bromide, hydrochlorofluorocarbons (HCFCs), carbon tetrachloride (CCl_4), and methyl chloroform, except for the use of certain ODSs (mainly CCl_4, CFC-113, and CFC-114) as feedstock for the industrial production of other compounds (Bourguet & Lickley, 2024; Lickley et al., 2024). As a result of the Montreal Protocol phase-out of the industrial production of ODSs, the abundance of stratospheric chlorine has declined since the late 1990s (Dhomse et al., 2018; Keeble et al., 2018), although not as quickly as expected (Chrysanthou et al., 2025; Dubé, et al., 2025a; Hossaini et al., 2024b). Recent, new production of CFC-11 not allowed under the terms of the Montreal Protocol (Montzka et al., 2018) played a role in the slower than expected decline of CFC-11; however, this production has been curtailed (Montzka et al., 2021) and the majority of the slower than expected decline of stratospheric chlorine is attributed to atmospheric release of ODSs from the feedstock process, as well as from existing equipment, chemical stockpiles, and foams (Lickley et al., 2024). Most importantly, observations show that total column ozone

(TCO) at midlatitudes has not been recovering since the early 2000s as quickly as projected by chemistry and climate models (CCMs), which include a wide-range of dynamical, radiative, and chemical factors (Ball et al., 2018, 2020; Benito-Barca et al., 2025; Dietmüller et al., 2021; Morgenstern et al., 2017). The slower-than-expected recovery of the ozone layer at midlatitudes due to the decline of ODSs is more acute for the Northern Hemisphere (NH) compared to the Southern Hemisphere (SH) (Ball et al., 2019; Benito-Barca et al., 2025; Weber et al., 2022). A recent analysis of observed and simulated ozone trends for the 2000 to 2024 time interval shows similar behavior as had been found in prior studies that examined trends from 2000 to earlier end years (Sofieva et al., 2026).

The reason for the slower-than-expected recovery of the ozone layer at NH midlatitudes over the past two decades is unclear. Several studies attribute this model-observation discrepancy to dynamic influences such as changes in the strength of the Brewer Dobson Circulation (BDC) (Ball et al., 2020; Wargan et al., 2018; Weber et al., 2022). Orbe et al. (2020) emphasized the importance of proper model representation of the Quasi-Biennial Oscillation (QBO) of the direction and strength of winds in the tropical lower stratosphere, to accurately account for variations in the concentration of stratospheric ozone in midlatitude NH. Weather systems that affect the strength of the Arctic polar vortex can also have an appreciable effect on the thickness of the ozone layer at NH midlatitudes, especially during boreal spring. Newman et al. (2024) showed that an unusually warm Arctic vortex for winter 2023-2024 was associated with unusually high values of TCO at NH midlatitudes in spring 2024. Conversely, the very cold Arctic vortex in winter 2019-2020 (Kuttippurath et al., 2021; Manney et al., 2020; von der Gathen et al., 2021) was associated with unusually low values of TCO at NH midlatitudes in spring 2020 (Ardra et al., 2022).

The recovery of stratospheric ozone is predicated on attribution of increases in TCO to the decline in the abundance of stratospheric halogens (Bodeker et al., 2007). The abundance of stratospheric chlorine peaked in the late 1990s (Waugh et al., 2001). The subsequent recent decline of stratospheric chlorine, as quantified by Atmospheric Chemistry Experiment - Fourier Transform Spectrometer (ACE-FTS) measurements of HCl in the upper stratosphere, has also been slower than the expected decline computed from the measured surface abundances of long-lived, well mixed ODSs (Raymond et al., 2026). This slower than expected decline of HCl has been attributed, in part, to increasing emissions of very-short-lived chlorine (VSL-Cl) compounds that are not regulated by the Montreal Protocol (Hossaini et al., 2017, 2019, 2024; Raymond et al., 2026). While the impact of VSL-Cl has been found to be too small to explain the model-observation discrepancy noted above for TCO at NH midlatitudes, several studies have suggested that the future recovery of ozone in this region would be delayed should the emission of VSL-Cl compounds continue to rise (Bednarz et al., 2023; Hossaini et al., 2024b). Finally, Chrysanthou et al. (2025) highlight the importance of chemical feedbacks that couple dynamical variability with the temporal variation of stratospheric chlorine and ozone.

Here, we compare trends in stratospheric profiles of $HCl+ClONO_2$ and N_2O observed at midlatitudes by ACE-FTS, for March 2004 to December 2025, to trends of these quantities from output of eight CCMs that participated in new Chemistry-Climate Model Initiative 2022 (CCMI-2022) (Plummer et al., 2021). Trends in N_2O are a particularly important indicator of changes in the strength of the BDC (Dubé et al., 2023). We also examine the time evolution of total column chlorine ($HCl+ClONO_2$) divided by total column fluorine ($HF + 2\times COF_2$) observed over 1990 to 2025 by a ground-based Fourier-Transform Infrared Spectrometer (FTIR) at Jungfraujoch, Switzerland (46.54°N, 7.98°E) that is part of the Network for Detection of Atmospheric

Composition Change (NDACC) (Mahieu et al., 2014). These comparisons are focused on providing insight into the causes of substantial differences between measured and CCMI-2022-based computed trends in TCO for midlatitude regions.

4.2 Methods

4.2.1 ACE-FTS Retrievals

Measurements from the ACE-FTS instrument that resides onboard Canadian Space Agency SCISAT satellite are central to this study. ACE-FTS has been operational since February 2004 (Boone et al., 2023). We utilize version 5.3 ACE-FTS retrievals of N_2O, HCl, $ClONO_2$, COF_2, HF, and SF_6, as described in Boone et al. (2023) and Raymond et al. (2026). The data are filtered according to the data quality flags and procedures outlined in Sheese et al. (2015). Measurements that are 2.5 times greater or less than the median at each altitude are filtered out (Sheese et al., 2015). The native ACE-FTS retrievals are output as a function of geometric altitude with a vertical resolution of 1 km, which is common for measurements obtained by space-borne, solar occultation instruments. Below, we show results as a function of pressure, on a uniform pressure grid that corresponds to 1 km altitude spacing. Data are interpolated onto this pressure grid using the pressure versus altitude information associated with each retrieval. Monthly mean profiles are weighted by cosine latitude for the 35°S to 60°S and 35°N to 60°N latitude regions, then deseasonalized, prior to further analysis. We deseasonalize the data on a quarterly basis, for December-February (DJF), March-May (MAM), June-August (JJA), and September to November (SON), at each pressure level, following a procedure outlined in Bernath et al. (2018). Trends in the volume mixing ratio (VMR) of HCl+$ClONO_2$ and N_2O are found from a linear least squares fit to the deseasonalized, cosine latitude weighted, quarterly data at each pressure level. The ACE-FTS measurements of HCl, $ClONO_2$, and N_2O have

reported precisions of 2.9, 5.7, and 170 ppt, respectively. Similarly, the accuracies for HCl, $ClONO_2$, and N_2O are 1–2%, 4.5–5.5%, and 2–5% (table 1 of Schmidt et al., 2024). In the analysis that follows, we show error bars for profiles of ACE-FTS data representing the standard deviation of the mean, for annual averaged profiles. Similarly, for our trend analysis, the error bars represent the standard error of the linear squares fit. The differences between ACE-FTS based trends of HCl+$ClONO_2$ and N_2O and similar trends computed from CCMI-2022 model output are much larger than the ACE-FTS uncertainties.

For the analysis of Jungfraujoch data (Section 4.2.2), we make use of age of air (AoA) derived from ACE-FTS measurements of SF_6 (Saunders et al., 2025). Here, we use the so-called consolidated method to calculate AoA, as described in section 4.1.5 of Garny et al. (2024). This method makes use of surface measurements of SF_6 from NOAA Global Monitoring Laboratory (GML) network (Lan et al., 2026) for the tropical, marine boundary layer.

4.2.2 Jungfraujoch Columns

We also analyze measurements of total column HCl, $ClONO_2$, HF, and COF_2 measured by the ground-based, high spectral resolution (0.003–0.006 cm^{-1}) FTIR at Jungfraujoch, Switzerland (46.54°N, 7.98°E). Monthly mean retrievals, based on solar absorption spectra collected under clear-sky conditions, are used (Prignon et al., 2021). The time series used to compute total column Cl (HCl+$ClONO_2$) and total column F (HF+2×COF_2) originate from the Zenodo link associated with the Prignon et al. (2021) paper, as well as more recent measurements archived at the NDACC website. Following the analysis approach used in Chapter 1 of WMO (2022), we use monthly mean column abundances collected during the months of June, July, August, September, October, and November. This restriction limits the variability in the column abundances caused by stratospheric transport, which is particularly active in winter

and spring. The data shown in Section 4.3 represent a continuation of the total column chlorine and total column fluorine trends shown in figures 1-12 and 1-18 of WMO (2022).

4.2.3 EESC, VSL-Cl, Fluorine from HFCs

Equivalent effective stratospheric chlorine (EESC) is a metric that relates surface atmospheric abundances of ODSs to the VMR of inorganic halogens in the stratosphere (Daniel et al., 1995). The formula for the calculation of EESC, described in section 2.1 of Lickley et al. (2024), accounts for the number of chlorine and bromine atoms present in an ODS. EESC is found using fractional release factors (FRFs) and an estimate of the distribution of times required for air to be transported from stratospheric entry to the region of interest (G). Here, as in WMO (2022), we rely on two sets of values of FRFs and G from Tables 1 and 2 of Engel et al. (2018). One set is for 3-year-old air, commonly used for analysis of trends in ozone at midlatitudes in regression models (Lean, 2014; Stolarski et al., 2006; Yang et al., 2006), and the other for 5.5-year-old air, used to analyze trends in polar ozone (Dhomse et al., 2006; Newman et al., 2006; Yang et al., 2008). Bromine scaling factors of 60 and 65 are used to find EESC for 3 and 5.5-year-old air, respectively (Sinnhuber et al., 2009).

The influence of chlorine from VSL-Cl compounds not regulated by the Montreal Protocol is a central part of our analysis of data from ACE-FTS and Jungfraujoch. For the analysis of ACE-FTS profiles of HCl+$ClONO_2$, we estimate the contribution of VSL-Cl as a function of altitude by first computing an AoA profile, for 35°N to 60°N and for 35°N to 60°S, based on cosine latitude weighted values of the multi-year (February 2004 to February 2021) AoA as a function of altitude and latitude from Saunders et al. (2025). Their estimate is based on analysis of SF_6 measurements from ACE-FTS and the Michelson Interferometer for Passive Atmospheric Sounding (MIPAS) instrument. Next, a monthly mean time series for the product

gas injection (PGI) and source gas injection (SGI) of stratospheric chlorine from four VSL-Cl compounds (dichloromethane:CH_2Cl_2, chloroform:$CHCl_3$, tetrachloroethene:C_2Cl_4, and 1,2-dichloroethane:$C_2H_4Cl_2$) in the tropical tropopause transition layer (TTL) archived by Bednarz et al. (2022) is convolved with the age of air spectrum of Waugh & Hall (2002) (that is, their Γ), for an assumption that the width of the spectrum equals one-half of the age. Implicit in this estimate is the assumption FRFs = 1 for all VSL-Cl species, which is a reasonable assumption given the rapid photochemical loss of these gases in the stratosphere. Since the time series of Cl_{TOT} for VSL-Cl from Bednarz et al. (2022) is provided only to the end of 2019, we extend this time series out to the end of 2025 by assuming a 3.8 ppt/yr growth rate for VSL-Cl, obtained from Hossaini et al. (2019). Also, since this time series starts in 2000, we assume for prior years a value of 63.3 ppt for Cl_{TOT} from VSL-Cl, which is the annual mean value for 2000 from Bednarz et al. (2022). Surface measurements of CH_2Cl_2, $CHCl_3$, and C_2Cl_4, which begin in 1994, 1995, and 1995, respectively, show fairly constant VMRs prior to 2000 and a rapid increase in the mid-2000s (e.g., figure 1-11 of Carpenter and Reimann, 2014).

Figure 4C.1 of Appendix C shows Cl_{TOT} from Bednarz et al. (2022) as well as the estimated time series of VSL-Cl in the stratosphere, for AoAs of 3 and 5.5 years. The values of VSL-Cl for AoAs of 3 and 5.5 years are added directly to the chlorine contribution to EESC (EESC-Cl) from long-lived ODSs, to arrive at estimates for the time series EESC-Cl due to both ODSs and VSLs that is central to the analysis to total Cl from Jungfraujoch. As shown in Figure 4C.2, VSL-Cl is estimated to have a much larger effect on EESC-Cl for 3-year-old air than for 5.5-year-old air. This tendency follows expectation, since EESC-Cl from ODSs is much larger for 5.5-year-old air compared to 3-year-old air, and since the short photochemical lifetime of

VSL species leads to complete conversion to inorganic form of the full chlorine content of these gases present in the tropical TTL.

Figure 4C.1b shows Cl_{TOT} from Bednarz et al. (2022) and estimated contributions of VSL-Cl to stratospheric air masses with AoAs of 2, 4, and 6 years. For analysis of the ACE-FTS time series of $HCl+ClONO_2$, for an air mass with an AoA of 4 years, the contribution of VSL-Cl to stratospheric inorganic loading is based on the difference between the closed purple squares (VSL-Cl content of 4-year-old air in December 2025 and VSL-Cl content of 4-year-old air in March 2004). These two dates, March 2004 and December 2025, correspond to the start and end times of the ACE-FTS analysis. Numerical values of the contribution of VSL-Cl to stratospheric air, as a function of AoA, are given in Table 4C.1.

Central to our analysis of total Cl and total F from Jungfraujoch is the consideration of the stratospheric decay of hydrofluorocarbons (HFCs). As the atmospheric VMRs of HFCs have risen over the past decade, these compounds make an ever-increasing contribution to the stratospheric fluorine budget. Figure 4C.3 shows the fluorine contribution to EESC (EESC-F), from ODSs as well as ODSs and HFCs, for 3-year and 5.5-year-old airmasses. The contributions from HFCs are based on time series of global-mean VMRs of the ten HFCs with stratospheric lifetimes less than 1000 yrs that are measured by the Advanced Global Atmospheric Gases Experiment (AGAGE) surface network (Prinn et al., 2018). Here, we are using estimates of global annual mole fractions of HFCs (Table 4C.2) from version 20260305 of this dataset, which extends back to 1973 for most gases (Western et al., 2025). Values of FRFs and mean release time ($\Gamma^{\#}$) for these HFCs need to estimate the contribution to inorganic fluorine for 3-year-old and 5.5-year-old airmasses are based on quadratic fits of FRF and $\Gamma^{\#}$ for ODSs as a function of the logarithm of atmospheric lifetime, using data for ODSs from Tables 1 and 2 of Engel et al.

(2018) (Figure 4C.4). Numerical values of the FRF and $\Gamma^{\#}$ are given in Table 4C.2. We neglect HFC-23 in this analysis since its estimated stratospheric lifetime of 3636 years (Chapter 7, WMO 2022) means that the contribution to stratospheric inorganic chlorine measured over Jungfraujoch should be negligible. Of course, HFC-23 is a very important greenhouse gas due to its extremely large GWP (Miller & Kuijpers, 2011).

4.2.4 Chemistry-Climate Model Output

In this study, we evaluate output from the REF-D2 simulations of eight CCMs that participated in the Chemistry Climate Model Initiative 2022 (CCMI-2022) modeling effort. The CCMI-2022 simulations were designed to support the 2026 WMO/UNEP Scientific Assessment of Ozone Depletion (SAOD) report (Plummer et al., 2021). Measured and CCMI-2022 modeled trends in profiles of stratospheric ozone have been recently analyzed by Benito-Barca et al. (2025) and Sofieva et al. (2026); readers are directed toward these papers, as well as the Plummer et al. (2021) article published in the Stratosphere-troposphere Processes and their Role in Climate (SPARC) newsletter, for detail descriptions of the REF-D2 simulations. Below, we provide a brief overview that is most relevant to our study.

The REF-D2 experiments cover the 1960 to 2100 time period. These simulations are designed to provide estimates of the timing and magnitude of ozone layer recovery, due to the success of the Montreal Protocol. Another simulation, REF-D1, covers 1960 to 2018. The CCM simulations conducted for REF-D1 used observed sea surface temperature (SST) and sea ice cover (SIC), as described in section 2.2 of Benito-Barca et al. (2025). On the other hand, the CCM simulations for REF-D2 used either fully coupled 3-D ocean models (ACCESS, CESM2-WACCM, and MIROC-ES2H) or prescribed SST and SIC from ocean models that are not coupled to the CCM. Past and future abundances of ODSs, for CCMI-2022, are based upon

Appendix Table 6-4 of WMO (2018). For long-lived greenhouse gases (GHGs), the simulations rely upon VMRs in the historical CMIP6 database until 2014, and future VMRs from the SSP2-4.5 scenario (Meinshausen et al., 2020). Similarly, the simulations rely upon CMIP6 (historical) and SSP2-4.5 (future) emission inventories for tropospheric aerosols, as described in Table 8 of Plummer et al. (2021).

A total of 12 CCMs participating in CCMI-2022, as described in Benito-Barca et al. (2025). Table 4.1 lists the eight CCMs that have submitted REF-D2 model output for HCl, $ClONO_2$, and N_2O to the Center for Environmental Data Analysis (CEDA) archive, as of 22 April 2026. The number of REF-D2 realizations, the home institute of each model, and literature references are also given. Monthly mean, model output VMR profiles as a function pressure are cosine weighted for the 35°S to 60°S and 35°N to 60°N latitude regions, then deseasonalized on a quarterly basis. Trends are then derived from a simple linear fit to the resulting time series at each pressure level. The CCMI-2022 simulations build upon the CCMI-1 simulations utilized in Chapter 3 of the 2022 WMO/UNEP SAOD report (Dhomse et al., 2018; Morgenstern et al., 2017; WMO, 2022), as discussed in section 3.1 of Benito-Barca et al. (2025).

Table 4.1. List of the CCMI-2022 Models Used in This Study

Model	Number of Realizations	Institution	Reference
ACCESS-CM2-Chem	1	ACCESS consortium; Australia	Dennison & Woodhouse (2023)
CCSRNIES-MIROC3.2	1	NIES; Tsukuba, Japan	Akiyoshi et al. (2023)
CESM2-WACCM	3	NCAR; USA	Gettelman et al. (2019)
CMAM	3	CCCma; Canada	Jonsson et al. (2004) Scinocca et al. (2008)

EMAC	3	MESSy-Consortium; Germany	Jöckel et al. (2016)
GEOSCCM	1	NASA/GSFC; USA	Liu et al. (2022) Oman et al. (2013)
MIROC-ES2H	3	JAMSTEC, Japan	Kawamiya et al. (2020) Tatebe et al. (2019)
NIWA-UKCA	3	NIWA; New Zealand	Morgenstern et al. (2009)

4.3 Results and Discussion

4.3.1 Analysis of ACE-FTS and CCMI-2022 Profiles

Figure 4.1 compares annual average volume mixing ratio (VMR) profiles of HCl, $ClONO_2$, HCl+$ClONO_2$, and N_2O measured at 35°N to 60°N by ACE-FTS (black lines) to computed values of these quantities from the CCMI-2022 REF-D2 model simulations (various colored lines). The top panels (Fig. 4.1a-4.1d) show results for 2005 (the first full year of ACE-FTS data); the bottom panels (Fig. 4.1e-4.1h) show comparisons for 2025. The measured vertical decline of N_2O with respect to decreasing pressure at NH midlatitudes, for both 2005 and 2025, is simulated particularly well by each of the eight CCMI-2022 models. The ACE-FTS profiles of HCl and $ClONO_2$ generally fall within the range of the eight CCMI-2022 model estimates, with the notable exception of $ClONO_2$ in 2025, which has a peak value measured by ACE-FTS that is larger than the simulated peak within all of the models. For altitudes above about 10 hPa, the profile of HCl simulated by NIWA-UKCA2 exceeds measured HCl as well as the other modeled profiles. Similarly, HCl simulated by ACCESS-CM2-Chem is smaller than measured by ACE-FTS and the other models at the lowest pressures (highest altitudes). These tendencies of HCl for these two models are mirrored in the comparison for HCl+$ClONO_2$, since the VMR of $ClONO_2$

falls off at low pressure. Figure 4.2 shows comparisons for 35°S to 60°S. Here, the measured peak of $ClONO_2$ is simulated slightly better than in the NH, and the tendency of the NIWA-UKCA2 and ACCESS-CM2-Chem models to overestimate and underestimate HCl as well as $HCl+ClONO_2$, respectively, is also apparent.

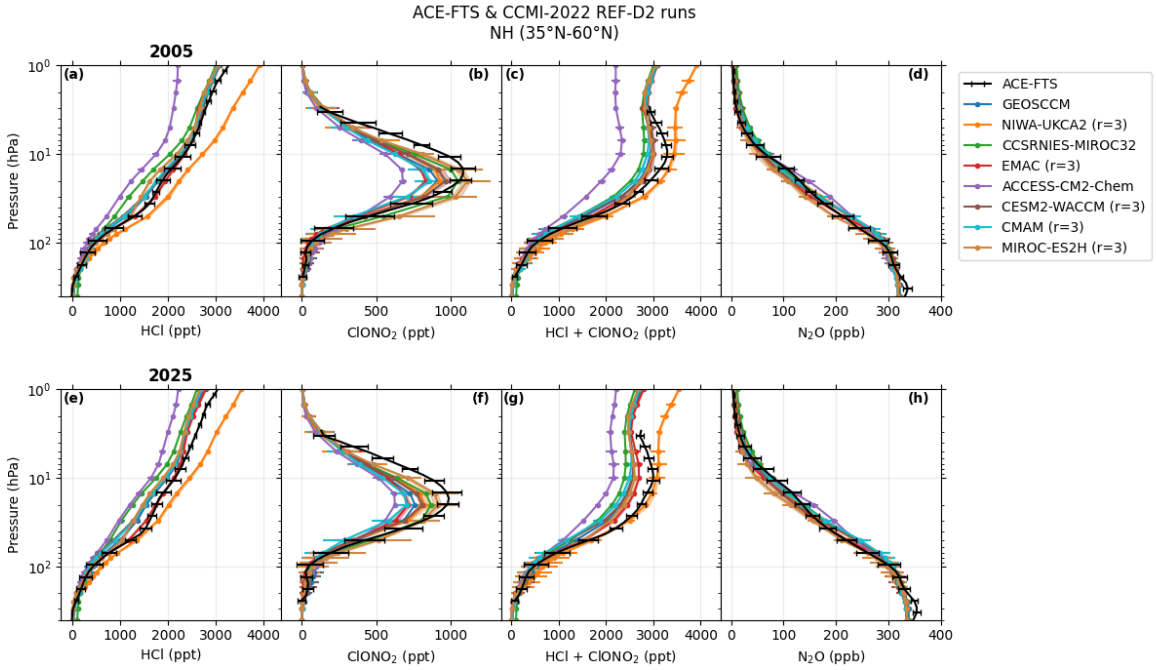


Figure 4.1. Profiles of HCl (a, e), $ClONO_2$ (b, f), $HCl+ClONO_2$ (c, g), and N_2O (d, h) for the NH midlatitudes (35°N-60°N) observed by ACE-FTS (solid black lines) and simulated in CCMI-2022 REF-D2 simulations (colored lines) during 2005 (a-d) and 2025 (e-h). Profiles derived from CCMI-2022 REF-D2 model simulations are shown in the solid blue (GEOSCCM), orange (NIWA-UKCA-2), green (CCSRNIES-MIROC32), red (EMAC), purple (ACCESS-CM2-Chem), brown (CESM2-WACCM), turquoise (CMAM), and gold (MIROC-ES2H) lines. Error bars indicate the standard deviation of the quantities at each pressure level. The number of realizations is given in parentheses after each model name, if greater than one. For models with more than one realization, the standard deviations are combined in a root-sum-of-squares fashion and the solid lines show the average of the realizations at each pressure level.

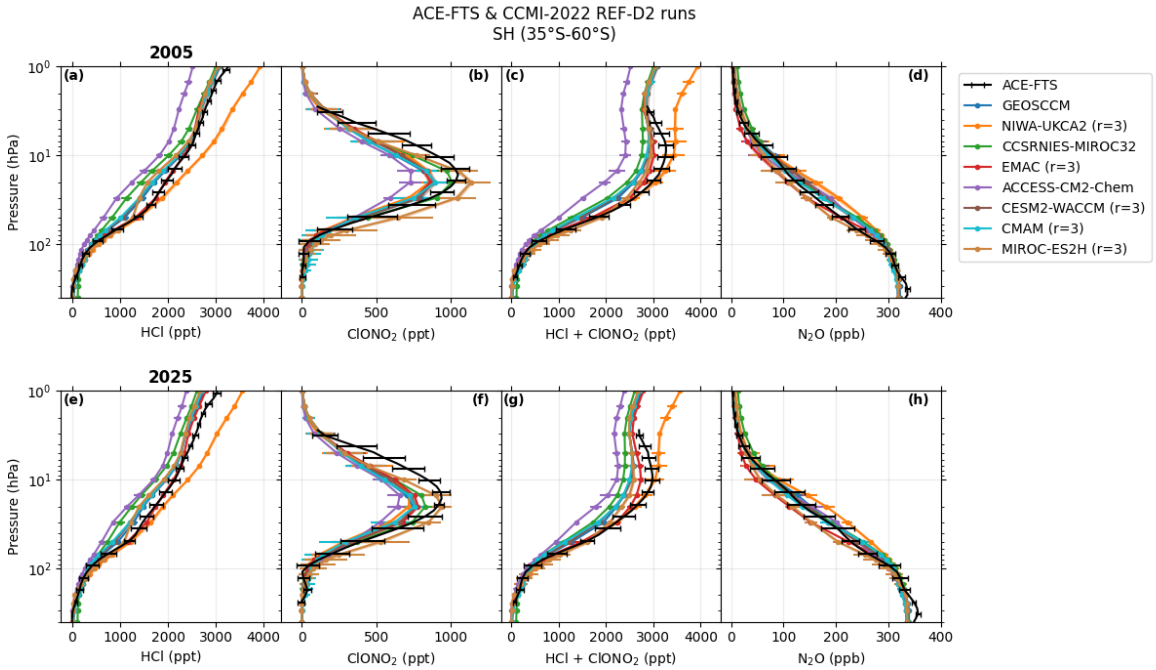


Figure 4.2. Same as Figure 4.1, except for SH midlatitudes (35°S-60°S).

Figure 4.3 shows profiles of the trends in the VMR of HCl+$ClONO_2$ and N_2O observed by ACE-FTS and computed from CCMI-2022 REF-D2 model output, for March 2004 to December 2025. The top two panels (Fig. 4.3a and 4.3b) show results for 35°N to 60°N; the bottom panels (Fig. 4.3c and 4.3d) are for 35°S to 60°S. The profiles are shown for the 100 hPa to1 hPa pressure range, to facilitate stratospheric comparisons. The horizonal blue line, placed at 30 hPa, denotes the top of the shallow branch of the BDC at midlatitudes (Birner & Bönisch, 2011; Diallo et al., 2019; Ploeger & Garny, 2022). The vertical, dashed blue line on Figs. 4.3b and 4.3d denotes the 3%/decade increase in surface N_2O over 2004 to 2025, based on a linear fit to globally averaged surface VMRs of N_2O provided by the NOAA Global Monitoring Laboratory (GML) (Lan et al., 2026).

The observed decline in the VMR of HCl+$ClONO_2$ observed by ACE-FTS at NH midlatitudes, over 2004 to 2025, is notably smaller than simulated by seven of the eight CCMI-2022 models (Fig. 4.3a). The notable exception is ACCESS-CM2-Chem, which simulates a

smaller than observed decline for altitudes above ~20 hPa. The observed change in the VMR of N_2O at NH midlatitudes exhibits the unusual characteristic in that, for altitudes above 10 hPa (i.e., the upper stratosphere), the rise of N_2O is substantially faster than found by any of models, whereas for altitudes below about 30 hPa, observed N_2O exhibits a slight decline, whereas the models project a rise close to the surface N_2O trend. We next discuss the lower (p > 30 hPa) and upper (p < 30 hPa) branches of the BDC in the NH, before turning attention to the SH.

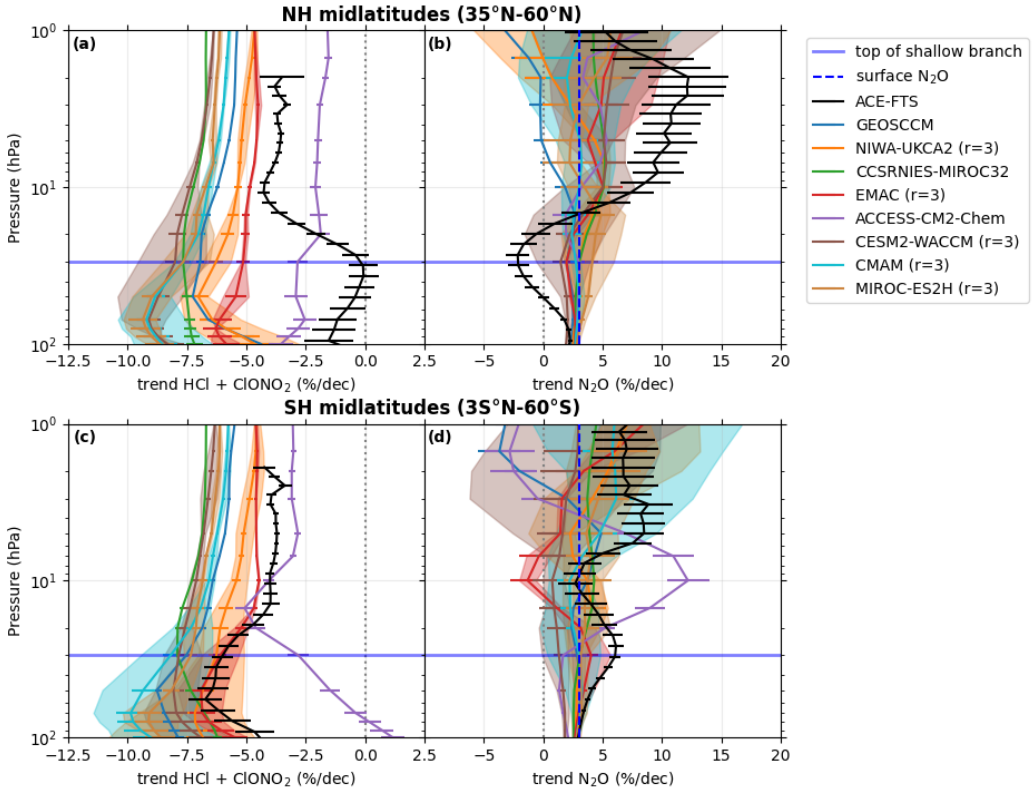


Figure 4.3. Trends in HCl+$ClONO_2$ (a, c) and N_2O (b, d) for the NH midlatitudes (35°N-60°N) (a, b) and the SH midlatitudes (35°S-60°S) (c, d) shown as a function of pressure for the 2004−2025 period. Linear trends are calculated from deseasonalized quarterly time series weighted by cosine latitude. The error bars for each of the trend lines show the standard error of the slope. Trends derived from ACE-FTS retrievals are shown in black. Trends derived from CCMI-2022 REF-D2 model simulations are shown in the solid blue (GEOSCCM), orange (NIWA-UKCA-2), green (CCSRNIES-MIROC32), red (EMAC), purple (ACCESS-CM2-Chem), brown (CESM2-WACCM), turquoise (CMAM), and gold (MIROC-ES2H) lines. For models with more than one realization, the solid lines represent the average of the realizations, and the shading represents the minimum and maximum of the realizations at each altitude. The standard errors for models with more than one realization are combined in a root-sum-of-squares fashion (error bars). The top of the shallow branch of the BDC (30 hPa) is represented by the horizontal blue line. Global mean surface N_2O has risen in a near linear fashion, with a growth rate of 3 % / decade, over 2004 to 2025, depicted by the dashed vertical line in panels (b) and (d).

Throughout the shallow branch of the BDC (p > 30 hPa) in the NH, ACE-FTS data show either a decline in the VMR of N_2O or a rise that is slower than the 3%/decade rise of surface N_2O (Fig. 4.3b). This observation is indicative of an enhancement in the downwelling component of the residual circulation, or slower meridional transport by the shallow branch of the BDC (Han et al., 2019; Krysztofiak et al., 2023). This dynamical tendency results in the transport of more photochemically aged air to altitudes below 30 hPa over time, resulting in a markedly slower rise in the VMR of N_2O compared to the 3%/decade rise in surface N_2O. Since HCl and $ClONO_2$ are produced from the photochemical destruction of ODSs, this dynamical tendency likely explains why the observed decline of $HCl+ClONO_2$ is near zero in the shallow branch of the BDC at NH midlatitudes. None of the eight CCMI-2022 models are able to reproduce this observed slight decline in $HCl+ClONO_2$, as well as the smaller than expected rising trend in N_2O.

For the upper branch of the BDC (p < 30 hPa) at NH midlatitudes, ACE-FTS data show a rise in the VMR of N_2O that is more than twice the 3%/decade rise of surface N_2O (Fig. 4.3b). Some of the CCMI-2022 models exhibit a tendency for a rise of N_2O in this geographic region that is faster than the 3%/decade rise N_2O. However, none of the models match the strength of the observed rise. Similarly, the observed decline in $HCl+ClONO_2$ in the upper branch of the NH midlatitude BDC is notably slower than the simulated by seven of the eight models (Fig. 4.3a). The observed, rapid rise of N_2O in this geographic region is indicative of enhanced poleward transport of air in the meridional branch of the residual circulation, which would result in more N_2O rich air masses being present at altitudes above 30 hPa, due to strong latitudinal gradient of N_2O above about 50 hPa (Han et al., 2019). This same transport change would also result in the transport of air with higher fractions of organic chlorine relative to inorganic chlorine, since the

photochemical loss the CFC-11 and CFC-12 exhibits a dependence on altitude and latitude that is similar to that of N_2O (Han et al., 2019; Minschwaner et al., 1993). Even though the observed decline in $HCl+ClONO_2$ is smaller than found by seven of the eight models for this region, the difference between the observed and modeled trends of $HCl+ClONO_2$ is not nearly as large as found in the shallow branch of the BDC.

We now turn attention to the SH. The observed rise in N_2O is close to the 3%/decade rise in surface N_2O for the shallow branch of the BDC ($p > 30$ hPa), a feature that is simulated fairly well by all of the models (Fig. 4.3d). This behavior is indicative of no major changes in the transport characteristics of the SH midlatitude BDC, over the 2004 to 2025 time period. Excluding results from the ACCESS-CM2-Chem model, which provides a trend for $HCl+ClONO_2$ that differs considerably than that found by the other models for the shallow branch of the BDC in the SH, the observed decline in $HCl+ClONO_2$ is close to the smallest absolute value of the decline simultaneously by the other seven models (Fig. 4.3c). The ACCESS-CM2-Chem simulates very small changes in $HCl+ClONO_2$ in this geographic region, for reasons that are not understood.

For the upper branch of the BDC ($p < 30$ hPa) at SH midlatitudes, ACE-FTS N_2O exhibits a rise that is somewhat faster than the 3%/decade rise of surface N_2O (Fig. 4.3d). Here, the observed rise in the VMR of N_2O lies well within the variability of the CCMI-2022 model values. The observed decline in $HCl+ClONO_2$ lies close to the smallest absolute value of declines found by the various models (Fig. 4.3c).

We now turn our attention to the multi model mean (MMM) of trends in $HCl+ClONO_2$ and N_2O at midlatitudes. Figure 4.4 is similar to Figure 4.3, except the solid line shows the MMM of the trends based on the average of the 18 realizations from the eight CCMI-2022

models. Error bars show the standard deviation (σ) of the trends. The data shown in Figure 4.4 (black solid line) is identical to that shown in Figure 4.3. However, for Figure 4.4, we also include an adjustment to the observed trend in $HCl+ClONO_2$ caused by VSL-Cl. As described in Section 4.2, this adjustment is based upon a profile for the AoA from Saunders et al. (2025) that is an average of conditions from 2004 to 2021, as well as a computed time series for the total Cl injection into the stratosphere from four VSL-Cl species (Bednarz et al., 2022). The MMM trend of N_2O over 2004 to 2025 from the eight models lies extremely close to the blue dashed line that marks the surface trend for N_2O, for both the shallow and deep branches of the BDC, at midlatitudes in both hemispheres (Figs 4.4b and 4.4d). Consequently, on average, the CCMI-2022 models show no change in the strength of the BDC. This finding is especially important, given the reliance on MMM estimates of trends in total column ozone (Dhomse et al., 2018; Keeble et al., 2018; Oman et al., 2010a; Weber et al., 2022). Some of the individual realizations of the CCMI-2022 model runs do exhibit large variations for the trend in N_2O, which in some cases either approach or encompass the vertical structure that is measured by ACE-FTS (Fig. 4.3b and 4.3d). The reasons for the success of some of these realizations, and the consequences for computed trends in total column ozone from these specific model runs, are outside the scope of this analysis.

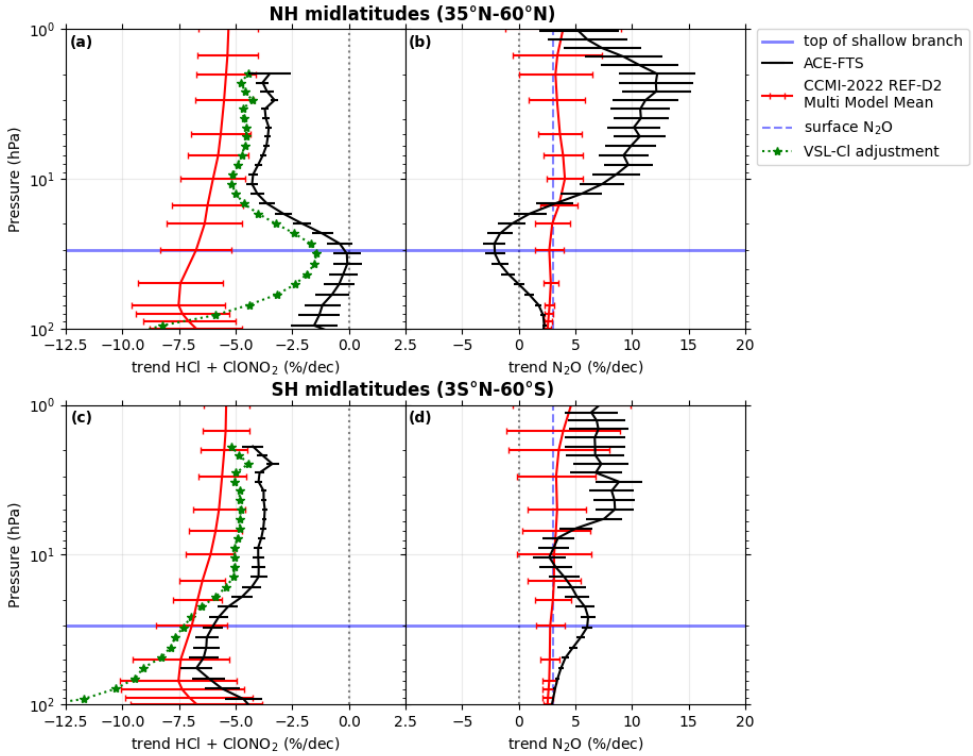


Figure 4.4. Same as for Figure 4.3, except here the red lines and error bars show the average and standard deviation of $HCl+ClONO_2$ (a, c) and N_2O (b, d) trends from the 18 model realizations of the CCMI-2022 model runs (Table 4.1). Here, if a model submitted more than one realization, the results for that model are averaged, before forming the multi model mean (MMM). The green line (star markers and dotted lines) in panels (a) and (c) represent an adjustment to the $HCl+ClONO_2$ trend (black lines) to remove the possible influence of VSL-Cl, as described in Section 4.2.

For the upper branch of the BDC in the NH, ACE-FTS shows a much faster rise in N_2O than is found by the MMM (Fig. 4.4b). As noted above, the data suggest enhanced poleward transport of air in the meridional branch of the residual circulation that is not apparent in the MMM profile. This dynamical tendency should cause a response to the trend in $HCl+ClONO_2$ that is of opposite sign as the trend in N_2O, particularly between 70 to 10 hPa, as explained above and shown in figure 2 of Han et al. (2019). For altitudes above 10 hPa, our analysis of ACE-FTS data (not shown) reveals a breakdown in the correlation of N_2O and $HCl+ClONO_2$, likely due shorter photochemical lifetimes and differences in geographic variation of chemical loss of N_2O and ODSs in the upper stratosphere (Han et al., 2019). The measured trend in N_2O crosses the MMM trend at about 15 hPa (Fig. 4.4b). For altitudes below 20 hPa in the NH, which

includes all of the shallow branch of the BDC as well as a small portion of the upper branch, the measured rise in N_2O is slower than the MMM value, whereas the measured decline in $HCl+ClONO_2$ is considerable larger than the MMM trend. The CCMI-2022 models exhibit a decline in $HCl+ClONO_2$ of about 7.5%/decade over 2004 to 2025, which is much smaller than the observed decline that lies between 0 and 4%/decade. These differences exhibit the expected opposite sign, which means that if the models were able, on average, to better simulate the observed change in N_2O, it is likely that there would be closer agreement with the measured trend in $HCl+ClONO_2$ at these lower altitudes. For the SH, the MMM trends in N_2O lie much closer to the observed trends in these quantities, throughout both branches of the BDC. As others have noted, there is evidence for stronger systematic changes in the strength of the BDC in the NH compared to SH (Ball et al., 2019; Benito-Barca et al., 2025; Dubé et al., 2023; Han et al., 2019; Weber et al., 2022).

For the NH, the MMM trend of $HCl+ClONO_2$ shows a much stronger decline, at all pressures, than the trend observed by ACE-FTS (Fig. 4.4a). For the SH, the MMM trend of $HCl+ClONO_2$ is larger than the observed decline, with some overlap between the standard deviation of the MMM and the ACE-FTS data (Fig. 4.4c). As noted in Section 4.2, the models were constrained using the WMO (2018) A1 scenario for the 16 principal ODSs. The value of chorine contribution to EESC for 3-year-old air in December 2025 found using the WMO (2022) baseline scenario for these 16 ODS is 1090.98 ppt, which is 0.77% larger than the value of 1082.61 ppt found using the 2018 A1 scenario. Consequently, we estimate that the use within the models of a faster decline in ODSs inherent in the 2018 A1 scenario, compared to the 2022 update, plays a minor role in the stronger modeled decline in $HCl+ClONO_2$ compared ACE-FTS data.

The possible impact of VSL-Cl on $HCl+ClONO_2$ is of particular importance. Upon adjustment for the influence of VSL-Cl on the measured trend in $HCl+ClONO_2$ (green symbols and line), the ACE-FTS data lie close to the MMM plus 1σ trend for altitudes above ~15 hPa (about 30 km) in both hemispheres (Fig. 4.4a and 4.4c). For the shallow branch of the BDC in the SH, the VSL-Cl adjustment generally lies within the range of the MMM and MMM minus 1σ value of the trend (Fig. 4.4c). Consequently, it is possible that part of the MMM shortcoming in the modeled trend for $HCl+ClONO_2$ is caused by the neglect of these unregulated, anthropogenic halogen compounds in the models. This finding is similar to conclusions reached by Hossaini et al. (2019) and Dubé et al. (2025a) based on their analysis of ACE-FTS trends in HCl compared to simulations from a chemical transport model, as well as Bednarz et al. (2022) who also analyzed trends in ACE-FTS compared to output from earlier runs of the UM-UKCA CCM.

Theory and observation of trends in $HCl+ClONO_2$ and N_2O are generally in better agreement for the SH, midlatitude stratosphere compared to the NH. The one exception is that near ~100 hPa in the SH, the VSL-Cl adjustment falls outside the MMM minus 1σ value of the trend (Fig. 4.4c). For shallow branch of the BDC in both the NH and SH, the VSL-Cl adjustment exhibits a strong dependence on pressure that is not reflected in the pressure dependence of the difference between the observed and MMM value of the trend in $HCl+ClONO_2$. At the lowest altitudes (near ~100 hPa), the VSL-Cl adjustment is subject to a high degree of uncertainty due to variations in transport time to the lower stratosphere (Hossaini et al., 2019) as well as the latitudinal gradient in the surface abundance of VSL-Cl gases that could cause us to overestimate the contribution of VSL-Cl species at midlatitudes of the SH (Bednarz et al., 2022), particularly for the lowermost stratosphere that is chemically influenced by overshooting convection (Howar

et al., 2025; Liang et al., 2025; Pan et al., 2024; Poulida et al., 1996). Recently, Pan et al. (2024) showed the stratospheric injection of large amounts of VSL-Cl by the Asian Summer Monsoon (ASM), including an important contribution from 1,2-dichloropropane ($C_3H_6Cl_2$) that to our knowledge has not yet been considered in any global model. The contribution of $C_3H_6Cl_2$ to the total stratospheric chlorine burden is uncertain, given its short photochemical lifetime of ~20 days (Perry et al., 1977) and a scarcity of UTLS observations of this compound. Finally, the model output from Bednarz et al. (2022) that drives our analysis is for the tropical TTL (Fueglistaler et al., 2009). We have assumed stratospheric injection of the full complement of product and source gases they calculated to be present in the tropical TTL. Removal of product gases by washout near the tropopause is possible (e.g., Fernandez et al., 2021) and could affect our estimate of VSL-Cl. Clearly, more work is needed to properly quantify the role of VSL-Cl species in resolving some the tendency for modeled HCl+$ClONO_2$ to decline more quickly than measured by ACE-FTS.

Between 20 hPa and 70 hPa in NH midlatitudes, where the concentration of O_3 is largest, a large discrepancy remains between the modeled and measured trend in HCl+$ClONO_2$, even upon accounting for the possible influence of VSL-Cl (Fig. 4.4a). The large magnitude of this gap suggests that changes in stratospheric transport have exerted a dominate influence on the tendency for the observed trend in HCl+$ClONO_2$ to lie far below the modeled trends in HCl+$ClONO_2$. The chlorine content of the stratosphere had been expected to decline from March 2004 to December 2025 due to the observed decrease in chlorine content of tropospheric ODSs brought about by the Montreal Protocol (e.g., figure 6 of Lickley et al., 2024), which is the factor driving the modeled trends. The atmospheric abundance of minor CFCs such as CFC-13 ($CClF_3$), CFC-112a ($C_2Cl_4F_2$), CFC-113a ($C_2Cl_3F_3$), and CFC-114a (C2Cl2F4) has risen over the

past decade, likely due to inadvertent release in the manufacturing process of HFCs (Western et al., 2025). These species are not included as input to the CCM simulations or our calculation of EESC. However, the increase in the abundance of these gases is much smaller than the difference between the modeled and measured trend in HCl+$ClONO_2$ below about 20 hPa shown in Fig. 4.4a. Since these species have long stratospheric lifetimes (Tuffnell et al., 2026), their possible impact would be at higher stratospheric altitudes (e.g., Fernandez et al., 2021).

4.3.2 Analysis of Jungfraujoch Columns

Analysis of trends in the total column inorganic chlorine and fluorine above Jungfraujoch research station (46.54°N, 7.98°E), measured using a ground-based FTIR instrument, have been a central element of recent SAOD assessment reports. Figure 4.5a shows the observed trend in column HCl, $ClONO_2$, and their sum (HCl+$ClONO_2$, denoted total Cl) over this research station. Data shown are means from June to November, to mimic the analysis method used in recent SAOD reports. As noted in Section 4.2.2, these months were chosen to limit the effect of stratospheric transport on the analysis.

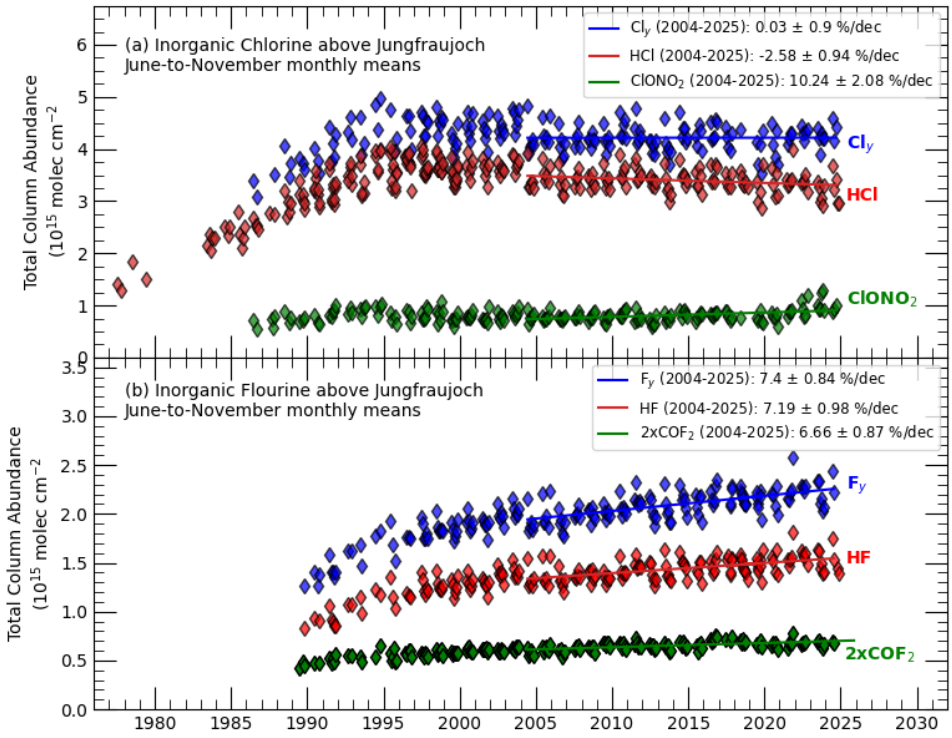


Figure 4.5. Time series of June-to-November monthly mean total column abundances of inorganic chlorine (a) and inorganic fluorine (b) measured by NDACC ground-based FTIR over Jungfraujoch, Switzerland. Panel (a) shows total column abundances of HCl+$ClONO_2$ (Cl_y) (blue diamonds), HCl (red diamonds), and $ClONO_2$ (green diamonds). The linear trend lines for Cl_y, HCl, and $ClONO_2$ for the 2004 to 2025 time period are shown in solid blue, red, and green lines, respectively, with numerical values of the slopes and the standard error of the slopes given in the caption. Panel (b) shows total column abundances of HF+2×COF_2 (F_y) (blue diamonds), HF (red diamonds), and 2×COF_2 (green diamonds). The linear trends in F_y, HF, and 2×COF_2 for the 2004 to 2025 time period are shown in solid blue, red, and green lines, respectively.

The concentration of HCl+$ClONO_2$ measured by ACE-FTS in 2025 peaks at ~50.6 hPa (~20.5 km). Section 1.4.1.2 of Laube et al. (2022) ascribed a 4-year AoA to the analysis of time series of total column HCl+$ClONO_2$, associated with this peak altitude for HCl+$ClONO_2$. Based upon our examination of the Cl content of EESC over the 2004 to 2025 time period due to ODSs, we estimate that column HCl+$ClONO_2$ should have declined by 7.13 ± 0.06 %/decade for 3-year-old air, and by 5.98 ± 0.04 %/decade for 5.5-year-old air. Clearly, total column inorganic chlorine is not declining nearly as quickly as expected over Jungfraujoch research station based on this simple analysis. Dubé et al. (2025a) reached a similar conclusion based on analysis of this dataset, over the 2004 to 2020 time period. The discrepancy between the observed and expected

decline in chlorine over Jungfraujoch has grown, over time, due to the observed recent rise in $ClONO_2$ readily apparent in Figure 4.6a.

From 2004 to 2025, total Cl increased by 0.03 ± 0.9 %/decade based on the slope of the linear least squares fit to the data. Interestingly, column HCl has declined by 2.58 ± 0.94 %/decade whereas column $ClONO_2$ has risen by 10.24 ± 2.08 %/decade. It is not clear why column $ClONO_2$ has risen during a time when column HCl has declined. The concentration of $ClONO_2$ peaks at a higher altitude (~22.5 km & 36.9 hPa) than the peak concentration of HCl (~20.5 km & 50.6 hPa). Therefore, the supply of stratospheric Cl from VSL-Cl species would be expected to have exerted a larger impact on trends in column HCl compared to trends in column $ClONO_2$. Regardless, the recent slight decline in HCl is much smaller than the expected 7.13 ± 0.06 %/decade and 5.98 ± 0.04 %/decade declines expected for 3-year-old and 5.5-year-old air.

Figure 4.5b shows total column HF, COF_2, and HF+2×COF_2 over Jungfraujoch. The trend in HF+2×COF_2, termed total F, is increasing a rate of 7.4 ± 0.8 %/decade. Importantly, hydrofluorocarbons (HFCs) in addition to ODSs contribute to the rising atmospheric burden of total F in the stratosphere.

The challenge in analyzing trends in total Cl is the possible influence of dynamical variability. Chapter 1 of WMO (2022) (Laube et al., 2022) limited the analysis of Jungfraujoch data to June through November to "limit the variability caused by atmospheric and subsidence during winter and spring". Here, we suggest a further way to remove the dynamical influence on the ground-based measurement of total Cl. Since the shape of the vertical profile of the concentration of HCl+$ClONO_2$ is nearly identical to the shape of the concentration of HF+2×COF_2 (Figure 4C.6), vertical motions should induce a change in total Cl that is similar to the dynamically induced change in total F. Consequently, the ratio of (total Cl) / (total F) should

mainly reflect chemical rather than dynamical influences. The correction for stratospheric, dynamical influence using ground-based measurements of total F builds upon the work of Wunch et al. (2010), who divided total column abundances of CO_2, CH_4, and N_2O measured by the Total Carbon Column Observing Network by total column HF.

Figure 4.6a shows (total Cl) / (total F) measured since 1986 over Jungfraujoch. Hereafter, we refer to this quantity as total_Cl_F. Figure 4.6b shows total_Cl_F measured by ACE-FTS, between 40^{o}N and 50^{o}N, since 2004. Figure 4.6 also includes estimated values of total_Cl_F we have found by considering the chlorine and fluorine contributions to EESC for 3- and 5.5-year-old air (Section 4.2.3), then interpolating these values to the AoA associated with the altitude of peak concentration of HCl+$ClONO_2$ measured by ACE-FTS between 40^{o}N and 50^{o}N (Figure 4C.7a). In this analysis, the total fluorine contribution to EESC includes the 12 principal ODSs that contain a fluorine atom, plus contributions from HFC-134a, HFC-32, HFC-125, and HFC-245fa (Section 4.2). The time series for AoA used in Figure 4.6 is based on a linear fit to monthly mean AoA computed using the convolution method outline in Garny et al. (2024), applied to ACE-FTS measurements of SF_6 (Figure 4C.7b).

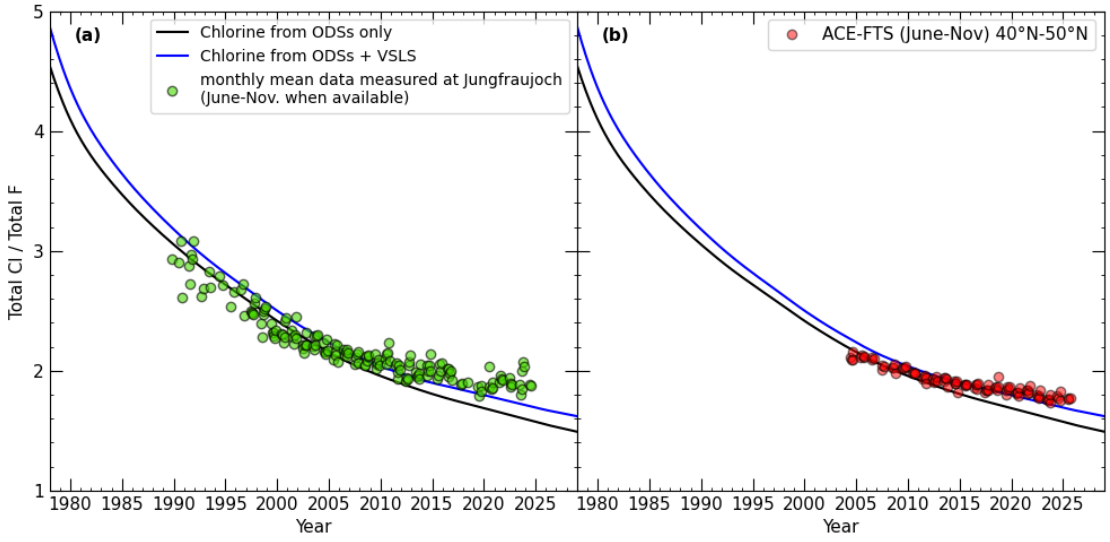


Figure 4.6. Time series of the ratio of total column chlorine ($HCl + ClONO_2$) to total column fluorine ($HF + 2xCOF_2$) observed by ground-based NDACC FTIR stationed at Jungfraujoch, Switzerland (46.54°N, 7.98°E) (Mahieu et al., 2014) (green markers, panel a) and observed by ACE-FTS in the 40°N−50°N latitude space in which Jungfraujoch resides (red markers, panel b). The black and blue curves show EESC determined from ODSs only, and EESC determined from ODS and VSL-Cl.

The observed time series of total_Cl_F measured over Jungfraujoch and by ACE-FTS are matched much better by the theoretical curve that includes VSL-Cl, compared to the curve that only allows for only the influence of long-lived ODSs. The growing influence of VSL-Cl over time, apparent in Figure 4.6, is caused by the steady recent growth of VSL-Cl over the past decade (Figure 4C.1). Our simple correction for the theoretical influence of VSL-Cl exhibits particularly strong agreement with the ACE-FTS measurement of total Cl_F (Fig. 4.6b). The gap between computed total_Cl_F without consideration of VSL-Cl and the Jungfraujoch time series, which grows appreciably since about 2010, is significantly reduced when VSL-Cl is added to our calculation.

We conclude by noting that a long time series for total_Cl also exists over Lauder, New Zealand (45.05°S, 169.67°E). However, this station does not report time series of COF_2, which prevents an empirical adjustment using total_F. While it would be advantageous to examine total_Cl from the CCMI-2022 models, these current runs do not archive model output for HF and

COF_2. The upcoming VSLS-MIP sponsored by the Atmosphere Processes and their Role in Climate (APARC), which will include extensive treatment of five anthropogenic VSL-Cl species CH_2Cl_2, $CHCl_3$, C_2Cl_4, and $C_2H_4Cl_2$ that have been discussed above, plus trichloroethylene: C_2HCl_3 (Hossaini et al., 2024a). This effort will provide an opportunity for robust evaluation of our suggestion of the importance of VSL-Cl in closing the gap between measured and modeled total_Cl at Jungfraujoch. These comparisons would be even more valuable if the most important HFCs for the stratospheric fluorine budget, such as HFC-134a, HFC-125, HFC-143a, and HFC-32 (Table 4C.2), were included as model inputs for these upcoming simulations.

4.4 Concluding Remarks

We compare temporal trends in ACE-FTS profiles of $HCl+ClONO_2$ and N_2O to output from the eight CCMs that submitted results for the REF-D2 (1960 to 2100 time period) simulation for the CCMI-2022 modeling initiative, for midlatitudes of the NH (35ºN to 60ºN) and SH (35ºS to 60ºS). We also compare calculated and measured total $HCl+ClONO_2$ (total Cl) and total $HF+2\times COF_2$ (total F) abundances over Jungfraujoch research station (46.54°N, 7.98°E). Here, the modeled curves are based on the chlorine and fluorine content of EESC for the 3-year-old and 5.5-year-old air masses (Engel et al., 2018; Dubé et al., 2025a).

All of these comparisons are motivated by the tendency for the observed recovery of the stratospheric ozone profile in the lower stratosphere, over the 1998 to 2018 time period (Benito-Barca et al., 2025) and the 2000 to 2024 time period (Sofieva et al., 2026), to significantly lag the simulated increase by CCMs due to declining total chlorine content of ODSs measured at the surface. The discrepancy between the modeled and observed recovery of stratospheric ozone at midlatitudes is particularly acute in the NH (Benito-Barca et al., 2025; Sofieva et al., 2026). This tendency for the recovery of total column ozone to lag the modeled increase due to the expected

decline in stratospheric halogen loading was a central element of the 2022 WMO/UNEP Scientific Assessment of Ozone Depletion (SAOD) report (WMO, 2022; Weber et al., 2022). As shown in figure 1 of Benito-Barca et al. (2025), observations show a decline in the partial column abundance (PCA) of ozone over NH midlatitudes from 1998 to 2018, whereas output from the CCMI-1 model runs used for the 2022 SAOD as well as the REF-D2 simulation conducted for the 2026 SAOD all show increases in the PCA of ozone for this region, over the same time period.

The comparisons of measured and modeled trends of $HCl+ClONO_2$ and N_2O are conducted for the deep ($p < 30$ hPa) and shallow ($p > 30$ hPa) branches of the BDC in both hemispheres (Birner and Bonisch, 2011; Diallo et al., 2019; Ploeger & Garny, 2023). Furthermore, we analyze trends in N_2O relative to the 3%/decade increase in globally averaged surface N_2O over 2004 to 2025 measured by NOAA GML (Lan et al., 2026). If stratospheric transport were unchanged over the two-decades of the ACE-FTS data, then the trend in stratospheric profiles of N_2O would match this rise of surface N_2O (Dubé et al., 2023; Krysztofiak et al., 2023). The MMM of the CCMI-2022 output of profiles of N_2O lies close to this 3%/decade rise throughout the upper and shallow branch of the BDC at midlatitudes of both hemispheres, indicating that on average the CCMI-2022 model simulations show no significant change in the strength of the BDC. This result is especially important because analysis of MMM trends in O_3 from these models is the central element of the theoretical understanding of ozone depletion and recovery used in the WMO/UNEP SAOD reports. Finally, we assess the importance of VSL-Cl compounds, which are not regulated by the Montreal Protocol (Hossaini et al., 2017, 2019, 2024; Raymond et al., 2026) and are also not included in the CCMI-2022 simulations (Plummer et al., 2021; Benito-Barca et al., 2025; Sofieva et al., 2026), on the

difference between modeled and measured $HCl+ClONO_2$. The contribution of VSL-Cl species to stratospheric chlorine has risen considerably over the two-decade long period of observation (Dubé et al., 2025a; Bednarz et al., 2022).

The change in the VMR of N_2O observed by ACE-FTS at NH midlatitudes, over 2004 to 2025, exhibits a sharp variation with respect to pressure. Above about 10 hPa, the rise of N_2O is substantially faster than both the rise in stratospheric N_2O found by any of the models as well as the 3%/decade rise in surface N_2O. The ACE-FTS data suggest enhanced poleward transport of air in the meridional component of the residual circulation for the highest levels of the upper branch of the BDC. Conversely, altitudes below about 20 hPa, the ACE-FTS observed rise of N_2O is considerably slower than that found by any of the models as well as the 3%/decade rise in surface N_2O. For the shallow branch of the BDC in the NH, the ACE-FTS measurements of stratospheric N_2O suggest either an enhancement in the downwelling component of the residual circulation or a slowdown of meridional transport, over the two-decade period of observation. This pattern for the change in the strength of the BDC at NH midlatitudes is similar to that found in prior analyses (Han et al., 2019; Krysztofiak et al., 2023; Dubé et al., 2025b). Han et al. (2019) show that trends in N_2O, CH_4, and HCl observed by MLS are consistent with enhanced downwelling in NH midlatitudes, a weakening of the NH shallow branch, and a strengthening of the NH deep branch, similar to our findings from ACE-FTS data. Here, we extend the analysis of ACE-FTS data to the end of 2025 and compare measured trends in N_2O to output of the latest set of runs by eight CCM groups.

For the shallow branch of the BDC at SH midlatitudes, the observed increase in N_2O is close to the 3%/decade rise of surface N_2O. This behavior is simulated rather well by the CCMI-2022 models. Consequently, our analysis supports the prevailing view of no major changes in the

strength of the shallow branch of the BDC in the SH (e.g., Dubé et al., 2025b). For the upper branch of the BDC at SH midlatitudes, the rise in N_2O measured by ACE-FTS is somewhat faster than the 3%/decade rise in surface N_2O. The ACE-FTS trend in N_2O for this region lies well within the variability of the various CCMI-2022 model realizations.

The observed decline in the VMR of HCl+$ClONO_2$ observed by ACE-FTS at NH midlatitudes, over 2004 to 2025, is notably smaller than the decline that is simulated by seven of the eight CCMI-2022 models. The exception is ACCESS-CM2-Chem, which simulates a smaller decline in HCl+$ClONO_2$ than is found by the other CCMs, for reasons that are not currently understood. We show that the neglect of VSL-Cl species by the CCMI-2022 models could explain a significant part of the slower than expected decline of stratospheric HCl+$ClONO_2$, especially for altitudes above ~15 hPa. For the SH, the MMM of the CCMI-2022 trend in HCl+$ClONO_2$ exhibits a larger decline than observed by ACE-FTS, over the entire 100 hPa to 1 hPa pressure range. Consideration of the possible impact of VSL-Cl species resolves a considerable portion of this difference throughout the midlatitudes of the SH. However, as discussed in Section 4.3.1, there is considerable uncertainty associated with our adjustment for the possible impact of VSL-Cl on this comparison, particularly for the SH.

Total Cl over the NH, midlatitude Jungfraujoch research station is not declining as quickly as expected. Our linear least squares analysis of data collected between the months of June to November reveals a slight rise in total Cl of 0.03 ± 0.9 %/decade between 2004 to 2025. This observation starkly contrasts the expected 5 to 6 %/decade decline in total Cl over this time period. We suggest that analysis of the ratio of total Cl divided by total F over Jungfraujoch could remove the influence of changes in stratospheric transport on HCl and $ClONO_2$, since ACE-FTS profiles of the concentration of HCl+$ClONO_2$ exhibit a variation with respect to

altitude that has a similar shape to the concentration of HF+2×COF_2 at NH midlatitudes. Ground-based observations of this ratio over Jungfraujoch, termed total_Cl_F, are simulated quite well by a calculation that accounts for the impact of VSL-Cl gases on the stratospheric chlorine budget. We also present observations of total_Cl_F from ACE-FTS that are simulated exceptionally well by this same calculation. An important component of this calculation is the estimate of contributions to stratospheric fluorine due to the decomposition of HFCs, in addition to ODSs.

The most important unresolved aspect of this study is the large difference between the observed and modeled values of trends in HCl+$ClONO_2$ throughout the midlatitude NH stratosphere, at altitudes below about 20 hPa. The CCMI-2022 models exhibit a decline in HCl+$ClONO_2$ of about 7.5%/decade over 2004 to 2025, which is much larger than the observed decline that lies between 0 and 4%/decade. This mismatch between measured and modeled HCl+$ClONO_2$ is apparent both for individual realizations from the CCMI-2022 models (Fig. 4.3a) as well as the MMM value (Fig. 4.4a). We suggest this unresolved difference warrants further research by the atmospheric science community. If this difference is due to some sort of systematic change in stratospheric transport that is driven either by rising GHGs or some other non-ODS related forcing, this tendency is not simulated by any of the eight CCM models that have submitted output of HCl, $ClONO_2$, and N_2O for the REF-D2 run of CCMI-2022. It is incumbent on the community to continue to assess and quantify the dramatic differences in the observed and modeled trends of HCl+$ClONO_2$ for the shallow branch of the BDC in the NH, and to also quantify the implications for trends in current trends of total column ozone as well as the future projected recovery of column ozone at NH midlatitudes.

Appendix C

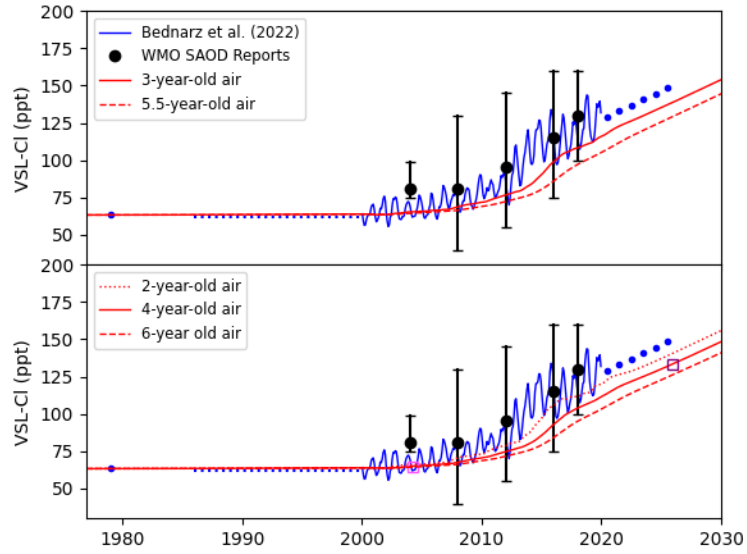


Figure 4C.1. Monthly mean time series of the stratospheric injection of chlorine (Cl_{TOT}) from product gas injection (PGI) + source gas injection (SGI) of the four VSL-Cl compounds (CH_2Cl_2, $CHCl_3$, C_2Cl_4, $C_2H_4Cl_2$) for 17 km, 25°S to 25°N, found from Bednarz et al. (2022) for the 2000-2020 time period (blue lines, panels a and b). We assume a constant annual mean value of 62.3 ppt for years prior to 2000, which is the annual mean from Bednarz et al. (2022) for 2000, and a constant growth rate of 3.8 ppt/yr of VSL-Cl (Hossaini et al., 2019) for the 2020-2025 time period (blue dotted lines). The solid and dashed red lines in panel (a) show an estimated time series of VSL-Cl in the stratosphere for AoAs of 3 and 5.5 years, respectively. The dotted, solid, and dashed red lines in panel (b) show estimated time series of stratospheric VSL-Cl for AoAs of 2, 4, and 6 years, respectively. The filled purple squares in panel (b) show VSL-Cl content of 4-year-old air in March 2004 and December 2025, respectively. The black circles with error bars show the estimated best value and range of uncertainty for Cl_{TOT} due to PGI and SGI from the last four WMO/UNEP SAOD reports.

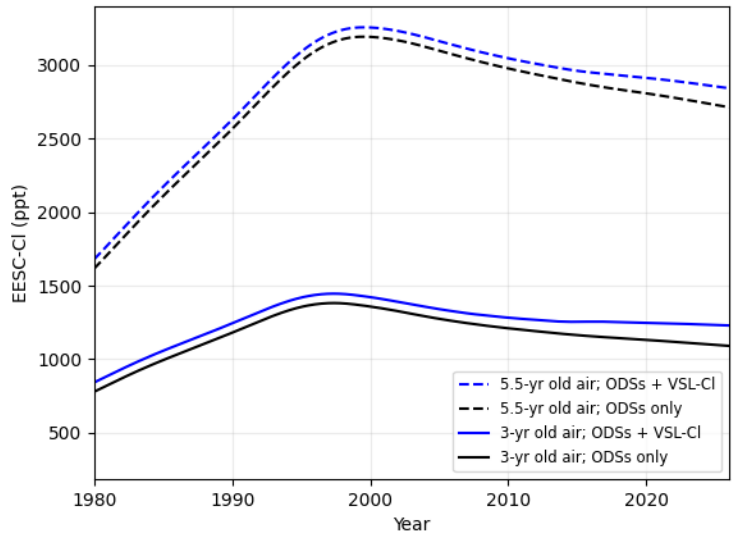


Figure 4C.2. Chlorine contribution to EESC (EESC-Cl), from ODSs (black lines) as well as ODSs and VSL-Cl (blue lines), for 3-year (solid lines) and 5.5-year-old air masses (dashed lines).

Table 4C.1. Contribution of VSL-Cl to stratospheric chlorine as a function of age of air.

Age of Air (AoA)	VSL-Cl contribution
0.0	80.39
1.0	77.57
2.0	74.84
3.0	71.65
4.0	68.50
5.0	65.24
6.0	61.87
7.0	58.44
8.0	55.03
9.0	51.69
10.	48.48

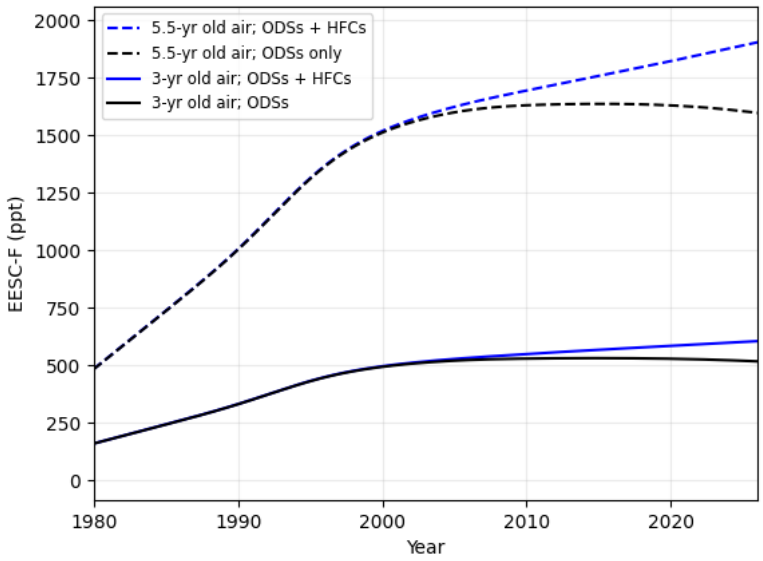


Figure 4C.3. Fluorine contribution to EESC (EESC-F), from ODSs (black lines) as well as ODSs and HFCs (blue lines), for 3-year (solid lines) and 5.5-year-old air masses (dashed lines).

Table 4C.2. The 2024 annual mean surface abundance, total fluorine content, stratospheric lifetime, Fractional Release Factor (FRF), and mean release time ($\Gamma^{\#}$) for HFCs measured by the AGAGE network. The stratospheric lifetimes are from the Annex of the 2022 WMO/UNEP SAOD report (Burkholder and Hodnebrog, 2023). Values of FRF and $\Gamma^{\#}$ are based on quadratic least squares fits to values of FRFs and $\Gamma^{\#}$ for ODS, obtained from Engel et al. (2018) and shown in Figures 4C.4 and 4C.5.

Species	2024 surface		Stratospheric Lifetime (yrs)	FRF		Mean Release Time ($\Gamma^{\#}$)	
	VMR (ppt)	F-Content (ppt)		3yr	5.5yr	3yr	5.5yr
HFC-134a (CH_2FCF_3)	134.738	538.95	313	0.112	0.431	8.10	7.71
HFC-125 (CHF_2CHF_2)	49.024	245.12	665	0.085	0.271	10.49	9.14
HFC-143a (CH_3CF_3)	32.782	98.35	548	0.092	0.307	9.82	8.74
HFC-32 (CH_2F_2)	42.233	84.47	146	0.185	0.642	6.27	6.61
HFC-245fa ($CHF_2CH_3CF_3$)	3.754	18.77	555	0.092	0.305	9.86	8.77
HFC-152a (CH_3CHF_2)	7.686	15.37	44	0.575	1.	4.58	5.57
HFC-227ea (CF_3CHFCF_3)	2.555	17.89	754	0.081	0.664	10.94	9.41
HFC-365mfc ($CH_3CF_2CH_2CF_3$)	1.173	5.87	50	0.522	1.	4.69	5.64
HFC4310mee ($CF_3CHFCHFCF_2CF_3$)	0.307	3.07	360	0.107	0.398	8.50	7.95
HFC-236fa (CF_3CH_3CF3)	0.264	1.58	136	0.201	0.664	6.13	6.52

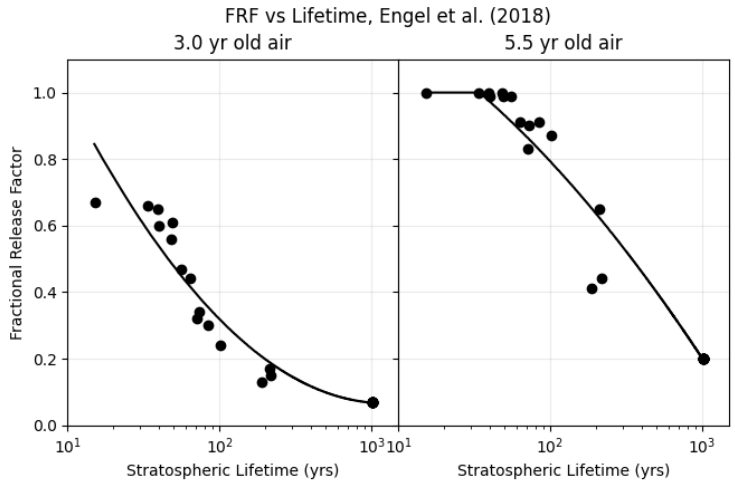


Figure 4C.4. Fractional release factors (FRFs) as a function of stratospheric lifetime for ODSs given in tables 1 and 2 of Engel et al (2018), for 3-year-old and 5.5-year-old air masses (circles), as well as the quadratic least squares fit (line) used to find the values of FRFs for HFCs that are reported in Table 4C.2. A piecewise fit is used for 5.5-year-old air masses, with FRF set to unity for short lifetimes, due to the nature of the data for ODSs.

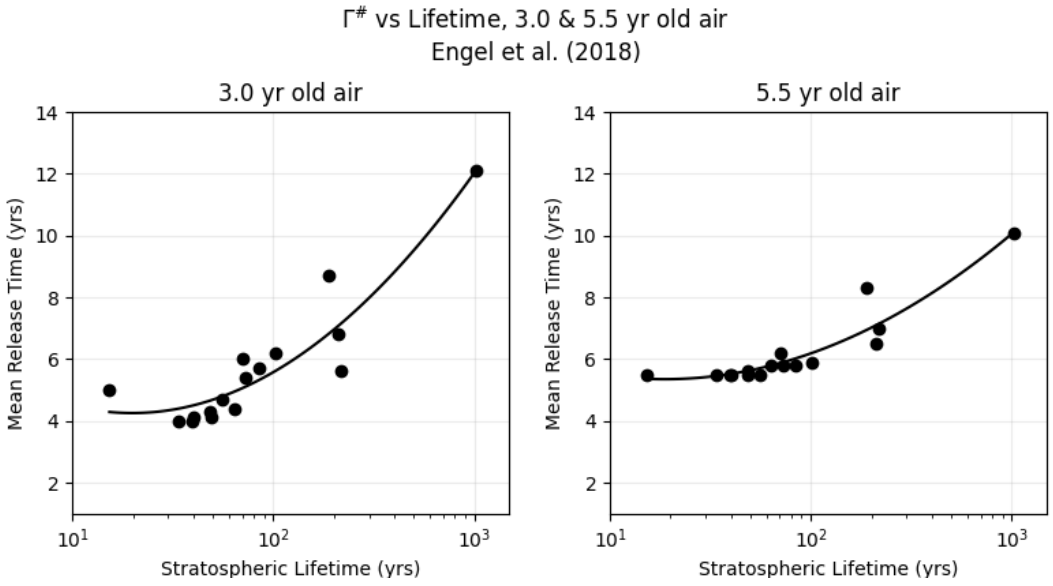


Figure 4C.5. Mean release time ($\Gamma^{\#}$) as a function of stratospheric lifetime for ODSs given in tables 1 and 2 of Engel et al (2018), for 3-year-old and 5.5-year-old air masses (circles), as well as the quadratic least squares fit (line) used to find the values of $\Gamma^{\#}$ for HFCs reported in Table 4C.2.

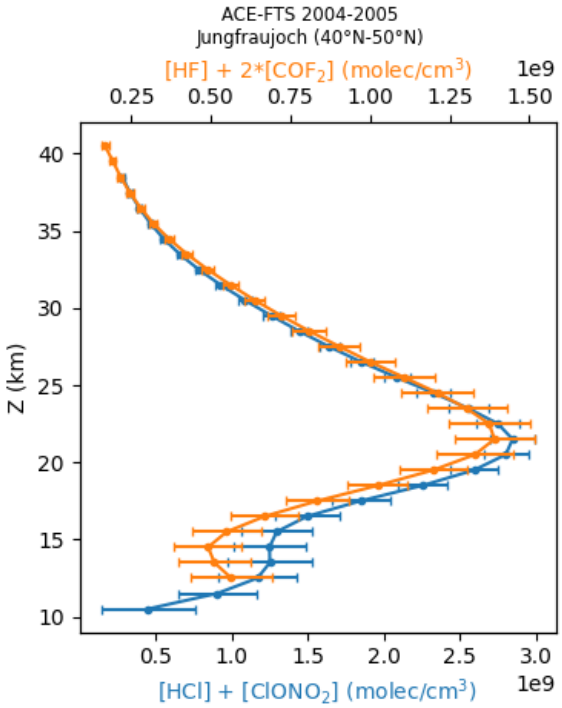


Figure 4C.6. Profile of [HCl]+[$ClONO_2$] (blue line; bottom x-axis), and [HF]+2×[COF_2] (orange line; top axis) observed by ACE-FTS, averaged over the 2004−2025 time period over Jungfraujoch (40°N-50°N). The error bars indicate the standard deviation of the deseasonalized averages.

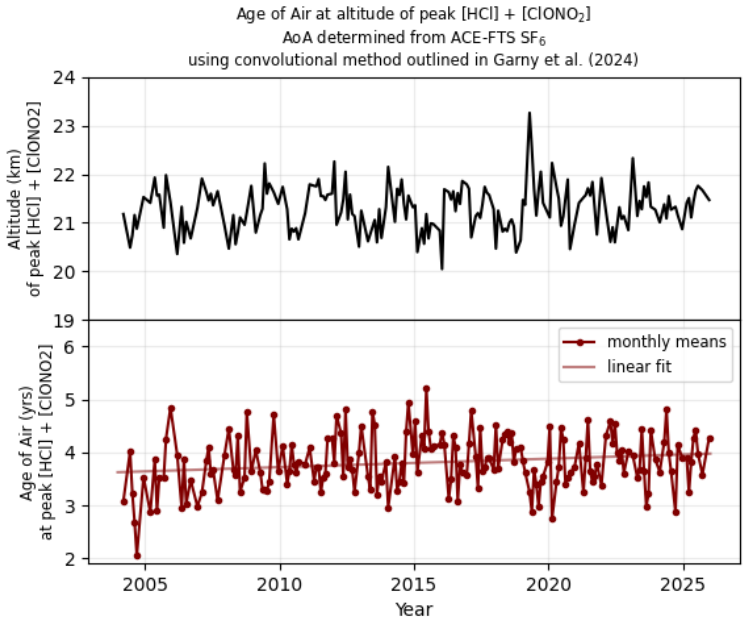


Figure 4C.7. Time series of altitude at which the concentration of deseasonalized latitude-weighted HCl+$ClONO_2$ peaks, as observed by ACE-FTS (top-panel). The bottom panel shows the mean age of stratospheric air at the altitude at which the concentration of HCl+$ClONO_2$ peaks, as derived from ACE-FTS observations of SF_6 using the convolutional method and code provided by Garny et al. (2024).

Chapter 5 : Conclusions and Future Opportunities

5.1 Summary and Conclusions

The results of this dissertation highlight the need improve our understanding of mechanisms controlling ozone abundances in the midlatitude stratosphere, such as the rates of reactions that control chlorine and nitrogen partitioning; the cause of transport changes in the NH lower stratosphere over the past two decades; the role of VSL-Cl species; and, possible harm to the ozone layer by stratospheric sulfate injection. Below, a brief description of Chapters 2, 3, and 4 of this dissertation are provided.

Chapter 2 of this dissertation evaluates heterogeneous chlorine activation as a controlling mechanism for photochemical loss of ozone in the midlatitude LS. Prior to the Dynamics and Chemistry of the Summer Stratosphere (DCOTSS) mission, it was suggested that ClO could be enhanced within convectively influenced air in the North American Monsoon Anticyclone (NAMA), potentially leading to significant photochemical loss of ozone in the midlatitude, lowermost stratosphere. Based on measurements of ClO, $ClONO_2$, H_2O, aerosol surface area, organic chlorine species, temperature, and pressure obtained by a suite of instruments onboard the NASA ER-2 over the continental U.S. during DCOTSS in summer 2021 and 2022, we show that chlorine activation large enough to affect photochemical loss of ozone is unlikely in the midlatitude LS under background aerosol loading conditions. However, we show that aerosol surface area density enhancements would dramatically accelerate chlorine activation for the conditions observed during DCOTSS. Therefore, it is vital for the community to assess how the injection of sulfate into the stratosphere, at levels sufficient to mitigate global warming, would impact chlorine activation and catalytic loss of stratospheric ozone in the midlatitude

stratosphere. The contents of Chapter 2 of this dissertation are published to the Journal of Geophysical Research: Atmospheres, available online at: https://doi.org/10.1029/2025JD043786.

In Chapter 3 of this dissertation, in-situ observations of NO_2, $ClONO_2$, and ClO obtained during the DCOTSS mission are used to assess our understanding of the kinetic processes governing photochemical loss of ozone in the midlatitude lower stratosphere by catalytic cycles involving halogens (ClO_x + BrO_x), nitrogen oxides (NO_x), and hydrogen oxides (HO_x). Photochemical steady-state modeling analysis of the DCOTSS dataset reveals that calculations employing recommendations from the Jet Propulsion Laboratory (JPL) kinetic compendium systematically overestimate observed NO_2 and $ClONO_2$ in the 18 to 21 km altitude region and provide relatively fair agreement with observed ClO. The rate coefficients of 12 key reactions are perturbed to their ± 2σ uncertainty limits in a Monte-Carlo framework to identify reactions in which may contribute the large sources of uncertainty in modeled mixing ratios of NO_2, $ClONO_2$, ClO. We find a 23% increase and a 12% decrease in the rate coefficients for NO_2+OH+M and ClO+NO_2+M, respectively, substantially improve the agreement between observations and model output. The kinetics adjustments that allow for 1σ model-observation agreement suggest the current JPL kinetic recommendations may overestimate NO_x-driven ozone loss, and underestimate halogen and HO_x contributions. These results demonstrate that shifts in the rate coefficients of key reactions controlling the chlorine and nitrogen partitioning, within their specified uncertainty bounds, can have a large influence on modeled radical concentrations and ozone loss pathways. As such, these findings highlight a possible important source of uncertainty in chemistry-climate model predictions of ozone layer recovery that adopt kinetic recommendations from the JPL kinetic compendium. Future laboratory work dedicated towards

understanding the uncertainties in the HNO_3 and $ClONO_2$ formation reactions would be a great benefit to the atmospheric modeling community.

In Chapter 4 of this dissertation, trends in Cl_y ($HCl + ClONO_2$) and N_2O observed by the ACE-FTS instrument in the NH and SH midlatitudes are compared to those simulated by global chemistry-climate models participating in CCMI-2022 REF-D2 simulations for the 2004 to 2025 time period. These comparisons reveal significant model-observation discrepancies in inorganic chlorine and N_2O trends, particularly in the NH midlatitude LS. In the SH, observed trends in $HCl+ClONO_2$ and N_2O are in better agreement with the modeled trends, generally residing within the variability of the model realizations. However, in the NH midlatitudes, significant discrepancies between modeled and observed $HCl+ClONO_2$ trends exist below ~30 km. Trends in N_2O observed by ACE-FTS indicate changes in transport by the BDC have occurred over the 2004 to 2025 time period in both hemispheres. The inability for models to reproduce the observed N_2O trends in the NH midlatitudes suggests that model-observations discrepancies in $HCl+ClONO_2$ may arise from model inadequacies in dynamics. However, we show that the neglect of VSL-Cl species by CCMs may also contribute to model underestimates of $HCl+ClONO_2$ trends. These comparisons suggest that the VSL-Cl may contribute non-negligibly to stratospheric halogen abundances and therefore, may contribute to the slower-than-expected recovery of ozone in the midlatitude LS, in addition to the possible model deficiencies in stratospheric transport. The large spread in N_2O trends simulated by the CCMI-2022 models warrants further investigation.

5.2 Future Directions

Chapter 2 of this dissertation demonstrates that heterogeneous chlorine activation on sulfate aerosols is not a controlling mechanism of ozone destruction in the midlatitude LS for

background aerosol loading conditions. However, recent studies (Salawitch & McBride, 2022; Solomon et al., 2023) have shown that chlorine activation proceeds effectively on oxidized organic-sulfate aerosols injected into the stratosphere by Pyro-cumulonimbus clouds (pyroCb). Following the Australian New Years (ANY) wildfires of late 2019 and early 2020, organic aerosols from pyroCb injection were observed to coincide with enhanced levels of ClO and $ClONO_2$ and a substantial suppression in HCl throughout broad regions of the Southern Hemisphere midlatitude stratosphere (Bernath et al., 2022; Santee, 2022; Strahan et al., 2022). These changes in the partitioning of inorganic chlorine have been attributed to the dissolution of HCl within the organic aerosol phase and subsequent heterogeneous chemistry (Solomon et al., 2023).

Figure 5.1 from Solomon et al. (2023) shows the laboratory-determined solubility of HCl as a function of temperature for various organics, pure water, and sulfate-water aerosols. This figure illustrates that at temperatures typical of the midaltitude stratosphere (~200 to 230 K), the solubility of HCl on mixed organic-sulfate aerosols, typical of wildfire aerosol composition, is far greater than that of the background sulfate (sulfuric-acid) aerosol composition. These findings raise new questions regarding the role of wildfire-driven perturbations in stratospheric ozone chemistry.

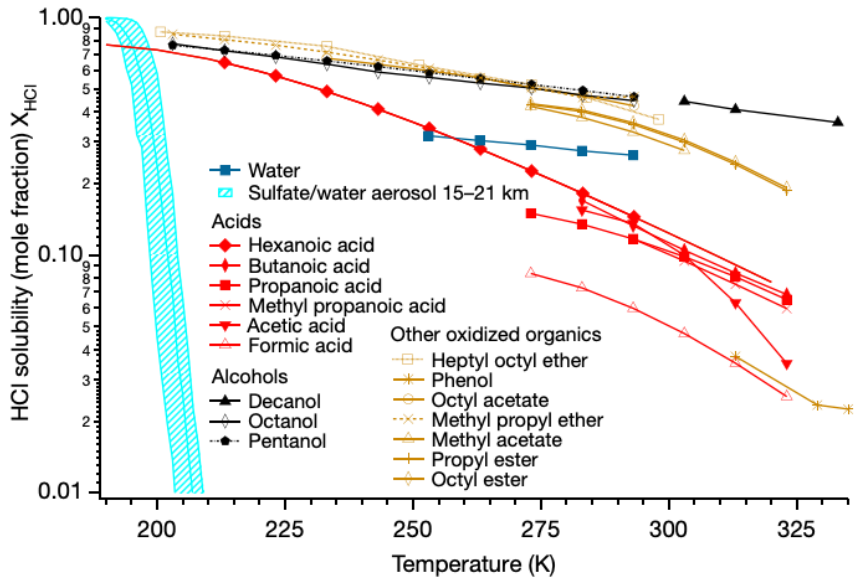


Figure 5.1. Laboratory-determined solubility of HCl in pure-water (blue), sulfate water aerosols (cyan), and various organics (red, blue, and black lines) as a function of temperature. The values are shown for typical stratospheric conditions over the height range of about 15 to 21 km. Figure 1 from Solomon et al. (2023).

Anthropogenically induced global warming has resulted in an increase in wildfire intensity and frequency, particularly in the Western U.S and boreal forests of Canada and Russia (Law et al., 2025; W. Wang et al., 2025). It remains unknown how intense wildfires would affect heterogeneous chlorine activation and ozone loss in the NH midlatitude stratosphere, and whether the heterogeneous mechanisms differ from those observed during the Australian wildfires. This mechanism is especially uncertain given that the composition of wildfire aerosols differs significantly in urban and suburban areas from that of vegetative biomass in wildlands (Holder et al., 2023; S. Wang et al., 2025).

Figure 5.2 displays organic-sulfate mass fractions sampled during DCOTSS 2022 by Particle Analysis by Laser Mass Spectrometry - Next Generation (PALMS-NG) instrument (Jacquot et al. 2024), colored by biomass burning particle fraction (also measured by PALMS-NG). This figure illustrates that a large portion of the background stratosphere contained elevated organic-sulfate mass fractions and significant biomass burning signals, in addition to a pyroCb plume sampled on 21 June 2022. Figure 5.3 from Wilmouth et al. (2026) shows that elevated

VMRs of ClO and $ClONO_2$ were not elevated when the organic-sulfate and/or biomass-burning mass fractions were large. The stratospheric aerosol surface area density (SAD) enhancements associated with the pyroCb and/or organic aerosols sampled during DCOTSS were much smaller than the SAD enhancement in the SH midlatitude stratosphere caused by the Australian Wildfires (Solomon et al., 2023). It is not clear whether the elevated ClO and $ClONO_2$ caused by chemical reactions on the surface of the Australian Wildfire aerosols was due to the much larger SAD in the SH, or perhaps a different organic aerosol composition sampled during DCOTSS compared to the SH aerosols.

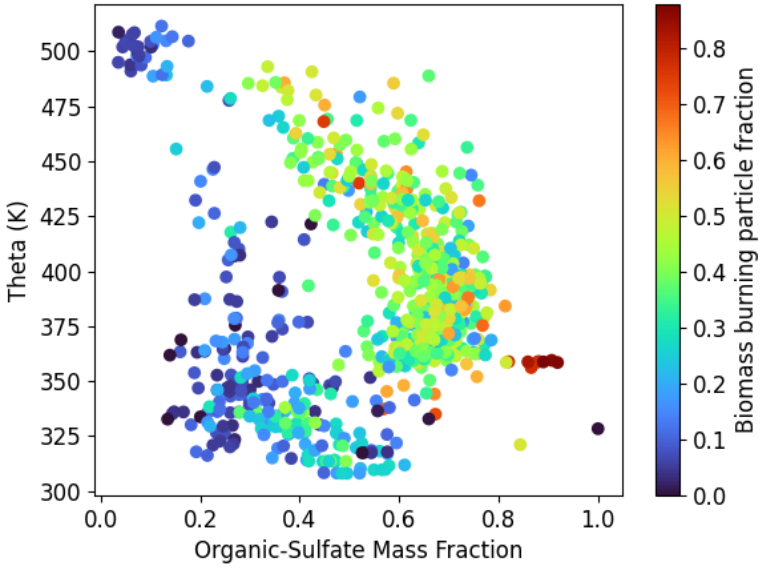


Figure 5.2. Organic sulfate-mass fractions measured by the Particle Analysis by Laser Mass Spectrometry - Next Generation (PALMS-NG) versus potential temperature, sampled during the DCOTSS 2022 mission. Data are colored by biomass burning particle fractions also measured by the PALMS-NG instrument (Jacquot et al. 2024).

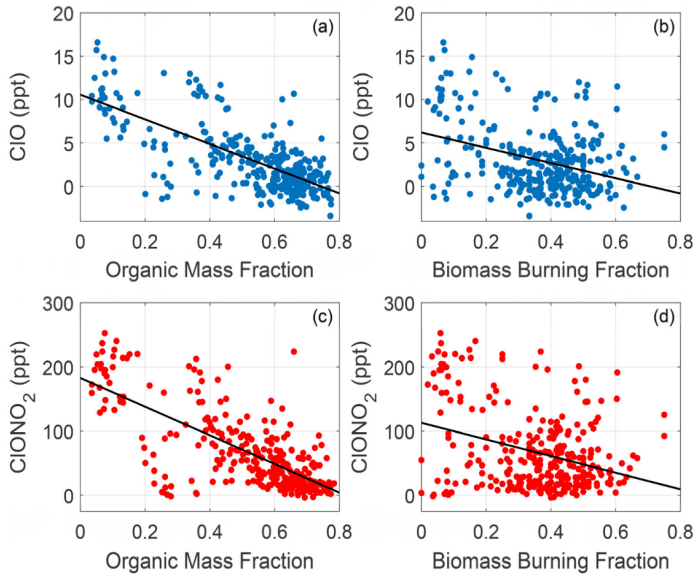


Figure 5.3. Volume mixing ratios of ClO (a, c) and $ClONO_2$ (b, d) versus organic mass fraction (a, c) and biomass burning fraction (b,d) sampled during DCOTSS 2022. Data are shown for $\theta \geq 390$ K and SZA $\leq 75°$. The black lines in all panels show the least-squares fit to the data. Figure 8 from Wilmouth et al. (2026).

Future work is needed to determine whether the composition of NH wildfire aerosols, of different sources, have similar heterogeneous reactivity as those observed after the Australian wildfires, and how mixing or aerosol layering might play a role. Future studies could assess whether incorporating laboratory data for enhanced solubility of HCl on oxidized organics improves model representation of chlorine and nitrogen partitioning within pyroCb plumes over North America. Such comparisons would provide quantitative means for evaluating the influence of wildfire aerosols on heterogeneous chlorine activation in the midlatitude NH stratosphere.

Chapter 3 of this dissertation shows that current JPL kinetic recommendations (Burkholder et al., 2019) for $NO_2+OH+M \rightarrow HNO_3+M$ and $ClO+NO_2+M \rightarrow ClONO_2+M$ contribute a potentially important source of uncertainty in modeled chlorine and nitrogen partitioning in the midlatitude LS and associated ozone loss pathways. CCMs used to provide ozone loss and recovery estimates adopt kinetic recommendations from the JPL kinetic compendium (Burkholder et al., 2019). As such, we suggest future modeling studies quantify the

sensitivity of ozone loss and recovery estimates to alternative kinetic parameterizations for these reactions, including recommendations from both current and prior JPL and IUPAC evaluations. In addition, future work could apply the Monte Carlo framework developed in Chapter 3 to other aircraft campaigns. The Asian Summer Monsoon Chemical & CLimate Impact Project (ACCLIP) would be an important field mission to evaluate the relative contribution of catalytic ozone loss cycles and assess the effect of kinetic uncertainties for. During the ACCLIP mission, significant amounts of VSL-Cl species, and other pollutants, were injected into the stratosphere by deep convection within the Asian Summer Monsoon (ASM) (Pan et al., 2024). Therefore, the relative contributions of the catalytic ozone loss cycles are likely to differ from those observed during DCOTSS. It is important to assess whether a decrease in NO_x-catalyzed ozone loss would have a larger effect on halogenated and HO_x-catalyzed ozone loss for the ASM, compared to the NAMA. Such comparisons would also elucidate whether the kinetic sensitivities identified for the DCOTSS mission are specific to the dynamic and chemical conditions sampled, or the measurement techniques employed.

In Chapter 4, we show that CCMs participating in the CCMI-2022 REF-D2 simulations are unable to reproduce trends in Cl_y ($HCl + ClONO_2$) observed by ACE-FTS for the 2004 to 2025 time period in the NH LS. The objective of Chapter 4 is to broadly understand and elucidate factors that may contribute to the slower-than-expected recovery of ozone, and inability of global chemistry-climate models to reproduce observed ozone trends. A key next step would be to quantitatively evaluate the individual contributions of declining long-lived source gases, increasing VSL-Cl emissions, and dynamic variability, to observed Cl_y trends in the lower stratosphere. In addition, future work could develop a goodness of fit (χ^2) metric with respect to observations of Cl_y in the LS as a quantitative tool for evaluating return dates in multi-model

assessments. Such work could compare total inorganic chlorine (Cl_y) from CCMI-2022 REF-D2 simulations based on the use of N_2O to select 3-yr-old air, to time series of HCl+$ClONO_2$ from long-term records from Jungfraujoch, Lauder, Mauna Loa (Mahieu et al., 2014), as well as ATMOS (Zander et al., 1996) and ACE-FTS (Boone et al., 2023).

Future CCM simulations should consider the complete inventory of halogen emissions, including all natural and anthropogenic VSLS, in their ozone trend and recovery estimates. Such simulations are vital for assessing the future evolution of stratospheric ozone and evaluating the need for tighter restrictions on anthropogenic source gas emissions. A new model intercomparison project (VSL-MIP1) sponsored by APARC will provide means for future studies to evaluate the impact of anthropogenic VSLs on stratospheric ozone, through a multi-model assessment (Hossaini et al., 2024a). This project will provide new and improved estimates of industrial VSL-Cl emissions, involving several leading global chemistry-climate modeling groups. The CCM simulations for VSL-MIP1 are required to explicitly treat the five anthropogenic VSL-Cl species: dichloromethane, chloroform, perchloroethylene, 1,2-dichloroethane, and trichloroethane. These model simulations will be vital for assessing whether continued industrial emissions pose a threat to future ozone recovery and evaluating the need for tighter restrictions on anthropogenic source gas emissions. It is important for the CCM output conducted under VSL-MIP1 to be compared to observations from DCOTSS (Howar et al., 2025), as well as ACCLIP (Pan et al., 2024).

Finally, MLS is reaching the end of its operational lifetime, and ACE-FTS is currently 18 years beyond its expected lifetime (Salawitch et al., 2025). The MLS instrument provides near-global, daily observations of N_2O (a tracer of stratospheric transport) and the critically important inorganic chlorine species ClO and HCl. The ACE-FTS instrument provides high vertical

resolution profiles of O_3, H_2O, and about 44 other tracer gas products, including isotopologues (Bernath et al., 2018). The Aura satellite that supports MLS will be decommissioned due to loss of power and propellant no later than 2028. Once data from MLS cease to exist, the daily near-global observations of N_2O, ClO, and HCl will no longer be available. This loss of observational capability can be partially overcome by using data from ACE-FTS. However, daily near-global observations from ACE-FTS are not possible, due to the orbit of the SCISAT-1 satellite that houses this instrument, along with the solar occultation measurement technique.

Recently, NASA announced the selection of the STRIVE (Stratosphere Troposphere Response using Infrared Vertically-resolved light Explorer) satellite mission (NASA Press Release, 5 February 2026). STRIVE consists of two instruments that will provide high vertical resolution, spatially dense, daily global measurements of tracers of stratospheric transport, and chemically reactive gases during day and night. However, the STRIVE missions is not yet confirmed. If confirmed, STRIVE will launch no earlier than 2030. If STRIVE successfully launches, the data from the two strive instruments will be essential for advancing our understanding of the stratospheric transport issues identified in Chapter 4. However, STRIVE will not measure either ClO or HCl. As such, the stratospheric chemistry issues discussed throughout this dissertation will lack any further near-global, daily observational basis once Aura MLS ceases to operate.

5.3 Contributions to Other Papers

In addition to the three papers discussed in Chapters 2, 3, and 4 of this dissertation, I have also made contributions to three related studies, including Bowman et al. (2026), “The dynamics and chemistry of the summer stratosphere (DCOTSS) Project”, published in the Bulletin of the American Meteorological Society (BAMS); Wilmouth et al. (2026), “Analysis of inorganic

chlorine chemistry in the midlatitude summer stratosphere using aircraft and satellite observations" under discussion in Atmospheric Chemistry and Physics (ACP); and Delaria et al. (2026, *submitted*), "Deep Convection of Formaldehyde Precursors Accelerates Photochemistry in the Upper Troposphere and Lower Stratosphere" for submission to Journal of Geophysical Research: Atmospheres. Below, I provide a brief description of my contribution to each of these papers.

The Bowman et al. (2026) paper, titled "The Dynamics and Chemistry of the Summer Stratosphere (DCOTSS) Project", published in the Bulletin of the American Meteorological Society (BAMS) provides an overview of the DCOTSS mission. This paper describes the scientific motivations for the campaign, the sampling strategy and measurements collected, and the major findings from studies conducted using DCOTSS observations. For this paper, I prepared Figure 9, shown below as Figure 5.4. This figure illustrates that the majority of heterogeneously suitable conditions, with low temperature and enhanced water vapor, were observed near the tropopause, where inorganic chlorine is too low to facilitate enhancements of ClO capable of causing significant ozone depletion. The central element of Figure 5.4 was the basis of the Chapter 2 investigation of convection perturbed heterogeneous chlorine activation.

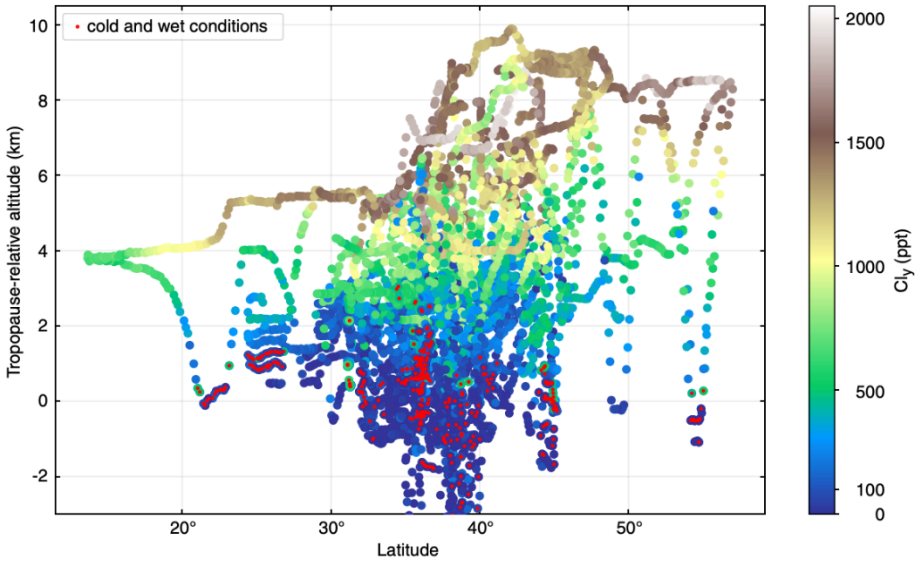


Figure 5.4. Calculated total inorganic chlorine (Cl_y; colors) as a function of latitude and ERA5 tropopause-relative altitude for DCOTSS flights during 2021 and 2022. Red dots labeled "cold and wet conditions" indicated locations where the MMS temperature reaches the frost point. Figure 9 from Bowman et al. (2026).

Wilmouth et al. (2026) evaluates the budget and partitioning of inorganic chlorine in the North American midlatitude stratosphere during the DCOTSS 2021 and 2022 deployments for background conditions and conditions influenced by biomass burning and overshooting convection. For this paper, I provided photodissociation frequencies used in this study to compute steady-state abundances of $ClONO_2$, analyzed back-trajectories for a select number of parcels, and helped guide the analysis and writing of the manuscript. Similar to Chapter 2 of this dissertation, this study concludes no chlorine activation was observed in the lower stratosphere under low temperature and high-water vapor conditions observed during DCOTSS. Similar to Chapter 3 of this dissertation, Wilmouth et al. (2026) concludes that a reduction in the recommended rate coefficient for $ClONO_2$ production (i.e., $ClO+NO_2+M$) would provide better agreement between measured and steady-state $ClONO_2$ mixing ratios. The need for a reduction in the uncertainty in the $ClONO_2$ formation reaction is further described in Chapter 3 of this dissertation, as well as in Wilmouth et al. (2026). To supplement the discussion of this study, I analyzed back-trajectories to evaluate whether high abundances of ClO and $ClONO_2$ observed

during May 2022 of the DCOTSS mission were influenced by the Hunga-Tunga eruption, or rather, were sourced from higher latitudes. The back-trajectory analysis showed no evidence of polar origin or Hunga-Tunga influence, suggesting that the high levels of ClO and $ClONO_2$ were instead associated with the seasonal cycle of inorganic chlorine, which typically reaches higher levels in spring. Wilmouth et al. (2026) is under discussion in Atmospheric Chemistry and Physics (ACP) as "Observations and Analysis of Inorganic Chlorine Chemistry in the Northern Hemisphere Midlatitude Summer Stratosphere".

Delaria et al. (2026, *submitted*) examined measurements of formaldehyde (HCHO) within convectively influenced air masses obtained during the DCOTSS campaign and Asian Summer Monsoon Chemical and CLimate Impact Project (ACCLIP) mission. This paper shows that elevated mixing ratios of HCHO in the upper troposphere-lower stratosphere (UTLS) are due to convective transport over heavily populated industrial regions and the secondary production from the decomposition of boundary layer volatile organic compounds (VOCs). For this paper, I provided photodissociation frequencies that are a central element of their analysis. The photodissociation frequencies were used to calculate the steady-state abundances of HCHO, NO_x, and others, along the DCOTSS flight tracks. The comparison between steady-state and observed HCHO revealed that RO_2 radicals formed from the decomposition of VOCs contribute to elevated HCHO abundances in the UTLS, as the deviation from steady-state cannot be explained by direct convective transport of HCHO alone. In summary, this paper shows that convective injection of volatile organic compounds (VOCs) over the populated industrial regions, and resulting enhancements in formaldehyde, may alter the radiative balance of the UTLS, and alter the O_3 and HO_x production regimes near the tropopause. This study, titled

“Deep Convection of Formaldehyde Precursors Accelerates Photochemistry in the Upper Troposphere and Lower Stratosphere” was submitted to JGR: Atmospheres in July of 2026.

Bibliography

Akiyoshi, H., Kadowaki, M., Yamashita, Y., & Nagatomo, T. (2023). Dependence of column ozone on future ODSs and GHGs in the variability of 500-ensemble members. *Scientific Reports*, *13*(1), 320. https://doi.org/10.1038/s41598-023-27635-y

Amedro, D., Berasategui, M., Bunkan, A. J., Pozzer, A., Lelieveld, J., & Crowley, J. N. (2020). Kinetics of the OH+NO_2 reaction: effect of water vapour and new parameterization for global modelling. *Atmospheric Chemistry and Physics*, *20*(5), 3091-3105. https://doi.org/10.5194/acp-20-3091-2020

Amedro, D., Bunkan, A. J. C., Berasategui, M., & Crowley, J. N. (2019). Kinetics of the OH + NO_2 reaction: Rate coefficients (217-333 K, 16-1200 mbar) and fall-off parameters for N_2 and O_2 bath gases. *Atmospheric Chemistry and Physics*, *19*(16), 10643–10657. https://doi.org/10.5194/acp-19-10643-2019

Anderson, J. G., & Clapp, C. E. (2018). Coupling free radical catalysis, climate change, and human health. *Physical chemistry chemical physics*, 20(16), 10569-10587. https://doi.org/10.1039/C7CP08331A

Anderson, J. G., Weisenstein, D. K., Bowman, K. P., Homeyer, C. R., Smith, J. B., Wilmouth, D. M., et al. (2017). Stratospheric ozone over the United States in summer linked to observations of convection and temperature via chlorine and bromine catalysis. *Proceedings of the National Academy of Sciences*, 114(25), E4905-E4913. https://doi.org/10.1073/pnas.1619318114

Anderson, J. G., Wilmouth, D. M., Smith, J. B., & Sayres, D. S. (2012). UV dosage levels in summer: Increased risk of ozone loss from convectively injected water vapor. *Science*, *337*(6096), 835–839. https://doi.org/10.1126/science.1222978

Ardra, D., Kuttippurath, J., Roy, R., Kumar, P., Raj, S., Müller, R., & Feng, W. (2022). The Unprecedented Ozone Loss in the Arctic Winter and Spring of 2010/2011 and 2019/2020. *ACS Earth and Space Chemistry*, *6*(3), 683–693. https://doi.org/10.1021/acsearthspacechem.1c00333

Atkinson, R., Baulch, D. L., Cox, R. A., Crowley, J. N., Hampson, R. F., Hynes, R. G., et al. (2004). Evaluated kinetic and photochemical data for atmospheric chemistry: Volume I-gas phase reactions of O_x, HO_x, NO_x and SO_x species. *Atmospheric chemistry and physics*, *4*(6), 1461-1738. https://doi.org/10.5194/acp-4-1461-2004

Atkinson, R., Baulch, D. L., Cox, R. A., Crowley, J. N., Hampson, R. F., Hynes, R. G., et al. (2007). Evaluated kinetic and photochemical data for atmospheric chemistry: Volume III–gas phase reactions of inorganic halogens. Atmospheric Chemistry and Physics, 7(4), 981-1191. https://doi.org/10.5194/acp-7-981-2007

Baikhadzhaev, R., Ploeger, F., Preusse, P., Ern, M., & Birner, T. (2025). A dynamics-based separation of deep and shallow stratospheric circulation branches. *Atmospheric Chemistry and Physics*, *25*(19), 12753–12777. https://doi.org/10.5194/acp-25-12753-2025

Ball, W. T., Alsing, J., Mortlock, D. J., Staehelin, J., Haigh, J. D., Peter, T., et al. (2018). Evidence for a continuous decline in lower stratospheric ozone offsetting ozone layer recovery. *Atmospheric Chemistry and Physics*, *18*(2), 1379–1394. https://doi.org/10.5194/acp-18-1379-2018

Ball, W. T., Alsing, J., Staehelin, J., Davis, S. M., Froidevaux, L., & Peter, T. (2019). Stratospheric ozone trends for 1985–2018: sensitivity to recent large variability.

Atmospheric Chemistry and Physics, *19*(19), 12731–12748. https://doi.org/10.5194/acp-19-12731-2019

Ball, W. T., Chiodo, G., Abalos, M., Alsing, J., & Stenke, A. (2020). Inconsistencies between chemistry–climate models and observed lower stratospheric ozone trends since 1998. *Atmospheric chemistry and physics*, *20*(16), 9737-9752. https://doi.org/10.5194/acp-20-9737-2020

Barnes, P. W., Williamson, C. E., Lucas, R. M., Robinson, S. A., Madronich, S., Paul, N. D., et al. (2019). Ozone depletion, ultraviolet radiation, climate change and prospects for a sustainable future. *Nature Sustainability*, 2(7), 569-579. https://doi.org/10.1038/s41893-019-0314-2

Bates, D. R., & Nicolet, M. (1950). The photochemistry of atmospheric water vapor. *Journal of Geophysical Research*, *55*(3), 301–327. https://doi.org/10.1029/jz055i003p00301

Bednarz, E. M., Hossaini, R., & Chipperfield, M. P. (2023). Atmospheric impacts of chlorinated very short-lived substances over the recent past - Part 2: Impacts on ozone. *Atmospheric Chemistry and Physics*, *23*(21), 13701–13711. https://doi.org/10.5194/acp-23-13701-2023

Bednarz, E. M., Hossaini, R., Chipperfield, M. P., Abraham, N. L., & Braesicke, P. (2022). Atmospheric impacts of chlorinated very short-lived substances over the recent past – Part 1: Stratospheric chlorine budget and the role of transport. *Atmospheric Chemistry and Physics*, *22*(16), 10657–10676. https://doi.org/10.5194/acp-22-10657-2022

Benito-Barca, S., Abalos, M., Calvo, N., Garny, H., Birner, T., Abraham, N. L., et al. (2025). Recent Lower Stratospheric Ozone Trends in CCMI-2022 Models: Role of Natural Variability and Transport. *Journal of Geophysical Research: Atmospheres*, *130*(9). https://doi.org/10.1029/2024JD042412

Bernath, P., Boone, C., & Crouse, J. (2022). Wildfire smoke destroys stratospheric ozone. *Science*, *375*(6586), 1292-1295. https://doi.org/10.1126/science.abm5611

Bernath, P., & Fernando, A. M. (2018). Trends in stratospheric HCl from the ACE satellite mission. Journal of Quantitative Spectroscopy and Radiative Transfer, 217, 126-129. https://doi.org/10.1016/j.jqsrt.2018.05.027

Bernhard, G. H., Bais, A. F., Aucamp, P. J., Klekociuk, A. R., Liley, J. B., & McKenzie, R. L. (2023). Stratospheric ozone, UV radiation, and climate interactions. *Photochemical & Photobiological Sciences*, *22*(5), 937-989. https://doi.org/10.1007/s43630-023-00371-y

Bernhard, G. H., Neale, R. E., Barnes, P. W., Neale, P. J., Zepp, R. G., Wilson, S. R., et al. (2020). Environmental effects of stratospheric ozone depletion, UV radiation and interactions with climate change: UNEP Environmental Effects Assessment Panel, update 2019. *Photochemical & Photobiological Sciences*, *19*(5), 542–584. https://doi.org/10.1039/d0pp90011g

Berthet, G., Huret, N., Lefèvre, F., Moreau, G., Robert, C., Chartier, M., et al. (2006). On the ability of chemical transport models to simulate the vertical structure of the N_2O, NO_2 and HNO_3 species in the mid-latitude stratosphere. *Atmospheric Chemistry and Physics*, *6*(6), 1599-1609. https://doi.org/10.5194/acp-6-1599-2006

Birks, J. W., Shoemaker, B., Leck, T. J., & Hinton, D. M. (1976). Studies of reactions of importance in the stratosphere. I. Reaction of nitric oxide with ozone. *The Journal of Chemical Physics*, *65*(12), 5181-5185. https://doi.org/10.1063/1.433059

Birner, T., & Bönisch, H. (2011). Residual circulation trajectories and transit times into the extratropical lowermost stratosphere. *Atmospheric Chemistry and Physics*, *11*(2), 817–827. https://doi.org/10.5194/acp-11-817-2011

Boedecker, G. E., Waugh, D. W., Akiyoshi, H., Braesicke, P., Eyring, V., Fahey, D. W., et al. (2007). The ozone layer in the 21st century, Chapter 6 in Scientific Assessment of Ozone Depletion: 2006. Global Ozone Research and Monitoring Project − Report No. 50. Geneva, Switzerland: World Meteorological Organization.

Bonne, G. P., Stimpfle, R. M., Cohen, R. C., Voss, P. B., Perkins, K. K., Anderson, J. G., et al. (2000). An examination of the inorganic chlorine budget in the lower stratosphere. *Journal of Geophysical Research: Atmospheres*, *105*(D2), 1957-1971. https://doi.org/10.1029/1999JD900996

Boone, C. D., Bernath, P. F., & Lecours, M. (2023). Version 5 retrievals for ACE-FTS and ACE-imagers. *Journal of Quantitative Spectroscopy and Radiative Transfer*, 108749. https://doi.org/10.1016/j.jqsrt.2023.108749

Borders, R. A., & Birks, J. W. (1982). High-precision measurements of activation energies over small temperature intervals: Curvature in the Arrhenius plot for the reaction NO + O_3 −> NO_2 + O_2. *Journal of Physical Chemistry*, 86(17), 3295–3302. https://doi.org/10.1021/j100214a007

Bourguet, S., & Lickley, M. (2024). Bayesian modeling of HFC production pipeline suggests growth in unreported CFC by-product and feedstock production. *Nature Communications*, *15*(1), 10883. https://doi.org/10.1038/s41467-024-55250-6

Bowman, K. P., Keutsch, F. N., Homeyer, C. R., Sayres, D. S., Smith, J. B., Wilmouth, D. M., et al. (2026). The Dynamics and Chemistry of the Summer Stratosphere (DCOTSS) Project. *Bulletin of the American Meteorological Society*, BAMS-D. https://doi.org/10.1175/BAMS-D-24-0177.1

Brash, D. E., Rudolph, J. A., Simon, J. A., Lin, A., McKenna, G. J., Baden, H. P., et al. (1991). A role for sunlight in skin cancer: UV-induced p53 mutations in squamous cell carcinoma. *Proceedings of the National Academy of Sciences*, *88*(22), 10124-10128. https://doi.org/10.1073/pnas.88.22.10124

Brasseur, G. P., & Solomon, S. (2005). *Aeronomy of the Middle Atmosphere*. Springer Netherlands. https://doi.org/10.1007/1-4020-3824-0

Brewer, A. W. (1949). Evidence for a world circulation provided by the measurements of helium and water vapour distribution in the stratosphere. *Quarterly Journal of the Royal Meteorological Society*, *75*(326), 351-363. https://doi.org/10.1002/qj.49707532603

Burkholder, J. B., Sander, S. P., Abbatt, J. P. D., Barker, J. R., Cappa, C., Crounse, J. D., et al. (2019). Chemical kinetics and photochemical data for use in atmospheric studies; evaluation number 19. Pasadena, CA: Jet Propulsion Laboratory, National Aeronautics and Space Administration, 2019. http://jpldataeval.jpl.nasa.gov

Butchart, N. (2014). The brewer-dobson circulation. *Reviews of geophysics*, *52*(2), 157-184. https://doi.org/10.1002/2013RG000448

Butkovskaya, N., Kukui, A., & Le Bras, G. (2007). HNO3 Forming Channel of the HO2+ NO Reaction as a Function of Pressure and Temperature in the Ranges of 72− 600 Torr and 223− 323 K. The Journal of Physical Chemistry A, 111(37), 9047-9053. https://doi.org/10.1021/jp074117m

Butkovskaya, N., Kukui, A., Pouvesle, N., & Le Bras, G. (2005). Formation of nitric acid in the gas-phase HO2+ NO reaction: Effects of temperature and water vapor. The Journal of Physical Chemistry A, 109(29), 6509-6520. https://doi.org/10.1021/jp051534v

Carpenter, L. J., Reimann, S., Burkholder, J. B., Clerbaux, C., Hall, B. D., Hossaini, R., Laube, J. C., et al. (2014). Update on Ozone-Depleting Substances (ODSs) and Other Gases of Interest to the Montreal Protocol. *Scientific Assessment of Ozone Depletion: 2014* (pp. 1.1-1.101). Geneva, Switzerland: World Meteorological Organization.

Chang, K. W., Bowman, K. P., & Rapp, A. D. (2023). Transport and Confinement of Plumes From Tropopause-Overshooting Convection Over the Contiguous United States During the Warm Season. *Journal of Geophysical Research: Atmospheres*, *128*(2), e2022JD037020. https://doi.org/10.1029/2022JD037020

Chang, K. W., Bowman, K. P., Siu, L. W., & Rapp, A. D. (2021). Convective forcing of the North American monsoon anticyclone at intraseasonal and interannual time scales. *Journal of the atmospheric sciences*, *78*(9), 2941-2956. https://doi.org/10.1175/JAS-D-21-0009.1

Chapman, S. (1930) A Theory of Upper Atmospheric Ozone. *Memoirs of the Royal Meteorological Society*, 3, 103-125.

Chiodo, G., & Polvani, L. M. (2019). The Response of the Ozone Layer to Quadrupled CO2 Concentrations: Implications for Climate. *Journal of Climate*, *32*(22), 7629–7642. https://doi.org/10.1175/JCLI-D-19-0086.1

Chipperfield, M. P., & Bekki, S. (2024). Opinion: Stratospheric ozone – depletion, recovery and new challenges. In *Atmospheric Chemistry and Physics* (Vol. 24, Number 4, pp. 2783–2802). Copernicus Publications. https://doi.org/10.5194/acp-24-2783-2024

Chipperfield, M. P., Hossaini, R., Montzka, S. A., Reimann, S., Sherry, D., & Tegtmeier, S. (2020). Renewed and emerging concerns over the production and emission of ozone-depleting substances. *Nature Reviews Earth & Environment*, *1*(5), 251-263. https://doi.org/10.1038/s43017-020-0048-8

Chrysanthou, A., Dubé, K., Tegtmeier, S., & Chipperfield, M. P. (2025). Hemispheric Asymmetry in Stratospheric Trends of HCl and Ozone: Impact of Chemical Feedback on Ozone Recovery. *Journal of Geophysical Research: Atmospheres*, *130*(3). https://doi.org/10.1029/2024JD042161

Clapp, C. E., Smith, J. B., Bedka, K. M., & Anderson, J. G. (2021). Identifying Outflow Regions of North American Monsoon Anticyclone-Mediated Meridional Transport of Convectively Influenced Air Masses in the Lower Stratosphere. *Journal of Geophysical Research: Atmospheres*, *126*(10), e2021JD034644 https://doi.org/10.1029/2021JD034644

Claxton, T. (2020). Chlorinated Very Short-Lived Substances: Modelling their global emissions and impact on stratospheric ozone. (Doctoral dissertation, Lancaster University).

Cohen, R. C., Perkins, K. K., Koch, L. C., Stimpfle, R. M., Wennberg, P. O., Hanisco, T. F., et al. (2000). Quantitative constraints on the atmospheric chemistry of nitrogen oxides: An analysis along chemical coordinates. *Journal of Geophysical Research: Atmospheres*, *105*(D19), 24283-24304. https://doi.org/10.1029/2000JD900290

Copernicus Sentinel-5P (2018). TropOMI Level 2 Ozone Total Column products (Version 2.01) [Dataset]. European Space Agency. https://doi.org/10.5270/S5P-fqouvyz

Crutzen, P. J. (1970). The influence of nitrogen oxides on the atmospheric ozone content. *QJ Roy. Meteor. Soc., 96, 320–325*. https://doi-org.proxy-um.researchport.umd.edu/10.1002/qj.49709640815

Crutzen, P. J. (1971). Ozone production rates in an oxygen-hydrogen-nitrogen oxide atmosphere. *Journal of Geophysical Research*, 76(30), 7311-7327. https://doi.org/10.1029/JC076i030p07311

Crutzen, P. J. (1972). SST's: A threat to the earth's ozone shield. *Ambio*, 41-51. https://www.jstor.org/stable/4311946

Crutzen, P. J. (2006). Albedo enhancement by stratospheric sulfur injections: a contribution to resolve a policy dilemma?. *Climatic change*, *77*(3-4), 211. https://doi.org/10.1007/s10584-006-9101-y

Dall'Amico, M., Gray, L. J., Rosenlof, K. H., Scaife, A. A., Shine, K. P., & Stott, P. A. (2010). Stratospheric temperature trends: impact of ozone variability and the QBO. *Climate Dynamics*, *34*(2), 381–398. https://doi.org/10.1007/s00382-009-0604-x

Daniel, J. S., Reimann, S., Ashford, P., Fleming, E., Hossaini, R., Lickley, M., et al. (2022). Scenarios and Information for Policymakers, Chapter 7 in Scientific Assessment of Ozone Depletion: 2022, GAW Report No. 278, World Meteorological Organization.

Daniel, J. S., Solomon, S., & Albritton, D. L. (1995). On the evaluation of halocarbon radiative forcing and global warming potentials. *Journal of Geophysical Research: Atmospheres*, *100*(D1), 1271–1285. https://doi.org/10.1029/94JD02516

Del Negro, L. A., Fahey, D. W., Gao, R. S., Donnelly, S. G., Keim, E. R., Neuman, J. A., et al. (1999). Comparison of modeled and observed values of NO2 and JNO2 during the Photochemistry of Ozone Loss in the Arctic Region in Summer (POLARIS) mission. *Journal of Geophysical Research: Atmospheres*, *104*(D21), 26687-26703. https://doi.org/10.1029/1999JD900246

Delaria, E. R., St Clair, J. M., Wolfe, G. M., Hanisco, T. F., Hannun, R., Anderson, D.,C., Apel, E. C., et al. (2026, *submitted*). Deep Convection of Formaldehyde Precursors Accelerates Photochemistry in the Upper Troposphere and Lower Stratosphere. Submitted to *Journal of Geophysical Research: Atmospheres.*

DeMore, W. B., S. P. Sander, D. M. Golden, R. F. Hampson, M. J. Kurylo, C. J. Howard, A. R., et al. (1997). Chemical kinetics and photochemical data for use in stratospheric modeling, JPL, 97-4, Jet Propulsion Laboratory, 1997.

Dennison, F., & Woodhouse, M. T. (2023). ACCESS-CM2-Chem: Evaluation of southern hemisphere ozone and its effect on the southern Annular mode. Journal of Southern Hemisphere Earth Systems Science, 73(1), 17–29. https://doi.org/10.1071/es22015

Dhomse, S. S., Kinnison, D., Chipperfield, M. P., Salawitch, R. J., Cionni, I., Hegglin, M. I., et al. (2018). Estimates of ozone return dates from Chemistry-Climate Model Initiative simulations. *Atmospheric Chemistry and Physics*, *18*(11), 8409–8438. https://doi.org/10.5194/acp-18-8409-2018

Dhomse, S., Weber, M., Wohltmann, I., Rex, M., & Burrows, J. P. (2006). On the possible causes of recent increases in northern hemispheric total ozone from a statistical analysis of satellite data from 1979 to 2003. *Atmospheric Chemistry and Physics*, *6*(5), 1165–1180. https://doi.org/10.5194/acp-6-1165-2006

Diallo, M., Konopka, P., Santee, M. L., Müller, R., Tao, M., Walker, K. A., et al. (2019). Structural changes in the shallow and transition branch of the Brewer-Dobson circulation

induced by El Niño. *Atmospheric Chemistry and Physics*, *19*(1), 425–446. https://doi.org/10.5194/acp-19-425-2019

Dickerson, R. R., Doddridge, B. G., Poulida, O., & Owens, M. A. (1994). The gradient of meteorological and chemical variables across the tropopause. *NASA. Goddard Space Flight Center, Ozone in the Troposphere and Stratosphere, Part 1*. https://ntrs.nasa.gov/citations/19950004220

Dietmüller, S., Garny, H., Eichinger, R., & T. Ball, W. (2021). Analysis of recent lower-stratospheric ozone trends in chemistry climate models. *Atmospheric Chemistry and Physics*, *21*(9), 6811–6837. https://doi.org/10.5194/acp-21-6811-2021

Douglass, A. R., Schoeberl, M. R., Stolarski, R. S., Waters, J. W., Russell III, J. M., Roche, A. E., & Massie, S. T. (1995). Interhemispheric differences in springtime production of HCl and ClONO2 in the polar vortices. *Journal of Geophysical Research: Atmospheres*, 100(D7), 13967-13978. https://doi.org/10.1029/95JD00698

Drdla, K. & Müller, R. (2012). Temperature thresholds for chlorine activation and ozone loss in the polar stratosphere. *Ann. Geophys.,* 30, 1055–1073. https://doi.org/10.5194/angeo-30-1055-2012

Dubé, K., Tegtmeier, S., Bourassa, A., Laube, J. C., Engel, A., Saunders, L. N., et al. (2025a). Chlorinated very short-lived substances offset the long-term reduction of inorganic stratospheric chlorine. *Communications Earth and Environment*, *6*(1). https://doi.org/10.1038/s43247-025-02478-9

Dubé, K., Tegtmeier, S., Bourassa, A., Zawada, D., Degenstein, D., Sheese, P. E., et al. (2023). N_2O as a regression proxy for dynamical variability in stratospheric trace gas trends. *Atmospheric Chemistry and Physics*, *23*(20), 13283–13300. https://doi.org/10.5194/acp-23-13283-2023

Dubé, K., Tegtmeier, S., Ploeger, F., & Walker, K. A. (2025b). Hemispheric asymmetry in recent stratospheric age of air changes. *Atmospheric Chemistry and Physics*, *25*(2), 1433–1447. https://doi.org/10.5194/acp-25-1433-2025

Dubey, M. K., McGrath, M. P., Smith, G. P., & Rowland, F. S. (1998). HCl yield from OH+ ClO: Stratospheric model sensitivities and elementary rate theory calculations. *The Journal of Physical Chemistry A*, *102*(18), 3127-3133. https://doi.org/10.1021/jp9808476

Dutton, G. S., Hall, B. D., Dlugokencky, E. J., Lan, X., Nance, J. D., & Madronich, M. (2023). Combined Atmospheric Sulfur Hexafluoride Dry Air Mole Fractions from the NOAA GML Halocarbons Sampling Network, 1995-2023 (Version: 2023-04-13) [Dataset]. https://doi.org/10.15138/TQ02-ZX42

Engel, A., Bönisch, H., Ostermöller, J., Chipperfield, M. P., Dhomse, S., & Jöckel, P. (2018). A refined method for calculating equivalent effective stratospheric chlorine. *Atmospheric Chemistry and Physics*, *18*(2), 601–619. https://doi.org/10.5194/acp-18-601-2018

Engel, A., Bönisch, H., Ullrich, M., Sitals, R., Membrive, O., Danis, F., & Crevoisier, C. (2017). Mean age of stratospheric air derived from aircore observations. Atmospheric Chemistry and Physics, 17(11), 6825–6838. https://doi.org/10.5194/acp-17-6825-2017

Engel, A., Strunk, M., Müller, M., Haase, H. P., Poss, C., Levin, I., & Schmidt, U. (2002). Temporal development of total chlorine in the high-latitude stratosphere based on reference distributions of mean age derived from CO_2 and SF_6. *Journal of Geophysical Research: Atmospheres*, *107*(D12), ACH-1. https://doi.org/10.1029/2001JD000584

Evan, S., Brioude, J., Rosenlof, K. H., Gao, R. S., Portmann, R. W., Zhu, Y., et al. (2023). Rapid ozone depletion after humidification of the stratosphere by the Hunga Tonga Eruption. *Science*, *382*(6668). https://doi.org/10.1126/science.adg2551

Eyring, V., Cionni, I., Bodeker, G. E., Charlton-Perez, A. J., Kinnison, D. E., Scinocca, J. F., et al. (2010). Multi-model assessment of stratospheric ozone return dates and ozone recovery in CCMVal-2 models. *Atmospheric Chemistry and Physics*, *10*(19), 9451–9472. https://doi.org/10.5194/acp-10-9451-2010

Fadnavis, S., Semeniuk, K., Schultz, M. G., Kiefer, M., Mahajan, A., Pozzoli, L., & Sonbawane, S. (2015). Transport pathways of peroxyacetyl nitrate in the upper troposphere and lower stratosphere from different monsoon systems during the summer monsoon season. *Atmospheric Chemistry and Physics*, *15*(20), 11477–11499. https://doi.org/10.5194/acp-15-11477-2015

Fahey, D. W., Kawa, S. R., Woodbridge, E. L., Tin, P., Wilson, J. C., Jonsson, H. H., et al. (1993). In situ measurements constraining the role of sulphate aerosols in mid-latitude ozone depletion. *Nature*, 363(6429), 509-514. https://doi.org/10.1038/363509a0

Fairlie, T. D., Vernier, J. P., Natarajan, M., & Bedka, K. M. (2014). Dispersion of the Nabro volcanic plume and its relation to the Asian summer monsoon. *Atmospheric Chemistry and Physics*, *14*(13), 7045-7057. https://doi.org/10.5194/acp-14-7045-2014

Fernandez, R. P., Barrera, J. A., López-Noreña, A. I., Kinnison, D. E., Nicely, J., Salawitch, R. J., et al. (2021). Intercomparison between surrogate, explicit, and full treatments of vsl bromine chemistry within the cam-chem chemistry-climate model. *Geophysical Research Letters*, *48*(4), e2020GL091125. https://doi.org/10.1029/2020GL091125

Filus, M. T., Atlas, E. L., Navarro, M. A., Meneguz, E., Thomson, D., Ashfold, M. J., et al.(2020). Transport of short-lived halocarbons to the stratosphere over the Pacific Ocean. *Atmospheric Chemistry and Physics*, *20*(2), 1163–1181. https://doi.org/10.5194/acp-20-1163-2020

Fischer, H., de Reus, M., Traub, M., Williams, J., Lelieveld, J., de Gouw, J., et al.(2003). Deep convective injection of boundary layer air into the lowermost stratosphere at midlatitudes. *Atmospheric Chemistry and Physics*, *3*(3), 739–745. https://doi.org/10.5194/acp-3-739-2003

Fischer, H., Wienhold, F. G., Hoor, P., Bujok, O., Schiller, C., Siegmund, P., et al. (2000). Tracer correlations in the northern high latitude lowermost stratosphere: Influence of cross-tropopause mass exchange. *Geophysical Research Letters*, *27*(1), 97-100. https://doi.org/10.1029/1999GL010879

Fish, D. J., & Burton, M. R. (1997). The effect of uncertainties in kinetic and photochemical data on model predictions of stratospheric ozone depletion. *Journal of Geophysical Research Atmospheres*, *102*(21), 25537–25542. https://doi.org/10.1029/97jd01971

Fleming, E. L., Jackman, C. H., Stolarski, R. S., & Douglass, A. R. (2011). A model study of the impact of source gas changes on the stratosphere for 1850–2100. *Atmospheric Chemistry and Physics*, *11*(16), 8515–8541. https://doi.org/10.5194/acp-11-8515-2011

Fromm, M., Alfred, J., Hoppel, K., Hornstein, J., Bevilacqua, R., Shettle, E., et al. (2000). Observations of boreal forest fire smoke in the stratosphere by POAM III, SAGE II, and lidar in 1998. *Geophysical Research Letters*, *27*(9), 1407-1410. https://doi.org/10.1029/1999GL011200

Fromm, M., Servranckx, R., Stocks, B. J., & Peterson, D. A. (2022). Understanding the critical elements of the pyrocumulonimbus storm sparked by high-intensity wildland

fire. *Communications Earth & Environment*, *3*(1), 243. https://doi.org/10.1038/s43247-022-00566-8

Fueglistaler, S., Dessler, A. E., Dunkerton, T. J., Folkins, I., Fu, Q., & Mote, P. W. (2009). Tropical tropopause layer. *Reviews of Geophysics*, *47*(1). https://doi.org/10.1029/2008RG000267

Fusco, A. C., & Salby, M. L. (1999). Interannual Variations of Total Ozone and Their Relationship to Variations of Planetary Wave Activity. *Journal of Climate*, *12*(6), 1619–1629. https://doi.org/10.1175/1520-0442(1999)012<1619:IVOTOA>2.0.CO;2

Gao, R. S., Fahey, D. W., Del Negro, L. A., Donnelly, S. G., Keim, E. R., Neuman, J. A., et al. (1999). A comparison of observations and model simulations of NOx/NOy in the lower stratosphere. *Geophysical research letters*, *26*(8), 1153-1156. https://doi.org/10.1029/1999GL900162

Garny, H., Hendon, H., Abalos M., Chiodo G., Purich A., Randel W., et al. (2022). Stratospheric Ozone Changes and Climate, Chapter 5 in Scientific Assessment of Ozone Depletion: 2022, GAW Report No. 278, 509 pp., World Meteorological Organization.

Gettelman, A., Mills, M. J., Kinnison, D. E., Garcia, R. R., Smith, A. K., Marsh, D. R., et al. (2019). The Whole Atmosphere Community Climate Model Version 6 (WACCM6). Journal of Geophysical Research: Atmospheres, 124(23), 12380–12403. https://doi.org/10.1029/2019JD030943

Grooß, J. U., Brautzsch, K., Pommrich, R., Solomon, S., & Müller, R. (2011). Stratospheric ozone chemistry in the Antarctic: what determines the lowest ozone values reached and their recovery?. *Atmospheric Chemistry and Physics*, 11(23), 12217-12226. https://doi.org/10.5194/acp-11-12217-2011

Grooß, J. U., Pierce, R. B., Crutzen, P. J., Grose, W. L., & Russell III, J. M. (1997). Re-formation of chlorine reservoirs in southern hemisphere polar spring. *Journal of Geophysical Research: Atmospheres*, 102(D11), 13141-13152. https://doi.org/10.1029/96JD03505

Hall, E. G., Jordan, A. F., Hurst, D. F., Oltmans, S. J., Vömel, H., Kühnreich, B., & Ebert, V. (2016). Advancements, measurement uncertainties, and recent comparisons of the NOAA frost point hygrometer. *Atmospheric Measurement Techniques*, *9*(9), 4295-4310. https://doi.org/10.5194/amt-9-4295-2016

Han, Y., Tian, W., Chipperfield, M. P., Zhang, J., Wang, F., Sang, W., Luo, J., Feng, W., Chrysanthou, A., & Tian, H. (2019). Attribution of the Hemispheric Asymmetries in Trends of Stratospheric Trace Gases Inferred From Microwave Limb Sounder (MLS) Measurements. *Journal of Geophysical Research: Atmospheres*, *124*(12), 6283–6293. https://doi.org/10.1029/2018JD029723

Hanisco, T. F., Lanzendorf, E. J., Wennberg, P. O., Perkins, K. K., Stimpfle, R. M., Voss, P. B., et al. (2001). Sources, sinks, and the distribution of OH in the lower stratosphere. *The Journal of Physical Chemistry A*, 105(9), 1543-1553. https://doi.org/10.1021/jp002334g

Haskins, J. D. (2014). The effects of volcanic aerosols on mid-latitude ozone recovery. (Doctoral dissertation, Massachusetts Institute of Technology).

Haynes, P. H., McIntyre, M. E., Shepherd, T. G., Marks, C. J., & Shine, K. P. (1991). On the "Downward Control" of Extratropical Diabatic Circulations by Eddy-Induced Mean Zonal Forces. *Journal of Atmospheric Sciences*, *48*(4), 651–678. https://doi.org/10.1175/1520-0469(1991)048<0651:OTCOED>2.0.CO;2

Haywood, J., Tilmes, S., Jones, A., Keutsch, F., Laakso, A., Niemeier, U., et al. (2022). Stratospheric Aerosol Injection and its Potential Effect on the Stratospheric Ozone Layer, Chapter 6 in Scientific Assessment of Ozone Depletion: 2022, GAW Report No. 278, WMO, Geneva, Switzerland. Geneva, Switzerland.

Heckendorn, P., Weisenstein, D., Fueglistaler, S., Luo, B. P., Rozanov, E., Schraner, M., et al. (2009). The impact of geoengineering aerosols on stratospheric temperature and ozone. Environmental Research Letters, 4(4), 045108. https://doi.org/10.1088/1748-9326/4/4/045108

Hersbach, H., Bell, B., Berrisford, P., Hirahara, S., Horányi, A., Muñoz-Sabater, J., et al. (2020). The ERA5 global reanalysis. *Quarterly Journal of the Royal Meteorological Society,* 146(730), 1999-2049. https://doi.org/10.1002/qj.3803

Hintsa, E. J., Moore, F. L., Hurst, D. F., Dutton, G. S., Hall, B. D., Nance, J. D., et al. (2021). UAS Chromatograph for Atmospheric Trace Species (UCATS)–a versatile instrument for trace gas measurements on airborne platforms. *Atmospheric Measurement Techniques*, *14*(10), 6795-6819. https://doi.org/10.5194/amt-14-6795-2021

Hintsa, E. J., Weinstock, E. M., Anderson, J. G., May, R. D., & Hurst, D. F. (1999). On the accuracy of in situ water vapor measurements in the troposphere and lower stratosphere with the Harvard Lyman-α hygrometer. *Journal of Geophysical Research: Atmospheres*, *104*(D7), 8183-8189. https://doi.org/10.1029/1998JD100110

Hofmann, D. J., & Solomon, S. (1989). Ozone destruction through heterogeneous chemistry following the eruption of El Chichon. *Journal of Geophysical Research*, *94*(D4), 5029–5041. https://doi.org/10.1029/JD094iD04p05029

Hofmann, D. J., Oltmans, S. J., Komhyr, W. D., Harris, J. M., Lathrop, J. A., Langford, A. O., et al. (1994). Ozone loss in the lower stratosphere over the United States in 1992–1993: Evidence for heterogeneous chemistry on the Pinatubo aerosol. *Geophysical Research Letters*, 21(1), 65-68. https://doi.org/10.1029/93GL02526

Holder, A. L., Ahmed, A., Vukovich, J. M., & Rao, V. (2023). Hazardous air pollutant emissions estimates from wildfires in the wildland urban interface. *PNAS Nexus*, *2*(6). https://doi.org/10.1093/pnasnexus/pgad186

Holton, J. R., P. H. Haynes, M. E. McIntyre, A. R. Douglas, R. B. Rood, & L. Pfister (1995), Stratosphere-troposphere exchange, *Rev. Geophys.*, **33**, 403–439. https://doi.org/10.1029/95RG02097

Homeyer, C. (2024). Data for JGR-Atmospheres Paper: Stratospheric Hydration Processes in Tropopause-Overshooting Convection Revealed by Tracer-Tracer Correlations from the DCOTSS Field Campaign [Data set]. *Zenodo*. https://doi.org/10.5281/zenodo.10909195

Homeyer, C. R., & Bowman, K. P. (2021). A 22-Year Evaluation of Convection Reaching the Stratosphere Over the United States. *Journal of Geophysical Research: Atmospheres*, *126*(13), e2021JD034808. https://doi.org/10.1029/2021JD034808

Homeyer, C. R., & Bowman, K. P. (2022). Algorithm description document for version 4.2 of the three-dimensional gridded NEXRAD WSR-88Dradar (GridRad) dataset (Tech. Rep.). Retrieved from http://gridrad.org/

Homeyer, C. R., Smith, J. B., Bedka, K. M., Bowman, K. P., Wilmouth, D. M., Ueyama, R., et al. (2023). Extreme altitudes of stratospheric hydration by midlatitude convection observed during the DCOTSS field campaign. *Geophysical Research Letters*, 50, e2023GL104914. https://doi.org/10.1029/2023GL104914

Hossaini, R., Atlas, E., Dhomse, S. S., Chipperfield, M. P., Bernath, P. F., Fernando, A. M., et al. (2019). Recent trends in stratospheric chlorine from very short-lived substances. *Journal of Geophysical Research: Atmospheres*, *124*(4), 2318-2335. https://doi.org/10.1029/2018JD029400

Hossaini, R., Carpenter, L., Chipperfield, M., Kinnison, D., & Tegtmeier, S. (2024a). *Impact of chlorinated very short-lived substances on stratospheric ozone (VSLS-MIP)*, APARC Newsletter No. 62, 2024, p. 20. https://lec-atmos.org/initiatives/vsls-mip1/

Hossaini, R., Chipperfield, M. P., Montzka, S. A., Leeson, A. A., Dhomse, S. S., & Pyle, A. (2017). The increasing threat to stratospheric ozone from dichloromethane. *Nature Communications*, *8*(1), 15962. https://doi.org/10.1038/ncomms15962

Hossaini, R., Chipperfield, M. P., Saiz-Lopez, A., Harrison, J., von Glasow, R., Sommariva, R., et al. (2015). Growth in stratospheric chlorine from short-lived chemicals not controlled by the Montreal Protocol. *Geophysical Research Letters*, *42*(11), 4573-4580. https://doi.org/10.1002/2015GL063783

Hossaini, R., Sherry, D., Wang, Z., Chipperfield, M. P., Feng, W., Oram, D. E., et al. (2024b). On the atmospheric budget of 1,2-dichloroethane and its impact on stratospheric chlorine and ozone (2002–2020). *Atmospheric Chemistry and Physics*, *24*(23), 13457–13475. https://doi.org/10.5194/acp-24-13457-2024

Howar, L. V., Salawitch, R. J., Wilmouth, D. M., Hintsa, E. J., Hare, J. S., Hanisco, T. F., et al. (2025). Conditions necessary for chlorine activation in the midlatitude summer lower stratosphere. *Journal of Geophysical Research: Atmospheres*, *130*(20), e2025JD043786. https://doi.org/10.1029/2025JD043786

Howar, L., & Salawitch, R. (2025). Photodissociation Frequencies and Trajectory Model Output for JGR-Atmospheres Paper: Conditions Necessary for Chlorine Activation in the Midlatitude Summer Lower Stratosphere [Data set]. *Zenodo*. https://doi.org/10.5281/zenodo.14968099

Huntrieser, H., Lichtenstern, M., Scheibe, M., Aufmhoff, H., Schlager, H., Pucik, T., et al. (2016a). On the origin of pronounced O3 gradients in the thunderstorm outflow region during DC3. *Journal of Geophysical Research: Atmospheres*, *121*(11), 6600-6637. https://doi.org/10.1002/2015JD024279

Huntrieser, H., Lichtenstern, M., Scheibe, M., Aufmhoff, H., Schlager, H., Pucik, T., et al. (2016b). Injection of lightning-produced NOx, water vapor, wildfire emissions, and stratospheric air to the UT/LS as observed from DC3 measurements. Journal of Geophysical Research: Atmospheres, 121(11), 6638-6668. https://doi.org/10.1002/2015JD024273

Jackson, R. B., Saunois, M., Martinez, A., Canadell, J. G., Yu, X., Li, M., et al. (2024). Human activities now fuel two-thirds of global methane emissions. *Environmental Research Letters*, *19*(10), 101002. https://doi.org/10.1088/1748-9326/ad6463

Jaegle, L., Webster, C. R., May, R. D., Fahey, D. W., Woodbridge, E. L., Keim, E. R., et al. (1994). In situ measurements of the NO_2/NO ratio for testing atmospheric photochemical models. *Geophysical research letters*, *21*(23), 2555-2558. https://doi.org/10.1029/94GL02717

Jöckel, P., Tost, H., Pozzer, A., Kunze, M., Kirner, O., Brenninkmeijer, C. A. M., et al. (2016). Earth System Chemistry Integrated Modelling (ESCiMo) with the Modular Earth Submodel System (MESSy) version 2.51. Geoscientific Model Development, 9(3), 1153–1200. https://doi.org/10.5194/gmd-9-1153-2016

Johnston, P. V., & McKenzie, R. L. (1989). NO2 observations at 45 S during the decreasing phase of solar cycle 21, from 1980 to 1987. *Journal of Geophysical Research: Atmospheres*, 94(D3), 3473-3486. https://doi.org/10.1029/JD094iD03p03473

Jonsson, A. I., de Grandpré, J., Fomichev, V. I., McConnell, J. C., & Beagley, S. R. (2004). Doubled CO2-induced cooling in the middle atmosphere: Photochemical analysis of the ozone radiative feedback. Journal of Geophysical Research D: Atmosphere, 109(24), 1–18. https://doi.org/10.1029/2004JD005093

Jucks, K. W., Johnson, D. G., Chance, K. V., Traub, W. A., & Salawitch, R. J. (1999). Nitric acid in the middle stratosphere as a function of altitude and aerosol loading. *Journal of Geophysical Research Atmospheres*, *104*(D21), 26715–26723. https://doi.org/10.1029/1999JD900330

Jacquot, J. L., Shen, X., Abou-Ghanem, M., Froyd, K. D., Lawler, M., Schill, G. P., et al. (2024). A new airborne single particle mass spectrometer: PALMS-NG. Aerosol Science and Technology, 58(9), 991-1007. https://doi.org/10.1080/02786826.2024.2331549

Kawa, S. R., Stolarski, R. S., Newman, P. A., Douglass, A. R., Rex, M., Hofmann, D. J., et al. (2009). Sensitivity of polar stratospheric ozone loss to uncertainties in chemical reaction kinetics. *Atmospheric Chemistry and Physics*, *9*(22), 8651-8660. https://doi.org/10.5194/acp-9-8651-2009

Kawamiya, M., Hajima, T., Tachiiri, K., Watanabe, S., & Yokohata, T. (2020). Two decades of Earth system modeling with an emphasis on Model for Interdisciplinary Research on Climate (MIROC). Progress in Earth and Planetary Science, 7(1), 64. https://doi.org/10.1186/s40645-020-00369-5

Keeble, J., Brown, H., Abraham, N. L., Harris, N. R. P., & Pyle, J. A. (2018). On ozone trend detection: using coupled chemistry–climate simulations to investigate early signs of total column ozone recovery. *Atmospheric Chemistry and Physics*, *18*(10), 7625–7637. https://doi.org/10.5194/acp-18-7625-2018

Keeble, J., Hassler, B., Banerjee, A., Checa-Garcia, R., Chiodo, G., Davis, S., et al. (2021). Evaluating stratospheric ozone and water vapour changes in CMIP6 models from 1850 to 2100. *Atmospheric Chemistry and Physics*, 21(6), 5015-5061. https://doi.org/10.5194/acp-21-5015-2021

Keim, E. R., Fahey, D. W., Del Negro, L. A., Woodbridge, E. L., Gao, R. S., Wennberg, P. O., et al. (1996). Observations of large reductions in the NO/NOy ratio near the mid-latitude tropopause and the role of heterogeneous chemistry. *Geophysical Research Letters*, 23(22), 3223-3226. https://doi.org/10.1029/96GL02593

Kinnison, D. E., Grant, K. E., Connell, P. S., & Rotman, D. A. (1994). The chemical and radiative effects of the Mount Pinatubo eruption. *Journal of Geophysical Research: Atmospheres*, *99*(D12), 25705–25731. https://doi.org/10.1029/94jd02318

Klobas, E. J., Wilmouth, D. M., Weisenstein, D. K., Anderson, J. G., & Salawitch, R. J. (2017). Ozone depletion following future volcanic eruptions. *Geophysical Research Letters*, *44*(14), 7490-7499. https://doi.org/10.1002/2017GL073972

Ko, M. K., Poulet, G., Blake, D. R., Boucher, O., Burkholder, J. H., Chin, M., et al. (2003). Very Short-Lived Halogen and Sulfur Substances, Chapter 2 in Scientific Assessment of Ozone Depletion: 2002, Global Ozone Research and Monitoring Project–Report No. 47, World Meteorological Organization, Geneva, 2003

Ko, M. K., Sze, N. D., Scott, C. J., & Weisenstein, D. K. (1997). On the relation between stratospheric chlorine/bromine loading and short-lived tropospheric source gases. *Journal*

of Geophysical Research: Atmospheres, *102*(D21), 25507-25517. https://doi.org/10.1029/97JD02431

Kondo, Y., Sugita, T., Koike, M., Kawa, S. R., Danilin, M. Y., Rodriguez, J. M., et al. (2000). Partitioning of reactive nitrogen in the midlatitude lower stratosphere. *Journal of Geophysical Research Atmospheres*, *105*(D1), 1417–1424. https://doi.org/10.1029/1999JD901012

Krysztofiak, G., Catoire, V., de Wit, T., Kinnison, D. E., Ravishankara, A. R., Brocchi, V., et al. (2023). N2O Temporal Variability from the Middle Troposphere to the Middle Stratosphere Based on Airborne and Balloon-Borne Observations during the Period 1987–2018. *Atmosphere*, *14*(3). https://doi.org/10.3390/atmos14030585

Kuttippurath, J., Feng, W., Müller, R., Kumar, P., Raj, S., Gopikrishnan, G. P., & Roy, R. (2021). Exceptional loss in ozone in the Arctic winter/spring of 2019/2020. *Atmospheric Chemistry and Physics*, *21*(18), 14019–14037. https://doi.org/10.5194/acp-21-14019-2021

Lan, X., K.W. Thoning, and E.J. Dlugokencky: Trends in globally-averaged CH4, N2O, and SF6 determined from NOAA Global Monitoring Laboratory measurements. Version 2026-05, https://doi.org/10.15138/P8XG-AA10

Laube, J. C., Tegtmeier S., Fernandez R. P., Harrison J., Hu L., Krummel P., et al. (2022). Update on ozone-depleting substances (ODSs) and other gases of interest to the Montreal protocol. Chapter 1 in Scientific Assessment of Ozone Depletion 2022, *GAW Report No. 278*, 509 pp. WMO, Geneva.

Lauther, V., Vogel, B., Wintel, J., Rau, A., Hoor, P., Bense, V., et al. (2022). In situ observations of CH_2Cl_2 and $CHCl_3$ show efficient transport pathways for very short-lived species into the lower stratosphere via the Asian and the North American summer monsoon. *Atmospheric chemistry and physics*, *22*(3), 2049-2077. https://doi.org/10.5194/acp-22-2049-2022

Law, B. E., Abatzoglou, J. T., Schwalm, C. R., Byrne, D., Fann, N., & Nassikas, N. J. (2025). Anthropogenic climate change contributes to wildfire particulate matter and related mortality in the United States. *Communications Earth & Environment*, *6*(1), 336. https://doi.org/10.1038/s43247-025-02314-0

Lean, J. L. (2014). Evolution of Total Atmospheric Ozone from 1900 to 2100 Estimated with Statistical Models. *Journal of the Atmospheric Sciences*, *71*(6), 1956–1984. https://doi.org/10.1175/JAS-D-13-052.1

Lee-Taylor, J., Hu, Z., Kyle, J., Karipidis, K., Henderson, S., Landolfi, R., Tasich, C. M., & Madronich, S. (2026). Effects of Ozone-Depleting Substances on Ultraviolet Radiation and Skin Cancer Rates in Australia and the United States of America. *GeoHealth*, *10*(5), e2024GH001283. https://doi.org/10.1029/2024GH001283

Li, Q., Jacob, D. J., Park, R., Wang, Y., Heald, C. L., Hudman, R., Yantosca, R. M., Martin, R. V., & Evans, M. (2005). North American pollution outflow and the trapping of convectively lifted pollution by upper-level anticyclone. *Journal of Geophysical Research D: Atmospheres*, *110*(10), 1–18. https://doi.org/10.1029/2004JD005039

Li, Y., Pedersen, C., Dykema, J., Vernier, J. P., Vattioni, S., Pandit, A. K., et al. (2023). In situ measurements of perturbations to stratospheric aerosol and modeled ozone and radiative impacts following the 2021 La Soufrière eruption. *Atmospheric Chemistry and Physics*, *23*(24), 15351-15364. https://doi.org/10.5194/acp-23-15351-2023

Liang, Q., Newman, P. A., Fleming, E. L., Lait, L. R., Atlas, E., Pan, L., et al. (2025). Asian Summer Monsoon Anticyclone—The Primary Entryway for Chlorinated Very-Short-Lived Substances to the Stratosphere. *Geophysical Research Letters*, *52*(3). https://doi.org/10.1029/2024GL110248

Liang, Q., Strahan, S. E., & Fleming, E. L. (2017). Concerns for ozone recovery. *Science*, *358*(6368), 1257-1258. https://doi.org/10.1126/science.aaq0145

Lickley, M. J., Daniel, J. S., McBride, L. A., Salawitch, R. J., & Velders, G. J. M. (2024). The return to 1980 stratospheric halogen levels: a moving target in ozone assessments from 2006 to 2022. *Atmospheric Chemistry and Physics*, *24*(22), 13081–13099. https://doi.org/10.5194/acp-24-13081-2024

List, R. J. (1951). Smithsonian meteorological tables. *Smithsonian miscellaneous collections*.

Liu, J., Strode, S. A., Liang, Q., Oman, L. D., Colarco, P. R., Fleming, E. L., et al. (2022). Change in tropospheric ozone in the recent decades and its contribution to global total ozone. *Journal of Geophysical Research: Atmospheres*, 127(22). https://doi.org/10.1029/2022JD037170

Livesey, N. J., Read, W. G., Wagner, P. A., Froidevaux, L., Santee, M. L., Schwartz, M. J., et al. (2022). Earth observing system (EOS) aura microwave limb sounder (MLS) version 5.0 x level 2 and 3 data quality and description document, JPL D-105336 Rev A.

Livesey, N., et al. (2011), EOS MLS version 3.3 level 2 data quality and description document, Technical Report, Jet Propulsion Laboratory, California Institute of Technology, Pasadena, California.

Madronich, S., & Gruijl, F. R. D. (1994). Stratospheric ozone depletion between 1979 and 1992: implications for biologically active ultraviolet-B radiation and non-melanoma skin cancer incidence. *Photochemistry and Photobiology*, *59*(5), 541-546. https://doi.org/10.1111/j.1751-1097.1994.tb02980.x

Mahieu, E., Chipperfield, M. P., Notholt, J., Reddmann, T., Anderson, J., Bernath, P. F., et al. (2014). Recent Northern Hemisphere stratospheric HCl increase due to atmospheric circulation changes. *Nature*, *515*(7525), 104–107. https://doi.org/10.1038/nature13857

Mahieu, E., Zander, R., Duchatelet, P., Hannigan, J. W., Coffey, M. T., Mikuteit, S., et al. (2005). Comparisons between ACE-FTS and ground-based measurements of stratospheric HCl and $ClONO_2$ loadings at northern latitudes. *Geophysical research letters*, *32*(15). https://doi.org/10.1029/2005GL022396

Manney, G. L., Livesey, N. J., Santee, M. L., Froidevaux, L., Lambert, A., Lawrence, Z. D., et al. (2020). Record-Low Arctic Stratospheric Ozone in 2020: MLS Observations of Chemical Processes and Comparisons With Previous Extreme Winters. *Geophysical Research Letters*, *47*(16), e2020GL089063. https://doi.org/10.1029/2020GL089063

Marcy, T. P., Fahey, D. W., Gao, R. S., Popp, P. J., Richard, E. C., Thompson, T. L., et al. (2004). Quantifying Stratospheric Ozone in the Upper Troposphere with in Situ Measurements of HCl. *Science*, *304*(5668), 261–265. https://doi.org/10.1126/science.1093418

McElroy, M. B., Salawitch, R. J., & Minschwaner, K. (1992). The changing stratosphere. *Planetary and Space Science*, *40*(2), 373–401. https://doi.org/10.1016/0032-0633(92)90070-5

McElroy, M. B., Salawitch, R. J., Wofsy, S. C., & Logan, J. A. (1986). Reductions of Antarctic ozone due to synergistic interactions of chlorine and bromine. *Nature*, *321*(6072), 759–762. https://doi.org/10.1038/321759a0

Meinshausen, M., Nicholls, Z. R. J., Lewis, J., Gidden, M. J., Vogel, E., Freund, M., et al. (2020). The shared socio-economic pathway (SSP) greenhouse gas concentrations and their extensions to 2500. *Geoscientific Model Development*, *13*(8), 3571–3605. https://doi.org/10.5194/gmd-13-3571-2020

Mertens, L. A., Winiberg, F. A., Allen, H. M., Sander, S. P., & Okumura, M. (2022). Yields of HONO2 and HOONO products from the reaction of HO2 and NO using pulsed laser photolysis and mid-infrared cavity-ringdown spectroscopy. The Journal of Physical Chemistry A, 126(40), 7342-7360. https://doi.org/10.1021/acs.jpca.2c04643

Michael, J. V., Allen Jr, J. E., & Brobst, W. D. (1981). Temperature dependence of the nitric oxide + ozone reaction rate from 195 to 369 K. *The Journal of Physical Chemistry*, 85(26), 4109-4117. https://doi.org/10.1021/j150626a032

Michelsen, H. A., Salawitch, R. J., Gunson, M. R., Aellig, C., Kämpfer, N., Abbas, M. M., et al. (1996). Stratospheric chlorine partitioning: Constraints from shuttle-borne measurements of [HCl], [ClNO3], and [ClO]. *Geophysical Research Letters*, *23*(17), 2361–2364. https://doi.org/10.1029/96GL00787

Millan, L., Santee, M. L., Lambert, A., Livesey, N. J., Werner, F., Schwartz, M. J., et al. (2022). The Hunga Tonga-Hunga Ha'apai hydration of the stratosphere. *Geophysical Research Letters*, *49*(13), e2022GL099381. https://doi.org/10.1029/2022GL099381

Miller, B. R., & Kuijpers, L. J. M. (2011). Projecting future HFC-23 emissions. *Atmospheric Chemistry and Physics*, *11*(24), 13259–13267. https://doi.org/10.5194/acp-11-13259-2011

Minschwaner, K., Salawitch, R. J., & McElroy, M. B. (1993). Absorption of solar radiation by O2: implications for O3 and lifetimes of N2O, CFCl3, and CF2Cl2. *Journal of Geophysical Research*, *98*(D6). https://doi.org/10.1029/93jd00223

Molina, L. T., & Molina, M. J. (1987). Production of chlorine oxide (Cl2O2) from the self-reaction of the chlorine oxide (ClO) radical. *Journal of Physical Chemistry*, *91*(2), 433-436.

Molina, M. J., & Rowland, F. S. (1974). Stratospheric sink for chlorofluoromethanes: chlorine atom-catalysed destruction of ozone. *Nature*, *249*(5460), 810-812. https://doi.org/10.1038/249810a0

Montzka, S. A., Dutton, G. S., Portmann, R. W., Chipperfield, M. P., Davis, S., Feng, W., et al. (2021). A decline in global CFC-11 emissions during 2018−2019. *Nature*, *590*(7846), 428–432. https://doi.org/10.1038/s41586-021-03260-5

Montzka, S. A., Dutton, G. S., Yu, P., Ray, E., Portmann, R. W., Daniel, J. S., et al. (2018). An unexpected and persistent increase in global emissions of ozone-depleting CFC-11. *Nature*, *557*(7705), 413–417. https://doi.org/10.1038/s41586-018-0106-2

Morgenstern, O., Braesicke, P., O'Connor, F. M., Bushell, A. C., Johnson, C. E., Osprey, S. M., & Pyle, J. A. (2009). Evaluation of the new UKCA climate-composition model-Part 1: The stratosphere. Geoscientific Model Development, 2(1), 43–57. https://doi.org/10.5194/gmd-2-43-2009

Morgenstern, O., Hegglin, M. I., Rozanov, E., O'Connor, F. M., Abraham, N. L., Akiyoshi, H., et al. (2017). Review of the global models used within phase 1 of the Chemistry–Climate Model Initiative (CCMI). *Geoscientific Model Development*, *10*(2), 639–671. https://doi.org/10.5194/gmd-10-639-2017

Musin, O. R. (1997). Properties of the Delaunay triangulation. *Proceedings of the thirteenth annual symposium on Computational geometry* (pp. 424-426).

NASA Headquarters (2026, February 5). *NASA Selects Two Earth System Explorers Missions [Press release]*. https://www.nasa.gov/news-release/nasa-selects-two-earth-system-explorers-missions/

NASA/LARC/SD/ASDC. (2022a). Dynamics and Chemistry of the Summer Stratosphere Airborne Data Products [Dataset]. NASA Langley Atmospheric Science Data Center DAAC. https://doi.org/10.5067/ASDC/DCOTSS-Aircraft-Data_1

NASA/LARC/SD/ASDC. (2022b). Dynamics and Chemistry of the Summer Stratosphere Balloon Data Products [Dataset]. NASA Langley Atmospheric Science Data Center DAAC. https://doi.org/10.5067/ASDC/DCOTSS-Balloon-Data_1

NASA/LARC/SD/ASDC. (2022c). Dynamics and Chemistry of the Summer Stratosphere Radar and Satellite (Remote Sensing) Data Products [Dataset]. NASA Langley Atmospheric Science Data Center DAAC. https://doi.org/10.5067/ASDC/DCOTSS-Radar-Satellite-Data_1

NASA/LARC/SD/ASDC. (2022d). Dynamics and Chemistry of the Summer Stratosphere Model Output [Dataset]. NASA Langley Atmospheric Science Data Center DAAC. https://doi.org/10.5067/ASDC/DCOTSS-Model-Output_1

NASA/LARC/SD/ASDC. (2024). SAGE III/ISS L2 Solar Event Species Profiles (Native) (Version 5.3) [Dataset]. NASA Langley Atmospheric Science Data Center DAAC. https://doi.org/10.5067/ISS/SAGEIII/SOLAR_BINARY_L2-V5.3

Nassar, R., Bernath, P. F., Boone, C. D., Clerbaux, C., Coheur, P. F., Dufour, G., et al. (2006). A global inventory of stratospheric chlorine in 2004. *Journal of Geophysical Research: Atmospheres*, 111(D22). https://doi.org/10.1029/2006JD007073

National Academies of Sciences, Engineering, and Medicine. (2021). *Reflecting Sunlight: Recommendations for Solar Geoengineering Research and Research Governance*. Washington, DC: *The National Academies Press*. https://doi.org/10.17226/25762

Newman, P. A., Lait, L. R., Kramarova, N. A., Coy, L., Frith, S. M., Oman, L. D., & Dhomse, S. S. (2024). Record High March 2024 Arctic Total Column Ozone. *Geophysical Research Letters*, *51*(18), e2024GL110924. https://doi.org/10.1029/2024GL110924

Newman, P. A., Nash, E. R., Kawa, S. R., Montzka, S. A., & Schauffler, S. M. (2006). When will the Antarctic ozone hole recover? *Geophysical Research Letters*, *33*(12). https://doi.org/10.1029/2005GL025232

Oman, L. D., Douglass, A. R., Ziemke, J. R., Rodriguez, J. M., Waugh, D. W., & Nielsen, J. E. (2013). The ozone response to Enso in aura satellite measurements and a chemistry-climate simulation. Journal of Geophysical Research: Atmospheres, 118(2), 965–976. https://doi.org/10.1029/2012JD018546

Oman, L. D., Plummer, D. A., Waugh, D. W., Austin, J., Scinocca, J. F., Douglass, A. R., et al. (2010a). Multimodel assessment of the factors driving stratospheric ozone evolution over the 21st century. *Journal of Geophysical Research: Atmospheres*, 115(D24). https://doi.org/10.1029/2010JD014362

Oman, L. D., Waugh, D. W., Kawa, S. R., Stolarski, R. S., Douglass, A. R., & Newman, P. A. (2010b). Mechanisms and feedback causing changes in upper stratospheric ozone in the 21st century. *Journal of Geophysical Research Atmospheres*, *115*(5). https://doi.org/10.1029/2009JD012397

Orbe, C., Wargan, K., Pawson, S., & Oman, L. D. (2020). Mechanisms Linked to Recent Ozone Decreases in the Northern Hemisphere Lower Stratosphere. *Journal of Geophysical Research: Atmospheres*, *125*(9), e2019JD031631. https://doi.org/10.1029/2019JD031631

Osterman, G. B., Salawitch, R. J., Sen, B., Toon, G. C., Stachnik, R. A., Pickett, H. M., et al. (1997). Balloon-borne measurements of stratospheric radicals and their precursors: Implications for the production and loss of ozone. *Geophysical Research Letters*, *24*(9), 1107–1110. https://doi.org/10.1029/97GL00921

Osterman, G. B., Sen, B., Toon, G. C., Salawitch, R. J., Margitan, J. J., Blavier, J. F., et al. (1999). Partitioning of NOy species in the summer Arctic stratosphere. *Geophysical Research Letters*, *26*(8), 1157–1160. https://doi.org/10.1029/1999GL900166

Østerstrøm, F. F., Klobas, J. E., Kennedy, R. P., Cadoux, A., & Wilmouth, D. M. (2023). Sensitivity of stratospheric ozone to the latitude, season, and halogen content of a contemporary explosive volcanic eruption. *Scientific Reports*, *13*(1), 6457. https://doi.org/10.1038/s41598-023-32574-9

Ott, L. E., Bacmeister, J., Pawson, S., Pickering, K., Stenchikov, G., Suarez, M., et al. (2009). Analysis of Convective Transport and Parameter Sensitivity in a Single Column Version of the Goddard Earth Observation System, Version 5, General Circulation Model. *Journal of the Atmospheric Sciences*, *66*(3), 627–646. https://doi.org/10.1175/2008JAS2694.1

Pan, L. L., Atlas, E. L., Honomichl, S. B., Smith, W. P., Kinnison, D. E., Solomon, S., et al. (2024). East Asian summer monsoon delivers large abundances of very short-lived organic chlorine substances to the lower stratosphere. *Proceedings of the National Academy of Sciences*, *121*(12), e2318716121. https://doi.org/10.1073/pnas.2318716121

Pan, L. L., Paulik, L. C., Honomichl, S. B., Munchak, L. A., Bian, J., Selkirk, H. B., & Vömel, H. (2014). Identification of the tropical tropopause transition layer using the ozone-water vapor relationship. *Journal of Geophysical Research: Atmospheres*, 119(6), 3586-3599. https://doi.org/10.1002/2013JD020558

Pérez-Invernón, F. J., Gordillo-Vázquez, F. J., van der Velde, O., Montanyá, J., López Trujillo, J. A., Pineda, N., et al. (2023). Lightning-Produced Nitrogen Oxides Per Flash Length Obtained by Using TROPOMI Observations and the Ebro Lightning Mapping Array. *Geophysical Research Letters*, *50*(24), e2023GL104699. https://doi.org/10.1029/2023GL104699

Perry, R. A., Atkinson, R., & Pitts Jr, J. N. (1977). Rate constants for the reaction of OH radicals with dimethyl ether and vinyl methyl ether over the temperature range 299–427 K. *The Journal of Chemical Physics*, *67*(2), 611-614. https://doi.org/10.1063/1.434862

Pickering, K. E., Li, Y., Cummings, K. A., Barth, M. C., Allen, D. J., Bruning, E. C., & Pollack, I. B. (2024). Lightning NOx in the 29–30 May 2012 Deep Convective Clouds and Chemistry (DC3) Severe Storm and Its Downwind Chemical Consequences. *Journal of Geophysical Research: Atmospheres*, *129*(11), e2023JD039439. https://doi.org/10.1029/2023JD039439

Pittman, J. V., Daube, B. C., Wofsy, S. C., Atlas, E. L., Navarro, M. A., Hintsa, E. J., et al. (2025). Aircraft observations of biomass burning pollutants in the equatorial lower stratosphere over the tropical western Pacific during boreal winter. *Atmospheric Chemistry and Physics*, *25*(14), 7543-7562. https://doi.org/10.5194/acp-25-7543-2025

Ploeger, F., & Garny, H. (2022). Hemispheric asymmetries in recent changes in the stratospheric circulation. *Atmospheric Chemistry and Physics*, *22*(8), 5559–5576. https://doi.org/10.5194/acp-22-5559-2022

Plumb, R. A. (2002). Stratospheric Transport. In *Journal of the Meteorological Society of Japan* (Vol. 80, Number 4B). https://doi.org/10.2151/jmsj.80.793

Plummer, D., Nagashima, T., Tilmes, S., Archibald, A., Chiodo, G., Fadnavis, S., et al. (2021). CCMI-2022: a new set of Chemistry–Climate Model Initiative (CCMI) community simulations to update the assessment of models and support upcoming ozone assessment activities. *SPARC Newsletter*, *57*, 22-30. https://aparc-climate.org/wp-content/uploads/2025/10/SPARCnewsletter_Jul2021_web.pdf

Portmann, R. W., Brown, S. S., Gierczak, T., Talukdar, R. K., Burkholder, J. B., & Ravishankara, A. R. (1999). Role of nitrogen oxides in the stratosphere: A reevaluation based on laboratory studies. *Geophysical Research Letters*, *26*(15), 2387–2390. https://doi.org/10.1029/1999GL900499

Poulida, O., Dickerson, R. R., & Heymsfield, A. (1996). Stratosphere-troposphere exchange in a midlatitude mesoscale convective complex 1. Observations. *Journal of Geophysical Research Atmospheres*, *101*(D3), 6823–6836. https://doi.org/10.1029/95JD03523

Prasad, S. S. (2003). A modeling study of the stratospheric NOx/NOy and NOx/HNO3 ratios: Single- versus dual-channeled mode of OH, NO2 association. *Journal of Geophysical Research: Atmospheres*, *108*(15). https://doi.org/10.1029/2002jd002970

Prather, M. J. (1981). Ozone in the upper stratosphere and mesosphere. *Journal of Geophysical Research: Oceans*, *86*(C6), 5325-5338. https://doi.org/10.1029/JC086iC06p05325

Prignon, M., Chabrillat, S., Friedrich, M., Smale, D., Strahan, S. E., Bernath, P. F., et al. (2021). Stratospheric Fluorine as a Tracer of Circulation Changes: Comparison Between Infrared Remote-Sensing Observations and Simulations With Five Modern Reanalyses. *Journal of Geophysical Research: Atmospheres*, *126*(19). https://doi.org/10.1029/2021JD034995

Prinn, R. G., Weiss, R. F., Arduini, J., Arnold, T., DeWitt, H. L., Fraser, P. J., et al. (2018). History of chemically and radiatively important atmospheric gases from the Advanced Global Atmospheric Gases Experiment (AGAGE). *Earth System Science Data*, *10*(2), 985–1018. https://doi.org/10.5194/essd-10-985-2018

Ravishankara, A. R., Daniel, J. S., & Portmann, R. W. (2009). Nitrous Oxide (N_2O): The Dominant Ozone-Depleting Substance Emitted in the 21st Century. *Science*, *326*(5949), 123–125. https://doi.org/10.1126/science.1176985

Ray, E. A., Moore, F. L., Garny, H., Hintsa, E. J., Hall, B. D., Dutton, G. S., et al. (2024). Age of air from in situ trace gas measurements: insights from a new technique. *Atmospheric Chemistry and Physics*, *24*(21), 12425-12445. https://doi.org/10.5194/acp-24-12425-2024

Raymond, N., Bernath, P., Boone, C., & Chipperfield, M. P. (2026). Twenty-One Years of Global Atmospheric Chlorine Inventories From Atmospheric Chemistry Experiment Fourier Transform Spectrometer (ACE-FTS) Measurements. *Journal of Geophysical Research: Atmospheres*, *131*(5), e2025JD045176. https://doi.org/10.1029/2025JD045176

Revell, L. E., Bodeker, G. E., Huck, P. E., Williamson, B. E., & Rozanov, E. (2012). The sensitivity of stratospheric ozone changes through the 21st century to N_2O and CH_4. *Atmospheric Chemistry and Physics*, *12*(23), 11309–11317. https://doi.org/10.5194/acp-12-11309-2012

Revell, L. E., Bodeker, G. E., Smale, D., Lehmann, R., Huck, P. E., Williamson, B. E., Rozanov, E., & Struthers, H. (2012). The effectiveness of N2O in depleting stratospheric ozone. *Geophysical Research Letters*, *39*(15). https://doi.org/10.1029/2012GL052143

Robrecht, S., Vogel, B., Grooß, J. U., Rosenlof, K., Thornberry, T., Rollins, A., et al. (2019). Mechanism of ozone loss under enhanced water vapour conditions in the mid-latitude lower stratosphere in summer. *Atmospheric chemistry and physics*, 19(9), 5805-5833. https://doi.org/10.5194/acp-19-5805-2019

Robrecht, S., Vogel, B., Tilmes, S., & Müller, R. (2021). Potential of future stratospheric ozone loss in the midlatitudes under global warming and sulfate geoengineering. *Atmospheric Chemistry and Physics*, *21*(4), 2427-2455. https://doi.org/10.5194/acp-21-2427-2021

Roozitalab, B., Emmons, L. K., Hornbrook, R. S., Kinnison, D. E., Fernandez, R. P., Li, Q., et al. (2024). Measurements and Modeling of the Interhemispheric Differences of Atmospheric Chlorinated Very Short-Lived Substances. *Journal of Geophysical Research: Atmospheres*, *129*(2), e2023JD039518. https://doi.org/10.1029/2023JD039518

Rosenfield, J. E., Douglass, A. R., & Considine, D. B. (2002). The impact of increasing carbon dioxide on ozone recovery. *Journal of Geophysical Research: Atmospheres*, *107*(D6), ACH 7-1-ACH 7-9. https://doi.org/10.1029/2001JD000824

Salawitch, R. (2022). The Future Recovery of Stratospheric Ozone: Influence of ODSs, VSLS Cl, and GHGs. (p. 58). *Proposal to NASA ACMAP*. https://ui.adsabs.harvard.edu/abs/2022acma.prop...58S/abstract

Salawitch, R. J., & McBride, L. A. (2022). Australian wildfires depleted the ozone layer. *Science*, *378*(6622), 829–830. https://doi.org/10.1126/science.add2056

Salawitch, R. J., McBride, L. A., Thompson, C. R., Fleming, E. L., McKenzie, R. L., Rosenlof, K. H., et al. (2022). Twenty Questions and Answers About the Ozone Layer: 2022 Update, Scientific Assessment of Ozone Depletion: 2022, 75 pp. *World Meteorological Organization, Geneva, Switzerland*.

Salawitch, R. J., Smith, J. B., Selkirk, H., Wargan, K., Chipperfield, M. P., Hossaini, R., et al. (2025). The Imminent Data Desert: The Future of Stratospheric Monitoring in a Rapidly Changing World. *Bulletin of the American Meteorological Society*. https://doi.org/10.1175/BAMS-D-23-0281.1

Salawitch, R. J., Weisenstein, D. K., Kovalenko, L. J., Sioris, C. E., Wennberg, P. O., Chance, K., et al. (2005). Sensitivity of ozone to bromine in the lower stratosphere. *Geophysical research letters*, 32(5). https://doi.org/10.1029/2004GL021504

Salawitch, R. J., Wofsy, S. C., Wennberg, P. O., Cohen, R. C., Anderson, J. G., Fahey, D. W., et al. (1994a). The distribution of hydrogen, nitrogen, and chlorine radicals in the lower stratosphere: Implications for changes in O_3 due to emission of NO_y from supersonic aircraft. *Geophysical research letters*, *21*(23), 2547-2550. https://doi.org/10.1029/94GL02781

Salawitch, R. J., Wofsy, S. C., Wennberg, P. O., Cohen, R. C., Anderson, J. G., Fahey, D. W., et al. (1994b). The diurnal variation of hydrogen, nitrogen, and chlorine radicals: Implications for the heterogeneous production of HNO2. Geophysical research letters, 21(23), 2551-2554. https://doi.org/10.1029/94GL02782

Salby, M. L., & Callaghan, P. F. (2004). Systematic Changes of Northern Hemisphere Ozone and Their Relationship to Random Interannual Changes. *Journal of Climate*, *17*(23), 4512–4521. https://doi.org/10.1175/3206.1

Sander, S. P., Abbatt, J., Barker, J. R., Burkholder, J. B., Friedl, R. R., Golden, D. M., et al. (2011). Chemical kinetics and photochemical data for use in atmospheric studies, Evaluation No. 17. *JPL Publication*, (10-6)

Sander, S. P., Ravishankara, A. R., Friedl, R. R., Demore, W. B., Golden, D. M., Kolb, C. E., et al. (2000). Chemical kinetics and photochemical data for use in stratospheric modeling, Evaluation number 12: Update of key reactions, JPL Publication 00-3.

Santee, M. L., Lambert, A., Froidevaux, L., Manney, G. L., Schwartz, M. J., Millán, L. F., et al. (2023). Strong evidence of heterogeneous processing on stratospheric sulfate aerosol in

the extrapolar Southern Hemisphere following the 2022 Hunga Tonga-Hunga Ha'apai eruption. *Journal of Geophysical Research: Atmospheres*, *128*(16), e2023JD039169. https://doi.org/10.1029/2023JD039169

Santee, M. L., Lambert, A., Manney, G. L., Livesey, N. J., Froidevaux, L., Neu, J. L., et al. (2022). Prolonged and pervasive perturbations in the composition of the Southern Hemisphere midlatitude lower stratosphere from the Australian New Year's fires. *Geophysical Research Letters*, *49*(4), e2021GL096270. https://doi-org.proxy-um.researchport.umd.edu/10.1029/2021GL096270

Santee, M. L., Manney, G. L., Livesey, N. J., Schwartz, M. J., Neu, J. L., & Read, W. G. (2017). A comprehensive overview of the climatological composition of the Asian summer monsoon anticyclone based on 10 years of Aura Microwave Limb Sounder measurements. *Journal of Geophysical Research: Atmospheres*, *122*(10), 5491–5514. https://doi.org/10.1002/2016JD026408

Sargent, M. R., Sayres, D. S., Smith, J. B., Witinski, M., Allen, N. T., Demusz, J. N., et al. (2013). A new direct absorption tunable diode laser spectrometer for high precision measurement of water vapor in the upper troposphere and lower stratosphere. *Review of Scientific Instruments*, 84(7). https://doi.org/10.1063/1.4815828

Saunders, L. N., Walker, K. A., Stiller, G. P., Von Clarmann, T., Haenel, F., Garny, H., et al. (2025). Age of air from ACE-FTS measurements of sulfur hexafluoride. *Atmospheric Chemistry and Physics*, *25*(7), 4185–4209. https://doi.org/10.5194/acp-25-4185-2025

Sayres, D. S., Smith, J. B., Wilmouth, D. M., Pandey, A., Homeyer, C. R., Bowman, K. P., & Anderson, J. G. (2024). Using the NAMA as a Natural Integrator to Quantify the Convective Contribution to Lower Stratospheric Water Vapor Over North America. *Journal of Geophysical Research: Atmospheres*, *129*(17). https://doi.org/10.1029/2024JD041641

Schmidt, M., Bernath, P., Boone, C., Lecours, M., & Steffen, J. (2024). Trends in atmospheric composition between 2004–2023 using version 5 ACE-FTS data. In *Journal of Quantitative Spectroscopy and Radiative Transfer* (Vol. 325). Elsevier Ltd. https://doi.org/10.1016/j.jqsrt.2024.109088

Schoeberl, M. R., Pfister, L., Wang, T., Kummer, J., Dessler, A. E., & Yu, W. (2020). Erythemal radiation, column ozone, and the North American monsoon. *Journal of Geophysical Research: Atmospheres*, 125(13), e2019JD032283. https://doi.org/10.1029/2019JD032283

Schwartz, M. J, Froidevaux, L., Livesey, N., Read, W., and Fuller, R. (2021). MLS/Aura Level 3 Monthly Binned Ozone (O3) Mixing Ratio on Assorted Grids (Version 5.1) [Dataset]. NASA Goddard Earth Sciences Data and Information Services Center (GES DISC). http://doi.org/10.5067/AURA/MLS/DATA/3546

Schwartz, M. J., Read, W. G., Santee, M. L., Livesey, N. J., Froidevaux, L., Lambert, A., & Manney, G. L. (2013). Convectively injected water vapor in the North American summer lowermost stratosphere. *Geophysical Research Letters*, 40(10), 2316-2321. https://doi.org/10.1002/grl.50421

Scinocca, J. F., McFarlane, N. A., Lazare, M., Li, J., &Plummer, D. (2008). Technical note: The CCCma third generation AGCM and its extension into the middle atmosphere. Atmospheric Chemistry and Physics, 8(23), 7055–7074. https://doi.org/10.5194/acp-8-7055-2008

Scott, S. G., Bui, T. P., Chan, K. R., & Bowen, S. W. (1990). The meteorological measurement system on the NASA ER-2 aircraft. *Journal of Atmospheric and Oceanic Technology*, 7(4), 525-540. https://doi.org/10.1175/1520-0426(1990)007<0525:TMMSOT>2.0.CO;2

Sen, B., Osterman, G. B., Salawitch, R. J., Toon, G. C., Margitan, J. J., Blavier, J. F., et al. (1999). The budget and partitioning of stratospheric chlorine during the 1997 Arctic summer. *Journal of Geophysical Research Atmospheres*, *104*(D21), 26653–26665. https://doi.org/10.1029/1999JD900245

Sen, B., Toon, G. C., Osterman, G. B., Blavier, J. F., Margitan, J. J., Salawitch, R. J., & Yue, G. K. (1998). Measurements of reactive nitrogen in the stratosphere. *Journal of Geophysical Research Atmospheres*, *103*(D3), 3571–3585. https://doi.org/10.1029/97JD02468

Shah, V., Jacob, D. J., Dang, R., Lamsal, L. N., Strode, S. A., Steenrod, S. D., et al. (2023). Nitrogen oxides in the free troposphere: implications for tropospheric oxidants and the interpretation of satellite NO_2 measurements. *Atmospheric Chemistry and Physics*, *23*(2), 1227-1257. https://doi.org/10.5194/acp-23-1227-2023

Shaw, T. A., & Shepherd, T. G. (2008). Raising the roof. *Nature geoscience*, *1*(1), 12-13. https://doi.org/10.1038/ngeo.2007.53

Sheese, P. E., Boone, C. D., & Walker, K. A. (2015). Detecting physically unrealistic outliers in ACE-FTS atmospheric measurements. *Atmospheric Measurement Techniques*, *8*(2), 741–750. https://doi.org/10.5194/amt-8-741-2015

Shepherd, T. G. (2007). Transport in the Middle Atmosphere. *Journal of the Meteorological Society of Japan. Ser. II*, *85B*, 165–191. https://doi.org/10.2151/jmsj.85B.165

Shepherd, T. G., & McLandress, C. (2011). A Robust Mechanism for Strengthening of the Brewer–Dobson Circulation in Response to Climate Change: Critical-Layer Control of Subtropical Wave Breaking. *Journal of the Atmospheric Sciences*, *68*(4), 784–797. https://doi.org/10.1175/2010JAS3608.1

Silvern, R. F., Jacob, D. J., Travis, K. R., Sherwen, T., Evans, M. J., Cohen, R. C., et al. (2018). Observed NO/NO2 ratios in the upper troposphere imply errors in NO-NO2-O3 cycling kinetics or an unaccounted NOx reservoir. Geophysical Research Letters, 45(9), 4466-4474. https://doi.org/10.1029/2018GL077728

Smith, K., Atlas, E., Apel, E. C., Blake, D. R., Dutton, G., Hornbrook, R. S., et al. (2024). Chloromethanes in the North American troposphere and lower stratosphere over the past two decades. *Geophysical Research Letters*, *51*(15), e2024GL108710. https://doi.org/10.1029/2024GL108710

Sofieva, V. F., Szelag, M. E., Kramarova, N. A., Damadeo, R., Steinbrecht, W., Petropavlovskikh, I., et al. (2026). Updated global and regional trends of stratospheric ozone profiles. *Atmospheric Chemistry and Physics*, *26*(10), 7387–7405. https://doi.org/10.5194/acp-26-7387-2026

Solomon, S. (1999). Stratospheric ozone depletion: A review of concepts and history. *Reviews of Geophysics*, 37(3), 275-316. https://doi.org/10.1029/1999RG900008

Solomon, S., & Crutzen, P. J. (1981). Analysis of the August 1972 Solar Proton Event including chlorine chemistry. *Journal of Geophysical Research: Oceans*, *86*(C2), 1140–1146. https://doi.org/10.1029/JC086iC02p01140

Solomon, S., Dube, K., Stone, K., Yu, P., Kinnison, D., Toon, O. B., et al. (2022). On the stratospheric chemistry of midlatitude wildfire smoke. *Proceedings of the National Academy of Sciences*, *119*(10), e2117325119. https://doi.org/10.1073/pnas.2117325119

Solomon, S., Garcia, R. R., Rowland, F. S., & Wuebbles, D. J. (1986). On the depletion of Antarctic ozone. *Nature*, *321*(6072), 755–758. https://doi.org/10.1038/321755a0

Solomon, S., Portmann, R. W., Garcia, R. R., Randel, W., Wu, F., Nagatani, R., et al. (1998). Ozone depletion at mid-latitudes: Coupling of volcanic aerosols and temperature variability to anthropogenic chlorine. *Geophysical Research Letters*, *25*(11), 1871-1874. https://doi.org/10.1029/98GL01293

Solomon, S., Portmann, R. W., Garcia, R. R., Thomason, L. W., Poole, L. R., & McCormick, M. P. (1996). The role of aerosol variations in anthropogenic ozone depletion at northern midlatitudes. *Journal of Geophysical Research: Atmospheres*, 101(D3), 6713-6727. https://doi.org/10.1029/95JD03353

Solomon, S., Stone, K., Yu, P., Murphy, D. M., Kinnison, D., Ravishankara, A. R., & Wang, P. (2023). Chlorine activation and enhanced ozone depletion induced by wildfire aerosol. *Nature*, *615*(7951), 259–264. https://doi.org/10.1038/s41586-022-05683-0

St. Clair, J. M., Swanson, A. K., Bailey, S. A., & Hanisco, T. F. (2019). CAFE: A new, improved nonresonant laser-induced fluorescence instrument for airborne in situ measurement of formaldehyde. *Atmospheric Measurement Techniques*, 12(8), 4581-4590. https://doi.org/10.5194/amt-12-4581-2019

Steiner, A. K., Ladstädter, F., Randel, J., Maycock, A. C., Fu, Q., Claud, C., et al. (2020). Observed temperature changes in the troposphere and stratosphere from 1979 to 2018. *Journal of Climate*, *33*(19), 8165-8194. https://doi.org/10.1175/JCLI-D-19-0998.1

Stenchikov, G., Dickerson, R., Pickering, K., Ellis Jr., W., Doddridge, B., Kondragunta, S., Poulida, O., Scala, J., & Tao, W.-K. (1996). Stratosphere-troposphere exchange in a midlatitude mesoscale convective complex: 2. Numerical simulations. *Journal of Geophysical Research: Atmospheres*, *101*(D3), 6837–6851. https://doi.org/10.1029/95JD02468

Sterling, C. W., Johnson, B. J., Oltmans, S. J., Smit, H. G., Jordan, A. F., Cullis, P. D., et al. (2018). Homogenizing and estimating the uncertainty in NOAA's long-term vertical ozone profile records measured with the electrochemical concentration cell ozonesonde. *Atmospheric Measurement Techniques*, *11*(6), 3661-3687. https://doi.org/10.5194/amt-11-3661-2018

Stimpfle, R. M., Cohen, R. C., Bonne, G. P., Voss, P. B., Perkins, K. K., Koch, L. C., et al. (1999). The coupling of ClONO2, ClO, and NO2 in the lower stratosphere from in situ observations using the NASA ER-2 aircraft. *Journal of Geophysical Research Atmospheres*, *104*(D21), 26705–26714. https://doi.org/10.1029/1999JD900288

Stimpfle, R. M., Wilmouth, D. M., Salawitch, R. J., & Anderson, J. G. (2004). First measurements of ClOOCl in the stratosphere: The coupling of ClOOCl and ClO in the Arctic polar vortex. *Journal of Geophysical Research: Atmospheres*, *109*(D3). https://doi.org/10.1029/2003JD003811

Stolarski, R. S., & Cicerone, R. J. (1974). Stratospheric Chlorine: a Possible Sink for Ozone. *Canadian Journal of Chemistry*, *52*(8), 1610–1615. https://doi.org/10.1139/v74-233

Stolarski, R. S., & Douglass, A. R. (1986). Sensitivity of an atmospheric photochemistry model to chlorine perturbations including consideration of uncertainty propagation. *Journal of Geophysical Research: Atmospheres*, *91*(D7), 7853–7864. https://doi.org/10.1029/jd091id07p07853

Stolarski, R. S., Butler, D. M., & Rundel, R. D. (1978). Uncertainty propagation in a stratospheric model 2. Monte Carlo analysis of imprecisions due to reaction

rates. *Journal of Geophysical Research: Oceans*, *83*(C6), 3074-3078. https://doi.org/10.1029/JC083iC06p03074

Stolarski, R. S., Douglass, A. R., Steenrod, S., & Pawson, S. (2006). Trends in Stratospheric Ozone: Lessons Learned from a 3D Chemical Transport Model. *Journal of the Atmospheric Sciences*, *63*(3), 1028–1041. https://doi.org/10.1175/JAS3650.1

Strahan, S. E., Smale, D., Solomon, S., Taha, G., Damon, M. R., Steenrod, S. D., et al. (2022). Unexpected Repartitioning of Stratospheric Inorganic Chlorine After the 2020 Australian Wildfires. *Geophysical Research Letters*, *49*(14), e2022GL098290. https://doi.org/10.1029/2022GL098290

Strahan, S. E., Smale, D., Solomon, S., Taha, G., Damon, M. R., Steenrod, S. D., et al. (2022). Unexpected repartitioning of stratospheric inorganic chlorine after the 2020 Australian wildfires. *Geophysical Research Letters*, *49*(14), e2022GL098290. https://doi.org/10.1029/2022GL098290

Tatebe, H., Ogura, T., Nitta, T., Komuro, Y., Ogochi, K., Takemura, T., et al. (2019). Description and basic evaluation of simulated mean state, internal variability, and climate sensitivity in MIROC6. Geoscientific Model Development, 12(7), 2727–2765. https://doi.org/10.5194/gmd-12-2727-2019

Tevini, M., & Teramura, A. H. (1989). UV-B effects on terrestrial plants. *Photochemistry and Photobiology*, *50*(4), 479-487. https://doi.org/10.1111/j.1751-1097.1989.tb05552.x

Thomason, L. W., Poole, L. R., & Deshler, T. (1997). A global climatology of stratospheric aerosol surface area density deduced from Stratospheric Aerosol and Gas Experiment II measurements: 1984–1994. *Journal of Geophysical Research: Atmospheres*, *102*(D7), 8967-8976. https://doi.org/10.1029/96JD02962

Thornton, B. F., Toohey, D. W., Tuck, A. F., Elkins, J. W., Kelly, K. K., Hovde, S. J., et al. (2007). Chlorine activation near the midlatitude tropopause. *Journal of Geophysical Research: Atmospheres*, *112*(D18). https://doi.org/10.1029/2006JD007640

Tian, H., Pan, N., Thompson, R. L., Canadell, J. G., Suntharalingam, P., Regnier, P., et al. (2024). Global nitrous oxide budget (1980–2020). *Earth System Science Data*, *16*(6), 2543–2604. https://doi.org/10.5194/essd-16-2543-2024

Tilmes, S., Kinnison, D. E., Garcia, R. R., Salawitch, R., Canty, T., Lee-Taylor, J., et al. (2012). Impact of very short-lived halogens on stratospheric ozone abundance and UV radiation in a geo-engineered atmosphere. *Atmospheric Chemistry and Physics*, 12(22), 10945-10955. https://doi.org/10.5194/acp-12-10945-2012

Tilmes, S., Müller, R., & Salawitch, R. (2008). The Sensitivity of Polar Ozone Depletion to Proposed Geoengineering Schemes. *Science*, *320*(5880), 1201–1204. https://doi.org/10.1126/science.1153966

Tilmes, S., Visioni, D., Jones, A., Haywood, J., Séférian, R., Nabat, P., et al. (2022). Stratospheric ozone response to sulfate aerosol and solar dimming climate interventions based on the G6 Geoengineering Model Intercomparison Project (GeoMIP) simulations. *Atmospheric Chemistry and Physics*, *22*(7), 4557-4579. https://doi.org/10.5194/acp-22-4557-2022

Tilstra, L. G., de Graaf, M., Trees, V., Litvinov, P., Dubovik, O., & Stammes, P. (2024). A directional surface reflectance climatology determined from TROPOMI observations. *Atmospheric Measurement Techniques Discussions*, 17, 2235–2256. https://doi.org/10.5194/amt-17-2235-2024

Tracy, S. M., Moch, J. M., Eastham, S. D., & Buonocore, J. J. (2022). Stratospheric aerosol injection may impact global systems and human health outcomes. In *Elementa* (Vol. 10, Number 1). University of California Press. https://doi.org/10.1525/elementa.2022.00047

Tuffnell, E. C., Leedham-Elvidge, E., Sturges, W. T., Bönisch, H., Adcock, K. E., Fraser, P. J., et al. (2026). Observationally-derived Fractional Release Factors, Ozone Depletion Potentials, and Stratospheric Lifetimes of Four Long-Lived CFCs: CFC-13 (CClF3), CFC-114 (C2Cl2F4), CFC-114a (CF3CCl2F), and CFC-115 (C2ClF5). *Atmospheric Chemistry and Physics*, *26*(7), 4583–4599. https://doi.org/10.5194/acp-26-4583-2026

Veefkind, J. P., Aben, I., McMullan, K., Förster, H., De Vries, J., Otter, G., et al. (2012). TROPOMI on the ESA Sentinel-5 Precursor: A GMES mission for global observations of the atmospheric composition for climate, air quality and ozone layer applications. *Remote sensing of environment*, *120*, 70-83. https://doi.org/10.1016/j.rse.2011.09.027

Visioni, D., Kravitz, B., Robock, A., Tilmes, S., Haywood, J. M., Boucher, O., et al. (2023). Opinion: The scientific and community-building roles of the Geoengineering Model Intercomparison Project (GeoMIP)-past, present, and future. *Atmospheric chemistry and physics Discussions*, 23, 5149–5176. https://doi.org/10.5194/acp-23-5149-2023

Vogel, B., Feck, T., & Grooß, J.-U. (2011). Impact of stratospheric water vapor enhancements caused by CH4 and H2O increase on polar ozone loss. *Journal of Geophysical Research: Atmospheres*, *116*(D5). https://doi.org/10.1029/2010JD014234

Vollmer, M. K., Mühle, J., Henne, S., Young, D., Rigby, M., Mitrevski, B., et al. (2021). Unexpected nascent atmospheric emissions of three ozone-depleting hydrochlorofluorocarbons. *Proceedings of the National Academy of Sciences*, *118*(5), e2010914118. https://doi.org/10.1073/pnas.2010914118

Vömel, H., Evan, S., & Tully, M. (2022). Water vapor injection into the stratosphere by Hunga Tonga-Hunga Ha'apai. *Science*, *377*(6613), 1444-1447. https://doi.org/10.1126/science.abq2299

von der Gathen, P., Kivi, R., Wohltmann, I., Salawitch, R. J., & Rex, M. (2021). Climate change favours large seasonal loss of Arctic ozone. *Nature Communications*, *12*(1). https://doi.org/10.1038/s41467-021-24089-6

von Hobe, M., Grooß, J. U., Günther, G., Konopka, P., Gensch, I., Krämer, M., et al. (2011). Evidence for heterogeneous chlorine activation in the tropical UTLS. *Atmospheric Chemistry and Physics*, *11*(1), 241-256. https://doi.org/10.5194/acp-11-241-2011

Voss, P. B., Stimpfle, R. M., Cohen, R. C., Hanisco, T. F., Bonne, G. P., Perkins, K. K., et al. (2001). Inorganic chlorine partitioning in the summer lower stratosphere: Modeled and measured [$ClONO_2$]/[HCl] during POLARIS. *Journal of Geophysical Research: Atmospheres*, *106*(D2), 1713-1732. https://doi.org/10.1029/2000JD900494

Wales, P. A., Salawitch, R. J., Nicely, J. M., Anderson, D. C., Canty, T. P., Baidar, S., et al. (2018). Stratospheric injection of brominated very short-lived substances: Aircraft observations in the Western Pacific and representation in global models. *Journal of Geophysical Research: Atmospheres*, 123(10), 5690-5719. https://doi.org/10.1029/2017JD027978

Wamsley, P. R., Elkins, J. W., Fahey, D. W., Dutton, G. S., Volk, C. M., Myers, R. C., & Salawitch, R. J. (1998). Distribution of halon-1211 in the upper troposphere and lower stratosphere and the 1994 total bromine budget. *Journal of Geophysical Research: Atmospheres*, *103*(D1), 1513-1526. https://doi.org/10.1029/97JD02466

Wang, H. R., Damadeo, R., Flittner, D., Kramarova, N., Taha, G., Davis, S., et al. (2020). Validation of SAGE III/ISS solar occultation ozone products with correlative satellite and ground-based measurements. *Journal of Geophysical Research: Atmospheres*, *125*(11), e2020JD032430. https://doi.org/10.1029/2020JD032430

Wang, S., Bathras, B. L., Cui, W., Milazzo, M., Goldstein, A. H., & Gollner, M. J. (2025). Laboratory Quantification of Emissions from Wildland-Urban Interface Fuels Using Fourier-Transform Infrared Spectroscopy. *Environmental Science and Technology*, *59*(25), 12843–12852. https://doi.org/10.1021/acs.est.5c03514

Wang, W., Wang, X., Flannigan, M. D., Guindon, L., Swystun, T., Castellanos-Acuna, D., Wu, W., & Wang, G. (2025). Canadian forests are more conducive to high-severity fires in recent decades. *Science*, *387*(6729), 91–97. https://doi.org/10.1126/science.ado1006

Wargan, K., Orbe, C., Pawson, S., Ziemke, J. R., Oman, L. D., Olsen, M. A., Coy, L., & Emma Knowland, K. (2018). Recent Decline in Extratropical Lower Stratospheric Ozone Attributed to Circulation Changes. *Geophysical Research Letters*, *45*(10), 5166–5176. https://doi.org/10.1029/2018GL077406

Waugh, D. W., & Hall, T. (2002). Age of stratospheric air: Theory, observations, and models. *Reviews of Geophysics*, *40*(4), 1-1. https://doi.org/10.1029/2000RG000101

Waugh, D. W., Considine, D. B., & Fleming, E. L. (2001). Is upper stratospheric chlorine decreasing as expected? *Geophysical Research Letters*, *28*(7), 1187–1190. https://doi.org/10.1029/2000GL011745

Weber, M., Arosio, C., Coldewey-Egbers, M., Fioletov, V. E., Frith, S. M., Wild, J. D., et al. (2022). Global total ozone recovery trends attributed to ozone-depleting substance (ODS) changes derived from five merged ozone datasets. *Atmospheric Chemistry and Physics*, *22*(10), 6843–6859. https://doi.org/10.5194/acp-22-6843-2022

Webster, C. R., May, R. D., Jaeglé, L., Hu, H., Sander, S. P., Gunson, M. R., et al. (1994). Hydrochloric acid and the chlorine budget of the lower stratosphere. *Geophysical Research Letters*, *21*(23), 2575–2578. https://doi.org/10.1029/94GL02806

Weinstock, E. M., Hintsa, E. J., Dessler, A. E., Oliver, J. F., Hazen, N. L., Demusz, J. N., et al. (1994). New fast response photofragment fluorescence hygrometer for use on the NASA ER-2 and the Perseus remotely piloted aircraft. *Review of scientific instruments*, *65*(11), 3544-3554. https://doi.org/10.1063/1.1144536

Weinstock, E. M., Pittman, J. V, Sayres, D. S., Smith, J. B., Anderson, J. G., Wofsy, S. C., et al. (2007). Quantifying the impact of the North American monsoon and deep midlatitude convection on the subtropical lowermost stratosphere using in situ measurements. *Journal of Geophysical Research: Atmospheres*, *112*(D18). https://doi.org/10.1029/2007JD008554

Wennberg, P. O., Cohen, R. C., Stimpfle, R. M., Koplow, J. P., Anderson, J. G., Salawitch, R. J., et al. (1994). Removal of stratospheric O_3 by radicals: In situ measurements of OH, HO_2, NO, NO_2, ClO, and BrO. *Science*, *266*(5184), 398-404. https://doi.org/10.1126/science.266.5184.398

Western, L. M., Rigby, M., Mühle, J., Krummel, P. B., Lunder, C. R., O'Doherty, S., et al. (2025). Global emissions and abundances of chemically and radiatively important trace gases from the AGAGE network. *Earth System Science Data*, *17*(11), 6557–6582. https://doi.org/10.5194/essd-17-6557-2025

Wilmouth, D. M., Hare, J. S., Howar, L. V., Salawitch, R. J., Hintsa, E. J., Smith, J. B., Sayres, D. S., et al. (2026). Analysis of inorganic chlorine chemistry in the midlatitude summer

stratosphere using aircraft and satellite observations. *EGUsphere*, *2026*, 1–29. [preprint], https://doi.org/10.5194/egusphere-2026-3480

Wilmouth, D. M., Østerstrøm, F. F., Smith, J. B., Anderson, J. G., & Salawitch, R. J. (2023). Impact of the Hunga Tonga volcanic eruption on stratospheric composition. *Proceedings of the National Academy of Sciences,* 120(46), e2301994120. https://doi.org/10.1073/pnas.2301994120

Wofsy, S. C., McElroy, M. B., & Yung, Y. L. (1975). The chemistry of atmospheric bromine. *Geophysical Research Letters*, *2*(6), 215–218. https://doi.org/10.1029/GL002i006p00215

Wolff, M. A., Kerzenmacher, T., Strong, K., Walker, K. A., Toohey, M., Dupuy, E., et al. (2008). Validation of HNO_3, $ClONO_2$, and N_2O_5 from the Atmospheric Chemistry Experiment Fourier Transform Spectrometer (ACE-FTS). *Atmospheric Chemistry and Physics*, *8*(13), 3529-3562. https://doi.org/10.5194/acp-8-3529-2008

Woodbridge, E. L., Elkins, J. W., Fahey, D. W., Heidt, L. E., Solomon, S., Baring, T. J., et al. (1995). Estimates of total organic and inorganic chlorine in the lower stratosphere from in situ and flask measurements during AASE II. *Journal of Geophysical Research: Atmospheres*, *100*(D2), 3057-3064. https://doi.org/10.1029/94JD02744

World Meteorological Organization (WMO). *Scientific Assessment of Ozone Depletion: 2022*, GAW Report No. 278, 509 pp.; WMO: Geneva, 2022.

Wunch, D., Toon, G. C., Wennberg, P. O., Wofsy, S. C., Stephens, B. B., Fischer, M. L., et al. (2010). Calibration of the Total Carbon Column Observing Network using aircraft profile data. *Atmospheric Measurement Techniques*, *3*(5), 1351–1362. https://doi.org/10.5194/amt-3-1351-2010

Yang, E.-S., Cunnold, D. M., Newchurch, M. J., Salawitch, R. J., McCormick, M. P., Russell III, J. M., et al. (2008). First stage of Antarctic ozone recovery. *Journal of Geophysical Research: Atmospheres*, *113*(D20). https://doi.org/10.1029/2007JD009675

Yang, E.-S., Cunnold, D. M., Salawitch, R. J., McCormick, M. P., Russell III, J., Zawodny, J. et al. (2006). Attribution of recovery in lower-stratospheric ozone. *Journal of Geophysical Research: Atmospheres*, *111*(D17). https://doi.org/10.1029/2005JD006371

Yue, J., Russell III, J., Gan, Q., Wang, T., Rong, P., Garcia, R., & Mlynczak, M. (2019). Increasing Water Vapor in the Stratosphere and Mesosphere After 2002. *Geophysical Research Letters*, *46*(22), 13452–13460. https://doi.org/10.1029/2019GL084973

Zander, R., Mahieu, E., Gunson, M. R., Abrams, M. C., Chang, A. Y., Abbas, M., et al. (1996). The 1994 northern midlatitude budget of stratospheric chlorine derived from ATMOS/ATLAS-3 observations. Geophysical Research Letters, 23(17), 2357-2360. https://doi.org/10.1029/96GL01792

Zhang, J., & Donahue, N. M. (2006). Constraining the mechanism and kinetics of OH+ NO2 and HO2+ NO using the multiple-well master equation. The Journal of Physical Chemistry A, 110(21), 6898-6911. https://doi.org/10.1021/jp0556512

Zhang, J., Wang, P., Kinnison, D., Solomon, S., Guan, J., Stone, K., & Zhu, Y. (2024). Stratospheric chlorine processing after the unprecedented Hunga Tonga eruption. Geophysical Research Letters, 51(17), e2024GL108649. https://doi.org/10.1029/2024GL108649